

MODELING AND ANALYSIS OF WIND ENERGY CONVERSION SYSTEMS
AND ITS IMPACT ON POWER SYSTEM



Umesh Chaudhary



Modeling and Analysis of Wind Energy Conversion Systems and its Impact on Power System

A

Thesis submitted

for the award of the degree of

Doctor of Philosophy

By

Umesh Chaudhary



Department of Electronics and Electrical Engineering

Indian Institute of Technology Guwahati

Assam—781 039, India

October 2023





Dedicated

to

My beloved **Mother** Late Chameli Devi
for her blessings, love and unconditional support...



Certificate

This is to certify that the thesis entitled “**Modeling and Analysis of Wind Energy Conversion Systems and its Impact on Power System**” submitted by **UMESH CHAUDHARY** (11610226), a research scholar in the *Department of Electronics and Electrical Engineering, Indian Institute of Technology Guwahati*, for the award of the degree of **Doctor of Philosophy**, is a record of an original research work carried out by him under my supervision and guidance. The thesis has fulfilled all requirements as per the regulations of the institute and in my opinion has reached the standard needed for submission. The results embodied in this thesis have not been submitted to any other University or Institute for the award of any degree or diploma.

Dr. Praveen Tripathy

Associate Professor

Dept. of Electronics and Electrical Engg.

Indian Institute of Technology Guwahati

Guwahati - 781 039, Assam, India.

Prof. Sisir Kumar Nayak

Professor

Dept. of Electronics and Electrical Engg.

Indian Institute of Technology Guwahati

Guwahati - 781 039, Assam, India.

Dated:

Place: Guwahati

Dated:

Place: Guwahati



Acknowledgements

I am deeply honored and privileged to extend my heartfelt gratitude to my esteemed supervisors Dr. Praveen Tripathy and Prof. Sisir Kumar Nayak. Their constant supervision, encouragement, guidance, and personal support from the preliminary to the concluding level played an invaluable role in helping me develop a profound understanding of the subject matter. It was an honor for me to work under their supervision and be part of their research team in the Power and Control Laboratory. The successful completion of my thesis would not have been possible without the immense facilities and the freedom to work that they generously provided.

I extend my deep gratitude to the members of the doctoral committee Prof. Chitralkha Mahanta, Dr. Srinivasan Krishnaswamy and Dr. Ravindranath Adda for their valuable suggestions and scrutiny of this work. I am also grateful to Prof. Somanath Majhi and Prof. G. B. Shrestha for sparing their precious time to evaluate the progress of my work.

I would also like to thank the Head of the Department and the other faculty members for their kind help in carrying out this work. I am also grateful to all the members of the research and technical staff of the department without whose help I could not have completed this thesis. My special thanks to Dr. Sanjib Das, Dr. Madhuriya Pratim Das, Mr. Ridib Bharali and Mrs. Riju Rabha for helping me with simulation work during my research period.

I am indebted to all my seniors, especially Dr. Mukesh Singh, Dr. Ankit Dalal, and Dr. Mridul Kanti Malakar for providing a warm research atmosphere, sharing knowledge and personal support. I am also thankful to my friends and juniors, specially Dr. Dheeraj Sinha, Dr. Satbarat Dash, Dr. Nagraj Adiga, Dr. Kashayap Prabhakar, Dr. Himanshu Shekhar Sahu, Dr. Shekha Rai, Dr. Brijesh Kumar, Dr. Prosenjit Modal, Dr. Kitaba Tefera, Dr. Amit Baghel, Ms. Tako Nama, Dr. Jagath Vallabhai Missula, Dr. Rajendra Kumar, Mrs. Binita Nanda, Dr. Upasana Sarma and Ms. Himani Mattoo who have helped me and made my stay in IIT Guwahati exciting and gave me beautiful memories.

I owe my deepest gratitude to my parents and relatives for their love, affection, care, and constant encouragement throughout the research work. Finally, I would like to give special acknowledgment to my brothers Krishana Deo, Binod, and Rajesh, and my niece, Priya for their continuous support, love, and encouragement.

UMESH CHAUDHARY



Abstract

The development of industrial societies, witnessed a tremendous increase in energy demand to support socioeconomic development. The worldwide climate change and depleting fossil fuel are forced humankind to search for an alternate green energy sources. Renewable energy sources such as biogas/biomass, fuel cells, geothermal, hydro, tidal, solar, wind energy, etc., are become viable alternatives for power generation. Among them, wind energy has remained a popular source due to its commercial viability and low carbon footprint. It is observed that the net power production in the wind energy sector has undergone steady growth in the recent past.

The power production and efficiency of the wind turbine are mostly influenced by the airfoil profile and forces acting on the blades, which vary considerably from the aerodynamic structure. In this context, wind turbines are of two types depending upon their location, *i.e.*, onshore and offshore. Onshore wind turbines are easily accessible than offshore turbines and can be readily connected directly to the local power system. The wind speed in the onshore environment generally fluctuates due to various reasons, including its geographical features. Therefore, detailed analysis is necessary to select the appropriate airfoil shape and wind turbine location to ensure suitable blade structure and availability of the wind throughout the year.

In this thesis, the aerodynamic characteristics and the flow mechanism are investigated on two-dimensional (2-D) airfoils at a different angle of attack and changing wind speed. This work aims to calculate the optimum angle of attack to achieve the desired characteristics of the wind turbine. Here, the aerodynamic simulations are carried out using the computational fluid dynamics (CFD) techniques based on the finite-volume method. The governing-equations applied in the aerodynamic simulations are the Reynolds-averaged Navier-stokes (RANS) equations. The turbulent flow is modeled through the different turbulence models: Shear stress transport $k - \omega$ (SST) model, standard $k - \epsilon$ (SKE) model,

and realizable $k - \epsilon$ (RKE) model. The aerodynamic characteristics of both airfoils are used to find the optimum angle of attack.

After selection of appropriate airfoil, there is a need to develop a model for predicting the aerodynamic performance of the wind turbine. As per the standard IEC 61400-2, the primary blade design such as the chord length and twist angle of the wind turbines are calculated using optimal rotor theory. The aerodynamic performance of the wind turbine is analyzed using the blade element momentum (BEM) approach, including the Prandtl tip loss correction factor. The numerical computational technique is based on unsteady RANS equations with turbulence models. The results through simulations are also validated with the steady-state result obtained through the BEM theory. Since, the computational results takes significant time, hence, using the steady-state results obtained from BEM theory and computational results are utilized to propose a model which includes an equivalent second-order transfer function (TF) and BEM theory to estimate the aerodynamic performances of the wind turbine.

Presently, the energy generation from wind flow is gaining momentum worldwide due to the invention of new technologies related to the wind turbine installation. The wind power generation is observing a significant use of doubly-fed induction generator (DFIG) due to its improved efficiency, but the converter used in the configuration is sensitive to the presence of a fault in the grid. This thesis presents a fault ride-through (FRT) configuration, which includes a thyristor-based bridge-type non-superconducting fault current limiter (ThyBT-NSFCL) augmented with a buck converter. It has been observed that the proposed topology works fine under a temporary symmetrical fault. The analytical analysis has been carried out to observe the operating principle of the proposed ThyBT-NSFCL under both normal and fault conditions. The performance of the proposed topology is quite good, and it can be used as a reliable limiter for future wind energy applications.

The increasing capacity of generation from the wind energy sources has complicated the operational challenges related to stability, economic operation, etc., of an interconnected power system. Moreover, wind energy-based distributed generation (DG) plays a vital role in developing a sustainable grid. Due to the intermittent nature of wind energy source, the power output also poses potential technical challenges to the grid and utilities.

The technical challenges in the power system are the power quality issues such as voltage flicker, voltage sag, and swell of the distributed network. To study the influence of wind energy integration into the network, this thesis has utilized a modified distribution network of IIT Guwahati (MDN-IITG). Finally, the FRT capability of the wind generator is observed under the presence of FACTS devices in the system.

As power system technology increases the wind power penetration level of new types of generators in the existing transmission system, it experiences a change in the dynamics and functional characteristics of the whole system. Therefore, the impact of the wind power penetration on large-scale power systems stability becomes a crucial issue, hence, the influence of wind penetration on system dynamic stability needs to be properly investigated. In this thesis, an approach has been developed to analyze the impact of wind power penetration of wind power generators such as DFIG system after replacing it with a conventional synchronous machine of same capacity on the stability of power system in case of small disturbances. The effectiveness of the DFIG system with a control system is tested and validated on reduced North Eastern Regional Electricity Board (NEREB) 29-bus Indian power system. The simulation result reveals that integration of the wind turbine provides poor damping performance and the individual generators are affected under such conditions. From these results it has been concluded that the modern wind power penetration with power electronics and FRT capability can be integrated to large-scale power system without losing its stability. Moreover, the effectiveness of the observers has been verified through simulation study.



Contents

List of Figures	xxiii
List of Tables	xxix
List of Acronyms	xxxii
List of Symbols	xxxv
Glossary	xli
1 Introduction	1
1.1 Introduction	2
1.2 Wind Turbine and its Structural Evolution	4
1.3 Generator Configurations of WECS	6
1.3.1 DFIG-based Wind Turbine System	7
1.4 FRT Capability Enhancement Techniques	8
1.5 Power System Stability	9
1.5.1 Rotor Angle Stability	10
1.6 Literature Review	11
1.6.1 Literature Survey on Airfoil Profile	12
1.6.2 Literature Survey on Wind Turbine Design	12
1.6.3 Literature Survey on DFIG Controller	13
1.6.4 Literature Survey on FCL Configuration	14
1.6.5 Literature Survey on Power Quality Issues	15
1.6.6 Literature Survey on Stability Analysis	16
1.7 Motivation	16
1.8 Objective of the Thesis	17
1.9 Contribution	18

1.10 Thesis Organization	19
2 Qualitative Analysis of Aerodynamic Performance of Airfoil Profiles	23
2.1 Introduction	24
2.2 Theoretical Analysis: Basic Concepts of Aerodynamic Forces	27
2.3 Selection of the Aerodynamic Performance Influencing Parameters	31
2.3.1 Selection of 2–D NACA Series Airfoil	31
2.3.2 Study of NACA 63-412 and NACA 63-415 Airfoils Properties	32
2.3.3 Selection of the Free Wind Speed	32
2.3.4 Selection of Reynolds Number and Turbulence Intensity	33
2.4 Overview of Turbulence Models	33
2.4.1 Standard $k - \epsilon$ Model	34
2.4.2 Realizable $k - \epsilon$ Model	34
2.4.3 Shear-Stress Transport $k - \omega$ Model	34
2.5 Description and Methodology of the Numerical Set-up	35
2.5.1 Computational Domain Information and its Boundary Conditions	35
2.5.2 Solver Setting and Turbulence Model Selection	36
2.5.3 Mesh Refinement Strategy and its Grid Independence Study	38
2.6 Results and Discussion	40
2.6.1 Validation Process of the Computational Models	41
2.6.2 Investigation of Optimum Angle of Attack	42
2.6.3 Analysis of Pressure Coefficient	46
2.6.4 Analysis of Velocity Magnitude	47
2.6.5 Analysis of Pressure Field	47
2.7 Summary	54
3 Evaluation of Aerodynamic Performance of Wind Turbine	55
3.1 Introduction	56
3.2 Aerodynamics of the Wind Turbine	59
3.2.1 Kinematics of the Wind Turbine Blades	59
3.2.2 Conservation of Angular Momentum Theory	60
3.2.3 Blade Element Momentum (BEM) Theory	61

3.2.4	Loss Corrections	63
3.2.5	Overall Power Coefficient	64
3.2.6	Primarily Blade Geometry Design	65
3.2.7	Relationship Between Theoretical Coefficients	65
3.3	Approximation of Wind Turbine Dynamics with a Second Order Transfer Function . .	66
3.3.1	Steady-state Gain	66
3.3.2	Blade Natural Frequency	66
3.3.3	Formulation of the Aerodynamic Damping Ratio (ξ)	67
3.3.4	Overall Transfer Function	70
3.4	Algorithm Used for Design of the Blade Geometry and Implementation Procedure of the BEM Theory	71
3.5	Selection and Design of Wind Turbine Blade Parameters	71
3.5.1	Design of Free Wind Speed, Tip Speed Ratio, and Rotational Speed	71
3.5.2	Selection of 2–D Airfoil Profile and Angle of Attack	74
3.5.3	Calculation of Reynolds Number and Turbulent Intensity	76
3.6	Simulation Set-up Description and Methodology for Validation Purpose	76
3.6.1	Solid Geometry Model Development	77
3.6.2	Computational Domain Description and its Boundary Conditions	78
3.6.3	Solver Setting Details and Turbulence Model Selection	80
3.6.4	Meshing Topology and its Grid Independency Test	82
3.7	Results and Discussion	84
3.7.1	Validation of the Computational Simulations	85
3.7.1.1	Case–1: The $C_Q - \lambda$ and $C_P - \lambda$ curves of the Wind Turbine with R_1 (WT_{R1})	85
3.7.1.2	Case–2: The $C_Q - \lambda$ and $C_P - \lambda$ curves of the Wind Turbine with R_2 (WT_{R2})	85
3.7.1.3	Case–3: The $C_Q - \lambda$ and $C_P - \lambda$ curves of the Wind Turbine with R_3 (WT_{R3})	87
3.7.2	Analysis of the Torque Coefficient and Torque Response of the Wind turbines .	87

3.7.2.1	Case–1: The Torque Coefficient and Generated Torque Response with $R_1(WT_{R1})$	88
3.7.2.2	Case–2: The Torque Coefficient and Generated Torque Response with $R_2(WT_{R2})$	88
3.7.2.3	Case–3: The Torque Coefficient and Generated Torque Response with $R_3(WT_{R3})$	89
3.7.3	Accuracy of the developed approximate transfer function to represent the torque response	89
3.8	Summary	90
4	Development of Fault Ride Through for DFIG System	95
4.1	Introduction	96
4.2	Modeling of Turbine and Control Strategy	99
4.2.1	Dynamic Model of Wind Turbine	99
4.2.2	Control Strategy of the RSC	100
4.3	Proposed ThyBT-NSFCL Power Circuit Configuration and its Operating Principle	102
4.3.1	Proposed ThyBT-NSFCL Circuit Topology	102
4.3.2	Control Strategy	104
4.4	Analytical Analysis of the ThyBT-NSFCL	106
4.4.1	Under Normal Operating Condition	107
4.4.2	During Fault Operating Condition	108
4.4.2.1	Stage–1	108
4.4.2.2	Stage–2	108
4.4.3	Power Loss Calculations of the ThyBT-NSFCL	109
4.5	Design Methodologies and Estimation of Parameters for Proposed ThyBT-NSFCL	110
4.5.1	Design for DC Reactor Inductance	110
4.5.2	Design of Breaking Resistor	111
4.5.3	Design of Buck Converter for Series Charging Supply	111
4.6	Results and Discussion	112
4.6.0.1	Characteristics of Voltage Dip	113
4.6.0.2	Transient Stator Current Proficiency	114

4.6.0.3	Transient Rotor Current Proficiency	114
4.6.0.4	DC-Link Voltage	116
4.6.0.5	Electrical Torque Command	116
4.6.0.6	Active Power Transients	117
4.6.0.7	Voltage Dip at Machine Terminal Voltage	118
4.7	Summary	118
5	Impact of Integration of Wind Energy into the Micro-Grid	121
5.1	Introduction	122
5.2	A Typical Distribution Network with Distributed Generations	123
5.2.1	Detailed Description of Modified Distribution Network of IIT Guwahati (MDN-IITG) System	123
5.2.2	DFIG-Based Wind Turbine Power Unit	125
5.2.3	Distributed Static Synchronous Compensator (D-STATCOM) Model	125
5.2.4	Load Demands Curves	125
5.2.5	Wind Generation Profile	127
5.3	Results and Discussion	127
5.3.1	Steady-State Analysis	127
5.3.1.1	Voltage Regulation	128
5.3.1.1.1	Case #1: MDN-IITG without DFIG	128
5.3.1.1.2	Case #2: MDN-IITG with DFIG	128
5.3.1.2	Power Flows in Different Lines or Feeders	129
5.3.2	Dynamic Model Evaluation	133
5.3.2.1	Dynamic Stability Analysis Under Symmetrical (3L-G) Fault	133
5.4	Summary	138
6	Impacts of Wind Power Penetration on Dynamic Stability of Power System	139
6.1	Introduction	140
6.1.1	Stability Evaluation Index	141
6.2	Description of Test Cases	142
6.2.1	Reduced NEREB Indian Power System	142
6.3	Results and Discussion	144

6.3.1	Dynamic Stability on Reduced NEREB Indian Power System	144
6.3.1.1	Terminal Voltage of Generators	144
6.3.1.2	Rotor Angle of Generators	146
6.3.1.3	Rotor Speed of Generators	146
6.4	Summary	150
7	Summary and Conclusions	151
7.1	Important Findings	152
7.2	Contributions	154
7.3	Future work	155
A	Airfoil Data	157
A.1	Airfoil Coordinates Data	158
A.1.1	Profile of NACA 63-415 Airfoil Geometry Data for 2-D Simulation Modeling	158
A.2	Boundary Conditions of Airfoil for the Numerical Simulations.	159
B	Turbulence Models Derivation	163
B.1	Turbulence Model Derivations	164
B.1.1	Standard $k - \epsilon$ Model	164
B.1.2	Realizable $k - \epsilon$ Model	165
B.1.3	Shear-stress Transport $k - \omega$ Model	166
C	Wind Turbine Parameters	169
C.1	Wind Turbine Blade Design Calculation	170
C.1.1	Sectional Geometry Data of Optimum Blades Design for 3-D Simulation Modeling (For Optimum Chord Distribution)	170
C.1.2	Adopted Blade Design (For Linearised Chord Distribution)	170
C.2	Boundary Conditions of Wind Turbine for the Numerical Simulations.	172
D	Parameters of DFIG System	175
D.1	Appendices	176
D.2	Parameters of DFIG System	176
E	Data for MDN-IITG System	177
E.1	IIT Guwahati Parameter	178
E.2	DFIG-based System Parameter	180

E.3 D-STATCOM Parameter	181
F Data for Reduced NEREB Indian Power System	183
F.1 Data for 29-bus NEREB Indian Power System	184
F.2 DFIG-Based System Parameter	184
F.3 D-STATCOM Parameter	184
Bibliography	193
List of Publications	205
Bio-Data	207





List of Figures

1.2	A basic configuration of WECS.	3
1.3	Historical evolution in size of the wind turbine [1].	6
1.4	Different type of WECS configurations.	7
1.5	The DFIG-based wind turbine system configuration.	8
1.6	Classification of FCLs.	9
1.7	A typical wind turbine system includes electrical generator, converters, power transformer and utility grid (not to scale).	10
1.8	Classification of power system stability.	11
2.1	The resultant aerodynamic force and its components splits into two sets.	28
2.2	The aerodynamic forces (such as the pressure and shear-stress distributions) acting on an element of the airfoil surface.	29
2.3	The aerodynamic forces acting on an element of the airfoil (a) upper surface; (b) bottom surface.	29
2.4	Details of NACA six digit series [2,3].	31
2.5	The comparison fashion of the geometric shape of NACA 63-412 and NACA 63-415 airfoils cross-section curve.	32
2.6	The C-type computational flow domain: geometry and boundary conditions.	36
2.7	Generated mesh (Grid index 4) details (a) boundary layer elements near the leading edge (b) boundary layer elements near the trailing edge (c) whole C-type computational domain of the grid used.	39
2.8	The lift coefficient (C_L) compared with (a) experimental data by Bak <i>et al.</i> [4] for NACA 63-415 airfoil at $Re = 0.5 \times 10^6$; (b) Xfoil data by Drela and Youngren [3] for NACA 63-412 airfoil at $Re = 0.5 \times 10^6$	41

List of Figures

2.9	The drag coefficient (C_D) compared with (a) experimental data by Bak <i>et al.</i> [4] for NACA 63-415 airfoil at $Re = 0.5 \times 10^6$; (b) Xfoil data by Drela and Youngren [3] for NACA 63-412 airfoil at $Re = 0.5 \times 10^6$	42
2.10	The change in the lift coefficient (C_L) as a function of the angle of attack (α) for the five different wind speeds with (a) NACA 63-415 airfoil; (b) NACA 63-412 airfoil.	43
2.11	The change in the drag coefficient (C_D) as a function of the angle of attack (α) for the five different wind speeds with (a) NACA 63-415 airfoil; (b) NACA 63-412 airfoil.	43
2.12	The sliding ratio (C_L/C_D) as a function of the angle of attack (α) for simulations employing the SST model with (a) NACA 63-415 airfoil; (b) NACA 63-412 airfoil.	44
2.13	The optimum angle of attack for the selected NACA 63-415 and NACA 63-412 airfoil profiles at different wind speeds.	45
2.14	The sliding ratio of the NACA 63-415 and NACA 63-412 airfoil profiles at 7 m/s (a) at $\alpha = 0^\circ$, (b) at $\alpha = 5^\circ$, (c) at $\alpha = 10^\circ$, (d) at $\alpha = 15^\circ$, and (e) at $\alpha = 20^\circ$	45
2.15	Pressure coefficient plot of NACA 63-412 and NACA 63-415 airfoil profiles.	48
2.16	Voltage magnitude (m/s) superimposed on the streamlines computed using the SST, RKE and SKE models for NACA 63-415 airfoil.	49
2.17	Voltage magnitude (m/s) superimposed on the streamlines computed using the SST, RKE and SKE models for NACA 63-412 airfoil.	50
2.18	Pressure field superimposed on the streamlines computed using the SST, RKE and SKE models for NACA 63-415.	52
2.19	Pressure field superimposed on the streamlines computed using the SST, RKE and SKE models for NACA 63-412.	53
3.1	Schematic diagram of 2-D airfoil with the aerodynamic force components and velocity on a blade element.	60
3.2	Aerodynamic damping effect on the wind turbine structural model.	68
3.3	The velocity and force diagram for vibrating the blade according to the wind turbine structural model.	69
3.4	Geometric shape of NACA 63-415 airfoil cross-section curve [3].	75
3.5	Variation of chord length at radial position for different wind turbine.	77
3.6	Variation of twist angle at radial position for different wind turbine.	78

3.7	A 3–D solid model of the wind turbine with NACA 63-415 profile.	78
3.8	Schematic diagram of the computational domain (a) Front view; (b) Side view.	79
3.9	The side view of the cylindrical computational domain layout and its boundary conditions defined in ANSYS/Fluent software.	80
3.10	Typical wireframe mesh structure around the wind turbine rotor (a) Boundary conditions of the flow domain; (b) View of the wind turbine from axis of rotation.	83
3.11	Simulation results for $R_1 = 5$ m blade length (a) Variation of C_Q ; (b) Variation of C_P	86
3.12	Simulation results for $R_2 = 2.5$ m blade length (a) Variation of C_Q ; (b) Variation of C_P	86
3.13	Simulation results for $R_3 = 1.7053$ m blade length (a) Variation of C_Q ; (b) Variation of C_P	87
3.14	The time-dependent response for R_1 (a) Variation of the C_Q ; (b) Variation of the T_c	88
3.15	The time-dependent response for R_2 (a) Variation of the C_Q ; (b) Variation of the T_c	88
3.16	The time-dependent response for R_3 (a) Variation of the C_Q ; (b) Variation of the T_c	89
3.17	Procedure for validating the accuracy of the developed model.	90
3.18	Comparison of the developed, computational and proposed torque response for Case–1.	93
3.19	Comparison of the developed, computational and proposed torque response for Case–2.	93
3.20	Comparison of the developed, computational and proposed torque response for Case–3.	93
4.1	The proposed RSC control scheme of the DFIG wind turbine connected with the ThyBT-NSFCL.	99
4.2	Specific diagram of the proposed ThyBT-NSFCL (a) configuration; (b) control logic blocks.	103
4.3	The current conduction modes of thyristors before and during fault (a) DC reactor and line current; (b) gate pulse of each thyristor; (c) current of each thyristor.	106
4.4	Conduction modes of thyristor under fault (Thyristor of Gray colour \rightarrow OFF state and Black colour \rightarrow ON state).	107
4.5	The voltage dip at terminal of the DFIG system.	113
4.6	The DFIG system stator current behaviors (a) WCL; (b) with proposed ThyBT-NSFCL.	114
4.7	The DFIG system rotor current behaviors (a) WCL; (b) with proposed ThyBT-NSFCL.	115
4.8	The DC-link voltage behavior.	116
4.9	Electrical torque behavior.	117

List of Figures

4.10	Active power response at the PCC.	117
4.11	Effects of breaking resistance at the machine terminals.	118
5.1	The popular distributed energy generation resources.	122
5.2	A typical single-line layout of the MDN-IITG test system with renewable energy based DGs and load groups.	124
5.3	The residential area load profiles.	126
5.4	The hospital area load profile.	126
5.5	The central library and play ground area load profile.	126
5.6	The wind turbine generation profile.	127
5.7	The voltage profile without any distribution generation integration for M_1 in-feeder.	128
5.8	The voltage profile disturbance due to DFIG-based wind turbine integration in M_1 in-feeder.	129
5.9	The power distribution in the MDN-IITG test system for Case #1 & #2 (a) line flow 1–2; (b) line flow 3–4; (c) line flow 3–8; (d) line flow 3–12; (e) line flow 3–15.	131
5.10	The power distribution in the MDN-IITG test system for Case #2 (a) line flow 1–2; (b) line flow 3–4; (c) line flow 3–8; (d) line flow 3–12; (e) line flow 3–15.	132
5.11	The DFIG system with and without STATCOM device in the MDN-IITG test system (a) terminal voltage at bus 12; (b) terminal voltage at bus 14; (c) electromagnetic torque; (d) rotor position; (e) rotor speed; (f) DFIG slip; (g) active power; (h) reactive power.	135
5.12	The terminal voltage of the DFIG-WT in the MDN-IITG test system for Case #1 & 2 (a) at bus 1; (b) at bus 3; (c) at bus 6; (d) at bus 7; (e) at bus 10; (f) at bus 11; (g) at bus 13; (h) at bus 20.	136
5.13	The power flow in the MDN-IITG test system for Case #1 & #2 (a) line flow 1–2; (b) line flow 3–4; (c) line flow 3–8; (d) line flow 3–12; (e) line flow 3–15.	137
6.1	One-line diagram of reduced NEREB Indian power grid with DFIG system.	143
6.2	The terminal voltage of generators at different buses into reduced NEREB Indian power system for Case #1, #2 & #3	145

6.3	The rotor angle of synchronous machine at different buses of the NEREB test system for Case #1, #2 & #3	147
6.4	The rotor speed of synchronous machine at different buses of the NEREB test system for Case #1, #2 & #3	148





List of Tables

2.1	A summary of reported computational studies on airfoils at different Reynolds numbers.	26
2.2	Reynolds number (Re) and turbulent intensity (I) at different wind speeds.	33
2.3	The boundary conditions of the 2–D simulation [ANSYS USER GUIDE]	37
2.4	Discretizations of 2–D computational domain for the grid independency test on the airfoils. .	40
2.5	Calculated the mean square error at 7 m/s.	46
3.1	The design values of NACA 63-415 airfoil.	75
3.2	Calculation of Reynolds number (Re) and turbulent intensity (I) at different wind speed.	76
3.3	The boundary conditions of the 3–D wind turbines for the computational simulations.	81
3.4	Discretizations of 3–D computational domain for the grid independence test on the wind turbines.	84
3.5	Calculation of natural frequency, developed torque and MSE at different tip speed ratio.	91
3.6	Calculation of natural frequency, generated torque and MSE at different wind velocity.	92
5.1	Calculated average voltage and voltage deviation values at different buses.	130
5.2	Calculated average power and power deviation values in different lines.	133
6.1	Stability index at different buses.	149
A.1	Coordinates of NACA 63-415 airfoil section.	158
A.2	Coordinates of NACA 63-412 airfoil sections.	160
A.3	The boundary conditions of the 2–D airfoils for the numerical simulations [ANSYS USER GUIDE].	161
C.1	Geometry of the blade made of the wind turbine.	170
C.2	Adopted blade design calculation.	171

List of Tables

C.3	The specifications of the wind turbine characteristics.	171
C.4	Maximum glide ratio used for optimal calculation.	172
C.5	Wind turbine material properties.	172
C.6	Technical properties of the wind turbine.	172
C.7	The boundary conditions of the 2–D airfoils for the numerical simulations [ANSYS USER GUIDE].	173
E.1	Details of transmission line data of the MDN-IITG test system.	178
E.2	Details of load groups data.	178
E.3	Details of fixed shunt data.	178
E.4	Details of distributed generation sources and load groups.	179
E.5	Details of transformer data for the distribution network.	179
E.6	DFIG-based wind turbine parameters.	180
E.7	Voltage controller parameters.	181
E.8	Speed controller parameters.	182
E.9	Information on D-STATCOM.	182
F.1	Details of bus data.	185
F.2	Details of transmission line data.	186
F.3	Details of transformers data.	187
F.4	Details of fixed shunt data.	187
F.5	Synchronous machines data with inertia and governor models.	188
F.6	Parameters of the generator exciters (IEEE T1 voltage controllers).	188
F.7	Parameters of the generator exciters (IEEE T2 voltage controllers).	189
F.8	Parameters of the governor model (TGOV1 governor model).	189
F.9	DFIG-based wind turbine parameters.	190
F.10	Voltage controller parameters.	191
F.11	Speed controller parameters.	191
F.12	Details on STATCOM.	192

List of Acronyms

1–D	One–Dimensional
2–D	Two–Dimensional
3–D	Three–Dimensional
1–DOF	Single-degree of freedom
3– ϕ	Three Phase
B2B	Back-to-Back
BC	Boundary condition
BEM	Blade Element Momentum
BTFCL	Bridge-Type Fault Current Limiter
CB	Circuit Breaker
CB-NSFCL	Capacitor-Based Non-Superconducting Fault Current Limiter
CEA	Central Electricity Authority
CFD	Computational Fluid Dynamics
DFIG	Doubly-fed Induction Generator
DNS	Direct Numerical Simulation
DTC	Direct Torque Control
DTU	Technical University of Denmark
DVR	Dynamic Voltage Restorer
FACTS	Flexible AC Transmission System
FCL	Fault Current Limiter
FEC	Front-End Converter
FOC	Field-Oriented Control
FRT	fault Ride-Through

List of Acronyms

FVM	Finite-Volume Method
GWEC	Global Wind Energy Council
HFCL	Hybrid Fault Current Limiter
LE	Leading edge of the airfoil
LES	Large-eddy simulation
MDN-IITG	Modified Distribution Network of IIT Guwahati
MNRE	Ministry of New and Renewable Energy
MPPT	Maximum Power Point Tracking
NACA	National Advisory Committee for Aeronautics
NEREB	North Eastern Region Electricity Board
NREL	National Renewable Energy Laboratory
NSFCL	Non-Superconducting Fault Current Limiter
ORT	Optimal Rotor Theory
PI	Proportional Integral
PLL	Phase Lock Loop
PoI	Point of Interconnection
RANS	Reynolds-Averaged Navier-Stokes
RKE	Realizable $k - \epsilon$ Model
RNG	Renormalization Group $k - \epsilon$ Model
RSC	Rotor Side Converter
RSM	Reynolds Stress Model
S-PLL	Simple-Phase Locked Loop
SA	Spalart-Allmaras Model
SDBR	Series Dynamic Braking Resistor
SFCL	Superconducting Fault Current Limiter
SFCL-MES	Superconducting Fault Current Limiter-Magnetic Energy Storage
SFO	Stator Flux Orientation
SKE	Standard $k - \epsilon$ Model
SPWM	Sine Pulse Width Modulation
SSFCL	Solid-State Fault Current Limiter

SSSC	Static Synchronous Series Compensator
SST	Shear-Stress Transport $k - \omega$ Model
SS-HAWT	Small-Scale Horizontal Axis Wind Turbine
SSWT	Small-Scale Wind Turbine
STATCOM	Static Synchronous Compensation
TE	Trailing Edge of the Airfoil
TF	Transfer Function
ThyBT-NSFCL	Thyristor-Based Bridge-type Non-Superconducting Fault Current Limiter
Trans. SST	Transition SST Model ($\gamma - Re_{\theta t}$ Model)
TSR	Tip Speed Ratio
TT-NSFCL	Switched Impedance Transformer-Type Non-Superconducting Fault Current Limiter
UDF	User Defined Function
UIUC	University of Illinois at Urbana-Champaign
UPFC	Unified Power Flow Controller
URANS	Unsteady Reynolds-averaged Navier-stokes
VAWT	Vertical-Axis Wind Turbine
VSWT	Variable-Speed Wind Turbine
WCL	Without Any Current Limiter
WWEA	World Wind Energy Association
WECS	Wind Energy Conversion System



List of Symbols

Symbol	Definition	Units
a	Axial induction factor	1
a'	Tangential induction factor	1
a_c		
a_t	Swept area of the actuator disc (or rotor)	m^2
c_a	Aerodynamic damping	
c_{cr}	Critical damping	
C_D	Drag coefficient on airfoil	
$C_{D(\text{design})}$	Design drag coefficient	
$C_{D(\text{max})}$	Maximum drag coefficient	
C_L	Lift coefficient on airfoil	
$C_{L(\text{design})}$	Design lift coefficient	
$C_{L(\text{max})}$	Maximum lift coefficient	
C'_L	Rate of change of lift coefficient with angle of attack	
C_L/C_D	Lift/drag ratio	
$(C_L/C_D)_{\text{max}}$	Maximum lift/drag ratio	
C_p	Pressure coefficient	
C_P	Power coefficient of the wind turbine	
C_Q	Torque coefficient	
C_n	Normal force coefficient	
c_r	Chord length	
C_t	Tangential force coefficient	
D_{1-6}	Six diodes of rectifier	

List of Symbols

dS	Elemental area
dS_b	Bottom elemental airfoil surface area
dS_t	Upper elemental airfoil surface area
dr	Radial width
dv_r	Change in apparent axial wind velocity
F	Loss correction factor
F_A	Axial force
F'_A	Axial force per unit surface area
F'_{A_b}	Axial force acting on the bottom elemental airfoil surface area
F'_{A_t}	Axial force acting on the upper elemental airfoil surface area
F_D	Drag force
F_L	Lift force
F_N	Normal force
F_r	Resultant thrust force
F'_N	Normal force per unit surface area
F'_{N_b}	Normal force acting on the bottom elemental airfoil surface area
F'_{N_t}	Normal force acting on the upper elemental airfoil surface area
f_{sw}	Switching frequency
I	Turbulent intensity
i_{ms}	Stator magnetizing current
i_{sa}, i_{sb}, i_{sc}	3- ϕ stator currents
$i_{s\alpha}$ and $i_{s\beta}$	Stator currents in stationary reference frame
i_{rA}, i_{rB}, i_{rC}	3- ϕ Rotor currents
i_{xr}, i_{yr}	Rotor currents in rotor reference frame
i_{dr}, i_{qr}	Rotor currents in synchronously rotating reference frame
i_{dr}^*, i_{qr}^*	Reference rotor currents in synchronously rotating reference frame
k	Stiffness constant
k_G	Steady-state gain of the model
$k_{pd\omega}, k_{id\omega}$	Proportional and integral gain constants of the speed
k_{pdv}, k_{idv}	Proportional and integral gain constants of d -axis current

k_{pqv}, k_{iqv}	Proportional and integral gain constants of q -axis current
l	Span length of airfoil
L_m	Mutual inductance
L_r	Rotor inductance
L_s	Stator inductance
m_a	Modal moment of the wind turbine rotor
n	Number of turns
n_s	Number of sections across the whole blade strip
p	Pressure distribution over the surface of the airfoil
P_a	Wind power available
P_e	Electrical power generated by the generator
p_t	Pressure distribution on upper surface
P_T	Mechanical power generated
p_o	Static pressure on the airfoil surface
p_∞	Free stream pressure on the airfoil surface
$p_b(s_b)$	Pressure distribution on the bottom surface
q_o	Dynamic pressure on airfoil surface
Q_s	Stator reactive power
Q_T	Torque generated
r	Normal distance along the blade span
R	Turbine radius (or blade length)
R_1	Radius of first wind turbine blades for 1
R_2	Radius of second wind turbine blades for 2
R_3	Radius of third wind turbine blades for 3
R_h	Blade root radius
$R_{\text{mid-section}}$	mid-section of the blade length
Re	Reynolds number
s_{1-6}	Signals for the converter switches
s_b	Bottom surface of airfoil
s_t	Upper surface of airfoil

List of Symbols

T_{1-6}	Six thyristors of bridge rectifier
T'	Change in the axial force per unit length
T_d	Torque generated by the wind turbine
T_F	Thrust force
T_n	Forces acting in axial direction
T_t	Forces acting in tangential direction
u	Change in the axial wind velocity
v_o	Free wind speed
v_{amws}	Annual mean wind speed
$v_{ar}^*, v_{br}^*, v_{cr}^*$	3- ϕ rotor reference voltages
v_{dr}^*, v_{qr}^*	Rotor reference voltages in synchronously rotating reference frame
v_r	Axial flow velocity
V_r	Relative flow velocity
v_{ra}, v_{rb}, v_{rc}	3- ϕ rotor voltages
v_{sa}, v_{sb}, v_{sc}	3- ϕ stator voltages
v_t	Tangential flow velocity
$v_{s\alpha}, v_{s\beta}$	Stator voltages in stationary reference frame
\dot{x}	Structural velocity
\dot{x}_{tip}	Perturbation in the wind direction with velocity
\ddot{x}	Structural acceleration

Greek letter

α	Angle of attack
α_d	Design angle of attack
α_p	Firing angle
β	Pitch angle
η_e	Efficiency of electrical energy conversion system
η_m	Efficiency of mechanical energy conversion system
γ	Local twist angle
κ	Safety gap

λ	Tip speed ratio	
λ_d	Design tip speed ratio	
λ_r	Local tip speed ratio	
μ	Dynamic viscosity	
ϕ	Inflow angle	°
ψ_{ds}	Stator d -axis flux linkage	
ψ_s	Stator flux linkage	
ρ	Air density	kg/m ²
σ	Leakage factor	
σ_r	Blade solidity	
τ	Shear-stress distribution over the surface of the airfoil	
τ_t	Shear-stress distribution on upper surface	
$\tau_b(s_b)$	Shear-stress distribution on the bottom surface	
θ_e	Stator voltage vector angle	
θ_r	Rotor position	
θ_{sl}	Slip angle	
Υ	Sectional pitch angle	
φ	Oriented angle relative to the horizontal axis	
ω_e	Angular frequency of the stator voltage	
ω_{er}	Rotor speed error	
ω_n	Natural frequency	
ω_{n1}	Fundamental natural frequency	
ω_{n2}	Second natural frequency	
ω_{nLower}	Lower bound of natural frequency	
ω_{nUpper}	Upper bound of natural frequency	
ω_r	Rotor rotational speed	
ω_r^*	Rotor rotational reference speed	
ω_t	Rotational speed of the turbine	
ξ	Aerodynamic damping ratio of the wind turbine rotor	

Subscripts

- ds, qs denotes d and q -axis of stator quantities in rotating reference frame.
- dr, qr denotes d and q -axis of rotor quantities in rotating reference frame.
- i, j denotes integers vary from 1 to 4
- $\alpha s, \beta s$ denotes α and β -axis of stator quantities in stationary reference frame.
- $\alpha r, \beta r$ denotes α and β -axis of rotor quantities in stationary reference frame.
- xr, yr denotes x and y -axis of rotor quantities in arbitrary rotating reference frame.
- xs, ys denotes x and y -axis of stator quantities in arbitrary rotating reference frame.

Superscripts

- \times denotes complex conjugate.
- $*$ denotes a commanded or reference quantity.
- \rightarrow denotes a vector.
- δ denotes an error (reference - adjustable).
- \cdot denotes a differential operator.

Glossary

- ***ac to dc***: Converts alternating current into direct current.
- ***dc to ac***: It receives dc voltage input side and converts ac voltage at output side. The output voltage can be controlled by varying the on and off time of the converter switch.
- ***dc to dc***: Converts dc voltage to regulated dc voltage. Regulation can be achieved by controlling the duty ratio.
- ***Distribution Node***: Here distribution node means 11 kV/400 kV system.
- ***Feeder***: It is the main 11 kV line from which many subfeeder is branched.
- ***Substation***: Station means 33 kV distribution substation. This substation is a reduced network of typical Guwahati city distribution substation.
- ***Subfeeder***: Subfeeder means 11 kV/400 kV line spread across different area of the distribution network such as residential, office or commercial area.





1

Introduction

Contents

1.1	Introduction	2
1.2	Wind Turbine and its Structural Evolution	4
1.3	Generator Configurations of WECS	6
1.4	FRT Capability Enhancement Techniques	8
1.5	Power System Stability	9
1.6	Literature Review	11
1.7	Motivation	16
1.8	Objective of the Thesis	17
1.9	Contribution	18
1.10	Thesis Organization	19

1.1 Introduction

The intense use of fossil fuels to meet the increasing global energy demand over the last few decades has significantly aggravated the problem of global warming. To mitigate the effect of global warming, the world should now move towards the use of renewable energy sources such as wind, solar, biomass, geothermal, small-hydro, tidal, etc., for the environmentally friendly, and sustainable generation of electric power [5,6]. Among the various available green energy resources, wind energy is considered to have the least carbon footprint, and hence, widely used globally to produce electricity [7]. It is also one of the fastest-growing energy technology in the world.

At the end of 2022, the worldwide capacity of wind power generators reached 906 GW, growing by 77.6 GW over the preceding year. As per the data published by the world wind energy association (WWEA) and global wind energy council (GWEC), the industries related to wind power generation can generate 2000 TWh/annum, which is about 7% of worldwide total electricity usage [8,9].

According to the report published by CEA 2022 [10], the first five leading countries in terms of installed cumulative wind power capacity are China (365,964 MW), United States (140,862 MW), Germany (66,315 MW), India (41,930 MW), and Spain (29,308 MW). India still has not utilized its full wind potential, and it is in the 4th position based on installed capacities among the leading countries utilizing renewable power [11]. Amongst various renewable energy sources, about 41.10% of power is produced from wind (CEA Report, 2022) [10]. Fig. 1.1 shows the contribution of power from various renewable energy sources in India.

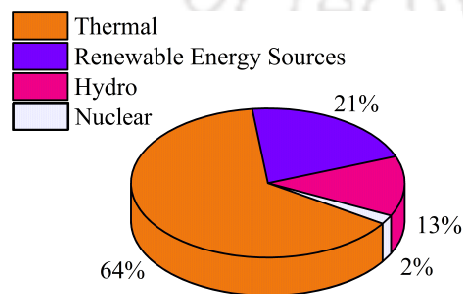


Fig. 1.1: Contribution of various energy sources.

It is to be noted that India's vision is to increase its installed capacity, the target is about 450 GW of renewable energy within 2030, an Ministry of New and Renewable Energy (MNRE) statement [11]. However, there are numerous wind turbine technologies available in the market for large wind turbines [12]. But these technologies are not suitable for locations with low wind speed. Hence, there is a need to design and develop wind turbines that can operate at low speeds. The large numbers of them can meet the energy requirements of a small town or a village. These small wind turbines are much affected by terrains and topographies, are found to affect the characteristics of wind flow significantly [13,14]. Therefore, these scenarios motivate us to pursue a thesis work in the small-scale wind turbines (SSWT).

The wind energy conversion system (WECS) unit integrated with power system mainly consists of (a) the wind turbine, (b) a mechanical power transmission device *i.e.*, gearbox, (c) an electric generator, (d) controller, and (e) an electricity storage and consumers/grid system as shown in Fig. 1.2. The wind turbine can be defined as a rotating machine that converts the kinetic energy of wind flows movement into mechanical power. With the help of electrical generators, the mechanical energy is converted into electricity. Generally, the electricity produced through the generators is supplied directly to the grid system in the grid-connected WECS. However, the generated power from the WECS can be stored in the battery or supplied to the consumers directly to meet the individuals' electricity demands.

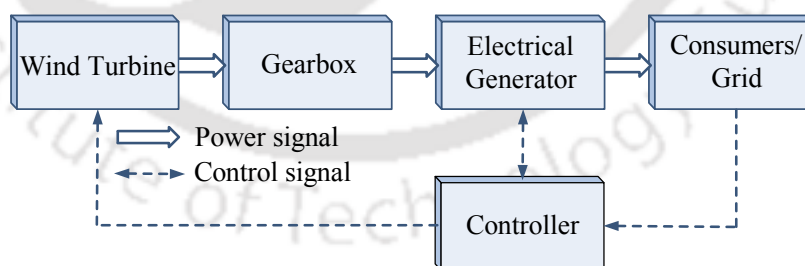


Fig. 1.2: A basic configuration of WECS.

The wind turbine is the most important part of the WECS. They can be broadly categorized into two groups according to their axis of rotation [15] *i.e.*, vertical-axis wind turbine (VAWT) and horizontal-axis wind turbine (HAWT). The wind turbines which are rotating about their horizontal axis are called HAWT, and those that are rotating about the vertical axis are called VAWT. The VAWT can operate independently of wind direction and are typically small in size, easy to construct, transport, install, requires low initial and maintenance costs. However, horizontal-axis turbines are

1. Introduction

more popular, as it can produce more power and is also commercially viable for a large population. These turbines can be installed on land or in the ocean, where a vast area is available with significant wind flow throughout the year. Therefore, wind turbines can be further classified into two groups based on their location *i.e.*, onshore wind turbines and offshore wind turbines.

To have a more efficient WECS, it is important to increase the aerodynamic efficiency of the wind turbine blade. In this regard, the present work attempts to improve the efficiency of the wind turbine by selecting the optimum geometric parameters of the airfoil profile. Further, computing the aerodynamic performance evaluation of a wind turbine requires significant time [16], hence, the present work tries to fit a simple model to the data obtained from these computations. This developed model can be used for real-time control of the wind turbine.

The variable-speed wind turbine (VSWT) connected generators such as, the doubly-fed induction generator (DFIG), permanent magnet generator, and synchronous reluctance generator. Among these generators, the DFIG is most popular due to its low installation cost, high efficiency, and robustness. Furthermore, the DFIG provides numerous features such as decoupled control of active and reactive power, variable speed operation within $\pm 30\%$ of slip speed, and converter rating is about 20–30% of the generator rating, thus significantly lowering the cost of the system [17]. The DFIG system is observed to be affected by the presence of grid faults, hence, there is a need for a suitable fault ride-through mechanism for its protection from grid disturbances [18].

The present scenario of large-scale wind farms integration to the grid has a major impact on the safety, stability, reliability, and security of the power system [19]. Among these issues, maintaining stability and security are some of the prime concerns during the real-time operation of the grid. To ensure them, it is important to analyze the steady-state limit violations and stability of the power system [20].

The aerodynamic performance analysis of wind turbine blades, different types of generators used in the WECS, different configurations of FCL, and their comparative study are discussed in the subsequent section.

1.2 Wind Turbine and its Structural Evolution

Historically, the earliest known wind turbines were found in Sistan, the eastern province of Iran, during 9th century. These machines, then known as windmills, were primarily used for pumping

water, grinding flour, or driving the machinery [21]. With some changes in the design, these machines were used to produce electricity in rural areas during the late 19th century. These machines include multiple numbers of blades. A further major design modification was observed in 1957s when the Danish engineer Johannes Juul built three blades horizontal axis wind turbines.

The aerodynamics of a wind turbine blade is similar to that of an aircraft wing. The airfoil shape of the blade creates a difference in velocity on its two sides. Using Bernoulli's principle, the pressure of moving fluid decreases when the velocity increases and vice versa. This pressure difference on either side of the rotor leads to the net lift force that turns the blade. Thus, the power produced by a wind turbine is given by

$$P = \frac{1}{2} \rho a_t C_P v_o^3 \quad (1.1)$$

where, ρ is the air density, a_t is the rotor area, C_P is the wind turbine's efficiency, known as the power coefficient of the wind turbine, which depends on the blade parameters such as the aerodynamic profile, chord length, twist angle, pitch angle, tip speed ratio, etc., and v_o is the velocity of incoming wind.

For an ideal wind turbine, the maximum power coefficient is equal to 59.25%, as proved by German scientist *Albert Betz* in the early 1920s [22]. This is the maximum amount of energy that can be extract from the in-flowing wind, which is hard to achieve in reality due to the losses by the drag and blade surface roughness [23, 24]. Therefore, an actual wind turbine's power coefficient is around 35 ~ 40%, which is evaluated as a function of tip speed ratio, and the blade pitch angle. In general, the pitch angle is adjusted to maintain power output. The amount of electrical power generated by the turbine is expressed as

$$P_e = \eta_e \eta_m P \quad (1.2)$$

where, η_e and η_m are the coefficient of electrical and mechanical energy conversion, respectively.

The electrical power produced by a wind turbine as given by (1.1) indicates that a bigger rotor size produces more power. At present, the World's largest wind turbine, Haliade-X 12 MW [25], has a rotor diameter of 220 m. It is a 3-bladed offshore turbine whose first prototype was installed in Rotterdam port, the Netherlands, in 2019. Fig. 1.3 shows the evolution of wind turbines in terms of their size and power generation.

In general, the wind turbines rotate with a blade tip speed of around 80 ~ 90 m/s. As the tip

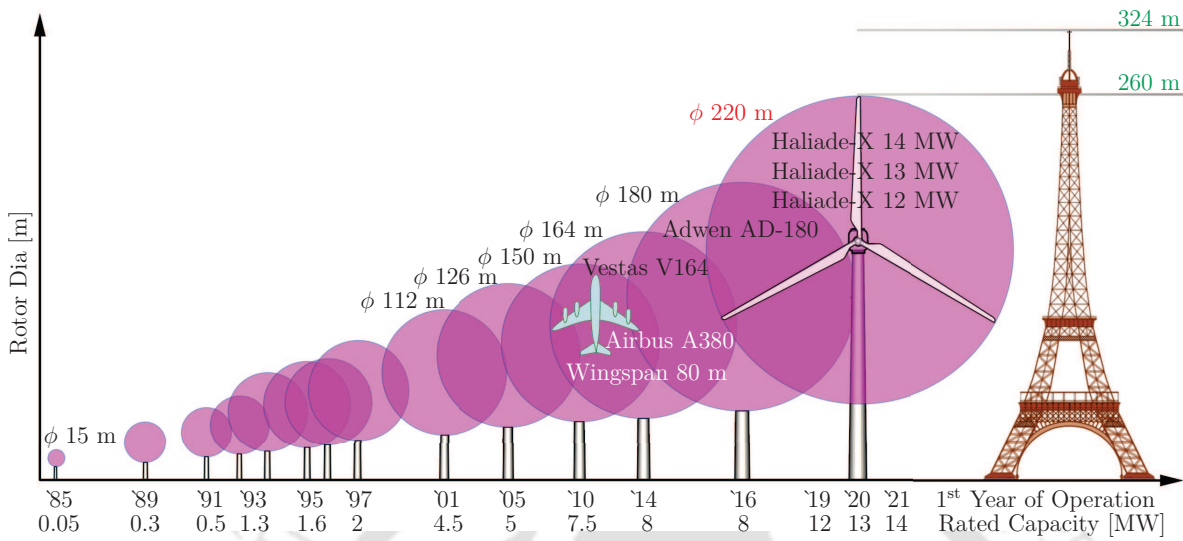


Fig. 1.3: Historical evolution in size of the wind turbine [1].

speed ratio increases, the wind turbines produce more noise due to friction with the air. Due to this reason, wind turbines of bigger size, *i.e.*, more than ~ 50 m (diameter) tend to make noise, which is prominent in its nearby areas. Further, its efficiency reduces due to the energy loss caused by friction and blade vibration. This also causes damage to the blade, which requires frequent maintenance. Hence, vibration control of wind turbine blades is essential in its design to make this technology commercially viable.

1.3 Generator Configurations of WECS

The WECS can be broadly classified into three major categories based on their operational speed: 1) Fixed speed, 2) Limited speed, and 3) Full variable speed. They are also categorized into five different types based on the types of generators used in the WECSs. Here, Type-1 considered for fixed-speed, Type-2 and Type-3 considered for limited speed, and Type-4 and Type-5 considered for full variable speed. The different types of WECS are summarized in Fig 1.4.

The merits and demerits of the different WECS configuration are as follows:

- (i) **Fixed Speed System:** The construction is reliable, and it has a simple electrical interface. However, severe stresses are observed on the mechanical parts, which requires additional attention on the safety during design. Moreover, the continuous cut-in and cut-off of capacitors are required to maintain the power factor, causing undesirable transients in line current and voltage.

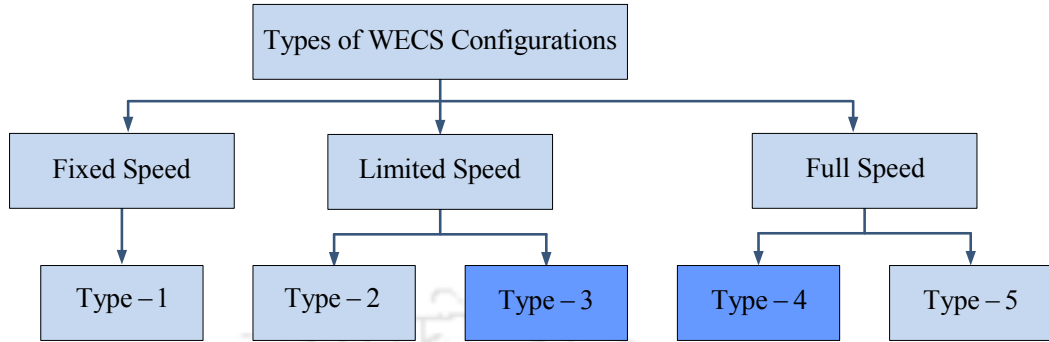


Fig. 1.4: Different type of WECS configurations.

- (ii) **Limited Speed System:** Overall converter cost is reduced since it requires to deliver only slip power instead of complete machine power. The rotor side converter (RSC) allows positive and negative power control. It also enables the operation of the machine in sub- and super-synchronous speed range. Moreover, the reactive power is supplied by DC-link capacitors, and hence, the power factor control on the stator side is possible. Here, the front end converter (FEC) works as an active filter that allows the unity power factor of the machine. Finally, it reduced system losses which improves the overall system efficiency.
- (iii) **Full Variable Speed System:** The mechanical oscillations are absent in the drive-train due to direct control of torque using techniques like direct torque control (DTC) or field-oriented control (FOC). The gearbox requirement is absent in the case of a multi-pole synchronous machine. The converter rating is be equal to the machine rating, as the total generated power passes through the converter. Here, the super-synchronous operation of the machine is not possible.

Among the different types of WECS, the present thesis mainly discuss the use of the DFIG system, which belongs to Type-4 category as shown in Fig 1.4. A brief overview of the DFIG-based WECS is given in the following subsection.

1.3.1 DFIG-based Wind Turbine System

A generic schematic diagram of a DFIG-based wind turbine system is shown in Fig. 1.5. In this figure, the back-to-back (B2B) converters of DFIG are referred to as rotor side converter (RSC) and front-end converter (FEC), respectively. The output of the FEC is connected to the utility grid through the $3-\phi$ grid filter. The RSC provides independent control of stator active and reactive powers. The active and reactive power flows between the converter and the grid are controlled by

FEC by using decoupled control strategy.

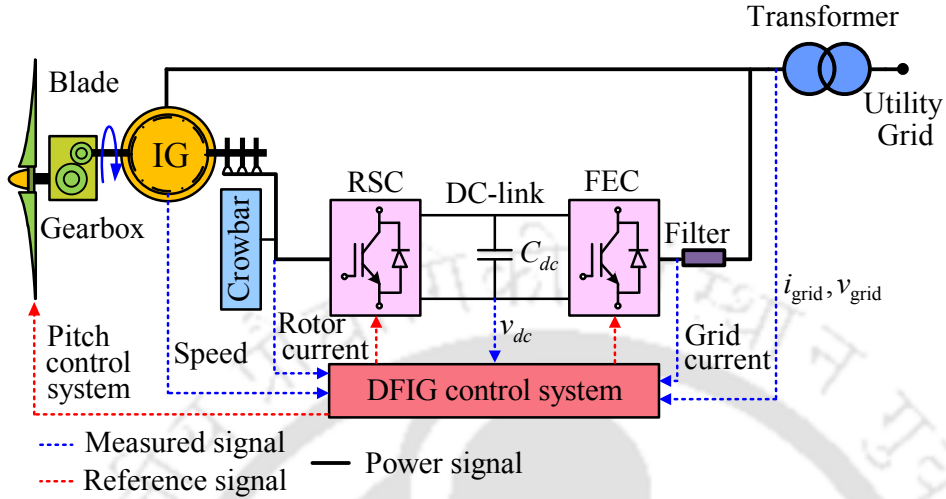


Fig. 1.5: The DFIG-based wind turbine system configuration.

The shaft of the DFIG system is connected to the wind turbine through the gearbox assembly unit. The turbine speed is controlled to extract maximum energy from the wind. This speed control of the wind turbine can be achieved through either control of the generated electrical power by the DFIG or through pitch angle control.

1.4 FRT Capability Enhancement Techniques

The power electronics converters used in the integration of renewable sources into the grid are severely affected by the presence of grid disturbances. Hence, the use of fault current limiters (FCLs) plays an important role in the integration of renewable sources into the grid. The technology associated with the FCLs are classified into four groups *i.e.*, superconducting FCLs (SFCLs), solid-state FCLs (SSFCLs), hybrid FCLs (HFCLs), and other techniques [26–28]. The main element in the SFCL is the superconducting material. This type of FCL is characterized by its low-loss and automatic fault limiting properties. The SSFCLs operate based on the power electronics switching principle. The HFCLs are recognized as a combination of SFCLs and SSFCLs. Finally, other types of FCLs are the ones whose operating principle is not similar to the other three classes. Fig. 1.6 shows the classification of FCLs.

The schematic diagram of the DFIG-based wind turbine system connected with the grid is shown in Fig. 1.7. The DFIG-based wind turbine system consists of a gearbox, RSC, FEC, DC-link, step-up transformer, point of interconnection (PoI), transmission lines, circuit breakers (CBs). The output

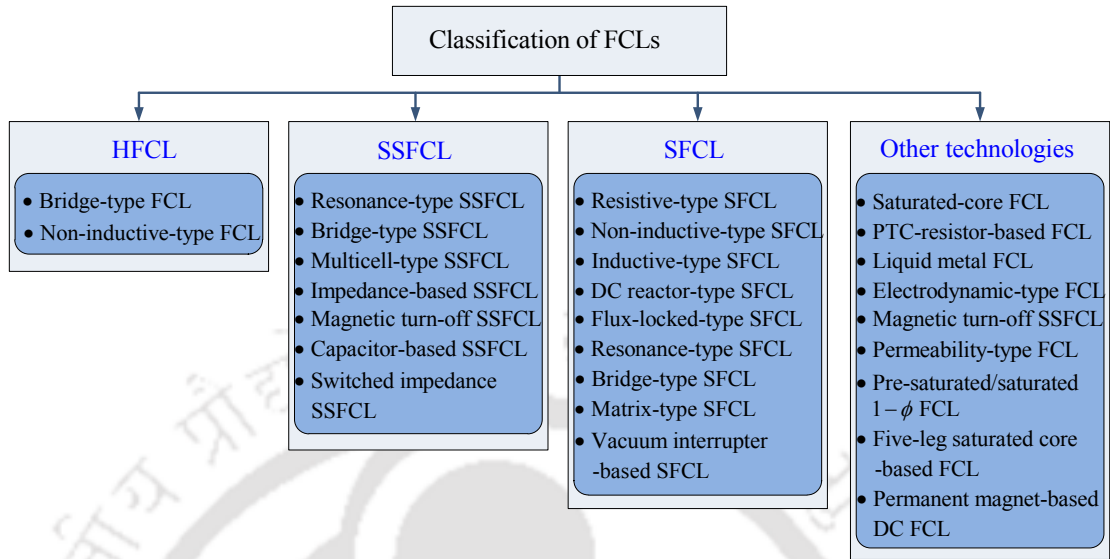


Fig. 1.6: Classification of FCLs.

power of the DFIG system is delivered to the utility grid through the power transformer and the transmission lines. The placement of the FCLs into grid is also mentioned as shown in Fig. 1.7.

1.5 Power System Stability

The joint Task Force of the IEEE-CIGRE group has defined power system stability [29] as “*the ability of an electric power system, for a given initial operating condition, to regain a state of operating equilibrium after being subjected to a physical disturbance, with most system variables bounded so that practically the entire system remains intact*”. The power system may experience different forms of instabilities, and it is difficult to analyse it by considering as a single problem and hence, requires proper classification. As cited in [29], the power system stability is mainly classified on the basis of 1) physical characteristics of the resulting mode of instability, 2) size of the occurred disturbances, and 3) time duration during which the stability phenomena occurs. On the basis of these criteria, the power system stability is broadly categorized into three types:

- (i) Rotor angle stability
- (ii) Frequency stability
- (iii) Voltage stability

The classification of power system stability is shown in Fig. 1.8. Voltage stability [29] is defined as “*the ability of a power system to maintain steady voltage at all buses in the system after being*

1. Introduction

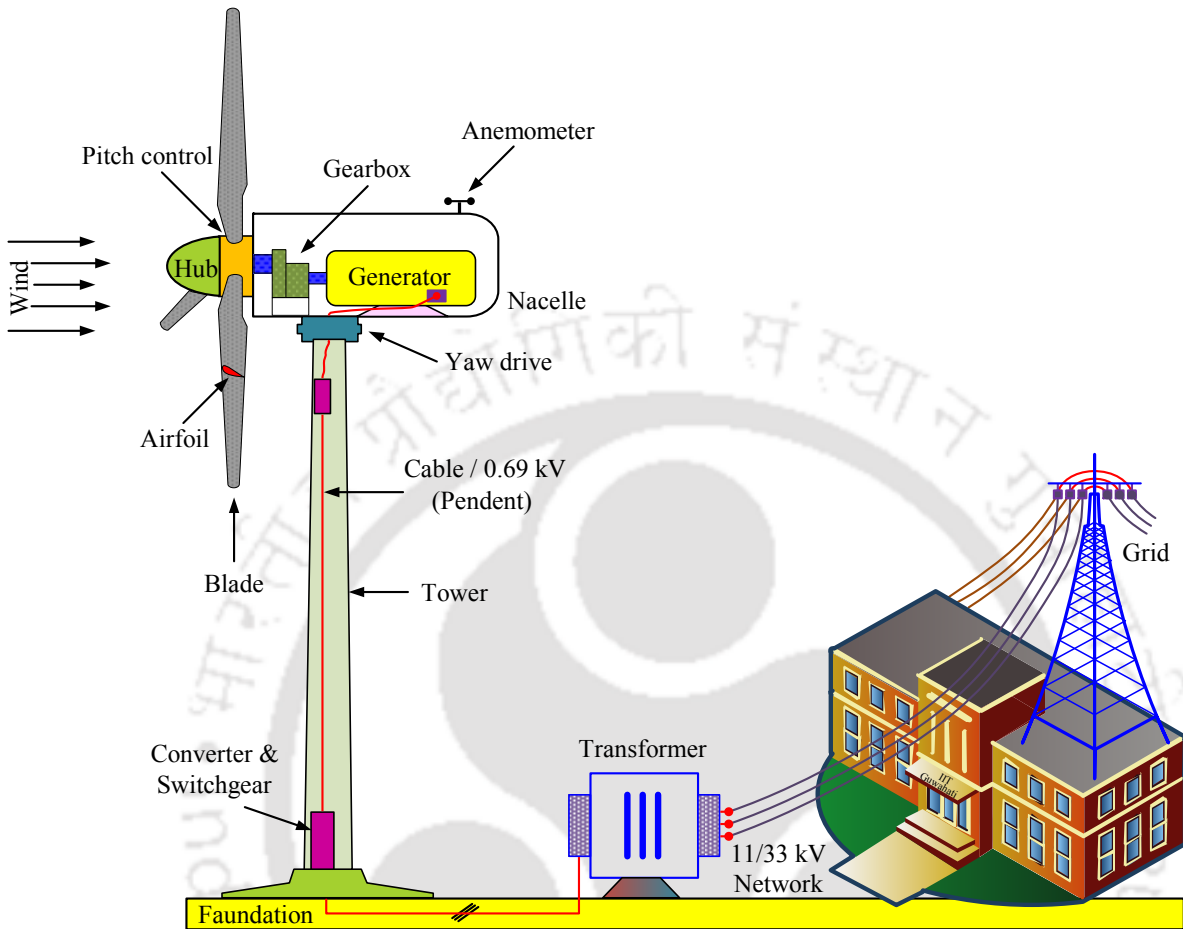


Fig. 1.7: A typical wind turbine system includes electrical generator, converters, power transformer and utility grid (not to scale).

subjected to a disturbance from a given initial operating condition”. It is again sub-classified into small disturbance and large disturbance voltage stability. These instability problems may range from a few seconds to tens of minutes, and therefore this phenomenon may either be short-term or long-term. Frequency stability [29] is defined as “the ability of a power system to maintain steady frequency following a severe upset resulting in a significant imbalance between generation and load”. It is further categorized into a short-term or long-term phenomenon. As the main focus of this thesis is on the estimation of the small-signal rotor angle stability, a detailed discussion of these instability phenomena is provided in the subsequent section.

1.5.1 Rotor Angle Stability

Rotor angle stability is defined [29] as “the ability of synchronous machines of an interconnected power system to remain in synchronism after being subjected to a disturbance”. It depends on the

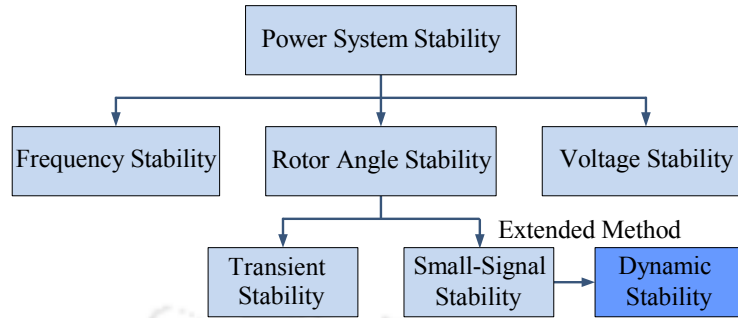


Fig. 1.8: Classification of power system stability.

ability to maintain or restore equilibrium between electromagnetic torque and mechanical torque of each synchronous machine connected to the power system.

The rotor angle stability is characterized into two subcategories.

- **Small disturbance or dynamic stability:** It is defined as the ability of the power system to maintain synchronism under small disturbances. The small-signal stability analysis is known as dynamic stability analysis. This stability analysis is mainly based on the linearized model of the power system at an operating point.
- **Large disturbance rotor angle stability or transient stability:** It is defined as the ability of the power system to maintain synchronism when subjected to a severe disturbance, such as a short circuit on a transmission line. It involves large rotor angle deviation, influenced by the nonlinear power versus angle relationship. The system stability to these transients depends on both the initial operating state of the system and the severity of the disturbance. This stability analysis mainly utilizes a non-linear model of the power systems.

1.6 Literature Review

Major challenges in the technological development of wind energy are associated with the design of the blades, the tower which supports the rotor, and other electrical equipments. The following subsections illustrate the current literature review of wind turbines' airfoil type, HAWT blades design, blade vibration control, electrical machine modeling and control, power quality issues, and stability analysis of the power system under disturbance.

1.6.1 Literature Survey on Airfoil Profile

The blade of the HAWT is divided into several elements or sections, consisting of an airfoil with an unsymmetrical curve surface. Several airfoil profiles are available in the literature, the National Advisory Committee for Aeronautics (NACA) series are widely used in the wind turbine design. The aerodynamic structure of the airfoil for wind turbine blades is extremely important for its aerodynamic performance [30, 31].

The accuracy of aerodynamic performance and power mainly depends on the reliability of airfoil data [32]. The aerodynamic forces such as lift and drag forces created as a consequence of the unequal pressure across the upper and bottom surfaces of the airfoil. Here, the lift force generates the required torque for the wind turbine rotor rotation, whereas the drag force causes stress on the structure of the wind turbine [33]. The lift/drag ratio is also known as the sliding ratio which is considered an important criterion of the aerodynamic efficiency of airfoil. The maximum sliding ratio of each airfoil depends on the relevant parameters such as the optimum angle of attack, structure of the airfoil profile, and wind conditions [34].

Simulation of the flow mechanism of aerodynamic features around airfoil profiles using computational fluid dynamics (CFD) software received the attention of many researchers in the last decade [35–37]. Singh *et al.* [38] developed a 2–D CFD software coupled with turbulence model using the Reynolds-averaged Navier-stokes (RANS) equations. Suvanjumrat *et al.* [39] presented the comparative study of the different turbulence models over an airfoil. Sayed *et al.* [34] performed the aerodynamic analysis of the flow over S809 and S826 blade profiles at low Reynolds number using 2–D computational finite-volume method [35]. Vendan *et al.* [40] analyzed the flow around the NACA 63-415 airfoil for low Reynolds number. Erkan and Ozkan [41, 42] investigated a 2–D, incompressible flow around the NACA 63-415 airfoil for Reynolds number. The computational analysis is used to examine the optimum angle of attack as the lift and drag forces are mainly dependent on the angle of attack.

1.6.2 Literature Survey on Wind Turbine Design

The optimal rotor theory (ORT) is used to design the blade parameters such as twist angle and chord length of the wind turbine blade sections [43]. The blade element momentum (BEM) theory is a concept that combines both one-dimensional (1–D) momentum theory and two-dimensional (2–D)

blade element theory. It is used to calculate the aerodynamic forces on the wind turbine blade. The BEM theory is the most popular tool for estimating aerodynamic forces acting on a rotating blade due to its efficiency and simplicity compared to other methods like CFD software. The National Renewable Energy Laboratory (NREL) developed software called AeroDyn [44] for estimating aerodynamic loads from the simulated wind field using BEM theory.

The BEM theory assumes that aerodynamic forces on a blade element (*i.e.*, airfoil) are independent (*i.e.*, no interaction between the elements) and solely depend on lift and drag coefficients. Therefore, tip loss corrections are suggested in the literature to improve the accuracy of the estimated aerodynamic performance using the BEM theory [45–47]. However, if the axial induction factor exceeds 0.4, the BEM theory fails, as the relation between the axial induction factor and the thrust coefficient is not valid in this case. Glauert [46] proposed an empirical relationship based on the experimental data to address this issue. But, this empirical curve does not accommodate tip and hub losses. Later, Buhl [47] extended this empirical solution with tip and hub loss corrections.

The traditional BEM theory solves the induction factors iteratively with these corrections, which frequently experience numerical convergence issues. Ning *et al.* [48] proposed a modified approach for solving the BEM theory with guaranteed convergence. This method evaluates the optimal flow angle instead of induction factors by segmenting the BEM equation into three regions (*i.e.*, momentum, empirical and propeller break) to enhance the convergence. Finally, Ning *et al.* [48] considered Buhl’s empirical relationship that incorporates various corrections to obtain a more accurate solution. In addition, Lanzafame and Messina [49] also introduced a new relationship of tangential induction factor in terms of the axial induction factor and local tip speed ratio to achieve the most accurate solution.

Duque *et al.* [50] developed a CFD software coupled with turbulence model using the RANS equations. Goundarzi [51] presented a comprehensive review of BEM theory and CFD analysis. The author proposed CFD with the BEM approach to calculate the aerodynamic loads more accurately at a low computational cost. But, the CFD software takes high computational time, the process of reducing aerodynamic load is also a point of concern.

1.6.3 Literature Survey on DFIG Controller

The DFIG-based WECS is recently gaining popularity due to its low cost as compared with the fully converter-based generation. For a grid-connected DFIG system, it is possible to achieve maximum

1. Introduction

power point tracking (MPPT) [52], the VSWT operation [17], and independent control of active and reactive powers [53]. In WECSs, the main aim is to maximize the turbine aerodynamic efficiency by controlling the turbine rotor speed for a partially steady load. The control of the turbine rotor speed is mainly done either by controlling the generated power or by blade pitch angle control.

The more difficult task is to design a controller which maximizes conversion efficiency while reducing the transient load which mainly arises due to vibration in the turbine. These vibrations are observed due to fluctuations in wind speed. Moreover, it is a challenging task to regulate both DFIG power output and generator speed at their optimal values. These fluctuations in power lead to variations in the torque and power supplied to the grid. The aerodynamic torque [54] variations also increase the voltage flicker. The non-linearity in system dynamics and continuous variation of the operating point makes the process of controller designing far more challenging.

Since, the stator side of the DFIG system is directly connected to the grid and the rotor side is connected *via* a B2B converter, the DFIG becomes very sensitive to the grid faults [55]. The wind turbine must continue to supply power to the grid even under the grid voltage dips or fault (symmetrical/asymmetrical) [56]. Therefore, it is important to explore a cost-effective and suitable method to enhance the FRT capability of the DFIG system for uninterrupted power flow operations under balanced/unbalanced grid faults [57–59].

1.6.4 Literature Survey on FCL Configuration

During the fault condition, the DC-link voltage must be stable and current fluctuations of the FEC must be limited. The DC-link voltage fluctuations might influence the rotor current control strategy which is undesirable. The DC-Link capacitor sizing has to be optimized for high voltage applications because it is heavy, expensive and has issues related to its reliability. In addition, the circuit breaker (CB) is also a piece of a protective device, which can automatically or manually trip. Though the CB has high-current interrupting capabilities, it is expensive [60, 61].

The technique is the most popular technique to limit the fault current in the DFIG-based wind turbine [62]. There is another method for reducing the fault current such as a static series compensator/dynamic voltage restorer (DVR) [63–65] to improve the FRT of the DFIG. A series dynamic braking resistor (SDBR) is used to improve the FRT of a large-scale power system composed of induction generators, while the SDBR is connected to the RSC of the DFIG to improve its FRT capability [66–68]. However, these methods need further modification to be more effective.

Therefore, it is important to develop a suitable method to enhance the FRT capability of the DFIG system. In [69], the authors have focused on the bridge-type fault current limiter (BTFCL), which utilizes a $1-\phi$ diode bridge rectifier connected to an inductor using the superconducting coil. Similarly, in [70], a $3-\phi$ rectifier-type FCL has been reported with a superconducting coil as a DC reactor without a DC-bias voltage source. This superconducting fault current limiter (SFCL) is costly and requires more maintenance [71]. The passive resistance network [72] and series antiparallel thyristors are connected to the stator of a grid-connected DFIG system [73].

In [74], a capacitor-based non-superconducting fault current limiter (CB-NSFCL) has been proposed, which also suffers from the disadvantage of high cost due to the presence of the voltage source and capacitor. In [75, 76], the non-superconducting fault current limiter (NSFCL) topology uses the diode bridge as a DC-bias voltage source and a non-superconducting coil with controllable switches connected across the breaking resistor. In [77], the switched impedance transformer-type non-superconducting fault current limiter (TT-NSFCL) topology is used to protect the DC reactor against high fault current, and uses a battery for loss compensation during normal operation. The use of the constant battery is not very effective in voltage compensation; moreover, it also increases the cost of the system, hence, is not economically feasible.

1.6.5 Literature Survey on Power Quality Issues

The wind energy-based distribution generation uses a small-scale generation source connected into the distribution networks [78, 79]. This system also increases the efficiency of the system as it reduces transmission losses.

The distributed generation may suffer from the problem of voltage regulation, hence, there is a need to utilize flexible AC transmission system (FACTS) devices in the system [80, 81]. The suitable operation of these FACTS devices can reduce the flows of heavily loaded lines, maintain the bus voltages at desired levels, and improve the power quality of the distribution network. Consequently, they can enhance the power system security under contingency situations [82]. Unified Power Flow Controller (UPFC) is a versatile FACTS device that can independently or simultaneously control the active power, the reactive power, and the bus voltage to which it is connected [83, 84].

1.6.6 Literature Survey on Stability Analysis

With the continuous increase in the penetration level of renewable sources, power system stability becomes an important issue. Therefore, considerable research efforts have been dedicated to addressing the wind power integration into the power system. The DFIG can control its reactive power to maintain the constant generator terminal voltage. However, the capability of the DFIG voltage control terminal voltage is limited as compared to the synchronous generator. Thus, the stability of the power system is affected when the controller could not control voltage to its reference value in a DFIG based WECS [85].

The reactive power of the DFIG can be enhanced by increasing the size of the converters. However, this solution increases the overall cost, which is one of the main advantages of DFIG over full power converter-based WECS [86]. The effect of reactive power supplied by wind generation on the rotor angle stability is examined [87]. The study concludes that the transient stability could be improved if the terminal voltage of the wind generation is controlled.

The impact of the integration of wind power generators on the oscillation and damping is observed after replacing the synchronous generator with the DFIG [88, 89]. The transient stability can be improved by some level with proper control strategies [85]. However, there is a limitation on the control strategies as the DFIG behaves as a conventional induction generator under fault conditions [90]. The generator types typically used in wind turbines do not participate in power system oscillations, thus, decreasing the number of synchronous generators participating in power system oscillations which significantly reduces the equivalent inertia of the power system [89]. The increase in wind power penetration along with the congestion at weak interconnecting lines further reduces damping of the system [91].

The majority of the reported works in the literature discuss the issues related to the WECS such as the selection of airfoil, wind turbine blades design, interface between the mechanical and electrical systems, protection of the electrical system, related power quality issues, and rotor angle stability, etc. separately. To the best of our knowledge, none of the works reported in the literature consider all issues simultaneously associated with the whole wind turbine system under disturbance.

1.7 Motivation

Considering the aforementioned limitations, the motivation of this research work are as follows:

- In order to gain the maximum energy from the wind turbines, the selection of appropriate

blade airfoil profiles is extremely important to capture energy from the wind and convert it into mechanical energy.

- The wind turbine design plays a vital role in maximizing aerodynamic efficiency. The wind turbine blade design starts with the knowledge of the aerodynamic forces acting on the blades, which can be calculated by BEM theory. For accurate estimation of the aerodynamic performance, computational techniques are required. Generally, the computational simulations are computationally expensive and take a long time to converge. Therefore, a computationally less expensive and accurate method is required to predict the aerodynamic performance of the wind turbine. Hence, this fact motivates to implement a simple, less expensive, effective design of the wind turbine.
- The complete model should consist of mechanical and electrical parts. Therefore, the interface between mechanical and electrical systems is required. The whole WECS is consists of a DFIG-based wind turbine system. The DFIG system is sensitive towards grid fault because the rotor winding is directly connected with the RSC. Therefore, the grid-connected DFIG system requires protection mechanisms to protect from abnormal grid disturbances.
- Renewable energy-based distributed generation plays a vital role in developing a sustainable grid. Due to the intermittent nature of renewable energy sources, the power output poses potential technical challenges to the grid and utilities. Therefore, suitable control of the distributed generations, reactive power compensation devices, and energy storage components need to be designed for the distribution network.
- Moreover, the complexity of modern power systems has increased in response to the integration of renewable energy sources. The substantial increase in the power demand result in the transmission lines operating closer to their limits. Consequently, the transmission lines are heavily loaded, and the system stability becomes a crucial factor in power transfer. Therefore, the design of the sophisticated FACTS device controllers is required to solve the various power system operation problems to enhance the power system stability.

1.8 Objective of the Thesis

The main purpose of the present study is to understand the design of wind turbines and their interface with electrical systems. Also, observe the penetration of wind power into the grid under

disturbance.

The objectives of the work performed in this thesis are summarized as

- To select the suitable airfoil shape which can enhance the design of geometrical parameters of the blade profiles.
- To develop a theoretical method to reduce the computational load and time for predicting the aerodynamic performance of the wind turbine in real-time operation.
- To modify FCL for enhancing the FRT capability of the DFIG-based wind turbine system. The developed FCL device must be robust, efficient, and less costly.
- To analyze the effect such as stability of renewable energy-based distribution generation on a distribution network. For the study, the distribution network considered is the modified distribution network of the IIT Guwahati (MDN-IITG) system.
- To analyze the impact on the stability with the penetration of wind energy in a transmission network. For the study, the network considered the reduced North Eastern Region Electricity Board (NEREB) 29-bus Indian power system.

1.9 Contribution

Based on the work reported in the literature and keeping the above mentioned objectives, the contributions of this thesis are as follows:

- To investigate computationally the aerodynamic performance of a two-dimensional (2-D) incompressible flow around NACA 63-412 and NACA 63-415 airfoil profiles. The aerodynamic simulations are performed using a numerical computational technique based on the finite-volume approach. The governing equations used in the simulations are the RANS equations. The aerodynamic loads and the flow physics over a particular blade profile are examined in detail to calculate the optimum angle of attack for different wind conditions.
- The primary blade design such as the optimum chord length and twist angle of the HAWT blade are calculated using optimal rotor theory. The wind turbine's aerodynamic performance is analyzed using the BEM theory considering the Prandtl tip loss correction factor. According to the turbulence model, the numerical computational technique is based on an unsteady Navier-Stokes solver for the wind turbine rotor to account for the transition in the boundary layer. Here, the numerical solutions are done using ANSYS/Fluent software to predict the aero-

dynamic performance. The numerical computational results are validated with the BEM theory for different airfoil profile-based wind turbines at various rotating conditions. This numerical technique takes too much computational resources and time; therefore, this work proposes a theoretical method that includes an equivalent second-order transfer function model of HAWT to estimate aerodynamic performance.

- The FCL configuration that includes a thyristor-based bridge-type non-superconducting fault current limiter (ThyBT-NSFCL) augmented with a buck converter is proposed. The ThyBT-NSFCL utilizes a loss compensator circuit, consisting of a DC-bias voltage source (includes voltage transformer and uncontrolled diode bridge rectifier) along with the buck converter. The proposed configuration effectively reduces the DC reactor conduction losses under normal operation.
- A study has been conducted to analyze the power systems stability issues of grid-connected renewable energy-based distributed generation. Further, the D-STATCOM device is used to improve the FRT capability of DFIG-based wind turbine connected with MDN-IITG.
- A study has been conducted to analyze the impact of wind power penetration on the system stability of power systems. It includes the transient stability analysis with the presence of a has DFIG-based wind turbine. Further to improve the stability, a STATCOM is also connected to provide reactive power support. The system used for the study is a reduced North Eastern Region Electricity Board (NEREB) 29-bus Indian power system.

1.10 Thesis Organization

The work carried out in this thesis is organized into seven chapters. The present Chapter discusses the basic concepts of the aerodynamic design of the SS-HAWT rotor and its interaction with the electrical system, power quality issues, and power system stability in its introduction section. It also gives the motivation behind the present research work, followed by the aims and objectives of the thesis.

- **Chapter 2** introduces the basic concepts of aerodynamics forces acting on the airfoil. The aerodynamic characteristics and the flow mechanism are investigated on airfoil profiles at a different angle of attack and changing wind speed. The turbulent flow is modeled through the different turbulence models along with the RANS model for investigating the flow mechanisms

over different airfoils. To validate the computational simulations results obtained using the different turbulence models are compared with the reported Xfoil solver, and the experimental data in the literature. Here, the optimum angle of attack is calculated for the different airfoils for a wide range of operating conditions. The aerodynamic performance of the airfoil is compared to the existing efficient airfoil. Finally, the selected airfoil is used for further studies in other Chapters.

- **Chapter 3** presents the modeling of wind turbines using BEM theory to calculate the aerodynamic performance. The computational technique is employed to validate the aerodynamic performance observed by the BEM theory. The computational technique takes a long computation time for calculation due to a high number of the mesh elements, and hence, requires high computational resources. Hence, a proposed theoretical method includes an equivalent second-order transfer function and BEM theory to estimate the aerodynamic performance. Finally, it is observed that the proposed theoretical method can accurately predict the aerodynamic performance for different pitch angles in real-time.
- **Chapter 4** presents the effectiveness of the FCL configuration to improve the FRT capability of the DFIG-based wind turbine. The analytical analysis is carried out to analyze the operating principle of the proposed ThyBT-NSFCL under normal and fault conditions. A comparative analysis is also done with existing FCL topologies. The simulation of the proposed ThyBT-NSFCL connected in series with a DFIG system is done using PSCAD/EMTDC software. The simulation results show that the proposed ThyBT-NSFCL is a better fault current limiter as compared with existing FCL topologies. The performance of the proposed topology is quite good, and it can be used as a reliable limiter for future wind energy applications.
- **Chapter 5** presents the influence of renewable energy integration into the microgrid. The main potential challenges are voltage variations and poor power regulation that reduces the power quality of the distribution network. Therefore, a detailed steady-state and dynamic analysis are carried out to study the impacts of wind power penetration such as DFIG-based wind turbines on the stability issues related to a microgrid. Further, the FACTS device such as D-STATCOM is used on a modified distribution network of IIT Guwahati (MDN-IITG) to improve its stability. To simulate the complete system under normal and fault conditions, Siemens PTI PSS® Sincal software is used. This study may provide a guideline to the utilities

for integrating renewable energy based distributed generation sources into the grid.

- **Chapter 6** deals with the detailed analysis on the effects of replacing a conventional synchronous generator with the equivalent DFIG-based wind turbine for a reduced North Eastern Region Electricity Board (NEREB) 29-bus Indian power system. The available reactive power of the DFIG system is utilized to reduce the impact of the DFIG-based wind turbine on the rotor angle stability of synchronous generators connected to the power system. To further reduce its impact, a D-STATCOM is utilized as an FRT device with the DFIG. The whole simulations are done using the Siemens PTI PSS®Sincal software. It is observed that the D-STATCOM significantly improves the rotor angle stability.
- **Chapter 7** concludes the significant findings of the thesis and presents a few suggestions for future research work.



2

Qualitative Analysis of Aerodynamic Performance of Airfoil Profiles

Contents

2.1	Introduction	24
2.2	Theoretical Analysis: Basic Concepts of Aerodynamic Forces	27
2.3	Selection of the Aerodynamic Performance Influencing Parameters	31
2.4	Overview of Turbulence Models	33
2.5	Description and Methodology of the Numerical Set-up	35
2.6	Results and Discussion	40
2.7	Summary	54

Objective

To extract more energy from the wind turbine, the selection of appropriate airfoil profiles is extremely important. In this paper, the aerodynamic characteristics and the flow mechanism are investigated on two-dimensional (2-D) basic NACA 63-412 and NACA 63-415 airfoil profiles at a different angle of attack with changing wind speed. This work aims to calculate the optimum angle of attack to achieve the desired characteristics of the wind turbine. Here, the aerodynamic simulations are carried out using the computational fluid dynamics (CFD) techniques based on the finite-volume method. The governing-equations applied in the aerodynamic simulations are the Reynolds-averaged Navier-stokes (RANS) equations. The turbulent flow is modeled through the different turbulence models: Shear stress transport $k - \omega$ model, standard $k - \epsilon$ model, and realizable $k - \epsilon$ model. The computational simulations are performed using ANSYS/Fluent, standard commercial software and its findings are validated against Xfoil and experimental data reported in the literature. The aerodynamic characteristics of both airfoils are used to find the optimum angle of attack.

2.1 Introduction

The traditional approach of aerodynamic modeling using an analytical approach does not provide a complete understanding of the flow mechanism around the airfoil, hence, it is difficult to improve its aerodynamic efficiency. In recent times, the computational fluid dynamics (CFD) techniques using the finite-volume method have significantly increased the understanding of the flow mechanism of aerodynamic features [35,92]. The governing equations used to conduct the aerodynamic simulations are the Reynolds-averaged Navier-stokes (RANS) equations [93–95]. The RANS equations along with the turbulence models are used to precisely predict the complex flow over the airfoil such as flow separation, flow reattachment, the laminar-turbulent transition of the flow [96], etc. To the best of the author's knowledge, there are no systematic studies conducted to assess the accuracy of the different turbulence models. Moreover, the models need to be compared with the published experimental data in the literature to identify the best-performing models for the airfoil.

The analysis of the aerodynamic characteristics of the airfoil remains challenging and perceived as an important research topic [97]. It mainly depends on the airfoil shape and the operating conditions of the wind turbine such as angle of attack, wind speed, etc. During the aerodynamic analysis, it is important to calculate the optimum angle of attack. Moreover, wind speed also plays an essential role

in affecting the aerodynamic performance of the airfoil. The wind speed varies significantly across the country and around the world [98]. In the North-East region of India, the annual mean wind speed usually is modest *i.e.*, 5 m/s or less [99], whereas, in the coastal region of India is typically more than 7 m/s. Hence, there is significant scope in designing the wind turbine for lower wind speed. This involves work to choose an appropriate airfoil profile that can effectively convert lower-speed wind energy into electricity.

The detailed literature reviews are presented here to provide insight into the flow mechanism of aerodynamic features around airfoil profiles at different turbulence models [35–37]. Sayed *et al.* [34] performed the aerodynamic analysis of the flow over S809 and S826 blade profiles at low Reynolds number using 2–D computational finite-volume method [35]. Further, Sayed *et al.* [35] also investigated the 2–D aerodynamic analysis for different types of airfoil at high wind speeds. Hoogedoorn *et al.* [36] presents the aerodynamic analysis over NACA 0008, and NACA 0012 airfoil using 2–D CFD-RANS simulations at high Reynolds numbers ($Re > 10^6$) under varying wind conditions. Singh *et al.* [38] presents 2–D CFD-RANS simulations, and compared them with reported experimental data. It is observed that the pressure distribution obtained through simulation is very close to the experimental data obtained around the airfoil. Suvanjumrat *et al.* [39] compared the different turbulence models over NACA 0015 airfoil and found that the shear stress transport $k - \omega$ model provides more accurate results. Villalpando *et al.* [37] performs the computational simulations over 2–D clean and iced NACA 63-415 airfoil for different Reynolds numbers and changing angles of attack.

Omar *et al.* [100] presents the effect of leading and trailing edges deflection over the flow around NACA 63-415 airfoil. The simulation also includes the results corresponding to the airfoil lift, drag, and pitching moment at a wind speed of 7 m/s using CFD-RANS equations, for changing angles of attack and control surface deflection angles. Vendan *et al.* [40] analyzed the flow around the NACA 63-415 airfoil for low Reynolds number using the Spalart-Allmaras (SA) turbulence model. The results show that the optimum angle of attack is found 2° at a low Reynolds number. Erkan and Ozkan [41,42] investigated a 2–D, incompressible flow around the NACA 63-415 airfoil for Reynolds number, which varies from 1×10^5 to 3×10^6 using the SA, and shear-stress transport $k - \omega$ models. The computational analysis is used to examine the optimum angle of attack. Here, the computational result shows that the optimum angle of attack varies between 2.5° and 3.5° depending on the Reynolds number.

A summary of reported CFD simulation on a stationary airfoil at different Reynolds numbers is

2. Qualitative Analysis of Aerodynamic Performance of Airfoil Profiles

Table 2.1: A summary of reported computational studies on airfoils at different Reynolds numbers.

Authors	Airfoil types	Reynolds number	Turbulence model	Dimension	Edge modified	Influencing parameters
Jain <i>et al.</i> [101]	NACA 0012	2.1×10^6	RANS (SA, RNG)	2-D	Gurney flap	$c_r = 0.05$ m $v_o = 614$ m/s
Yao <i>et al.</i> [102]	NACA 0018	5×10^5	RANS (RNG, SKE Trans. SST, RSM)	2-D	—	$c_r = 1$ m $v_o = 7$ m/s $v_o = 15.4$ m/s
Sayed <i>et al.</i> [34]	S809, S826	7.5×10^5	RANS (Trans. SST)	2-D	—	$c_r = 1$ m $v_o = 11$ m/s
Moshfeghi <i>et al.</i> [103]	S809	1×10^6	RANS (SST)	2-D & 3-D	Split	$c_r = 1$ m $v_o = 10$ m/s
Sayed <i>et al.</i> [35]	S809, S814, S815, S817 to S823, S825 to S835	6.85×10^5	RANS (SST)	2-D	—	$c_r = 1$ m $v_o = 11$ m/s
Talukder <i>et al.</i> [104]	S819, S821	6.8×10^4	RANS (SA)	2-D & 3-D	—	$c_r = 0.2$ m $v_o = 5$ m/s
Erkan & Ozkan [41]	NACA 63-4151	1×10^5 5×10^5 7×10^5 1×10^6 3×10^6	RANS (SA)	2-D	—	$c_r = 0.1$ m $v_o = 14$ m/s 73 m/s, 102 m/s 146 m/s, 430 m/s
Villalpando <i>et al.</i> [105]	NACA 63-4151	1.6×10^6	RANS (RNG, SA, SST, RSM)	2-D	Iced	$c_r = 0.6$ m $v_o = 40$ m/s
Villalpando <i>et al.</i> [37]	NACA 63-4153	3×10^5 , 5.7×10^5 , 8.4×10^5	RANS (SST)	2-D	Iced	$c_r = 0.2$ m $v_o = 19.9$ m/s 38 m/s, 56 m/s
Omar <i>et al.</i> [100]	NACA 63-4150	5×10^6	RANS (SST)	2-D	LE & TE deflection	$c_r = 1$ m $v_o = 7$ m/s
Iham <i>et al.</i> [106]	NACA 63-4154	6×10^5	RANS (Trans. SST)	2-D	—	$c_r = 1$ m $v_o = 7$ m/s

LE→Leading edge, TE→Trailing edge, RANS→Reynolds-averaged Navier-stokes, RNG→Renormalization Group $k - \epsilon$ model, RSM→Reynolds Stress model, SA→Spalart-Allmaras model, SKE→Standard $k - \epsilon$ model, SST→Shear-Stress Transport $k - \omega$ model, Trans. SST→Transition SST model ($\gamma - Re_{\theta t}$ model), c_r →Chord length, v_o →Wind speed.

presented in Table 2.1. The simulation is done for the types of airfoil used, operating range of Reynolds number, turbulence models employed, the dimensions of the computational simulation domain and geometry (2-D, 3-D), edge modified, and the influencing parameters such as wind speed and chord shape. The present work is concentrated on the stationary airfoil with a low Reynolds number.

As per the previous investigations, many studies are reported on the aerodynamic performance analysis over 2-D airfoil profile. However, the most of the available literature is on higher wind speed, but very limited work is reported on the aerodynamic performance of airfoils with low wind speed. Therefore, the present investigations are concentrated on the aerodynamic characteristics and flow mechanism of the NACA 63-412 and NACA 63-415 airfoils at a different angle of attack with low wind speed. Here, the turbulent flow is modeled through the different turbulence models such as shear-stress transport $k-\omega$ model (SST), realizable $k-\epsilon$ model (RKE), and standard $k-\epsilon$ model (SKE) to find a suitable RANS model for investigating flow mechanism over NACA 63-412 and NACA 63-415 airfoils. Further, the computational simulations results obtained using the different turbulence models are compared with the reported Xfoil solver and the experimental data in the literature. The objective of this study is to calculate the optimum angle of attack for the NACA 63-412 and NACA 63-415 airfoils at a wide range of operating conditions. The aerodynamic performance of the NACA 63-412 and NACA 63-415 airfoils are compared to know efficient airfoil at low wind speed. The outcome of this study is utilized in the selection of airfoil shapes for the design of the wind turbine blades.

This paper is structured as follows: Section 2.2 presents the basic concepts of the aerodynamic forces generated on the airfoil. The selection process of airfoil profile and parameters used as mentioned in Section 2.3. Section 2.4 gives the details of the applied turbulence models to observe the flow mechanism across the airfoils. The details of the computational set-up and the methodology used in the various computational cases, are presented in Section 2.5. The computational simulations are calculated, validated with the existing data of literature in Section 2.6. Finally, the conclusions are presented in Section 2.7.

2.2 Theoretical Analysis: Basic Concepts of Aerodynamic Forces

In fluid, the force is applied through the pressure or shear-stress exerted by the fluid to the surface of the airfoil. Hence, the net aerodynamic force or momentum is obtained by integrating the pressure (p) and the shear-stress (τ) distributions over the surface of the airfoil as shown in Fig. 2.1.

2. Qualitative Analysis of Aerodynamic Performance of Airfoil Profiles

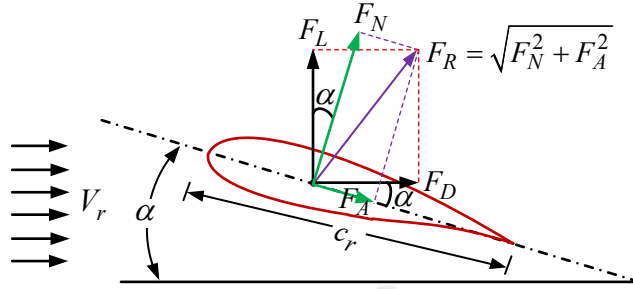


Fig. 2.1: The resultant aerodynamic force and its components splits into two sets.

The resultant aerodynamic force is split into perpendicular or normal force (F_N) and parallel or axial force (F_A) to the chord line of the airfoil as shown in Fig. 2.1. Whereas, the lift force (F_L) and the drag force (F_D) are the components of the aerodynamic forces in the parallel and perpendicular directions to the relative wind velocity, respectively. Here, the chord length of the airfoil is the linear distance between the leading and trailing edges, and the free wind speed (v_o) is considered as the flow far away from the airfoil. Whereas, the V_r is the relative wind speed near to the airfoil. The geometrical relation between the two sets of components are as follows:

$$F_D = F_N \sin \alpha + F_A \cos \alpha \quad (2.1)$$

$$F_L = F_N \cos \alpha - F_A \sin \alpha \quad (2.2)$$

where, α is the angle of attack, defined as the angle between chord line and relative wind velocity. Since, the blade is fixed, hence, the relative wind velocity is same as free wind velocity in the present study.

Consider the 2-D airfoil as shown in Fig. 2.2. The distance from the leading edge (LE) to an arbitrary point A on the top surface of the airfoil is denoted as s_t , whereas the distance between LE to an arbitrary point B on the bottom surface is denoted as s_b . The pressure and shear-stress distributions on upper surfaces are denoted by p_t and τ_t , respectively. They are also the function of s_t . Similarly, the pressure and shear-stress distributions on the bottom surfaces are denoted by $p_b(s_b)$ and $\tau_b(s_b)$, respectively. At every point, the pressure distributions are normal to an airfoil surface, whereas, the shear-stress distribution is tangential to airfoil surfaces, oriented at an angle of φ relative to the horizontal axis.

The total normal force (F'_N) and axial force (F'_A) due to the pressure and shear-stress distributions on the elemental area (dS). Here, the primes on F'_N and F'_A indicate force per unit span. The elemental

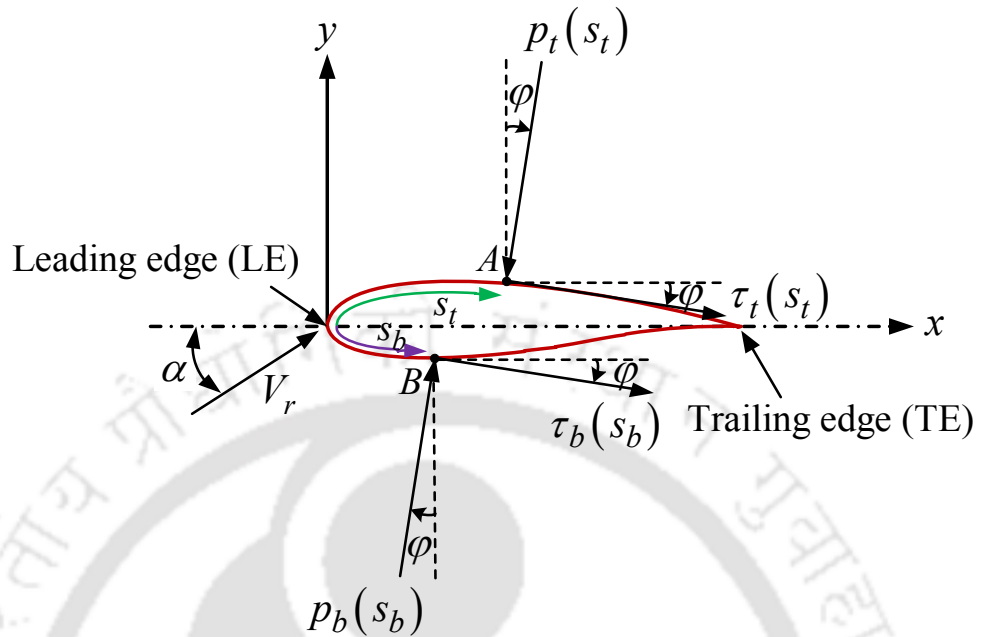


Fig. 2.2: The aerodynamic forces (such as the pressure and shear-stress distributions) acting on an element of the airfoil surface.

normal and axial forces acting on the upper elemental airfoil surface area (dS_t) [107] are as follows:

$$dF'_{N_t} = -p_t ds_t \cos \varphi - \tau_t ds_t \sin \varphi \quad (2.3)$$

$$dF'_{A_t} = -p_t ds_t \sin \varphi + \tau_t ds_t \cos \varphi \quad (2.4)$$

where, dS_t is the elemental airfoil upper surface area ($ds_t \times \text{span length}$), here, $l = 1$ is considered as airfoil span length as shown by the shaded area in Fig. 2.3.

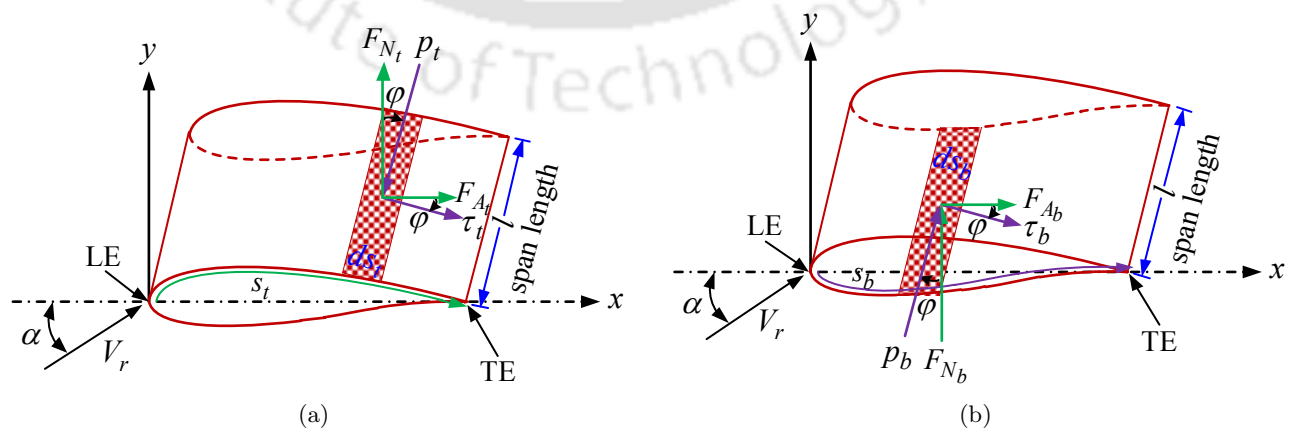


Fig. 2.3: The aerodynamic forces acting on an element of the airfoil (a) upper surface; (b) bottom surface.

2. Qualitative Analysis of Aerodynamic Performance of Airfoil Profiles

Similarly, the elemental normal and axial forces acting on the bottom elemental airfoil surface area (dS_b) are as follows:

$$dF'_{N_b} = p_b ds_b \cos \varphi - \tau_b ds_b \sin \varphi \quad (2.5)$$

$$dF'_{A_b} = p_b ds_b \sin \varphi + \tau_b ds_b \cos \varphi \quad (2.6)$$

where, dS_b is the elemental airfoil surface area ($ds_b \times \text{span length}$).

The integration of the pressure and shear-stress distributions acting on the upper and bottom surfaces from the leading edge (LE) to trailing edge (TE) of the airfoil is used to obtain the total normal force and axial forces per unit length, and which are obtained by integrating (2.3) to (2.6) and given in (2.7) and (2.8):

$$F'_N = - \int_{LE}^{TE} (p_t \cos \varphi + \tau_t \sin \varphi) ds_t + \int_{LE}^{TE} (p_b \cos \varphi - \tau_b \sin \varphi) ds_b \quad (2.7)$$

$$F'_A = \int_{LE}^{TE} (-p_t \sin \varphi + \tau_t \cos \varphi) ds_t + \int_{LE}^{TE} (p_b \sin \varphi + \tau_b \cos \varphi) ds_b \quad (2.8)$$

The total lift and drag forces per unit length (*i.e.*, $l = 1$) is obtained by substituting (2.7) and (2.8) into (2.1) and (2.2).

For a 2-D airfoil, the lift coefficient (C_L) and drag coefficient (C_D) in terms of the forces per unit length (*i.e.*, $l = 1$) are defined as

$$C_L = \frac{2F'_L}{\rho v_o^2 c_r} \quad (2.9)$$

$$C_D = \frac{2F'_D}{\rho v_o^2 c_r} \quad (2.10)$$

where, ρ is the air density, c_r is the chord length of the airfoil. These forces results into the torque and thrust forces on the wind turbine.

i.e., the sliding ratio (lift/drag ratio) can be defined by

$$\gamma = \frac{C_L}{C_D} = \frac{F'_L}{F'_D} \quad (2.11)$$

Further, the pressure coefficient in terms of the aerodynamic forces is presented as

$$C_p = \frac{p_\infty - p_o}{q_o}, \text{ where } q_o = \frac{1}{2} \rho v_o^2 \quad (2.12)$$

where, p_∞ is the static pressure on the airfoil surface, p_o is the free stream pressure, and q_o is the dynamic pressure.

This section aims to find the aerodynamic performance of the airfoil suitable for low wind speed.

2.3 Selection of the Aerodynamic Performance Influencing Parameters

Some organizations around the globe are extensively working towards the development of airfoil shapes such as the National Advisory Committee for Aeronautics (NACA) in the University of Illinois at Urbana-Champaign (UIUC) has developed four-digit NACA series [3], five-digit NACA series, and NACA six series. Similarly, the National Renewable Energy Laboratory (NREL) has developed S series of airfoil [108]. The other popular airfoil is Eppler airfoils [109] by Professor Richard Eppler, the Delft University airfoil profiles [110], and Risø airfoil by DTU national laboratory [111], etc.

The NACA six series airfoil is an extensively used airfoil to get maximum sliding ratio at low wind speed [2, 33]. The prefix NACA is accompanied by a sequence of digits, which helps identify the specific airfoil shape. This airfoil series is commonly used in the design process of efficient wind turbines, and commercial aeronautics.

2.3.1 Selection of 2-D NACA Series Airfoil

The selection of the appropriate airfoil plays a crucial role in designing small-scale wind turbines. NACA six series unsymmetrical airfoil profiles are often used to design and manufacture wind turbine blades. The definition of each digit of NACA series airfoil profiles and the different locations of the minimum pressure is explicitly defined in Fig. 2.4. With reference to the UIUC airfoil coordinates database developed by Michael Selig [3], NACA 63-412 and NACA 63-415 airfoils from NACA six series family are selected due to higher lift coefficient values, which is important to obtain the high power efficiency from the wind turbine.

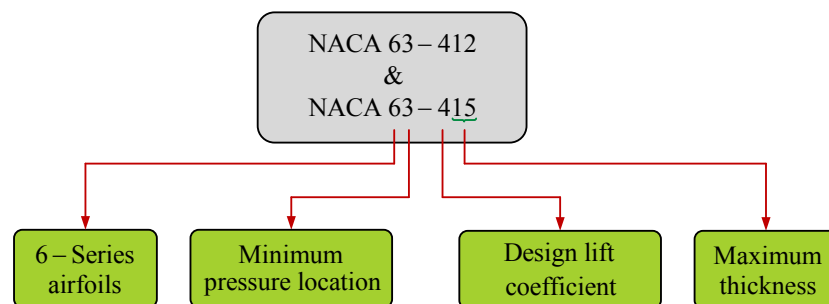


Fig. 2.4: Details of NACA six digit series [2, 3].

2.3.2 Study of NACA 63-412 and NACA 63-415 Airfoils Properties

These airfoils shape belongs to the NACA family with similar geometry, apart from their dimensions. The coordinates of the airfoils are taken from UIUC airfoil coordinate database [3]. The comparative curve of these airfoil profiles on the Cartesian plane is shown in Fig. 2.5. Here, the maximum thickness is 15% for NACA 63-415 and 12% for NACA 63-412 of its chord length (c_r), and the maximum camber is 2.2% of its chord length for both the airfoils. It is observed that NACA 63-415 airfoil is wider than NACA 63-412, hence, provides more flexibility for strengthening the blade structure. Earlier, these airfoils find their applications in small-scale variable-speed wind turbines with a rating of 2 to 20 kW.

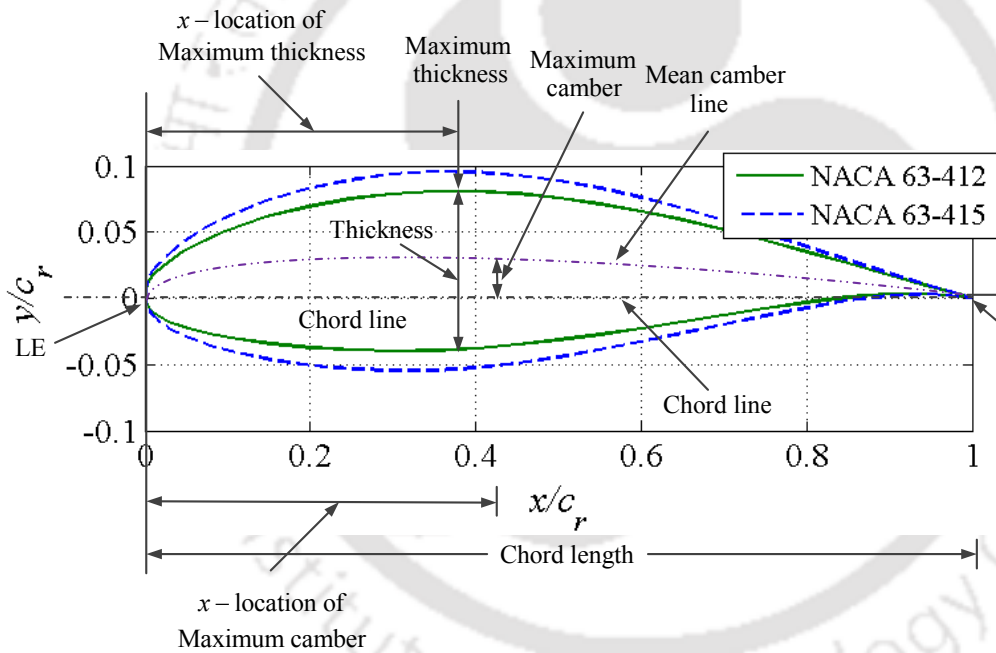


Fig. 2.5: The comparison fashion of the geometric shape of NACA 63-412 and NACA 63-415 airfoils cross-section curve.

2.3.3 Selection of the Free Wind Speed

IEC 61400-2 [112] standard related to the Class III wind turbine recommends the free wind speed for the variable-speed wind turbine blades to be 1.4 times of the annual mean wind speed (v_{amws}). Since, the present work assumes the annual mean wind speed of 5 m/s, hence, the free wind speed (v_o) is approximately equal to 7 m/s.

2.3.4 Selection of Reynolds Number and Turbulence Intensity

The airfoils aerodynamic performance is influence by the Reynolds number (Re) and is defined as [113]:

$$Re = \frac{\rho v_o c_r}{\mu} \quad (2.13)$$

where, μ is the dynamic viscosity of the air. The Reynolds number is physically a measure of the ratio of inertia forces to viscous forces in a flow.

Using the Reynolds number (Re), the turbulent flow parameters *i.e.*, the turbulent intensity (I) for the CFD study is defined as follows [114]:

$$I = 0.16(Re)^{-1/8} \quad (2.14)$$

The present study involves the analysis of the aerodynamic performances for both the airfoil profiles at changing wind speeds, and the results are shown in Table 2.2.

Table 2.2: Reynolds number (Re) and turbulent intensity (I) at different wind speeds.

v_o (m/s)	$\rho v_o c_r$ (kg/m·s)	Re	I (%)
5	6.08	3.4×10^5	3.26
7	8.59	4.8×10^5	3.12
10	12.17	6.8×10^5	2.99
15	17.89	1.0×10^6	2.85
20	25.05	1.4×10^6	2.73

The calculation of the optimum angle of attack for these particular airfoil profiles at low wind speed is hardly investigated in the literature. Hence, there is a need for performance validation through computational simulation and experimental verification for these airfoil profiles at low wind speed.

2.4 Overview of Turbulence Models

The concept of time-averaging to study the flow properties is one of the most widely used theories for modeling turbulence flows; here, the Reynolds-averaged Navier–Stokes equations (RANS) equations are solved. These RANS equations contain some of the fluctuating terms and are known as Reynolds Stress. Since, the RANS equations only solve the time average terms, hence, the Reynolds Stress is approximately modeled in terms of the time average terms. Now we will discuss some of the literature

2. Qualitative Analysis of Aerodynamic Performance of Airfoil Profiles

related to the development of these turbulence models for RANS equations. The earlier models were based on Boussinesq's assumption, here, the turbulent stresses are supposed to be proportional to the mean fluid flows [115]. This concept also gives rise to an imbalance between the unknowns and an available number of equations, and to solve this, related models are used [116,117]. Although it is not accurate, this is one of the most accepted methods for modeling the turbulence flows for industrial applications. Here, three types of two-equations eddy-viscosity turbulent models are named based on the additional equation that are solved along with the RANS equations, *i.e.*, shear-stress transport $k-\omega$ (SST) model, realizable $k-\epsilon$ (RKE) model, standard $k-\epsilon$ (SKE) model, etc. The computational economy, convergence limitations, and robustness of the eddy-viscosity models (two-equation models) are better for the steady flow simulation studies [118]. The details of the two-equation models are discussed below.

2.4.1 Standard $k-\epsilon$ Model

It is a two-equations model, and the classical method of it was proposed in 1972 by Launder and Spalding [119]. It's a two-equations model for the turbulence kinetic energy (k) and dissipation rate (ϵ) uses transport model equations. The $k-\epsilon$ model assumes that the flow is completely turbulent and that the effects of molecular-viscosity are minimal [120].

2.4.2 Realizable $k-\epsilon$ Model

The realizable $k-\epsilon$ model is developed by Shih *et al.* [121] to enhance the accuracy of the SKE models for a variety of flows, including rotation, boundary-layers with considerable high-pressure gradients, and vortex. It is obtained from the exact transport equations of the mean-square vorticity fluctuation, and uses an improved transport equation for the dissipation rate ϵ .

2.4.3 Shear-Stress Transport $k-\omega$ Model

The shear-stress transport $k-\omega$ model is associated with a blending function. It is one of the most popular turbulence models was developed by Menter in 1993 [122]. It includes the transport of the shear-stress turbulent with the derivation of the turbulent-viscosity to improve the prediction of the flow separation, reattachment, and recovery [123–127] over airfoils with adverse pressure gradients. These are the important aspects of the unsteady dynamic stalling phenomenon. The turbulent prediction of complex flow is improved by adding the SST terms that report for the transport quantities

of the primary turbulent shear layer [128]. The SST model and their mathematical equations are available in the literature [129].

The flow field is assumed to be fully turbulent in nature; the different turbulence models such as the SST model, SKE model, and RKE model are employed to determine the best turbulence model for this research. The SST model shows good agreement with the previous work presented by Erkan and Ozkan [42] and has improved performance in re-circulation regions.

2.5 Description and Methodology of the Numerical Set-up

In the current study, the computational analysis is carried out using ANSYS/Fluent standard commercial software [114] to study the flow field over 2–D airfoils and their aerodynamic performance in the different operating conditions.

2.5.1 Computational Domain Information and its Boundary Conditions

The process to build a 2–D computational domain for NACA 63-412 and NACA 63-415 airfoils by importing the coordinate points of the upper and bottom surfaces from the NACA airfoil coordinate database [3]. Here, the airfoil has 26 coordinate points on each upper surface and bottom surface. The Cartesian coordinate axes are fixed at the leading edge of the airfoil, and the point of the leading edge is considered as an origin (*i.e.*, semicircle center). Additionally, the coordinates of the airfoil profiles are loaded into the computer-aided design (CAD) software to build a 2–D geometric model. This domain is set-up as 2–D flow structures around the airfoil *i.e.*, the z –direction component is zero.

To create the mesh for the computational simulation, a C–type flow domain configuration is built as shown in Fig. 2.6. In this analysis, a C–type surface is created on the same plane as the airfoil. To allow the fluid flow to expand to its full capacity, the dimension of the arc radius is set at 12.5 times that of the chord length ($12.5c_r$), whereas the length of the rectangle in x –direction (horizontal component) is set to 30 times that of the chord length ($30c_r$). Here, the chord length is assumed to be of unit length ($c_r = 1$), *i.e.*, the chord length is used as a scale for representing the length. Additionally, in order to have greater control over the mesh generation, a small circle at the center point ($x = 0.3c_r$, $y = 0$) and rectangle domains are constructed just inside the C–type flow domain, with a radius of $3.5c_r$, span width of a rectangle is $4c_r$ with approximately the same span length of the large rectangle. Here, the airfoil profile can be rotated with the angle of attack (α) of our interest range (*i.e.*, $0^\circ \leq \alpha \leq 20^\circ$). This choice of the domain reduces the solution time by minimizing the

2. Qualitative Analysis of Aerodynamic Performance of Airfoil Profiles

number of equations to be solved [130].

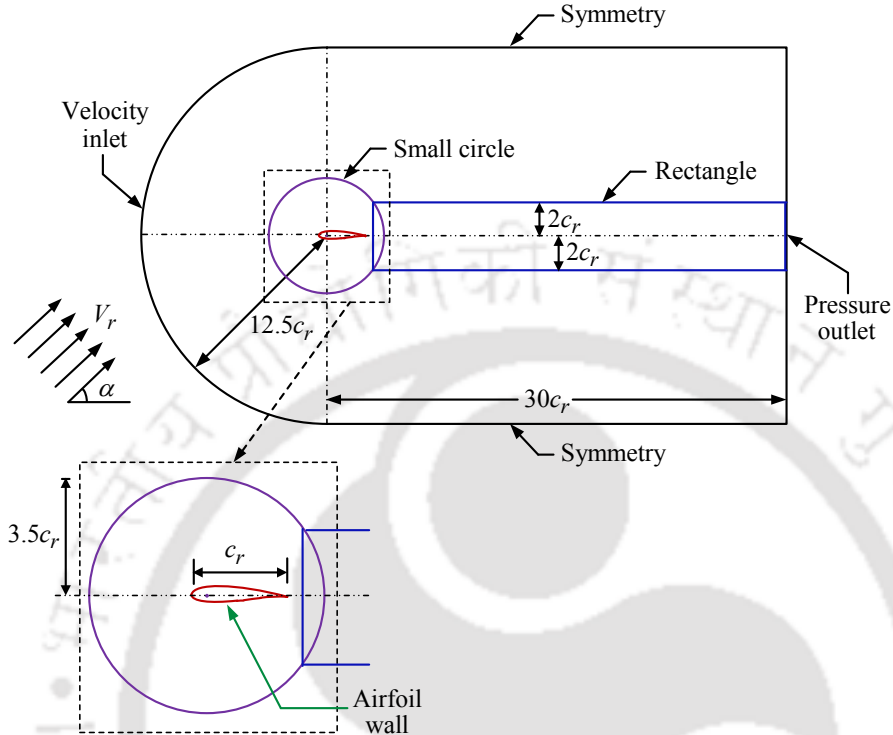


Fig. 2.6: The C-type computational flow domain: geometry and boundary conditions.

A different set of boundary conditions (BC) are considered: the velocity-inlet, symmetry, and pressure-outlet are assigned to the computational domain. The velocity-inlet type BC is applied at the inlet face with a constant wind velocity approaching the airfoil, consisting of a C-type side face. At the outlet face, the pressure-outlet type BC is fixed to the atmospheric pressure. The distance of the side faces in the computational domain is kept in the manner to ensure that the effect of the BC on the flow inside the C-type domain is negligible. Further, the symmetry type of the BC is applied on the upper and bottom surfaces. It uses the faces as the wall with no-slip shear conditions to ignore the wall effect. The no-slip condition is also allocated to the walls of the airfoil. The whole C-type computational domain builds with specified BC is shown in Fig. 2.6. Table 2.3 provides the boundary conditions of the 2-D simulations.

2.5.2 Solver Setting and Turbulence Model Selection

Before finishing the meshing process, the flow domain geometry of the airfoil is imported into the computational simulation. Additionally, the computational method uses the pressure-based solver to solve the RANS equations. In the present simulation, the fluid is assumed to be incompressible. The

Table 2.3: The boundary conditions of the 2–D simulation [ANSYS USER GUIDE]

Parameter	Values
Airfoil	NACA 63-412 and NACA 63-415
Simulation type	Steady-state simulation
Turbulence model	SST, SKE and RKE
Fluid material	Air
Temperature	10°C
Dynamic viscosity	1.778×10^{-5} kg/m·s
Air density	1.225 kg/m ³
Flow type	Incompressible flow
INLET boundary condition	Flow velocity = 5, 7, 10, 15 & 20 m/s
OUTLET boundary condition	Gauge pressure = 0 Pa
CFD algorithm	Simple (Default option)
Solution method	Pressure-velocity coupling Least-squares cell based Pressure (Standard) Density (Second-order upwind) Momentum (Second-order upwind) Turbulent kinetic viscosity (Second order upwind) Specific dissipation rate (Second-order upwind)
Solution controls	Pressure; 0.55 Momentum: 0.52 Density: 1.2 kg/m ³ Turbulent kinetic energy: 0.65
Boundary condition	Velocity inlet (7 m/s) Pressure outlet (Gauge pressure: 0) Stationary wall with no-slip shear condition
Number of mesh cells	About 4,19,911 and 4,16,296
Force monitors	Lift and drag coefficients
Residual convergence value	1×10^{-6}

2. Qualitative Analysis of Aerodynamic Performance of Airfoil Profiles

least-squares cell-based technique is selected for adverse pressure gradients that solve the secondary diffusion expressions and velocity derivatives. A second-order upwind discretization technique is used for other equations to reduce interpolation errors. The convergence is obtained when the difference between average lift and drag coefficients of the airfoil of two consecutive iterations is smaller than 0.1%. The post-processing of each case is carried out after the last iteration, which is generally around 1000 in our simulations. The simulations are performed using Intel® Xeon® E5-2650v4 2.2 GHz Quad-Core CPUs with 128 GB of RAM at the computer cluster of the Computer & Communication Centre, IIT Guwahati. The typical time required for each 2–D simulation is approximately 2 hours.

2.5.3 Mesh Refinement Strategy and its Grid Independence Study

According to the CFD principle, a C–type domain is discretized through unstructured 2–D meshes except for the near airfoil wall region. Here, the structural quadrilateral meshes in the normal direction to the wall are created as shown in Fig. 2.7. It is used to minimize the meshing challenges to ensure better accuracy. The mesh size near the boundary layer is kept small to accurately capture the phenomenon such as vortices and laminar separation bubble.

A proper mesh tries to reduce the computational cost while not compromising the accuracy of the solution. These two objectives are conflicting, hence, the mesh generation turns out to be an extremely challenging task. As the first step in meshing, automatic meshing is selected with a maximum element size of 0.1 m for the numerical model set (C–type domain). After that, the meshing of the bodies (*i.e.*, the body with influence containing a small circle and rectangle in C–type domain) is created with a maximum element size of 0.02 m. For analyzing the boundary layer, we considered the thickness of the mesh is to be less than or equal to 0.01 m near the airfoil wall. Finally, the node numbers, including 500 points, are selected to get a finer mesh for the numerical solution around the airfoil.

Here, the mesh structure includes 30 rows of quadrilateral mesh with a growth rate of 1.2 to ensure a smooth flow transition. This is done to fulfill the criteria of $y^+ \sim 1$ as given in ANSYS manual [114]. The present study focused more on near-wall physics instead of vortices away from the airfoil; hence the far zone is discretized with courser mesh. The total skewness of the mesh is < 0.33 , and the maximum aspect ratio is 141.

A grid independence study has been carried out to fix an optimum grid element size that will ensure the independence of the numerical solutions. For this purpose, six different mesh structures are created and analyzed with different cell sizes. The computational simulations are carried out over

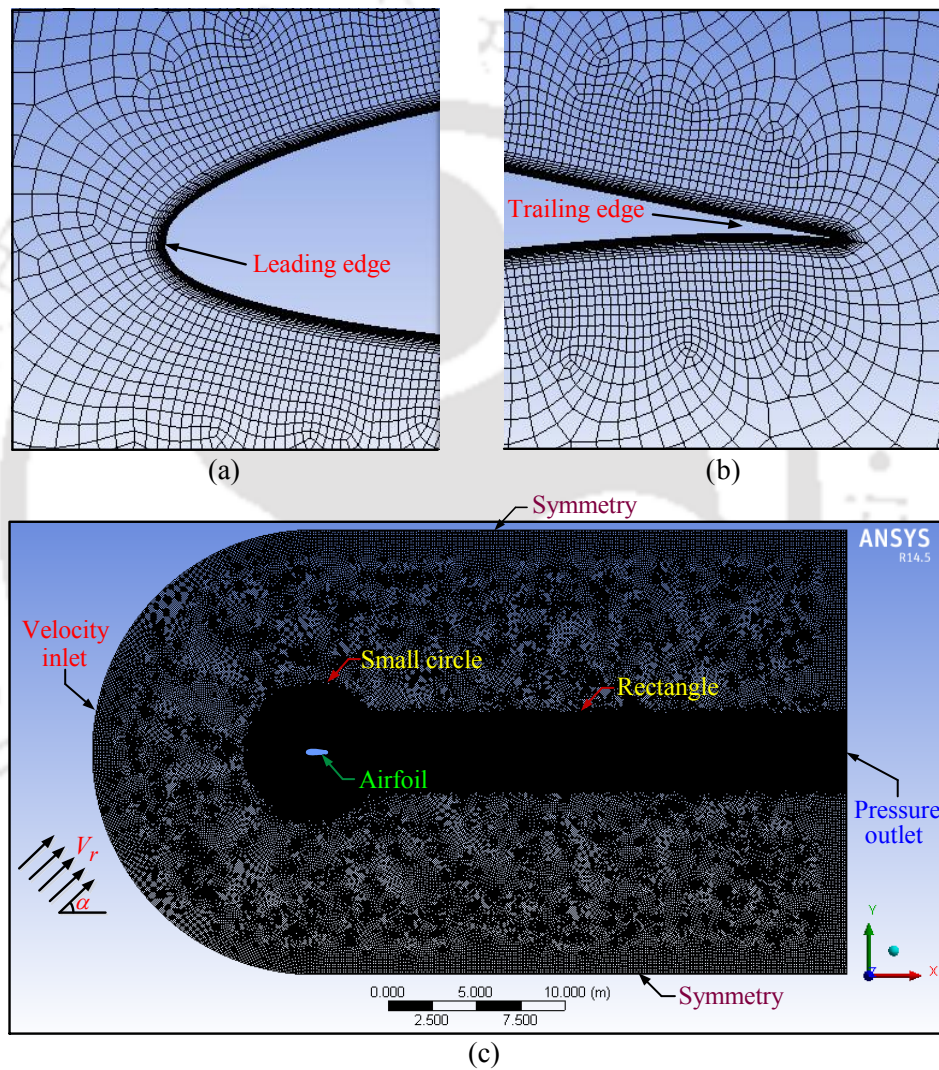


Fig. 2.7: Generated mesh (Grid index 4) details (a) boundary layer elements near the leading edge (b) boundary layer elements near the trailing edge (c) whole C-type computational domain of the grid used.

2. Qualitative Analysis of Aerodynamic Performance of Airfoil Profiles

NACA 63-412 and NACA 63-415 airfoils at Mach number, $Ma = 0.3$, and angle of attack is taken 0° . Different Grid indexes are taken for the validation of computational simulation results. The details of the grid independency test are enumerated in Table 2.4.

Table 2.4: Discretizations of 2–D computational domain for the grid independency test on the airfoils.

Grid index	NACA 63-412 airfoil			NACA 63-415 airfoil		
	Cells	C_L	C_D	Cells	C_L	C_D
1	225775	0.12482	0.00382	226134	0.12989	0.00389
2	268125	0.18787	0.00587	269417	0.19842	0.00542
3	325290	0.24763	0.00653	326594	0.25009	0.00709
4	416296	0.31599	0.00716	419911	0.32684	0.00826
5	588829	0.31254	0.00737	590809	0.32742	0.00832
6	667199	0.31317	0.00752	807445	0.32931	0.00842

The computational simulations are first performed with the coarse mesh structures with 2,25,775 mesh cells for NACA 63-412 airfoil and 2,26,134 mesh cells for NACA 63-415 airfoil. The amount of mesh cells is then gradually increased in consecutive steps to investigate the effect on the simulation results. The estimated lift coefficient (C_L), and the drag coefficient (C_D) with different mesh structures are presented in Table 2.4. From Table 2.4, it could be observed that after Grid index 4, the values of C_L and C_D remain almost constant. Hence, out of these six Grid indexes, the best configuration (*i.e.*, the Grid index 4) is considered for further study to do the computational simulation.

2.6 Results and Discussion

In this study, the aerodynamic performances are analyzed over the 2–D basic NACA 63-412 and NACA 63-415 airfoils at wind speeds, $v_\infty = 5, 7, 10, 15,$ and 20 m/s. The CFD standard commercial software ANSYS/Fluent is used to solve the Reynolds-averaged Navier–Stokes (RANS) equations based on a finite-volume approach. The lift coefficient (C_L), and drag coefficient (C_D) are calculated for the different angles of attack varying between $0^\circ \leq \alpha \leq 20^\circ$. The aim of these simulation is to determine the optimum angle of attack of both the airfoils which extract the maximum power from the wind turbine. The maximum power is extracted when the ratio of lift/drag forces is maximum.

2.6.1 Validation Process of the Computational Models

The lift and drag coefficients are obtained for twenty different angles of attack in the range of $0^\circ \leq \alpha \leq 20^\circ$. In the simulation three turbulence models are used *i.e.*, standard $k - \epsilon$ model (SKE), realizable $k - \epsilon$ model (RKE), and shear-stress transport $k - \omega$ model (SST). The results are compared with the available Xfoil solver and experimental data in the literature [3, 4].

Fig. 2.8(a) shows that the computational simulation results compared with the experimental data taken from Bak *et al.* [4] at $Re = 0.5 \times 10^6$ of NACA 63-415 airfoil. From the literature, it is found that Bak *et al.* [4] performed the 2-D wind tunnel tests over NACA 63-415 airfoil at $Re = 0.5 \times 10^6$ with a minimum trailing edge separation. Fig. 2.8(b) shows that the computational simulation results compared with the Xfoil data obtained by Drela and Youngren [3] at $Re = 0.5 \times 10^6$ of NACA 63-412 airfoil. From the literature, it is found that Drela and Youngren [3] conducted their 2-D Xfoil solver simulation of the NACA 63-412 airfoil at $Re = 0.5 \times 10^6$ with a minimum trailing edge separation.

Fig. 2.8(a) and 2.8(b) shows that the lift coefficient increases with the increase of the angle of attack up to a certain angle *i.e.*, the angle of attack ($\alpha = 14^\circ$) with NACA 63-415, and angle of attack ($\alpha = 13^\circ$) with NACA 63-412 airfoils after these angle of attack the value of lift coefficient decreases with the increase of angle of attack. These patterns of variation in lift coefficient are also observed in the experimental data available from the literature. It is observed that the lift coefficient obtained from the simulation which uses SST model is very close to the experimental data for the NACA 63-415 airfoil and the Xfoil solver for the NACA 63-412 airfoil.

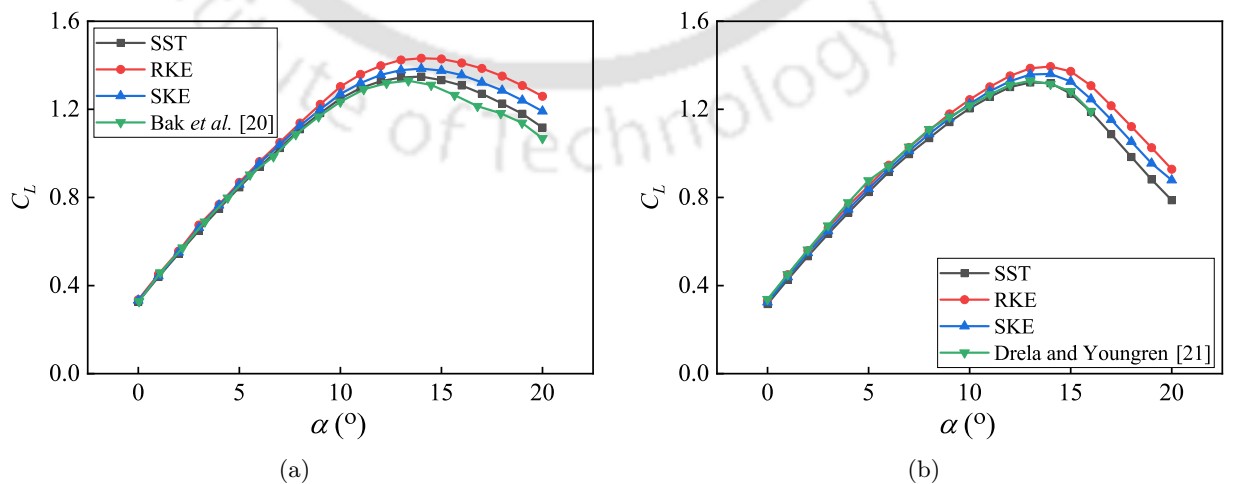


Fig. 2.8: The lift coefficient (C_L) compared with (a) experimental data by Bak *et al.* [4] for NACA 63-415 airfoil at $Re = 0.5 \times 10^6$; (b) Xfoil data by Drela and Youngren [3] for NACA 63-412 airfoil at $Re = 0.5 \times 10^6$.

2. Qualitative Analysis of Aerodynamic Performance of Airfoil Profiles

Fig. 2.9(a) shows the variation of the drag coefficient for the different turbulent models with the variation of the angle of attack. It also includes a comparison with the experimental data by Bak *et al.* [4] for the NACA 63-415 airfoil. It is observed that the drag coefficient obtained from the simulation which uses SST model is very close to the experimental data available in the literature [4].

Similarly, Fig. 2.9(a) shows the result with NACA 63-412 airfoil. Here, the simulated data is compared with Xfoil solver by Drela and Youngren [3] for the NACA 63-412 airfoil. Here, also the drag coefficient obtained from the simulation which uses SST model is very close to the Xfoil solver result.

From the results, as shown in Fig. 2.9(a), it is observed that till the angle of attack is less than 5° , the drag coefficient varies linearly and is approximately constant, after that exponential increase in the drag coefficient is observed.

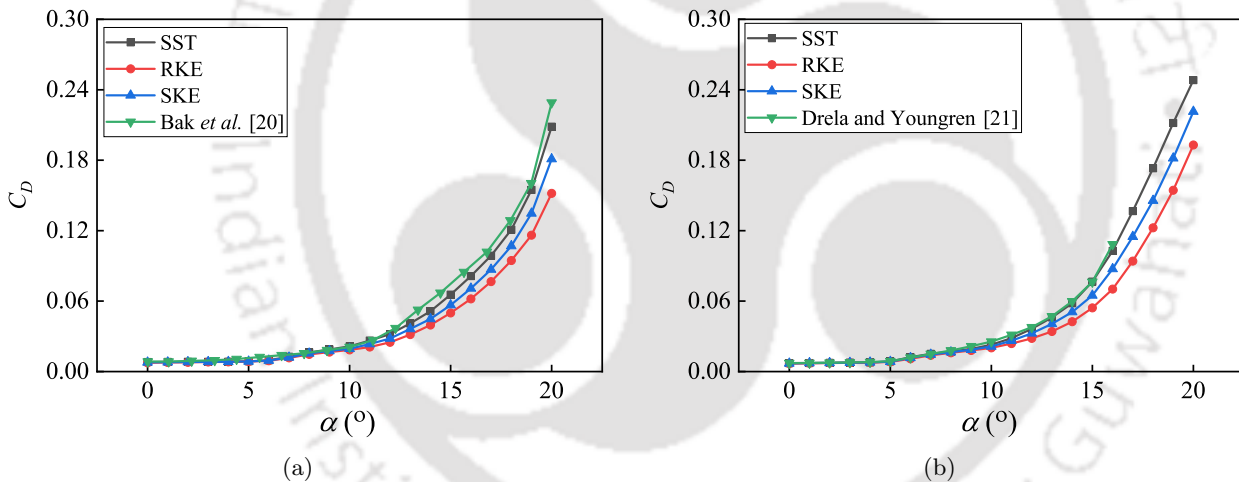


Fig. 2.9: The drag coefficient (C_D) compared with (a) experimental data by Bak *et al.* [4] for NACA 63-415 airfoil at $Re = 0.5 \times 10^6$; (b) Xfoil data by Drela and Youngren [3] for NACA 63-412 airfoil at $Re = 0.5 \times 10^6$.

2.6.2 Investigation of Optimum Angle of Attack

The optimum angle of attack of the NACA 63-415 and NACA 63-412 airfoils using the SST model is calculated for twenty different angles of attack with wind speeds of $v_\infty = 5$ m/s, 7 m/s, 10 m/s, 15 m/s, and 20 m/s, respectively.

Figs. 2.10(a) and 2.10(b) shows the variation of the lift coefficient (C_L) as a function of the angle of attack for different wind speeds.

Similarly, Figs. 2.11(a) and 2.11(b) depict the drag coefficient (C_D) values for different angles of attack for different wind speeds.

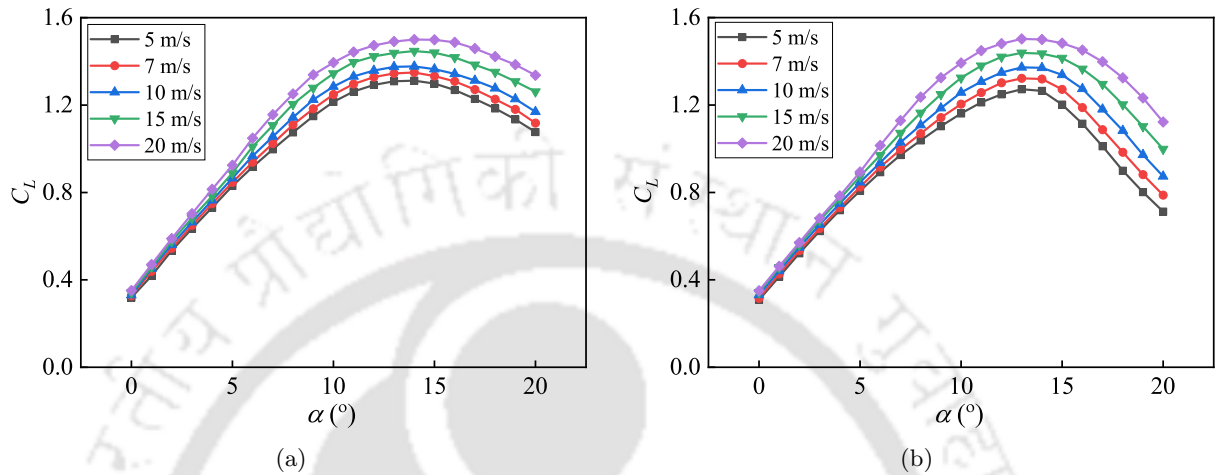


Fig. 2.10: The change in the lift coefficient (C_L) as a function of the angle of attack (α) for the five different wind speeds with (a) NACA 63-415 airfoil; (b) NACA 63-412 airfoil.

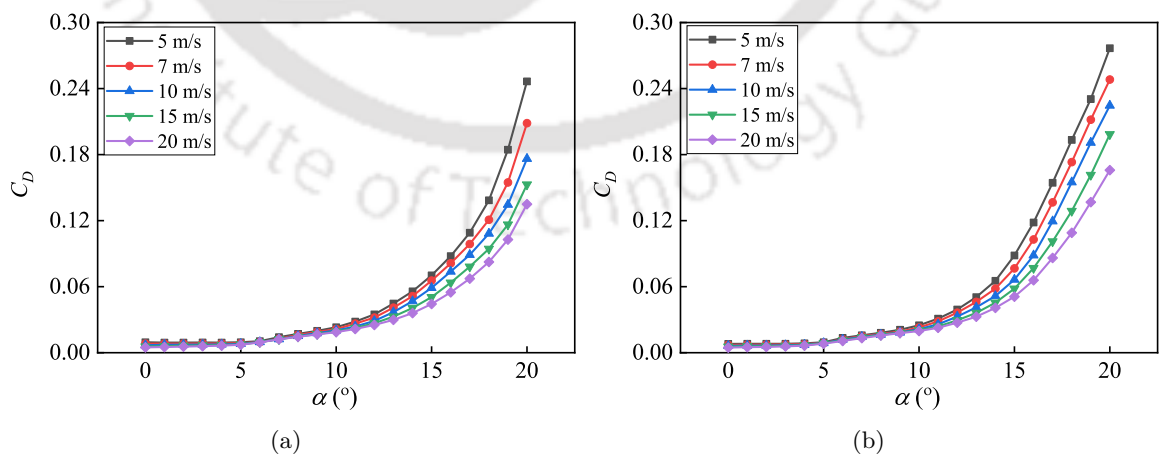


Fig. 2.11: The change in the drag coefficient (C_D) as a function of the angle of attack (α) for the five different wind speeds with (a) NACA 63-415 airfoil; (b) NACA 63-412 airfoil.

2. Qualitative Analysis of Aerodynamic Performance of Airfoil Profiles

For finding the optimal angle of attack, the ratio of lift/drag coefficients need to be maximum *i.e.*, sliding ratio, $\gamma = C_L/C_D$. This sliding ratio is also the measure of aerodynamic performance.

The estimated values of the sliding ratio of the airfoil profiles *i.e.*, NACA 63-415 and NACA 63-412 airfoil profiles are shown in Figs. 2.12(a) and 2.12(b), respectively. From Fig. 2.12, it is observed that the maximum sliding ratio appears somewhere between 5° and 6° for NACA 63-415 at different wind speeds. Similarly, from Fig. 2.12(b), it is observed that the maximum sliding ratio appears somewhere between 4° and 5° for NACA 63-412 at different wind speeds.

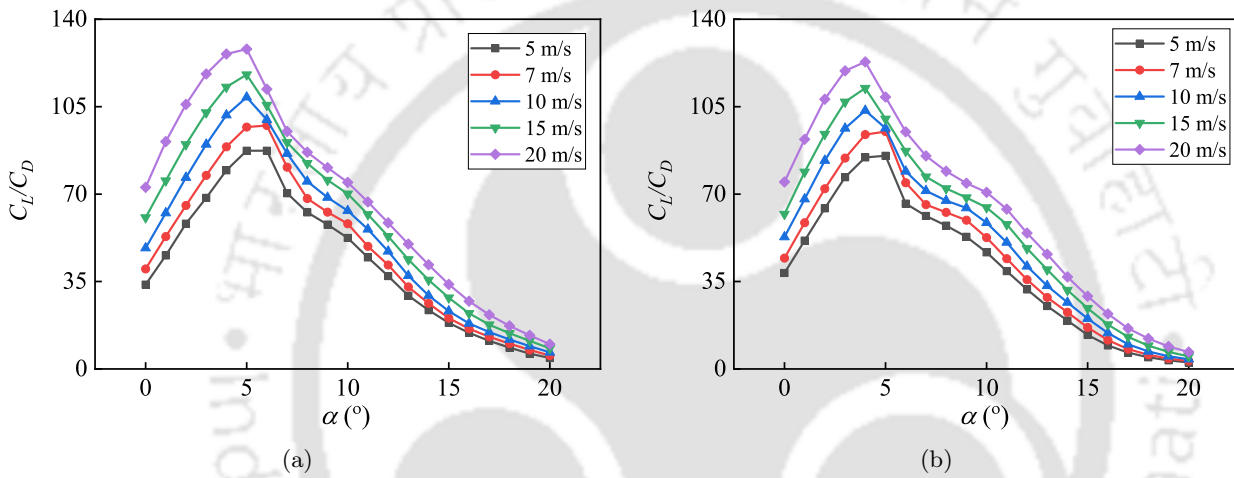


Fig. 2.12: The sliding ratio (C_L/C_D) as a function of the angle of attack (α) for simulations employing the SST model with (a) NACA 63-415 airfoil; (b) NACA 63-412 airfoil.

From Fig. 2.12 it is observed that the sliding ratio increases as the wind speed increases at the same operating angle of attack. For selected NACA 63-415 and NACA 63-412 airfoil profiles, the range of the optimum angle of attack with changing wind speeds is shown in Fig. 2.13. The appropriate profile at changing wind speed can be chosen according to the large sliding ratio in the range of the optimum angle of attack. The results show that the NACA 63-415 airfoil produces the maximum power at changing wind speed as they have the maximum value of the sliding ratio. Therefore, the NACA 63-415 airfoil profile is strongly suggested for the wind turbine blades. It is concluded that to get the maximum power from the wind turbine; it is observed that the optimum angle of attack is $\alpha \simeq 6^\circ$ for NACA 63-415 airfoil and $\alpha \simeq 5^\circ$ for NACA 63-412 airfoil at a wind speed of $v_o \leq 7$ m/s.

Further, Fig. 2.14(a)–(e) shows the variation of the sliding ratio at different angle of attack for NACA 63-415 and NACA 63-412 airfoil profiles for a wind speed of 7 m/s.

The present study tries to provide the optimum angle of attack which is around $\alpha \simeq 6^\circ$ for NACA

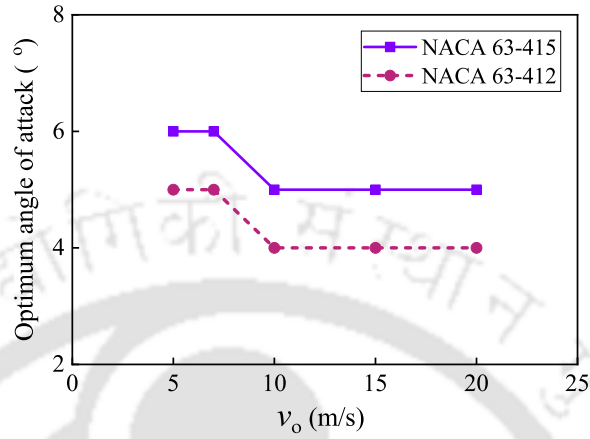


Fig. 2.13: The optimum angle of attack for the selected NACA 63-415 and NACA 63-412 airfoil profiles at different wind speeds.

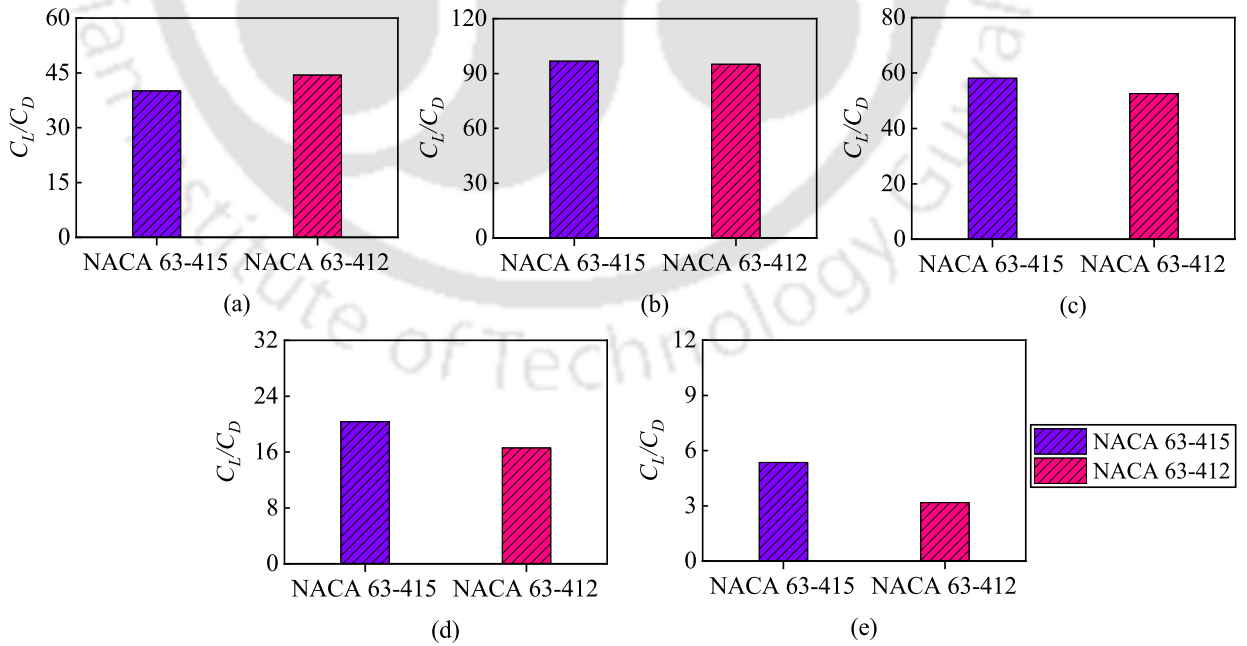


Fig. 2.14: The sliding ratio of the NACA 63-415 and NACA 63-412 airfoil profiles at 7 m/s (a) at $\alpha = 0^\circ$, (b) at $\alpha = 5^\circ$, (c) at $\alpha = 10^\circ$, (d) at $\alpha = 15^\circ$, and (e) at $\alpha = 20^\circ$.

2. Qualitative Analysis of Aerodynamic Performance of Airfoil Profiles

63-415 airfoil. It is also observed that there is a slight variation in the optimal angle with the change in wind speed. Similarly, for NACA 63-412 airfoil, the optimum angle of attack is around $\alpha \simeq 5^\circ$.

At the wind speed of 7 m/s, the optimal value of the sliding ratio is 97.47, *i.e.*, with C_L is 0.93863 and C_D is 0.00963 for NACA 63-415. Similarly, for NACA 63-412, the optimal value of the sliding ratio is 94.99, *i.e.*, with C_L is 0.82459 and C_D is 0.00868 at a wind speed of 7m/s.

The subsequent subsection examines the distribution of the surface pressure coefficient to validate the estimated optimal angle of the attack.

2.6.3 Analysis of Pressure Coefficient

Fig. 2.15 shows the estimated surface pressure coefficient (C_p) distributions obtained from ANSYS/Fluent for NACA 63-412 and NACA 63-415 airfoils at a different angle of attack with a wind speed of $v_o = 7$ m/s.

The estimated pressure coefficient distributions for NACA 63-415 airfoil are compared with the wind tunnel tests data as reported by Bak *et al.* [4]. This wind tunnel test data was obtained with $Re = 1.6 \times 10^6$ and $c_r = 0.6$ m. It is observed that the estimated pressure coefficient distributions are very close with the wind tunnel tests data available in the literature. To further quantify the closeness of the wind tunnel tests data to the estimated pressure coefficient (C_p) distributions over NACA 63-415 airfoil. The values of mean square error (MSE) is defined as

$$\text{MSE} = \frac{1}{N} \sum_{i=1}^N [C_{p-w}(i) - C_p(i)]^2 \quad (2.15)$$

where, N is the sample size, C_{p-w} is the pressure coefficient distribution reported in Bak *et al.* [4] from the wind tunnel tests, C_p is the pressure coefficient distribution obtained from the computation simulations (using ANSYS/Fluent). The MSE index is always positive value and a lower value means less error.

Table 2.5: Calculated the mean square error at 7 m/s.

α	Error with SST	Error with RKE	Error with SKE
0°	0.10223	0.11268	0.11316
5°	0.01729	0.01813	0.01977
10°	1.16871	1.17762	1.37957
15°	0.87538	0.97305	1.01159
20°	0.46506	0.48193	0.53897

However, due to the unavailability of proper experimental data in the literature for NACA 63-412 airfoil. The pressure coefficient distribution over NACA 63-412 is compared with the computational results obtained for the different turbulence models.

Fig. 2.15 shows the pressure coefficient distribution on the bottom and top surfaces of the airfoil. The lower portion of the curve corresponds to the top surface pressure coefficient distribution which is negative, whereas the upper portion of the curve represents the lower surface pressure coefficients which is positive. Together, these pressure coefficients produce the lift force on the airfoil which is in the upward direction. It can also be observed that the larger the area under the curve, the more the average lift force is on the airfoil. Further, it is also observed that since the difference between pressure coefficient is much larger on the leading edge than the trailing edge, thus, indicating that the airfoil's lift force is mainly generated from the leading edge.

2.6.4 Analysis of Velocity Magnitude

Figs. 2.16 and 2.17 shows the velocity profile of fluid around the NACA 63-415 and NACA 63-412 airfoils, respectively. Here, the lines with an arrow are used to represent the direction of fluid flow, whereas the color represents the magnitude of the velocity.

From Figs. 2.16 and 2.17, it is also observed that till the angle of attack is less than or equal to 5° , there is no significant reduction of velocity at the trailing edge. Whereas, at 10° and higher angle of attack, there is a significant reduction of velocity at the trailing edge resulting in the formation of eddies. This results in a reduction in aerodynamic efficiency for the higher angle of attack.

2.6.5 Analysis of Pressure Field

Figs. 2.18 and 2.19 shows that the pressure field for NACA 63-415 and NACA 63-412 airfoils at a different angle of attacks. The pressure distribution is calculated for the wind speed of $v_o = 7$ m/s. The figures show that the pressure distribution is low at the upper surface, whereas high at the bottom surface. As mentioned in Fig. 2.15, this pressure difference provides the lift force. The figures present a chronology of the static pressure fields on the airfoil locations superimposed on the steady streamlines to depict the complicated vortex patterns formed during the stalled process.

Figs. 2.18 and 2.19 demonstrates that the leading edge of NACA 63-415 and NACA 63-412 have a greater static force than the trailing edge. Figs. 2.16 and 2.17 show that the velocity at the upper

2. Qualitative Analysis of Aerodynamic Performance of Airfoil Profiles

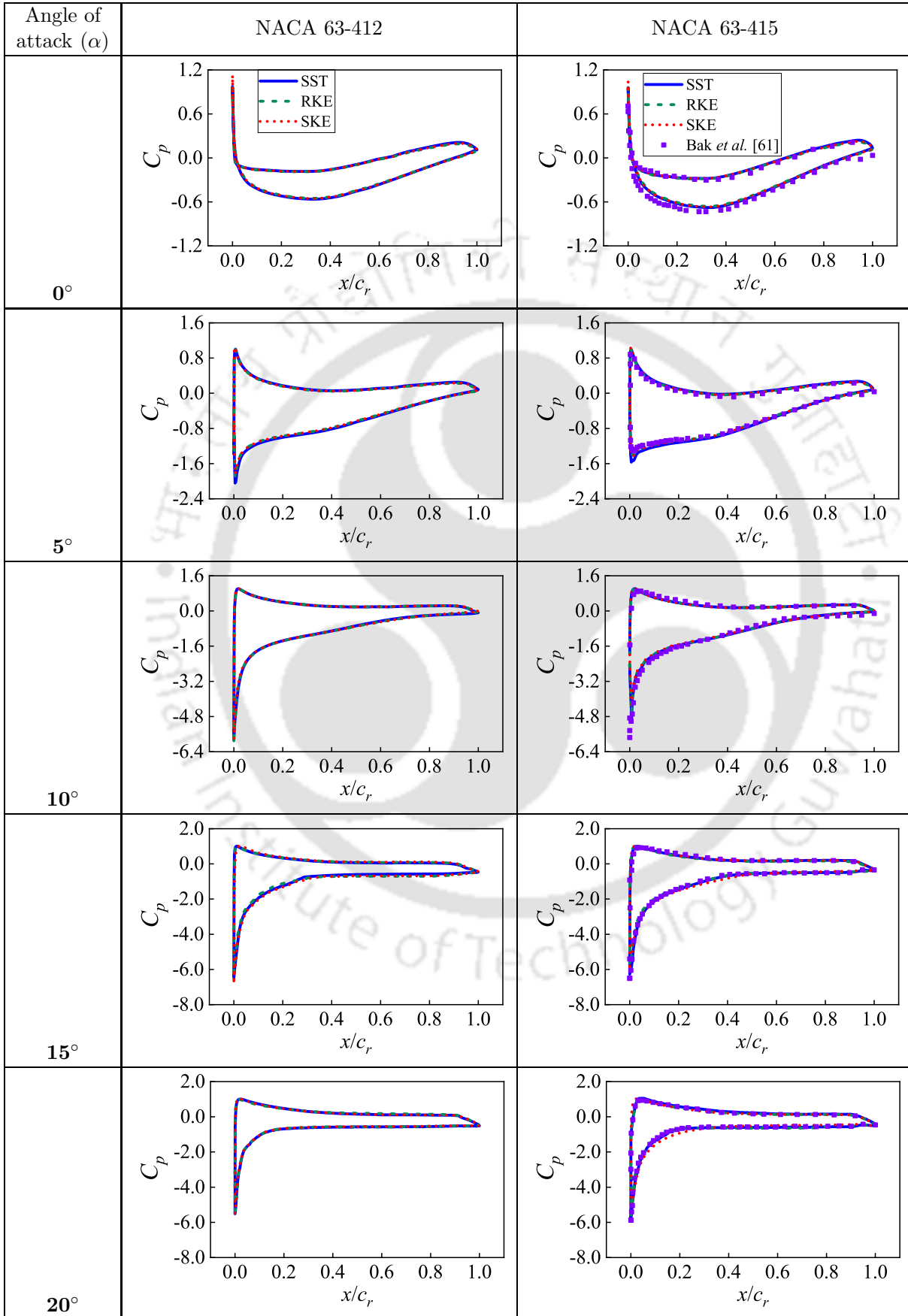


Fig. 2.15: Pressure coefficient plot of NACA 63-412 and NACA 63-415 airfoil profiles.

TH-3228_11610226

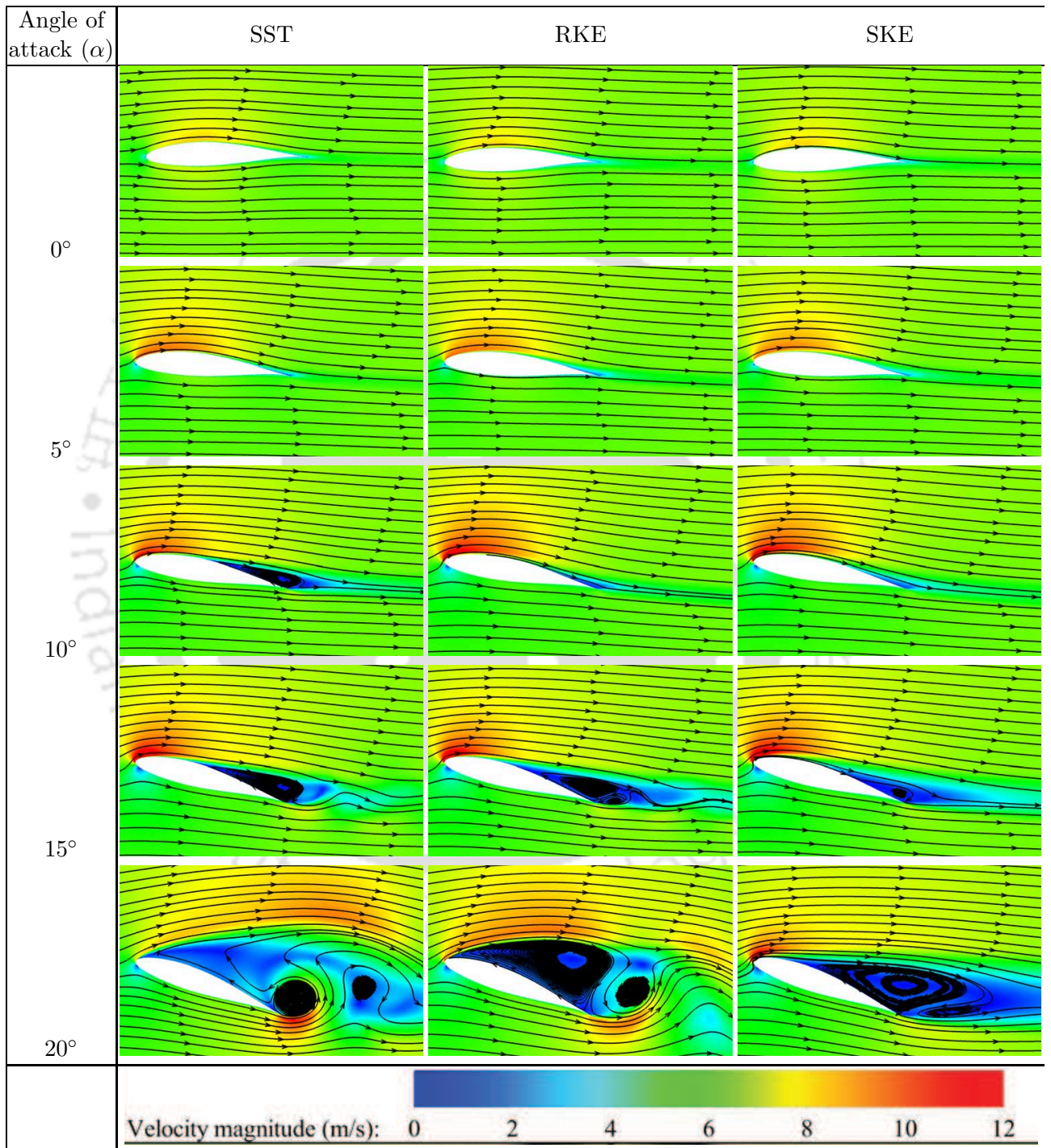


Fig. 2.16: Velocity magnitude (m/s) superimposed on the streamlines computed using the SST, RKE and SKE models for NACA 63-415 airfoil.

2. Qualitative Analysis of Aerodynamic Performance of Airfoil Profiles

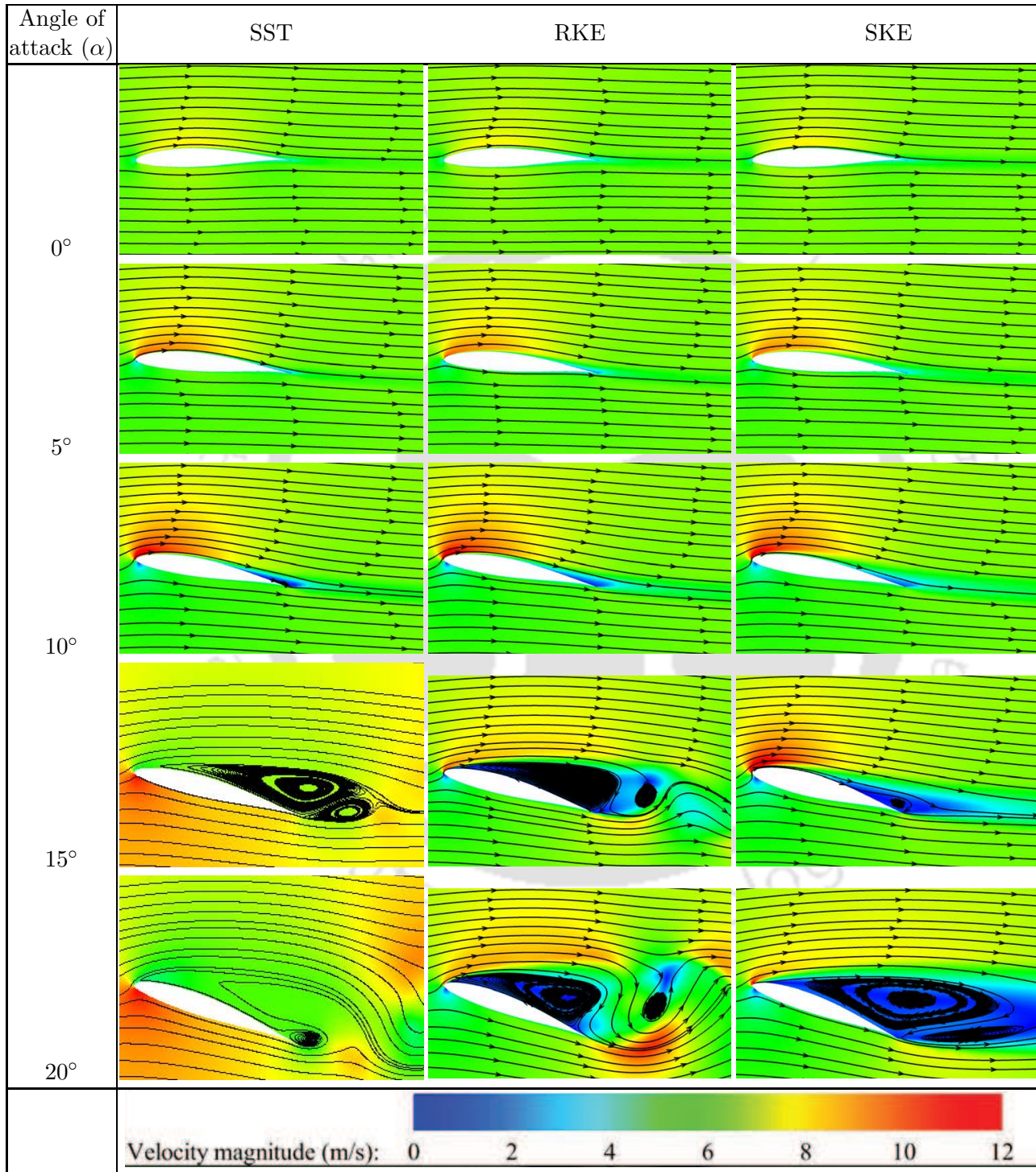


Fig. 2.17: Velocity magnitude (m/s) superimposed on the streamlines computed using the SST, RKE and SKE models for NACA 63-412 airfoil.

surface of the airfoil is higher than the bottom surface. Therefore, the lower velocity at the bottom surface produces a higher lift. After a certain angle of attack, there is a decrease in the lift coefficient and increases the drag coefficient due to the flow separation from the upper surface, and the formation of wake near the trailing edge.



2. Qualitative Analysis of Aerodynamic Performance of Airfoil Profiles

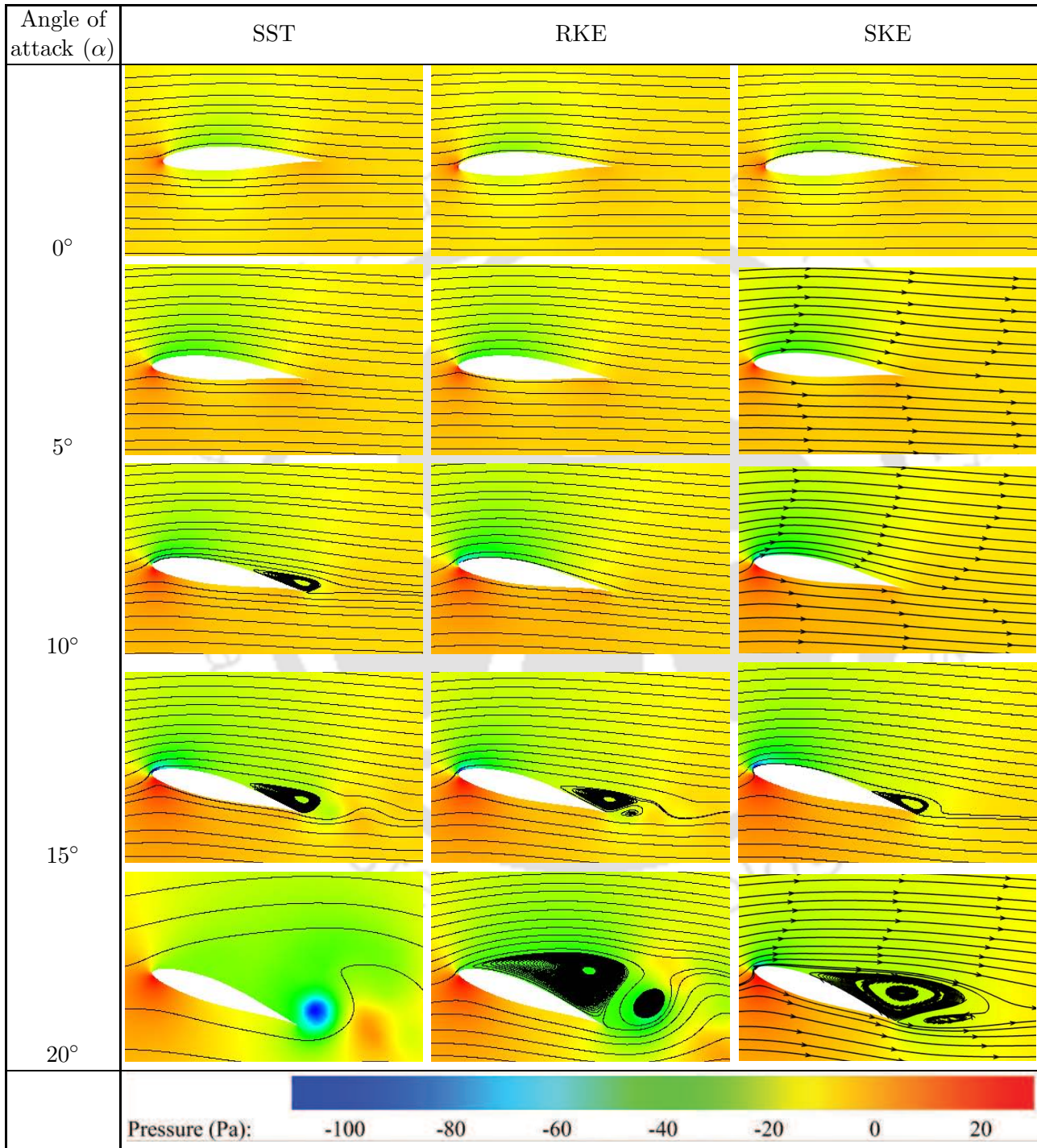


Fig. 2.18: Pressure field superimposed on the streamlines computed using the SST, RKE and SKE models for NACA 63-415.

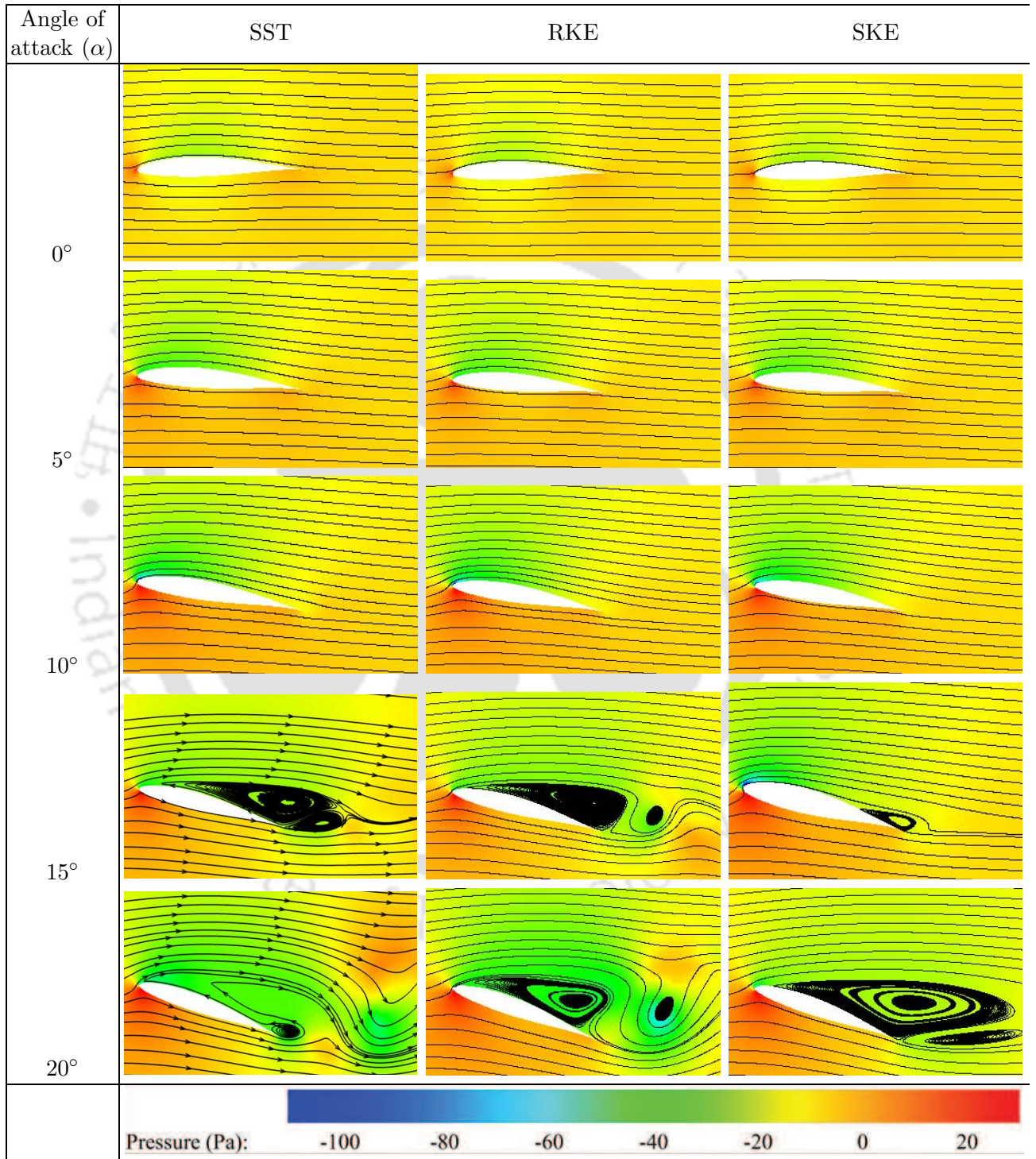


Fig. 2.19: Pressure field superimposed on the streamlines computed using the SST, RKE and SKE models for NACA 63-412.

2.7 Summary

In this chapter, a computational fluid dynamics (CFD) model (2-D) is developed to study the aerodynamic efficiency of NACA 63-415 and NACA 63-412 airfoils at a different angle of attack. For computational analysis, the Reynolds-averaged Navier-Stokes (RANS) equations with three different turbulence models such as shear stress transport $k-\omega$ (SST), realizable $k-\epsilon$ (RKE), and standard $k-\epsilon$ models (SKE) are used to analyze the fluid flow over the airfoils. The simulation results for NACA 63-412 airfoil obtained from different turbulence models are compared with Xfoil solver, whereas the simulation results obtained for NACA 63-415 airfoil are compared with the experimental data available in the literature. From the present computational analysis, the following significant findings are drawn:

- (i) From the computational fluid dynamic analysis, it is observed that the SST model provides results that are closer to the Xfoil solver and experimental data. Therefore, the SST model is used to find the optimum angle of attack.
- (ii) The lift and drag coefficients, which characterize the lift force and drag force acting on the airfoils are examined for the different angle of attack and the wind speeds.
- (iii) With the increase of angle of attack, initially, the lift coefficients increase, but this increase is till the angle of attack of 14° for NACA 63-415, whereas for NACA 63-412 it increases till 13° . After these angles, the lift coefficient decreases. Regarding the drag coefficients, it increases linearly till the angle of attack is approximately equal to 5° , however, after this angle, there is an exponential rise in the drag coefficient.
- (iv) The optimum angle of attack which corresponds to maxima of sliding ratio is observed at an angle of attack of $\alpha \simeq 6^\circ$ for NACA 63-415 airfoil, and at $\alpha \simeq 5^\circ$ for NACA 63-412 airfoil with the wind speed of $v_o = 7$ m/s.
- (v) From the pressure coefficient (C_p) distribution curves, it is observed that the difference of pressure coefficient increases as the angle of attack increases up to the optimum angle of attack, and it is significantly higher on the leading edge than trailing edge.
- (vi) The computational results of the velocity gradient and pressure contours for different turbulence models are compared. From the results, it is observed that the boundary layer formed nearer the airfoil is highly turbulent for the higher angle of attack.

The present study was mainly to find the aerodynamic efficiency of the NACA 63-415 and NACA 63-412 airfoil at a different angle of attack. Study tries to find optimal angle of attack of these airfoils.

3

Evaluation of Aerodynamic Performance of Wind Turbine

Contents

3.1	Introduction	56
3.2	Aerodynamics of the Wind Turbine	59
3.3	Approximation of Wind Turbine Dynamics with a Second Order Transfer Function	66
3.4	Algorithm Used for Design of the Blade Geometry and Implementation Procedure of the BEM Theory	71
3.5	Selection and Design of Wind Turbine Blade Parameters	71
3.6	Simulation Set-up Description and Methodology for Validation Purpose	76
3.7	Results and Discussion	84
3.8	Summary	90

Objective

The objective of this work is to develop a model for predicting the aerodynamic performance of the small-scale horizontal axis wind turbine (SS-HAWT). As per the standard IEC 61400-2, the primary blade design such as the chord length and twist angle of the SS-HAWT blade, are calculated using optimal rotor theory. The aerodynamic performance of the wind turbine is analyzed using the blade element momentum (BEM) approach, including the Prandtl's tip loss correction factor. The numerical computational technique is based on unsteady Reynolds-averaged Navier-Stokes (RANS) equations with turbulence models. Here, the numerical solutions are done using ANSYS/Fluent software to predict the aerodynamic performances of wind turbines rotating at different speeds. The results through simulations are also validated with the steady-state result obtained through the BEM theory. Since, the results from ANSYS/Fluent software takes significant time, hence, using the steady-state results obtained from BEM theory and simulated results of ANSYS/Fluent are utilized to propose a model which includes an equivalent second-order transfer function (TF) and BEM theory to estimate aerodynamic performances of wind turbine.

3.1 Introduction

There are significant works reported in the literature which is focused on improving the aerodynamic performance of the wind turbine blades [43, 131]. But, most of this work is done for a large wind turbine with a rated wind speed of 10 m/s or above. The present work is about the aerodynamic design of the SS-HAWT blades with rated wind speed in the range of 6 to 7 m/s [49, 132, 133].

In the early 1920s, *Betz law* has reported that 59.25% is the theoretical maximum wind power that can be extracted from the wind velocity [134]. The classical theory for the fluid dynamics to understand the wind turbine design is based on blade element momentum (BEM) theory, proposed by Glauert in 1935 [135, 136], which is extensively used to study, design, and predict the aerodynamics performance of the horizontal axis wind turbine (HAWT) rotor. The BEM theory approach is based on a combination of one-dimensional (1-D) momentum and two-dimensional (2-D) blade element theories, which uses the concept of the actuator disc with an infinite number of blades with no tip loss [33, 137]. Spera [138] has contributed towards the extensions of BEM theory along with Glauert's propeller theory for application of the blade design improvement. In practice, the BEM theory is applied for a finite number of blades; hence, the results obtained with this approach have some

inaccuracy. The accuracy of the results is further reduced by including tip losses at the end of the blade. Wilson & Lissaman [136] suggest to use tip loss factor [139] in the BEM theory, which was initially proposed by Prandtl's [45] and it is known as the Prandtl's tip-loss factor.

An airfoil produces lift and drag forces through pressure differences across its upper and lower surfaces. The geometric characteristics of an airfoil element such as optimal chord length, and twist angle distribution are estimated based on the design parameters, such as the rated wind speed, number of blades, design tip speed ratio, and design angle of attack [140]. The design is based on the BEM theory, an iterative process that calculates the axial and tangential induction factors, aerodynamic forces acting on blades, velocities, torque, and power at the rotor shaft.

Some of the reported literature related to the design and analysis of the wind turbine are given in references [16,141–143]. The wind turbine models are highly sensitive to the shape of the airfoil profile. There are some standard airfoils available in the literature, and the present work utilizes one selected in the previous chapter. The BEM theory is widely used to predict the aerodynamic performance of the rotating blade. But, its accuracy in predicting the aerodynamic load and power depends on the reliability of airfoil data [32]. Lee *et al.* [144], analyses the effect of various design parameters on the aerodynamic performance of wind turbines; they have also suggested a modified BEM theory to improve the accuracy of the estimated parameters. Kulunk and Yilmaz [145] have utilized the BEM theory for a 100 kW HAWT and analyses its aerodynamic performance. Similarly, Sedaghat and Mirhosseini [146] has used BEM theory to designed and extract maximum power coefficient for a 300 kW HAWT blade.

In [142], a 200 kW HAWT blade is designed using an adequate iterative algorithm based on BEM theory. It provides an analysis of off-design variations of the wind velocity on the HAWT performance. Moreover, Sharifi and Nobari [147] have used BEM theory to predict the sectional pitch angle distribution along the blade strip to extract maximum power for the wind speed based on a probability distribution function. In [148], the BEM theory for its design is utilized. But, it also uses a heuristic method to linearized the chord and twist angle distributions along the blade strip to maximize the annual energy production at the rated wind speed. Sedaghat *et al.* [149] studied the aerodynamics performance for optimally designed blades at variable-speed HAWT using a compact BEM theory. Ozair *et al.* [150] performed a computational analysis to analyze the designed HAWT. The manuscript uses the BEM approach to develop the HAWT with power rating of a 5 kW. The

3. Evaluation of Aerodynamic Performance of Wind Turbine

diameter of the rotor of the wind turbine is 2.8 m and is designed for the rated wind speed of 10 m/s.

Recently, several research works in the literature on the design and analysis of wind turbines are limited to theoretical studies. The field test or wind tunnels need extensive effort and resources. Hence, computer-aided design (CAD) software is considered to develop wind turbines. However, there are several commercial software, and open-source codes based on BEM theory, such as NREL FAST code and DNV GL 'Bladed' software for simulating HAWT are available. The aerodynamic performance of the wind turbines are analyzed using ANSYS/Fluent commercial software. Here, the computational domain geometry also plays an important role in the accuracy of the results. These numerical simulations provide the detailed structure of the flow mechanism and helps in the validation of results obtained through theoretical models such as the one based on BEM theory. Here, the turbulent flow is modeled through the different turbulence models [151]. Moreover, the computational approach is economical and quick compared to the experimental test for analyzing the aerodynamic performance.

In this chapter, the optimal rotor theory is used to design the primarily blade parameters such as the twist angle and the chord length of the wind turbine. The BEM approach with the Prandtl tip loss correction factor is applied to evaluate the steady-state aerodynamic performance of the wind turbine as per the standard IEC 61400-2 [112]. The computational technique is employed to validate the aerodynamic performance observed by the BEM approach. This computational technique is also used to analyze the complexity of the flow mechanism around the wind turbine rotor. Although the computational technique takes a long computation time for calculation due to a high number of the mesh elements [152]; therefore, it required high computational resources. Hence, this chapter proposes a theoretical method that includes an equivalent second order transfer function (TF) and BEM theory to estimate the aerodynamic performance. This theoretical method represents the approximate dynamics of the generated torque by the wind turbine. These developed approximate dynamic models are suitable for controlling the wind turbine system, as the turbine dynamics are simplified to a second-order system.

Rest of the chapter is organized as follows: Section 3.2 provides the wind turbine design procedure. An approximation of wind turbine dynamics with a second-order transfer function model has been presented in Section 3.3. Section 3.6 gives the outlines of the simulation set-up of the computational domain for the developed numerical model. In Section 3.7 provides the aerodynamic performance

analysis and accuracy of the proposed second-order dynamic model in details. Lastly, the main conclusion of the work is reported in Section 3.8.

3.2 Aerodynamics of the Wind Turbine

The theory behind the conversion of the energy from the wind turbine is explained using the actuator disc concept which is mainly based on the variation of the wind velocity when the air passes through the stream-tube [33, 153]. This section describes the basic theoretical calculation of the wind turbine.

3.2.1 Kinematics of the Wind Turbine Blades

The flow in the wake can be resolved into two velocity components, one in the axial direction and the other in the tangential direction of the blade rotation, which causes rotation in the wake. Therefore, the induced velocity on the rotor plane has two components, as shown in Fig. 3.1. From this figure, the relative flow velocity on the blade plane [154] can be obtained as

$$V_r = \sqrt{[v_o(1-a)]^2 + [\omega_t r(1+a')]^2} \quad (3.1)$$

or in another form, the relative flow velocity at the blade plane is

$$V_r = v_o \frac{(1-a)}{\sin \phi} \quad \text{or} \quad \omega_t r \frac{(1+a')}{\cos \phi} \quad (3.2)$$

here, the induced velocity is defined as $v_i \approx (-av_o, a'\omega_t r)$ via. a and a' are the axial and tangential induction factors, v_o is the free wind velocity, ω_t is the rotational speed of the turbine (or the rotor angular velocity), r is the normal distance along the blade span from the root ($0 < r < R$), and ϕ is the inflow angle.

In another way, the inflow angle with the rotor plane, can be calculated from Fig. 3.1 as

$$\phi = \tan^{-1} \frac{v_o(1-a)}{r\omega_t(1+a')} \quad \text{or} \quad \tan^{-1} \frac{(1-a)}{\lambda_r(1+a')} \quad (3.3)$$

where, λ_r is the local tip speed ratio.

As we need to obtain the angle of attack (α), as shown in Fig. 3.1, and can be expressed [33] as

$$\alpha = \phi - \gamma - \beta \quad \text{or} \quad \phi - \Upsilon \quad (3.4)$$

where, γ is the local twist angle, β is the pitch angle, and $\Upsilon (= \beta + \gamma)$ is the sectional pitch angle.

3. Evaluation of Aerodynamic Performance of Wind Turbine

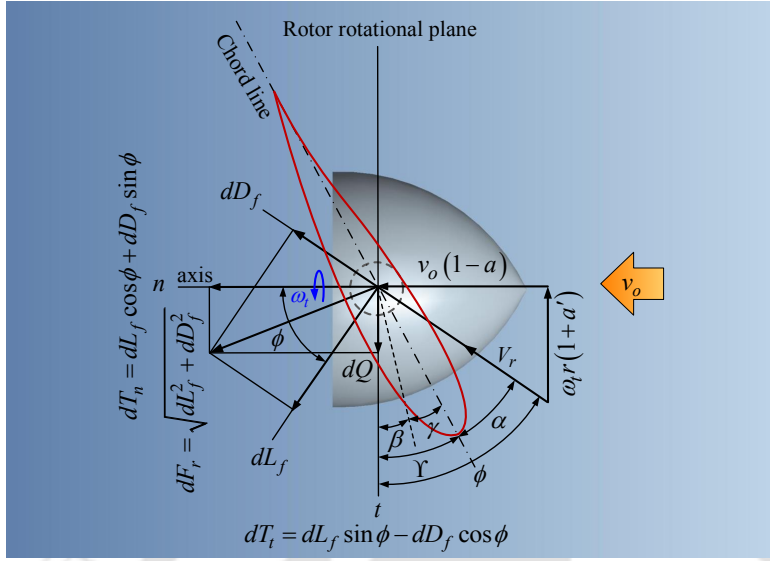


Fig. 3.1: Schematic diagram of 2-D airfoil with the aerodynamic force components and velocity on a blade element.

In the next section deals with the axial/tangential forces on the blade and the change of linear/angular momentum of the wind passing through the annulus.

3.2.2 Conservation of Angular Momentum Theory

The tangential velocity of the actuator disc section increases with the increase in the distance of the section from the center of rotation. Hence, an annular ring of the actuator disc at a radial distance r from the center, with radial width dr is considered for observing the variation of both induced velocities (*i.e.*, the axial and tangential velocities). The thrust force (T_F) per unit length due to the axial momentum on the annular ring is obtained as

$$\frac{dT_F}{dr} = 4\pi r \rho v_o^2 a (1-a) \quad (3.5)$$

where, ρ is the air density.

Using conservation of angular momentum, the rate of change of angular momentum or torque per unit length due to overall change in velocity can be written as

$$\frac{dQ_F}{dr} = 4\pi r^3 \rho \omega_t v_o a' (1-a) \quad (3.6)$$

3.2.3 Blade Element Momentum (BEM) Theory

The BEM theory is the most popular tool for estimating aerodynamic forces on a rotating blade due to its computational efficiency as compared to CFD simulation [33,138]. It models the behaviour of the rotor based on geometric and aerodynamic properties of the airfoil. The blade is assumed to be a collection of 2-D airfoils along its longitudinal dimension and the flow passing over each airfoil is modelled by balancing the momentum on the either side of the rotor plane. The derivation of aerodynamic loads based on blade element momentum theory, which is a combination of the two independent methods [43, 46], *i.e.*, 1-D momentum and 2-D blade element theories. The blade element theory assumes the aerodynamic force on different blade elements are independent (*i.e.*, no interaction between the elements) and solely depend on the lift and drag coefficients of the individual airfoil. On the other hand, the momentum theory (or actuator disc theory) is based on the conservation laws in fluid dynamics.

The aerodynamic forces acting at different points along the length of the blade change due to difference in chord length (c_r), rotational speed ($\omega_t r$) and twist angle (γ). Therefore, the blade is discretized into sufficiently large number of elements to evaluate the aerodynamic force at each element. The total aerodynamic load is evaluated by integrating them along the length of the blade. A set of equations are formed using these two theories, which are solved iteratively.

The lift and drag forces are acting on the blade element along the perpendicular and parallel to the direction of incoming flow, as shown in Fig. 3.1. These forces on a radial length dr of the blade element can be evaluated using coefficient of lift and drag, which are given by

$$dL_f = \frac{1}{2} \rho V_r^2 c_r C_L dr \quad (3.7)$$

$$dD_f = \frac{1}{2} \rho V_r^2 c_r C_D dr \quad (3.8)$$

where, c_r is the airfoil chord length, the lift and drag coefficients (C_L and C_D) in the above equations depend on the angle of attack (α) of the respective airfoil.

On the other hand, the normal force (F_N) (same as the axial force) and torque generated (Q_T) (which is also same as the torque) per unit length due to the tangential force acting on an annular ring of the rotor disc of the multiple bladed turbine are evaluated based on the known lift and drag

3. Evaluation of Aerodynamic Performance of Wind Turbine

coefficients of the airfoil as refer to Fig. 3.1; where, F_r is the resultant thrust force acted on the blade:

$$\frac{dF_N}{dr} = n_b dT_n = n_b \frac{1}{2} \rho c_r V_r^2 (C_L \cos \phi + C_D \sin \phi) \quad (3.9)$$

$$\frac{dQ_T}{dr} = n_b dT_t r = n_b \frac{1}{2} \rho c_r V_r^2 (C_L \sin \phi - C_D \cos \phi) r \quad (3.10)$$

where, $dT_n = dL_f \cos \phi + dD_f \sin \phi$ and $dT_t = dL_f \sin \phi - dD_f \cos \phi$ are the forces acting on each blade in the axial (or normal to the hub) and tangential direction, respectively.

The derivation of aerodynamic loads based on the BEM theory, which combining both momentum theory and blade element theory (or actuator disc theory). A set of equations can be developed to calculate the flow induction factors of the wind turbine. Further, equating the axial thrust acting on the annular ring from (3.5) and (3.9) gives the following form

$$n_b V_r^2 c_r C_n = 8\pi r v_o^2 a (1 - a) \quad (3.11)$$

where, $C_n = C_L \cos \phi + C_D \sin \phi$ is the normal force coefficient.

Similarly, equating the torque acting on the annular ring using 3.6 and (3.10) (*i.e.*, $dQ_T = n_b dT_t r$) gives the following form

$$n_b V_r^2 c_r C_t = 8\pi r^2 \omega_t v_o a' (1 - a) \quad (3.12)$$

where, $C_t = C_L \sin \phi - C_D \cos \phi$ is the tangential force coefficient.

Some algebraic manipulations are done for solving (3.11) and (3.12), the axial and tangential induction factors (a and a') are evaluated as

$$a = \left[\frac{4 \sin^2 \phi}{\sigma_r (C_L \cos \phi + C_D \sin \phi)} + 1 \right]^{-1} \quad (3.13)$$

$$a' = \left[\frac{4 \sin \phi \cos \phi}{\sigma_r (C_L \sin \phi - C_D \cos \phi)} - 1 \right]^{-1} \quad (3.14)$$

where, σ_r is the blade solidity, which is defined as the total blade area in an annular ring divided by the total area of the annular ring at a radial distance r , *i.e.*, $\sigma_r = n_b c_r / 2\pi r$. Since, the inflow angle in (3.13) and (3.14) is a function of the flow induction factors as given in (3.3), an iterative procedure is adopted to find them, *i.e.*, a and a' . Thus, the normal and tangential forces can be evaluated from (3.9) and (3.10) by substituting relative velocity obtained from (3.2) using these flow induction factors.

One of the major disadvantage of the BEM theory is that, it does not account for the effect of vortex shedding at the tip of the blade into wake. Therefore, some modifications are required in the

formulations of BEM theory to account for various correction including tip and hub losses.

3.2.4 Loss Corrections

The inflow angle in Fig. 3.1 becomes very small for a large axial induction factor and the contribution of lift force in the tangential direction also reduces. This is reflected in lower power production due to reduced torque, which generally occurs at the tip of the blade, *i.e.*, tip-loss. The azimuthal variation of axial induction factor is required to incorporate this loss. Some correction factors are used with BEM theory to address this issue.

The pioneer work of Prandtl [155] states that the behaviour of a particle in the downstream using actuator disc model and developed an approximate solution that account for tip-loss and root-loss (or hub-loss). This loss correction factor is given by

$$F = \frac{2}{\pi} \cos^{-1} [\exp(-f_{\text{root-loss}})] \times \frac{2}{\pi} \cos^{-1} [\exp(-f_{\text{tip-loss}})] \quad (3.15)$$

$$\text{Here, at the root side, } f_{\text{root-loss}} = \frac{n_b(r - R_h)}{2R_h \sin \phi} \quad (3.16)$$

$$\text{at the tip side, } f_{\text{tip-loss}} = \frac{n_b(R - r)}{2r \sin \phi} \quad (3.17)$$

where, R_h is the blade root radius, R is the turbine radius (or blade length). The tip correction factor always varies between 0 and 1 (*i.e.*, $0 \leq F \leq 1$), the value at most points of blades to be unity and near the tip of blade to the zero. Equation for root-loss (3.16) and tip-loss equation (3.17) are used. The results calculated from the BEM theory with the root-tip loss correction factor gives perfect agreement with practical field data for the attached flows on the blades surface.

Similarly, the thrust and torque forces in (3.5) and (3.6) are modified in the following form

$$\frac{dT_F}{dr} = 4F\pi r \rho v_o^2 a (1 - a) \quad (3.18)$$

$$\frac{dQ_F}{dr} = 4F\pi r^3 \rho \omega_t v_o a' (1 - a) \quad (3.19)$$

Therefore, the flow induction factors in (3.13) and (3.14) are modified in the following form

$$a = \left[\frac{4F \sin^2 \phi}{\sigma_r (C_L \cos \phi + C_D \sin \phi)} + 1 \right]^{-1} \quad (3.20)$$

$$a' = \left[\frac{4F \sin \phi \cos \phi}{\sigma_r (C_L \sin \phi - C_D \cos \phi)} - 1 \right]^{-1} \quad (3.21)$$

When the axial induction factor, $a > 0.4$ then the original BEM theory starts to break-down and

3. Evaluation of Aerodynamic Performance of Wind Turbine

does not converge [156]. Buhl [47] developed a correction to the rotor thrust for $a > 0.4$. In the above equation, $a_c \simeq 0.2$, the flow induction factor using Glauert's correction can be evaluated as

$$a = \frac{1}{2} \left[2 + k(1 - 2a_c) - \sqrt{(k(1 - 2a_c) + 2)^2 + 4(ka_c^2 - 1)} \right] \quad (3.22)$$

In the above expression,

$$k = \frac{4F \sin^2 \phi}{\sigma_r (C_L \sin \phi + C_D \cos \phi)} \quad (3.23)$$

This is valid for axial flow induction factor between $0.4 \leq a \leq 1$. Similar to Glauert's empirical relationship, many others have proposed empirical curves to fit the same experimental data. Therefore, this empirical curves do consider the tip and hub losses.

In addition to (3.14), Lanzafame and Messina [49] also introduced a new relationship of tangential induction factor in terms of the axial induction factor and local tip speed ratio as

$$a' = \frac{1}{2} \left(\sqrt{1 + \frac{4}{\lambda_r^2} a(1 - a)} - 1 \right) \quad (3.24)$$

Hence, the magnitude of a' is depends on radial length, wind speed, tip speed ratio and rotational speed in (3.24). In order to get accurate results, the developed algorithm takes advantage of this theory to calculate the aerodynamics of the blades.

3.2.5 Overall Power Coefficient

Utilizing the obtained induction factors (a , a'), the general form of the local power coefficient of the wind turbine can be written as

$$C_P = \frac{8}{\lambda^2} \int_{\lambda_h}^{\lambda} a' (1 - a) \lambda_r^3 F \left[1 - \frac{C_D}{C_L} \cot \phi \right] d\lambda_r \quad (3.25)$$

where, the value of λ is tip speed ratio, λ_h is tip speed ratio at the root. Note that, if $C_D \approx 0$, then (3.25) is given as $C_P = \frac{8}{\lambda^2} \int_0^{\lambda} a'(1 - a) \lambda_r^3 F d\lambda_r$.

Finally, the alternate expression for the power coefficient is obtained after simplification and approximating the integration by a summation. This results in approximate value of (3.25) as presented by Manwell *at el.* [43]. Using the simplified value of C_p , the total power coefficient is given as (3.26):

$$C_P = \sum_{q=1}^n \left[\left(\frac{8\Delta\lambda_r}{\lambda^2} \right) F_q \sin^2 \phi_q (\cos \phi_q - \lambda_{r_q} \sin \phi_q) (\sin \phi_q + \lambda_{r_q} \cos \phi_q) \left[1 - \frac{C_D}{C_L} \cot \phi_q \right] \lambda_{r_q}^2 \right] \quad (3.26)$$

where, n is the number of sections across the whole blade strip, $\Delta\lambda_r$ is expressed as $\lambda_{r_q} - \lambda_{r_{(q-1)}} = \lambda/n$, here, q and $q - 1$ indicate the edges of the blade section.

3.2.6 Primarily Blade Geometry Design

The primarily blade geometry design of the wind turbine is to calculate the airfoil chord length based on optimum rotor theory (ORT), which is written as [148]:

$$c_r = \frac{8\pi r F}{n_b C_{L(\text{design})}} \times \frac{1 - \lambda_r \tan \phi}{\tan \phi + \lambda_r} \times \sin \phi \quad (3.27)$$

where, $C_{L(\text{design})}$ is the design lift coefficient at optimum angle of attack, $\lambda_r = \lambda \times r/R$ is the local tip speed ratio.

The local inflow angle to the plane can be determined using inflow induction factors along the radial position and is expressed as

$$\phi = \tan^{-1} \frac{v_o(1-a)}{r\omega_t(1+a')} \quad (3.28)$$

The local twist angle (or the angle of relative wind from the root) is given as

$$\gamma = \phi - \beta - \alpha_d \quad \text{or} \quad \Upsilon - \beta \quad (3.29)$$

where, α_d is the design angle of attack at which the maximum lift/drag ratio is observed.

3.2.7 Relationship Between Theoretical Coefficients

The performance index of the wind turbine is more often expressed in terms of torque coefficient (C_Q) and power coefficient (C_P) [157, 158] and are articulated as

$$C_Q = \frac{T_d}{\frac{1}{2}\rho a_t v_o^2 R} \quad (3.30)$$

$$C_P = \frac{P_t}{P_a} = \frac{T_d \omega_t}{\frac{1}{2}\rho a_t v_o^3} = \frac{T_d}{\frac{1}{2}\rho a_t v_o^2 R} \frac{R \omega_t}{v_o} = C_Q \times \lambda \quad (3.31)$$

where, a_t is the swept area of the actuator disc (or rotor), P_t is the mechanical power generated, P_a is the wind power available. Here, T_d is the torque generated by the wind turbine, which is useful in evaluating the its self starting capacity.

3.3 Approximation of Wind Turbine Dynamics with a Second Order Transfer Function

In this section, we propose to use an equivalent second order transfer function to model the output generated torque by the wind turbine and is expressed as

$$T(s) = \frac{\omega_n^2 T_d}{s^2 + 2\xi\omega_n s + \omega_n^2} \quad (3.32)$$

The procedure for tuning the parameters of the dynamical model is explained in the subsequent subsections.

3.3.1 Steady-state Gain

The steady-state gain of the model (k_G) is

$$k_G \cong T(s)|_{s=0} = T_d \quad (3.33)$$

This steady state gain is estimated using the BEM theory.

3.3.2 Blade Natural Frequency

The natural frequencies ω_n of the structure is to be lies between an admissible bounds $[\omega_{n\text{Lower}}; \omega_{n\text{Upper}}]$ to avoid resonant conditions in the operating range of the rotor blade [48, 159, 160].

Typically the first blade rotational natural frequency (ω_{n1}) of the blade should be larger than the maximum rotor blade passing frequency [48, 159–161], *i.e.*,

$$\omega_n \geq \kappa(3\omega_t) \quad (3.34)$$

$$\geq \kappa(3\lambda v_o/R) \quad (3.35)$$

where, ω_{n1} is the fundamental natural frequency of the horizontal blade, and κ is a suitable multiplication factor which ensures a safety gap between the two frequencies. Through the several experimentation, it has observed that κ varies in the range of 1.04 to 1.9 [161]. The present work has chosen a safety gap of 1.2. The maximum rotation speed occurs at rated speed, and the factor of three came from the number of blades in (3.34).

The fundamental natural frequency of the horizontal blades decreases with increasing the values of the blade length. Therefore, it is obvious that $\omega_n \sim 1/R$. In general, the relation of the fundamental

natural frequencies between two blades are

$$\frac{\omega_{n1}}{\omega_{n2}} = \frac{R_2}{R_1} \quad (3.36)$$

where, R_1 and R_2 are the radius of two different wind turbine blades for 1 & 2.

Since, the rotor rotational speed also decreases with blade length, the tendency of the wind turbine to excite a particular resonance condition is independent of the blade length.

3.3.3 Formulation of the Aerodynamic Damping Ratio (ξ)

The aerodynamic damping is developed due to the interaction between the blade aerodynamics and the structural motion. Therefore, the proposed structural and aerodynamic damping model focuses on the vibrational response of the blade aerodynamics incorporating blades tip motion.

A flexible multi-body representation is adopted to describe the dynamic behaviour of the 3-bladed wind turbine. For a constant-speed, the aerodynamic damping model can be studied by considering a constant wind velocity of the wind turbine. The axial force per unit length given in (3.9) can be re-written as

$$\frac{dF_N}{dr} = nb \frac{1}{2} \rho \frac{v_t}{\cos \phi} \frac{v_r}{\sin \phi} c_r (C_L \cos \phi + C_D \sin \phi) \quad (3.37)$$

Considering the velocity components of the airfoil as shown in Fig. 3.2, define $v_t = \omega_t r (1 + a')$ is the tangential flow velocity and $v_r = v_o(1 - a) \pm \dot{x}_{tip}$ is the axial flow velocity (or induced velocity vector) at the actuator disc (or rotor plane). When blade tip experience a perturbation in the wind direction with velocity \dot{x}_{tip} , the apparent outside the rotor plane velocity component of the blade section, therefore, $v_o(1 - a)$ will be reduced by \dot{x}_{tip} as shown in Fig. 3.2.

Taking the following assumptions [162,163]:

$$\left\{ \begin{array}{ll} \bullet \text{ For attached flow/unstalled} & : C_L \gg C_D \\ \bullet \text{ For small inflow angle} & : \cos \phi \approx 1 \\ \bullet \text{ At high tip speed ratio} & : v_t \gg v_r \end{array} \right.$$

The high tip speed ratio ($v_t \gg v_r$) allows a simplified for the angle of inflow as

$$\phi \simeq \frac{v_r}{v_t} \quad (3.38)$$

3. Evaluation of Aerodynamic Performance of Wind Turbine

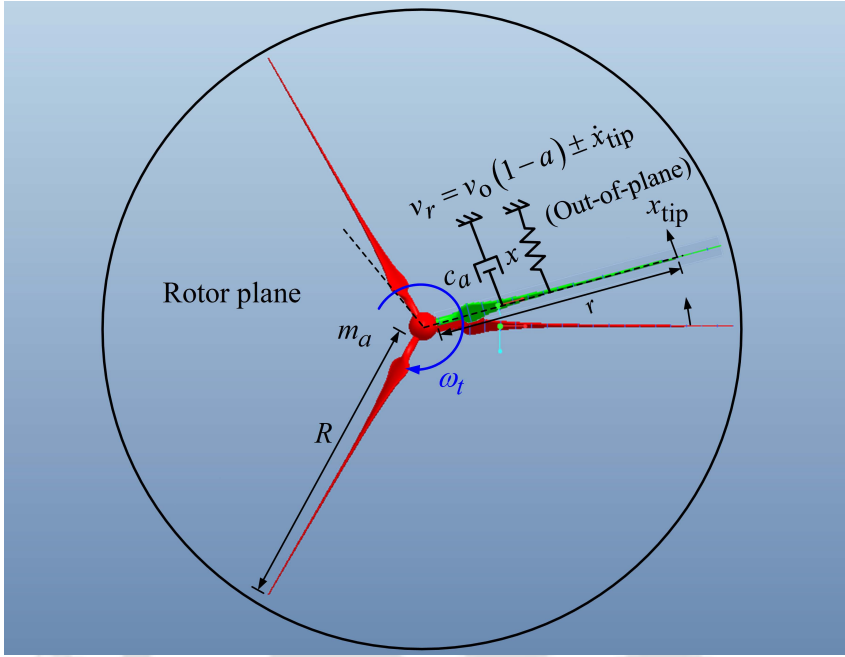


Fig. 3.2: Aerodynamic damping effect on the wind turbine structural model.

For a constant-rotational speed of the wind turbine, the change in angle of inflow is expressed as

$$d\phi \simeq \frac{dv_r}{v_t} \quad (3.39)$$

Slop of the lift coefficient in terms of the rate of change of lift coefficient and angle of attack is expressed by $C'_L = dC_L/d\alpha$ and written as

$$dC_L = C'_L d\phi = C'_L d\alpha = C'_L \frac{dv_r}{v_t} \quad (3.40)$$

Here, according to (3.4), $\phi = \alpha + \beta + \gamma$; here, β is considered to be zero and γ is considered as a constant term. When the blade is not in stall, the rate of change of lift coefficient with angle of attack (*i.e.*, $C'_L = dC_L/d\alpha$) is equal to 2π [33].

By differentiating (3.37) and its simplified form (here, considering $C_D \simeq 0$ from the BEM theory assumption) is given as

$$d\left(\frac{dF_N}{dr}\right) = n_b \frac{1}{2} \rho v_t v_r c_r dC_L = n_b \frac{1}{2} \rho v_t c_r C'_L dv_r \quad (3.41)$$

From Fig. 3.3, the change in apparent axial wind velocity v_r is strongly influenced due to changes in the structural motion and wind velocity. Therefore, this wind velocity can be divided into two

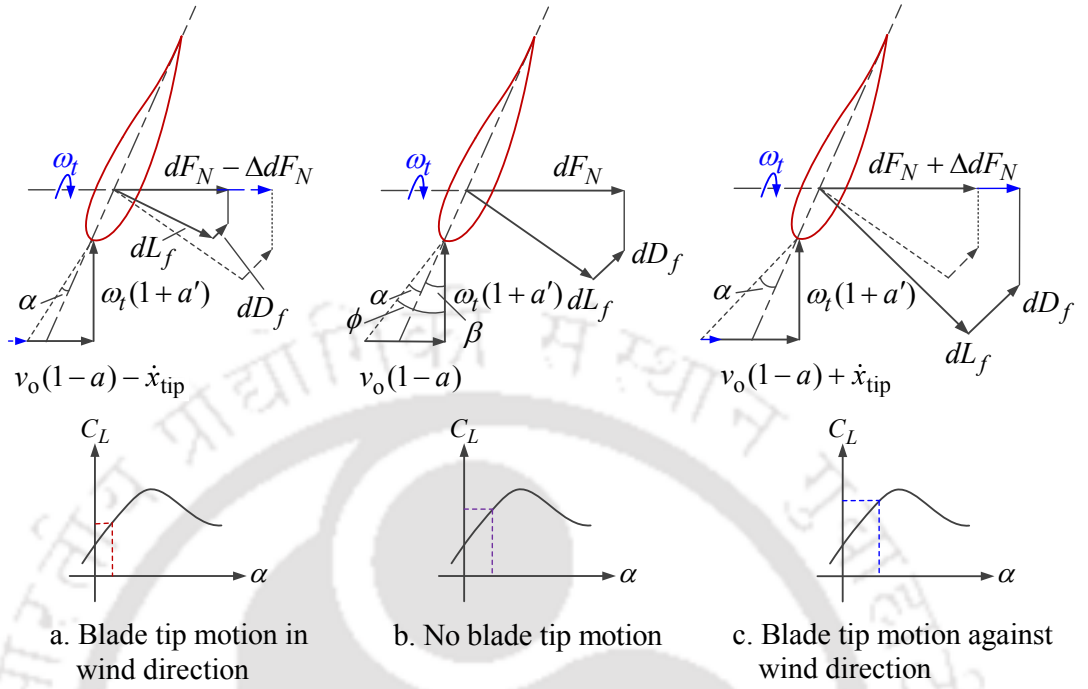


Fig. 3.3: The velocity and force diagram for vibrating the blade according to the wind turbine structural model.

components and written as

$$dv_r = dv_{r,wind} + dv_{r,blade\ tip} = u - \dot{x} \quad (3.42)$$

where, u is the change in the axial wind velocity and \dot{x} is the structural velocity whose sign is positive when aligned with the wind direction.

Here, the change in the axial force per unit length can be written as

$$T' = d \left(\frac{dF_N}{dr} \right) = n_b \frac{1}{2} \rho \omega_t r c_r C'_L (u - \dot{x}) \quad (3.43)$$

Assuming the blade element as a mass-spring system with a single-degree of freedom (1-DOF), the change is estimated using the principle equation of motion corresponding to the wind turbine vibration and is modeled by equation $m_a \ddot{x} + kx = T'$. Plugging the value of k and T' , the equation obtained is given below as

$$m_a \ddot{x} + kx = n_b \frac{1}{2} \rho \omega_t r c_r C'_L (u - \dot{x}) \quad (3.44)$$

$$\Rightarrow m_a \ddot{x} + n_b \frac{1}{2} \rho \omega_t r c_r C'_L \dot{x} + kx = n_b \frac{1}{2} \rho \omega_t r c_r C'_L u \quad (3.45)$$

3. Evaluation of Aerodynamic Performance of Wind Turbine

where, m_a is the modal moment of the wind turbine rotor and k is stiffness of spring. The solution of the translational vibration is analogous to linear vibration.

The aerodynamic damping per unit length is suggested by (3.45) and expressed as

$$\frac{dc_a}{dr} = n_b \frac{1}{2} \rho \omega_t r c_r C'_L \quad (3.46)$$

The aerodynamic damping of the wind turbine can be obtained by integration of (3.46) throughout the horizontal blade given as

$$c_a = n_b \frac{1}{2} \rho \omega_t \int_{R_h}^R c_r C'_L r dr \quad (3.47)$$

Therefore, the aerodynamic damping ratio of the wind turbine rotor for the fundamental mode of vibration can be expressed as

$$\xi = \frac{c_a}{2m_a \omega_n} = n_b \frac{\rho \omega_t}{4m_a \omega_n} \int_{R_h}^R c_r C'_L r dr, \quad \xi \in [0, 1] \quad (3.48)$$

where, $c_{cr} = 2m_a \omega_n$ is the critical damping.

Equation (3.48) is based on the approximations and may under predict the aerodynamic damping at higher wind velocity.

3.3.4 Overall Transfer Function

The aerodynamic model for getting torque response can be approximately represented in the form of the second order transfer function (TF), *i.e.*, $T(s)$ as given below

$$T(s) = \frac{T_d \left(\frac{3.6 \lambda v_o}{R} \right)^2}{s^2 + 2 \left(n_b \frac{\rho \omega_t}{4m_a \omega_n} \int_{R_h}^R c_r C'_L r dr \right) \left(\frac{3.6 \lambda v_o}{R} \right) s + \left(\frac{3.6 \lambda v_o}{R} \right)^2} \quad (3.49)$$

Here, the step signal will be applied to the second order system to get the dynamic response of the torque generated by the turbine. The steady-state value of the torque *i.e.*, T_d is obtained through the BEM theory.

3.4 Algorithm Used for Design of the Blade Geometry and Implementation Procedure of the BEM Theory

In this section, an algorithm is written for the calculation of the blade geometry based on the optimum rotor theory [113,164]. The iterative procedure is used for the calculation of optimum chord length, and twist angle at each blade element of the wind turbine is summarized in Algorithm 1. The preliminary blade design principle of the wind turbine is described in subsection 3.2.6. The step by step procedure of the proposed optimum rotor theory algorithm is discussed below:

An algorithm is written to predict the aerodynamic load of the wind turbine based on the BEM theory. Though conceptually simple, solving BEM theory with high accuracy and efficiently can be challenging. There are several solution strategies for numerical convergence of the axial and tangential induction factors are available in the literature [165]. These algorithms require a significant amount of computational time to achieve convergence, else they suffer numerical instability. In this case, a solution technique needs to be proposed to assure convergence at a super-linear rate. In this proposal, the solution of the BEM theory is categorized into three operating regions (*i.e.*, the momentum, empirical and propeller break) to evaluate the optimal inflow angle as opposed to the traditional approach for optimal induction factors for each of the elements to enhance the convergence. The step by step procedure of the proposed BEM theory algorithm is summarized in Algorithm 1.

3.5 Selection and Design of Wind Turbine Blade Parameters

In order to design the efficient wind turbine, the most important influencing parameters need to be study. In this section, the details of design parameters are presented below.

3.5.1 Design of Free Wind Speed, Tip Speed Ratio, and Rotational Speed

The profile of wind velocity is modeled as per the standard IEC 61400-2 [112]. An inlet wind velocity profile commonly design for 3-blade variable-speed wind turbine should be 1.4 times the annual mean wind speed (v_{amws}). In this design study, the wind turbine Class III has been selected v_{amws} is equal to 5 m/s or below [99]; therefore, the free wind speed (v_o) is approximately equal to 7 m/s. According to the literature, the tip speed ratio (TSR) for the 3-blades wind turbine at the free wind speed varies between 6 to 8 [148,166]. Here, the specific value of the design tip speed ratio (λ_d) is chosen to be 6 for different wind turbine blade length ($R_1 = 5$ m, $R_2 = 2.5$ m & $R_3 = 1.7053$ m) at

3. Evaluation of Aerodynamic Performance of Wind Turbine

Algorithm 1 Design procedure of the blade geometry based on optimal rotor theory algorithm.

Input: $v_o, n_b, \omega_t, R, \alpha_d, \beta, C_L$ and C_D

Initialize: Set an initial values to a and a'

Output: r, c_r, γ

```

1:  $\ell \leftarrow 20$  ▷ Blade span divided into 18–20 number of elements
2:  $\Delta r \leftarrow \frac{R}{\ell}$  ▷ Width of single differential element
3:  $\chi_1 \leftarrow \frac{\Delta r}{R}$  and  $\chi_2 \leftarrow \frac{2\Delta r}{R}$  ▷ Fractional radial position (dimensionless)
4:  $\Delta\chi \leftarrow \chi_2 - \chi_1$  ▷ Incremental length
5:  $\chi \leftarrow \chi_1 + \chi_2$  ▷ Fractional length
6: for  $i = 1 : \ell - 2$  do
7:   if  $i \geq 2$  then
8:      $\chi_i \leftarrow \chi_{i-1} + \Delta\chi$ 
9:   else
10:     $\chi_i \leftarrow \chi_i + 0$ 
11:   end if
12:    $r_i \leftarrow \chi_i R$  ▷ Local radial position
13:    $\lambda_{r_i} \leftarrow \lambda \frac{r_i}{R}$  ▷  $\chi \triangleq \frac{r}{R}$  is a dimensionless radial position ( $\chi \in [0, 1]$  while  $r \in [0, R]$ )
14:   while  $\varepsilon > \text{tolerance}$  do
15:     Start with initial guess values of the flow induction factors ( $a \leftarrow 0$  and  $a' \leftarrow 0$ )
16:     Compute the inflow angle ( $\phi_i$ ) of each blade element using (3.3) ▷  $\phi \in [0, \frac{\pi}{2}]$ 
17:     Look up the values of lift and drag coefficients ( $C_L$  and  $C_D$ ) at optimal angle of attack ( $\alpha$ )
18:     Compute the blade loss correction factor ( $F_i$ ) using (3.15), Prandtl model ▷  $F \in (0, 1)$ 
19:     Compute the local chord length ( $c_{r_i}$ ) using 3.27
20:     Compute the solidity factor ( $\sigma_{r_i}$ ) for the blade element
21:     Compute the axial and tangential induction factors ( $a$  and  $a'$ ) using (3.20) and (3.21)
22:     Compute the local twist angle ( $\gamma_i$ ) using (3.29)
23:      $|\phi^{\text{iter}+1} - \phi^{\text{iter}}| \leftarrow \varepsilon$  ▷ Convergence parameter  $\varepsilon$  is set to  $10^{-3}$ 
24:     iter  $\leftarrow$  iter + 1 ▷ Iteration is repeated until the desired convergence
25:   end while
26: end for
27: Compute blade geometry.

```

Algorithm 2 Implementation procedure of the BEM theory algorithm.

Input: $v_o, \rho, \mu, n_b, r, r_h, R, \gamma, c_r, \alpha_d, \beta, C_L, C_D, C_{L(\max)}, C_{D(\max)}$

Initialize: Set an initial values to $a, a', \alpha, F, P, C_P, C_n$ and C_t

Output: C_P, C_Q, P_t, T_d

```

1:  $\lambda \leftarrow [2 : 0.5 : 9]$ 
2:  $n \leftarrow \text{length}(r)$  ▷ Blade span divided into 18 number of elements
3:  $m \leftarrow \text{length}(\lambda), R \leftarrow \max(r), \beta \leftarrow 0$ 
4: Compute the rotational speed and solidity factor for each blade element
5: count  $\leftarrow 0$ 
6: for  $i = 1 : 1 : m$  do
7:   Compute the local tip speed ratio ( $\lambda_{r_i}$ ) of each blade elements
8:   Start with initial guess values of the flow induction factors are  $a \leftarrow 0$  and  $a' \leftarrow 0$ 
9:   Compute the inflow angle ( $\phi_i$ ) of each blade element using (3.3)
10:  Compute the relative wind velocity ( $V_{r_i}$ ) at the blade plane using (3.2)
11:  Compute the Reynolds number ( $Re_i$ ) for each of the element using (3.52)
12:  Compute the angle of attack ( $\alpha_i$ ) of each blade element by substituting twist angle
    from inflow angle using (3.4) as shown in Fig. 3.1
13:  for  $j = 1 : 1 : n$  do
14:    if  $\alpha_{i,j} \leq 14$  then
15:      Compute the lift and drag coefficients ( $C_{L_{i,j}}$  and  $C_{D_{i,j}}$ ) of each blade element corre-
        sponding angle of attack found in Step 12 depend on Reynolds number by interpolation
        of the airfoil database
16:    else
17:      Compute the lift and drag coefficients ( $C_{L_{i,j}}$  and  $C_{D_{i,j}}$ ) of each blade element from the
        airfoil database at optimum angle of attack using (3.50) and (3.51)
18:    end if
19:  end for
20:  Start with initial guess of the change in the flow induction factors are  $\Delta a \leftarrow 1$  and  $\Delta a' \leftarrow 1$ 
21:  while ( $\max(\Delta a) \geq 10^{-3}$  && count  $\leq 1000$ ) do
22:    Compute the blade loss correction factor ( $F_i$ ) using (3.15), Prandtl model
23:    Update the loss correction factors as  $F_{1,i} \leftarrow F_{2,i}$  and  $F_{n-1,i} \leftarrow F_{n,i}$ 
24:    Compute the normal ( $C_{n_i}$ ) and tangential ( $C_{t_i}$ ) force coefficients of each blade elements
25:    for  $j = 1 : 1 : n$  do
26:      if  $a_{i,j} < 0.4$  then
27:        Compute the axial induction factor ( $a_{i,j}$ ) using (3.20)
28:      else ▷ propeller brake region
29:         $a_c \leftarrow 0.2$ 
30:        Compute the constant  $k_{i,j}$  using (3.23)
31:        Compute the new axial induction factor (new_ $a_{i,j}$ ) using (3.22) ▷ if  $a > a_c$ 
32:      end if
33:    end for
    Calculate the new tangential induction factor (new_ $a'_i$ ) using (3.24)

```

3. Evaluation of Aerodynamic Performance of Wind Turbine

```
35: Compute the change in axial induction factor as  $\Delta a \leftarrow |\text{new\_}a_i - a_i|$   $\triangleright$  Iterate till
36: reached  $\Delta a \leq$  tolerance as set to  $10^{-3}$ , if the conditions are satisfied, then continue
37: Otherwise, update the new inflow induction factors are  $a_i \leftarrow \text{new\_}a_i$ ,  $a'_i \leftarrow \text{new\_}a'_i$ 
38: Update Step 9, Step 10 and Step 11
39: for  $j = 1 : 1 : n$  do
40:     if  $\alpha_{i,j} \leq 14$  then
41:         Compute the lift and drag coefficients ( $C_{L_{i,j}}$  and  $C_{D_{i,j}}$ ) of each blade element corre-
42:         sponding angle of attack found in Step 12 depend on Reynolds number by interpolation
43:         of the airfoil database
44:     else
45:         Compute the lift and drag coefficients ( $C_{L_{i,j}}$  and  $C_{D_{i,j}}$ ) of each blade element from the
46:         airfoil database at optimum angle of attack using (3.50) and (3.51)
47:     end if
48: end for
49: count  $\leftarrow$  count + 1
50: end while
51: Compute the change in tip speed ratio as  $\Delta \lambda_{r_i} \leftarrow \text{mean}(\text{diff}(\lambda_{r_i}))$ 
52: Compute the power coefficient ( $C_{P_i}$ ) using (3.26) and torque coefficient ( $C_{Q_i}$ ) using (3.30)
53: end for
54: Compute aerodynamic loads
```

the free wind velocity, which corresponds to the wind turbine rotor rotational speeds are 80.21 rpm, 160.43 rpm & 235.19 rpm, respectively. Assuming the operating wind speed varies from 5 m/s to 20 m/s, which corresponds to the change of TSR from 2.1 to 8.4 for each blade length. Generally, the rated wind speed of the variable-speed wind turbine is not defined at this stage. Therefore, it will be calculated through further investigation.

3.5.2 Selection of 2-D Airfoil Profile and Angle of Attack

The selection of suitable airfoil plays a vital role in design and analysis of the wind turbines that would help to get the better efficiency.

In the design process of the wind turbine blade geometry, the necessary parameters of the blade airfoil are the design lift coefficient ($C_{L(\text{design})}$), design drag coefficient ($C_{D(\text{design})}$), and design angle of attack (α_d). As discussed in Chapter 2, it was concluded that NACA 63-415 airfoil is better for wind turbine application, hence, the present Chapter gets these design values from Chapter 2 for the NACA 63-415 airfoil.

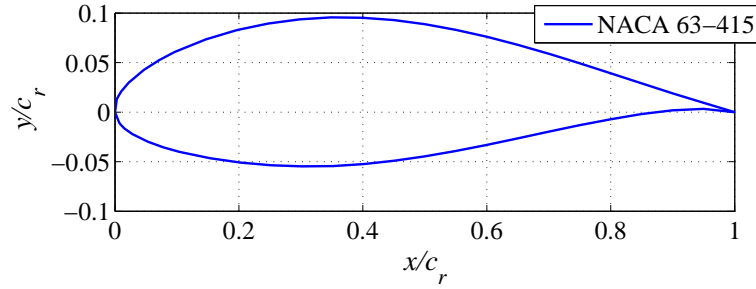


Fig. 3.4: Geometric shape of NACA 63-415 airfoil cross-section curve [3].

Table 3.1: The design values of NACA 63-415 airfoil.

Parameter	Symbol	Values
Angle of attack	α_d	6°
Design lift coefficient	$C_{L(\text{design})}$	0.93863
Design drag coefficient	$C_{D(\text{design})}$	0.00963
Max. lift/drag ratio	$(C_L/C_D)_{\text{max}}$	97.47
Max. lift coefficient	$C_{L(\text{max})}$	1.3446
Max. drag coefficient	$C_{D(\text{max})}$	0.0674

When the turbine begins to operate with an angle of attack more than its designed value, then the lift and drag properties tend to become independent of detailed blade geometry such as thickness and chord length *i.e.*, in other ways, the airfoil behaves like a ‘flat plate, fully stalled’. Under this condition, the calculation of the lift and drag coefficients is done using the Viterna method [167] as shown in the equation below:

$$C_L = 2C_{L(\text{max})} \sin \alpha \cos \alpha \quad (3.50)$$

$$C_D = 2C_{D(\text{max})} \sin^2 \alpha \quad (3.51)$$

where, $C_{L(\text{max})}$ and $C_{D(\text{max})}$ are the lift and drag coefficients at the maximum angle of attack *i.e.*, $C_{L(\text{max})} = C_L|_{\alpha=90^\circ}$ and $C_{D(\text{max})} = C_D|_{\alpha=90^\circ}$.

3. Evaluation of Aerodynamic Performance of Wind Turbine

3.5.3 Calculation of Reynolds Number and Turbulent Intensity

The wind turbine airfoils aerodynamic performance is influence by the Reynolds number (Re) and is defined as [113]:

$$Re = \frac{\rho V_r c_r}{\mu} \quad (3.52)$$

where, V_r is the relative wind velocity (which is defined by $V_r = \sqrt{v_o^2 + V_{tan}^2}$, where, the tangential velocity, $V_{tan} = \omega_t R_{mid-section} = (\text{blade tip speed})/2$), c_r is the chord of the mid-section of the blade, and μ is the dynamic viscosity (1.778×10^{-5} kg/m·s) of the air.

In this study, the aerodynamic performances are calculated for different rotor radius at constant wind speeds as shown in Table 3.2.

Table 3.2: Calculation of Reynolds number (Re) and turbulent intensity (I) at different wind speed.

v_o (m/s)	$R_1 = 5$ m			$R_2 = 2.5$ m			$R_3 = 1.7053$ m		
	V_r (m/s)	Re	I (%)	V_r (m/s)	Re	I (%)	V_r (m/s)	Re	I (%)
5	21.59	7.1×10^5	2.97	21.59	3.5×10^5	3.24	21.59	2.4×10^5	3.40
7	22.14	7.3×10^5	2.96	22.14	3.6×10^5	3.23	22.14	2.5×10^5	3.39
10	23.26	7.6×10^5	2.94	23.26	3.8×10^5	3.21	23.26	2.6×10^5	3.37
15	25.81	8.5×10^5	2.91	25.81	4.2×10^5	3.17	25.81	2.9×10^5	3.32
20	29.00	9.5×10^5	2.86	29.00	4.7×10^5	3.12	29.00	3.2×10^5	3.28

As shown in Table 3.2, the Reynolds number (Re) of these wind turbine (the blade length, *i.e.*, $R_1 = 5$ m, $R_2 = 2.5$ m, and $R_3 = 1.7053$ m, respectively) does not vary significantly, which is in the range of 2×10^5 to 1×10^6 , when the wind velocity varies from 5 m/s to 20 m/s. The present work has chosen $Re = 7.3 \times 10^5$ for R_1 , $Re = 3.6 \times 10^5$ for R_2 , and $Re = 2.4 \times 10^5$ for R_3 as the Reynolds number at $v_o = 7$ m/s.

3.6 Simulation Set-up Description and Methodology for Validation Purpose

In the current study, the computational simulations are carried out using ANSYS/Fluent standard commercial software [114] to analyze the flow field over 3-D wind turbine and the aerodynamic performance with different tip speed ratio (TSR).

3.6.1 Solid Geometry Model Development

The process of building a 3-D computational domain for the wind turbine, the NACA 63-415 airfoil is used throughout the blade span by importing the coordinates of the upper and bottom surfaces from the coordinate database [3]. Here, the airfoil has 26 coordinate points on upper surface as well as the same number of points in bottom surface.

The geometrical parameter and operating conditions includes the blade length (*i.e.*, rotor radius) for different wind turbine rotors. For each blade element, the chord length (c_r) is determine using (3.27) with design lift coefficient ($C_{L(\text{design})}$) of 0.93863, design drag coefficient ($C_{D(\text{design})}$) of 0.00963, number of blades (n_b) of 3 (3-blades) to optimize cost and weight balance, design tip speed ratio (λ) of 6, and the design angle of attack (α_d) of 6° . These design parameters are based on the maximum lift/drag ratio at the free wind speed (v_o) of 7 m/s.

The hub radius of the wind turbines are h_1 is 0.23 m for wind turbine with radius R_1 (WT_{R1}), h_2 is 0.12 m for WT_{R2} & h_3 is 0.08 m for WT_{R3} , respectively. Here, the blades are divided into 18 equidistant elements or sections from root to tip. The twist angle (γ) is determined using (3.29) at each span element. The inflow angle is affected by the inflow induction factors and is calculated using (3.28). For each blade element, the chord length and twist angle distributions are calculated based on the optimum rotor theory as explained in Algorithm 1.

Figs. 3.5 and 3.6 shows the calculated chord length and twist angle distributions rapidly increases close to the hub of the radial profile. The chord length (c_r) taken at the middle section of the blade length is 0.4755 m for WT_{R1} , 0.2377 m for WT_{R2} & 0.1622 m for WT_{R3} and the twist angle is 26.02° at the blade root to 0.31° at the tip of the blade for all turbines.

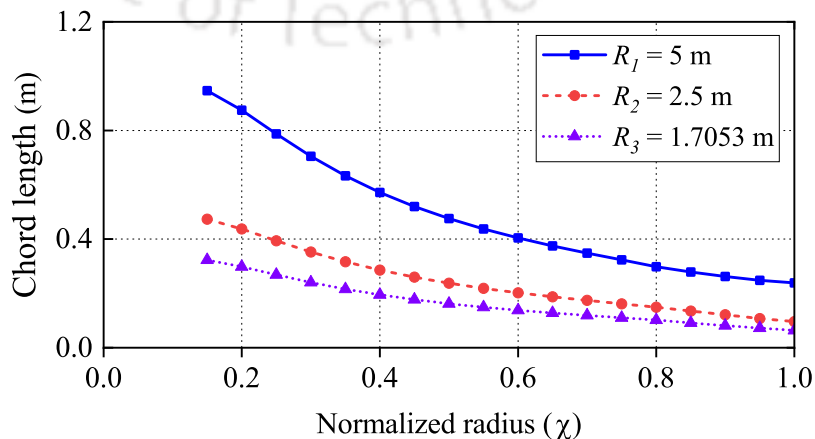


Fig. 3.5: Variation of chord length at radial position for different wind turbine.

3. Evaluation of Aerodynamic Performance of Wind Turbine

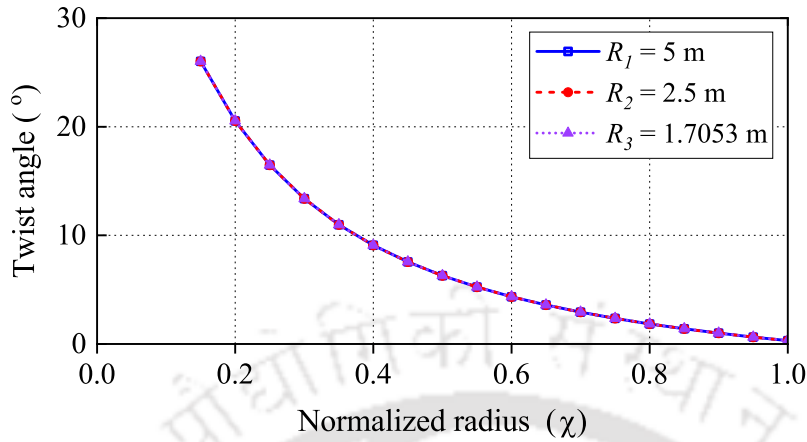


Fig. 3.6: Variation of twist angle at radial position for different wind turbine.

Using the above design parameters, a 3-D CAD model using Pro/ENGINEER is developed. Fig. 3.7 shows the airfoils wireframe, single blade structure, and overall the design of the wind turbine rotor.

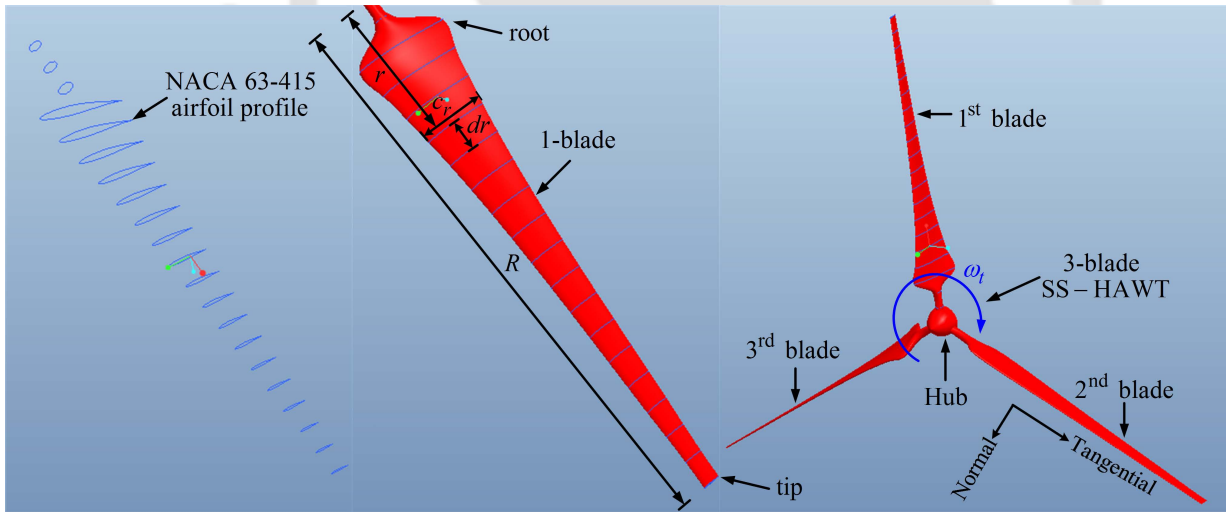


Fig. 3.7: A 3-D solid model of the wind turbine with NACA 63-415 profile.

3.6.2 Computational Domain Description and its Boundary Conditions

The designed 3-D CAD model of the wind turbine rotor using Pro/ENGINEER software is imported into ANSYS/Fluent software design modeler workbench to analyze its flow field and aerodynamic performance. The CFD domain uses a cylindrical domain. The wind turbine rotor is located at 4D (*i.e.*, four times the diameter of the turbine rotor) from the inlet-boundary, and the point of rotation is considered as the origin. Here, the z -axis is the axis of rotation with the blades rotating

in xy -plain.

The dimensions of the computational domain for the analysis are $5D$ radial span-wise direction and $12D$ downstream region in which the wake expansion happens. Additionally, one more medium cylindrical domain has been constructed inside the large cylinder to apply the body of influence method during meshing. Its geometry consists of $2D$ upstream length, $5D$ downstream length, and has approximately the same radial span as of the large cylinder. To investigate the proper rotational effect of the wind turbine. The simulation method used a 3-D transient computational model with the sliding mesh technique. The complete computational domain is then divided into two sub-domains; a stationary stator domain and one rotor domain that rotated with respect to the stationary domain.

The faces of the small inner cylinder serve as an interface between the stationary and rotating part of the model. Here, the ‘rotor-interface’ rotates while the ‘stator-interface’ and the large cylinder remain static. The two sub-domains are ‘rotor-interface’ and ‘stator-interface’ has been created in ANSYS/Fluent ‘design-modeler’ as shown in Fig. 3.8. This permit sliding of the adjacent cells at the boundary between the two sub-domains. The front view and side view of the whole computational domain is presented in Figs. 3.8(a) and 3.8(b).

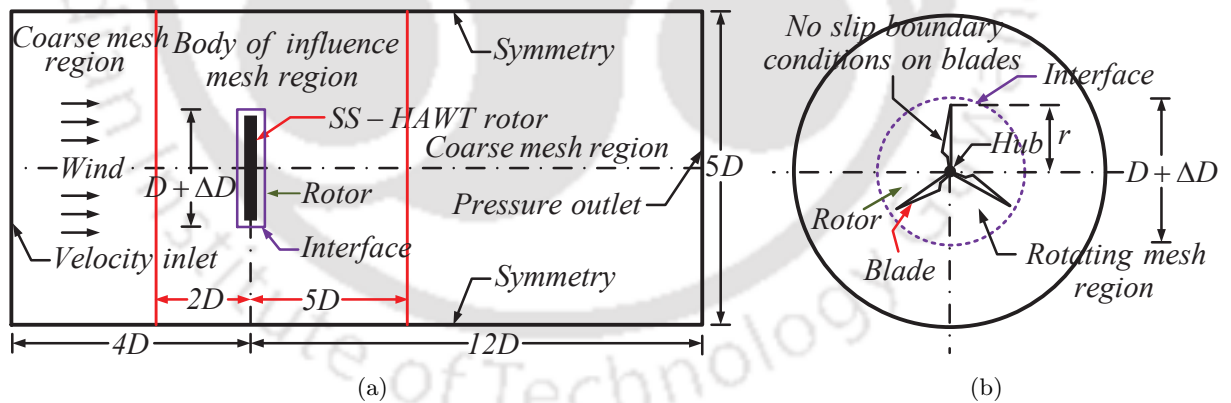


Fig. 3.8: Schematic diagram of the computational domain (a) Front view; (b) Side view.

The computational domain uses the boundary conditions (BC) at the velocity-inlet, symmetry, and pressure-outlet. The BC at velocity-inlet type is based on the standard IEC 61400-2 [112] (as discussed in Section 3.5.1). The inlet velocity profile is applied at the inlet face with a constant wind velocity approaching to the wind turbine rotor. Here, the flow of wind is over the larger cylinder. At the outlet face, the pressure-outlet type BC is specified with its value equal to the atmospheric pressure (where, the gauge pressure/relative pressure is set to zero).

The cylindrical length in the computational domain is fixed in a manner to ensure that the effect

3. Evaluation of Aerodynamic Performance of Wind Turbine

of the BC on the flow inside the cylinder domain is negligible and reduces the convergence difficulties. Further, the symmetry type BC is applied on the curved surface of the outer large-cylinder side. The surfaces between two domains are interfaced using the general grid interface method. The rotor-surface (3-blades + hub) of the wind turbine is defined as wall type BC, which is further classified as a moving walls with wall/no-slip shear conditions. Here, the wall-function approach used to avoid the real wall effects near these walls [114].

This near-wall treatment allows a smooth shift from low Reynolds number formulation to a wall function formulation. Interface type BC between two sub-zones along with the sliding mesh technique is used to keep the relative velocity of the turbine rotor and rotating cylinder as zero. The whole cylindrical computational domain builds with specified BC is defined in ANSYS/Fluent software as shown in Fig. 3.9. Table 3.3 shows the defined boundary conditions.

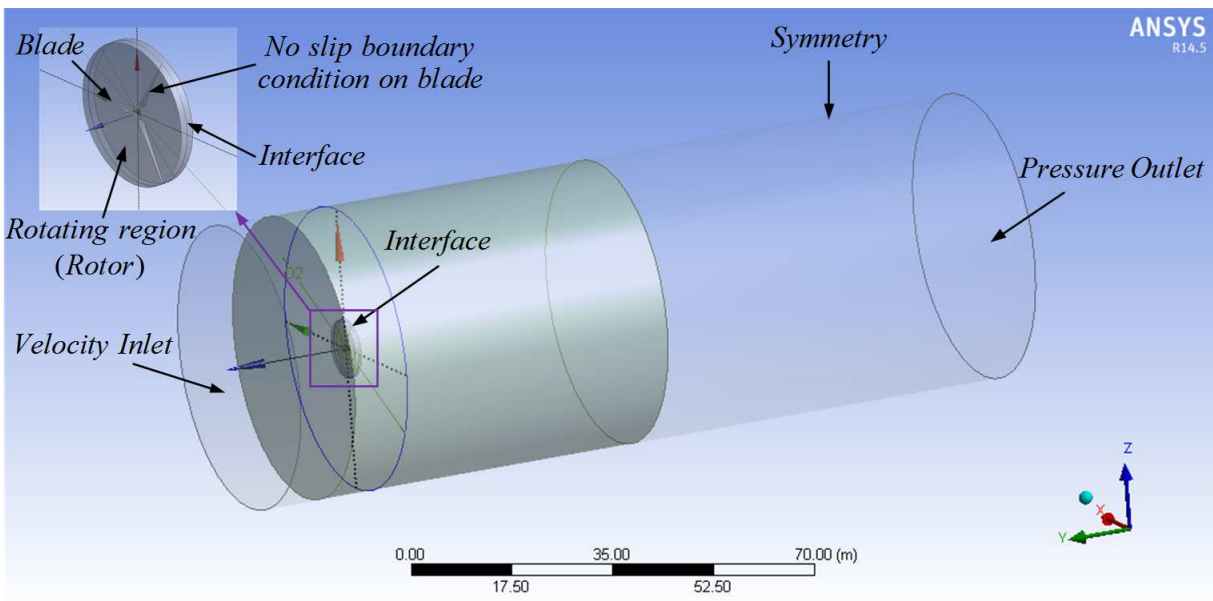


Fig. 3.9: The side view of the cylindrical computational domain layout and its boundary conditions defined in ANSYS/Fluent software.

3.6.3 Solver Setting Details and Turbulence Model Selection

There are several previous studies that are used to model the flow around wind turbines such as direct numerical simulation (DNS) [168], Large-eddy simulation (LES) [169], and Reynolds-averaged Navier-stokes (RANS) method with different turbulence models [128]. The choice is generally made based on the details of the flow and the computing resources available. The present work uses an [TH-3228_11610226](#)

Table 3.3: The boundary conditions of the 3–D wind turbines for the computational simulations.

Parameter	Values
Airfoil type	NACA 63-415
Simulation type	Unsteady simulation
Turbulence model	SST, SKE and RKE models
Fluid material	Air
Temperature	10°C
Dynamic viscosity	1.778×10^{-5} kg/m·s
Air density	1.225 kg/m ³
Blade length	$R_1 = 5$ m, $R_2 = 2.5$ m and $R_3 = 1.7053$ m
Flow type	Incompressible flow
Interface	Sliding mesh
INLET boundary condition	Flow velocity = 7 m/s
OUTLET boundary condition	Gauge pressure = 0 Pa
Discretized method	Finite volume method
CFD algorithm	Simple (Default option)
Solution methods	Pressure-velocity coupling Least-squares cell based Pressure (Standard) Density (Second-order upwind) Momentum (Second-order upwind) Turbulent kinetic viscosity (Second order upwind) Specific dissipation rate (Second-order upwind)
Solution controls	Pressure; 0.5 Momentum: 0.5 Density: 1.1 kg/m ³ Turbulent kinetic energy: 0.65
Boundary condition	Velocity inlet (7 m/s) Pressure outlet (Gauge pressure: 0) Moving wall with no-slip shear condition
Number of mesh cells	About 12,92,807 for R_1 , 8,69,854 for R_2 and 4,08,823 for R_3
Force monitors	Torque and power coefficients
Residual convergence criteria	1×10^{-6}

3. Evaluation of Aerodynamic Performance of Wind Turbine

unsteady RANS (URANS) equations.

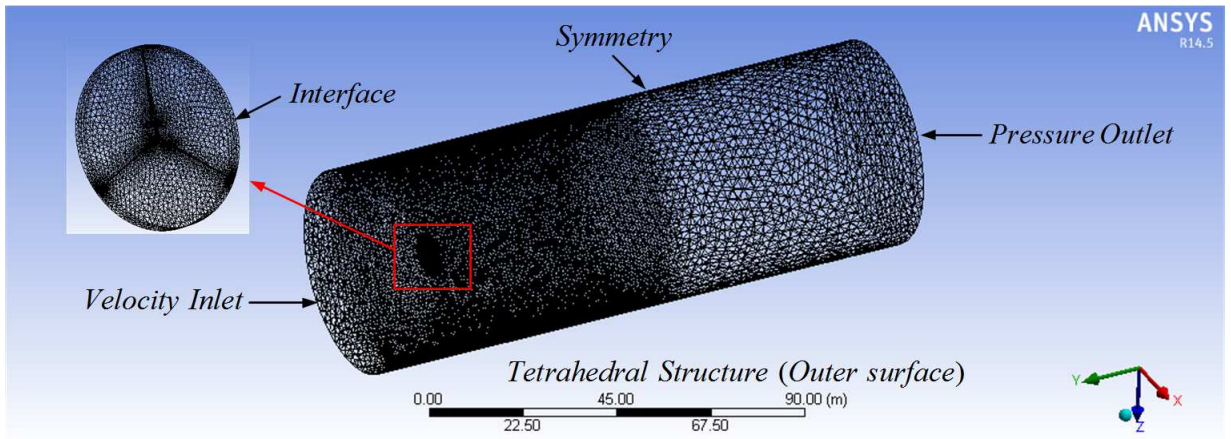
The computational method uses the semi-implicit method for the pressure-linked equations (Simple) algorithm, for solving the velocity-pressure coupled URANS equations. The fluid considered in the present model is assumed to be incompressible. The present work uses SST model for the turbulence. The least-squares cell-based technique is used to find pressure gradients that solve the secondary diffusion expressions and velocity derivatives. A second-order fully implicit temporal scheme is used to reduce interpolation errors. The convergence criteria for the residuals is set as 1×10^{-6} . Here, a step size of 0.01 s is utilized for the simulation. The computational simulations are performed with approximately 0.2 million to 2.5 million number of elements on Intel® Xeon® E5-2650v4 2.2 GHz Quad-Core CPUs with 128 GB of RAM at the computer cluster of the Computer & Communication Centre, IIT Guwahati. The typical time required for each 3-D computational solution is approximately ≈ 24 hours.

3.6.4 Meshing Topology and its Grid Independency Test

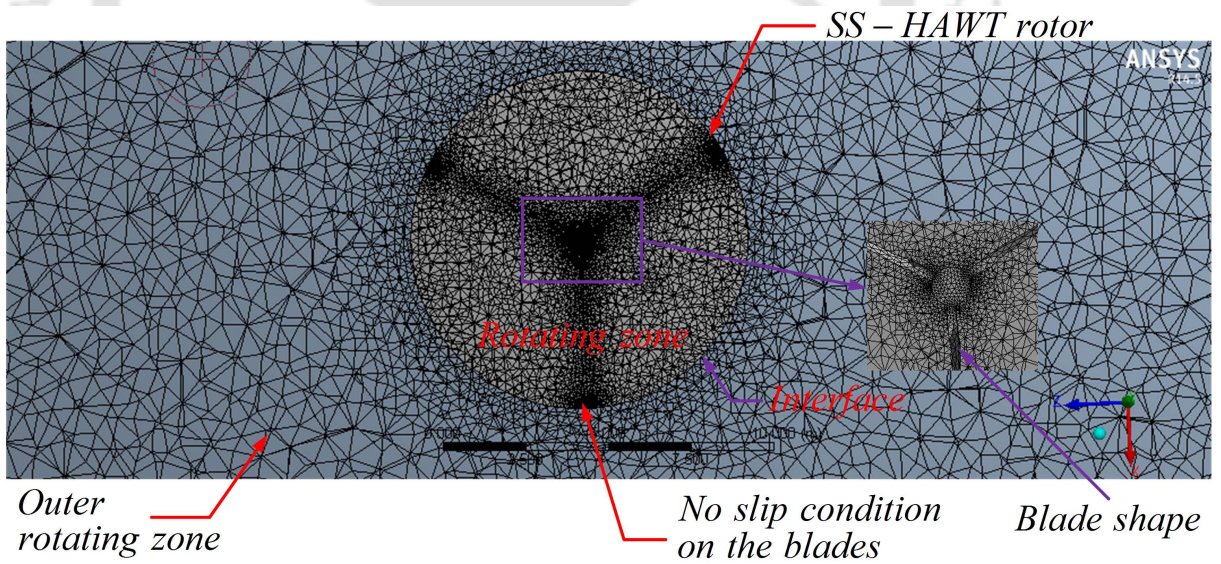
The cylindrical computational domain is discretized through the unstructured 3-D mesh. The unstructured triangular mesh is generated on the wind turbine blade and hub wall region, whereas the rest of the region employ tetrahedral meshes as shown in Fig. 3.10. Further, to enhance the mesh quality, a zonal approach is adopted based on the body of influence between the large cylinder and small cylinder.

Hence, the grid independence test is carried out to find the sub-optimal size of the mesh structure. In the present study, the dense mesh is generated for the wind turbine and small cylinder domain. The triangular mesh is implemented with the maximum element size of 0.02 m. A relatively coarser mesh is generated for the large cylindrical domain. The tetrahedron mesh is selected with the maximum element size of 0.1 m, moreover, the body of influence layer thickness is 0.005 m. A dense meshing may produce a better result compare to coarse meshing, but it takes high computational time with higher cost [170]. Hence, to find the sub-optimal size of the mesh, a suitable combination of dense meshing and coarse meshing is utilized. This provides a mesh structure with less number of grid cells with solution accuracy very close to that of a dense mesh. The mesh structure of the wind turbine surface and closer view of the grid in the vicinity of the wind turbine rotor are shown in Figs. 3.10(a) and 3.10(b).

Here, the mesh structure includes 30 rows of quadrilateral mesh with a growth rate of 1.2 to fulfill



(a)



(b)

Fig. 3.10: Typical wireframe mesh structure around the wind turbine rotor (a) Boundary conditions of the flow domain; (b) View of the wind turbine from axis of rotation.

3. Evaluation of Aerodynamic Performance of Wind Turbine

the criteria of $y^+ < 5$ over the entire surface as required [114] (where, $y^+ = yu_\tau/\nu$, $u_\tau = \sqrt{\tau_w/\rho}$, y is the wall normal distance, τ_w is the wall shear stress and ν is the kinematic viscosity).

The details of the grid independency test are enumerated in Table 3.4.

Table 3.4: Discretizations of 3-D computational domain for the grid independence test on the wind turbines.

Grid index	$R_1 = 5$ m		$R_2 = 2.5$ m		$R_3 = 1.7053$ m	
	Cells	$C_{P(\max)}$	Cells	$C_{P(\max)}$	Cells	$C_{P(\max)}$
1	606184	0.43271	562147	0.42795	287918	0.37497
2	908171	0.45932	644515	0.45122	353865	0.44161
3	1292807	0.48864	869854	0.48714	408823	0.48331
4	1643250	0.48663	1220858	0.48349	508646	0.48378
5	2261632	0.48764	1780872	0.48293	748307	0.48482

The computational simulations are initially conducted with the coarse mesh structures (with Grid index 1) having 6,06,184 mesh cells for WT_{R1} , 5,62,147 mesh cells for WT_{R2} and 2,87,918 mesh cells for WT_{R3} case. The number of mesh cells is gradually increased in consecutive steps and the accuracy in the overall estimation of the time-averaged values of power coefficient ($C_{P(\max)}$) of the wind turbine is observed, *i.e.*, in a second mesh indexed as Grid index 2 utilizes 12,92,807 number of cells for WT_{R1} , similarly, 8,69,854 number of cells for WT_{R2} and 4,08,823 number of cells for WT_{R3} . The table presents the quantitative values of the $C_{P(\max)} = 0.48864$ for WT_{R1} , $C_{P(\max)} = 0.48714$ for WT_{R2} , and $C_{P(\max)} = 0.48331$ for WT_{R3} . The table demonstrates that the values of the $C_{P(\max)}$ are almost constant after Grid index 3. The computational time for Grid index 5 is 3.5 times more than Grid index 4 elements. Therefore, in this present study, Grid index 3 is used to get solutions with less convergence time.

3.7 Results and Discussion

In this study, the aerodynamic performance of the wind turbines is analyzed. The optimal rotor theory is used to design the blade geometry at the optimal tip speed ratio for different blade lengths ($R_1 = 5$ m, $R_2 = 2.5$ m & $R_3 = 1.7053$ m). Here, fiberglass/epoxy is considered as the material property to design and analysis of wind turbines. The CFD simulations are implemented in ANSYS/Fluent standard commercial software [114] using the sliding mesh technique, while a user-defined function

[TH-3228_11610226](#)

(UDF) file is used for compiling, computing, and analyzing the results.

3.7.1 Validation of the Computational Simulations

The simulation uses the SST models for the modeling of the turbulent flow. The BEM theory based on Algorithm 2 is used to calculate the steady-state aerodynamic performance using MATLAB programming code and the aerodynamic performance is shown by CFD simulation using ANSYS/Fluent software. It is observed that steady-state results from both methods are very close to each other, thus verifying the results.

The CFD simulation provides torque coefficient (C_Q) and power coefficient (C_P). To eliminate the initial start-up effects, the C_Q and C_P values of the rotating turbine are averaged from 0.5 to 1.5 s to obtain time-averaged values of the time-evolution solution. The average values of these coefficients are calculated at various values of tip speed ratio *i.e.*, $\lambda = 2, 2.5, \dots, 9$.

3.7.1.1 Case-1: The $C_Q - \lambda$ and $C_P - \lambda$ curves of the Wind Turbine with R_1 (WT_{R1})

The variations of the C_Q and C_P as a function of tip speed ratio are shown in Figs. 3.11(a) and 3.11(b). The comparisons are shown between computational results (*i.e.*, CFD results) and BEM theory results. It is observed from Fig. 3.11 that the predicted $C_Q - \lambda$ and $C_P - \lambda$ curves of the SST model shows an acceptable agreement with the BEM theory results. The computational results appear to closely predict the C_P value, especially at the lower tip speed ratios. For tip speed ratios greater than 6 (up to 9), the C_Q and C_P obtained by CFD simulation are close with a maximum deviation of 1.84%. In the present case, the peak performance is obtained at C_Q and C_P values of 0.08143 and 0.4886, respectively, corresponding to a tip speed ratio of 6.

3.7.1.2 Case-2: The $C_Q - \lambda$ and $C_P - \lambda$ curves of the Wind Turbine with R_2 (WT_{R2})

The variations of the C_Q and C_P as a function of tip speed ratio are shown in Figs. 3.12(a) and 3.12(b). The comparisons are shown between computational results (*i.e.*, CFD results) and BEM theory results. It is observed from Fig. 3.12 that the predicted $C_Q - \lambda$ and $C_P - \lambda$ curves of the SST model shows an acceptable agreement with the BEM theory results. The computational results appear to closely predict the C_P value, especially at the lower tip speed ratios. For tip speed ratios greater than 6 (up to 9), the C_Q and C_P obtained by CFD simulation are close with a maximum deviation of 1.82%. In the present case, the peak performance is obtained at C_Q and C_P values of 0.08118 and 0.4871, respectively, corresponding to a tip speed ratio of 6.

3. Evaluation of Aerodynamic Performance of Wind Turbine

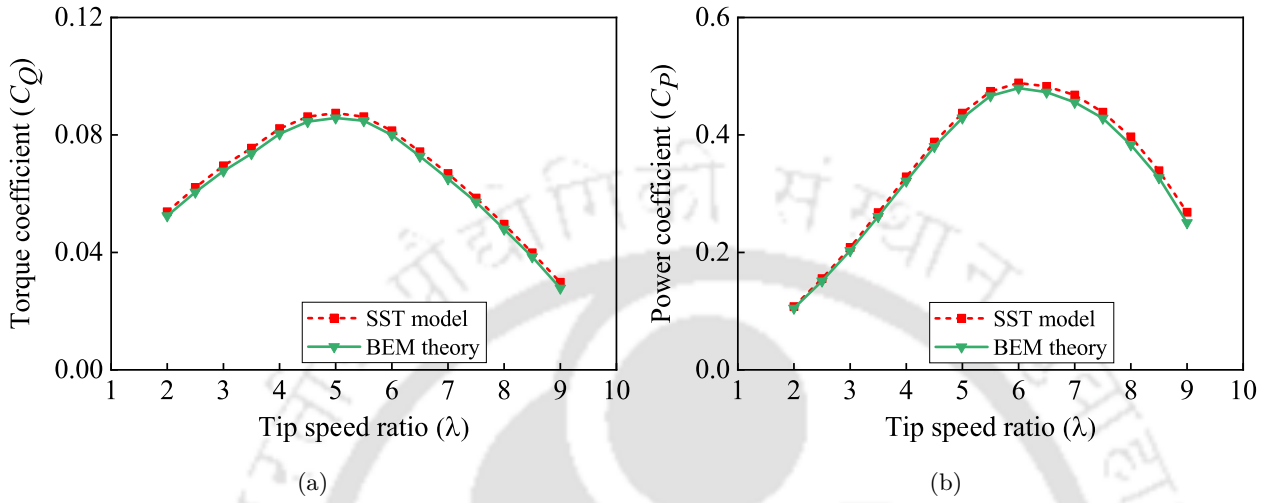


Fig. 3.11: Simulation results for $R_1 = 5$ m blade length (a) Variation of C_Q ; (b) Variation of C_P .

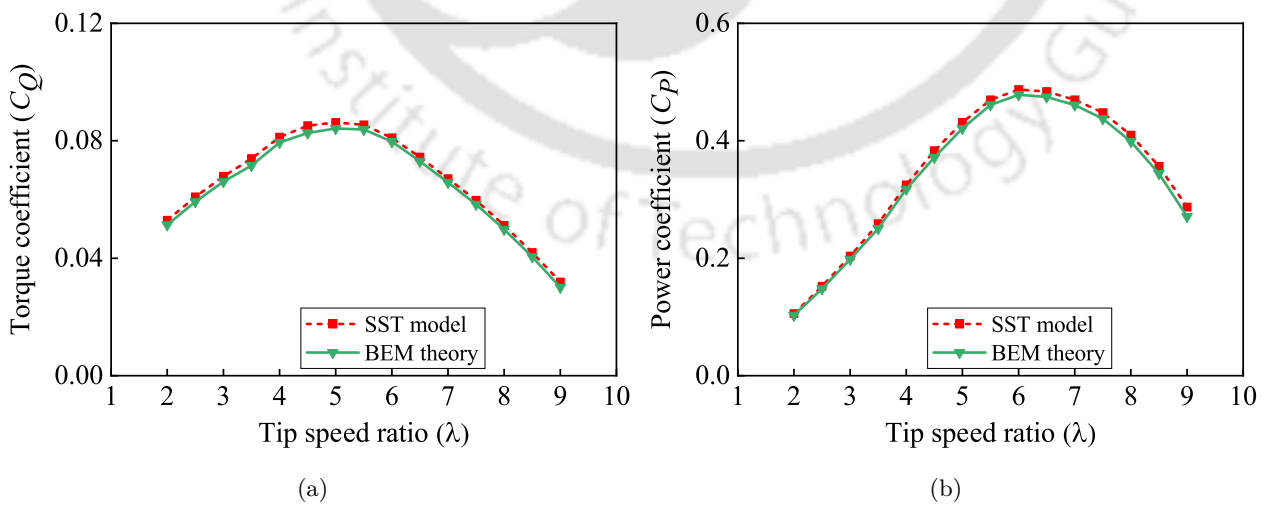


Fig. 3.12: Simulation results for $R_2 = 2.5$ m blade length (a) Variation of C_Q ; (b) Variation of C_P .

3.7.1.3 Case-3: The $C_Q - \lambda$ and $C_P - \lambda$ curves of the Wind Turbine with $R_3(WT_{R3})$

The variations of the C_Q and C_P as a function of tip speed ratio are shown in Figs. 3.13(a) and 3.13(b). The comparisons are shown between computational results (*i.e.*, CFD results) and BEM theory results. It is observed from Fig. 3.13 that the predicted $C_Q - \lambda$ and $C_P - \lambda$ curves of the SST model shows an acceptable agreement with the BEM theory results. The computational results appear to closely predict the C_P value, especially at the lower tip speed ratios. For tip speed ratios greater than 6 (up to 9), the C_Q and C_P obtained by CFD simulation are close with a maximum deviation of 1.14%. In the present case, the peak performance is obtained at C_Q and C_P values of 0.08055 and 0.4833, respectively, corresponding to a tip speed ratio of 6.

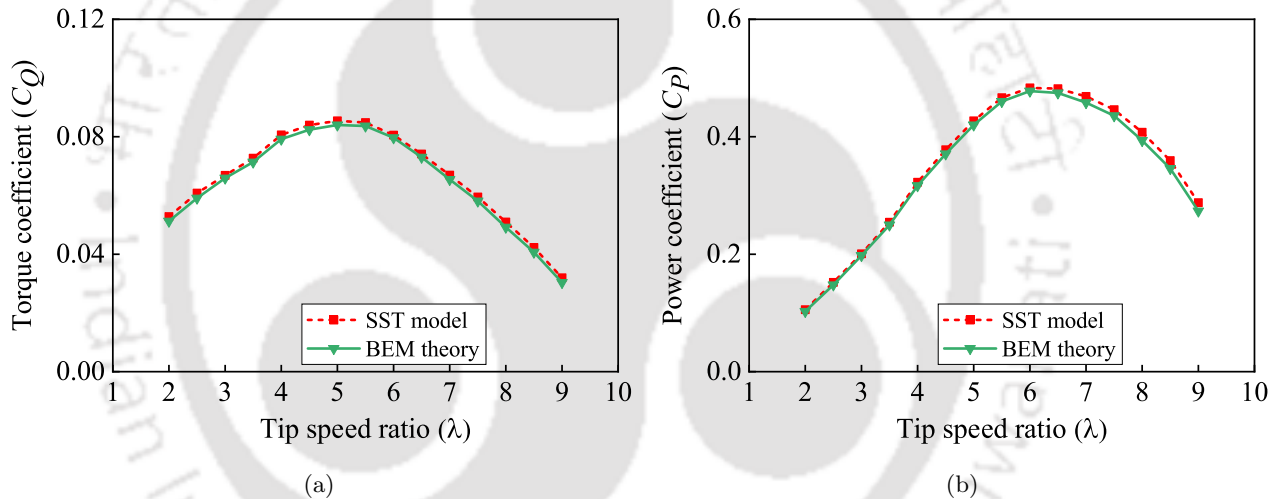


Fig. 3.13: Simulation results for $R_3 = 1.7053$ m blade length (a) Variation of C_Q ; (b) Variation of C_P .

The computational results of the different wind turbine rotors, the $C_Q - \lambda$ and $C_P - \lambda$ curves are compared for SST model. The $C_Q - \lambda$ and $C_P - \lambda$ curves at a range of tip speed ratio (*i.e.*, $\lambda = 2, 2.5, \dots, \& 9$) shows a good and acceptable agreement with BEM theory data.

3.7.2 Analysis of the Torque Coefficient and Torque Response of the Wind turbines

In the previous section, already C_Q is estimated for a wind turbine with a different radius. In this section using (3.30), the torque generated (T) by the wind turbine is calculated.

3. Evaluation of Aerodynamic Performance of Wind Turbine

3.7.2.1 Case-1: The Torque Coefficient and Generated Torque Response with R_1 (WT_{R1})

Figs. 3.14(a) and 3.14(b) shows the instantaneous generated torque by the wind turbine with radius R_1 using the computational model. It is observed that the C_Q and T_c response reaches its peak value at near 0.4 s and reaches its steady-state value in 1.2 s. In this case, the time-averaged C_Q and T_c values are 0.07997 and 942.034 N·m, respectively.

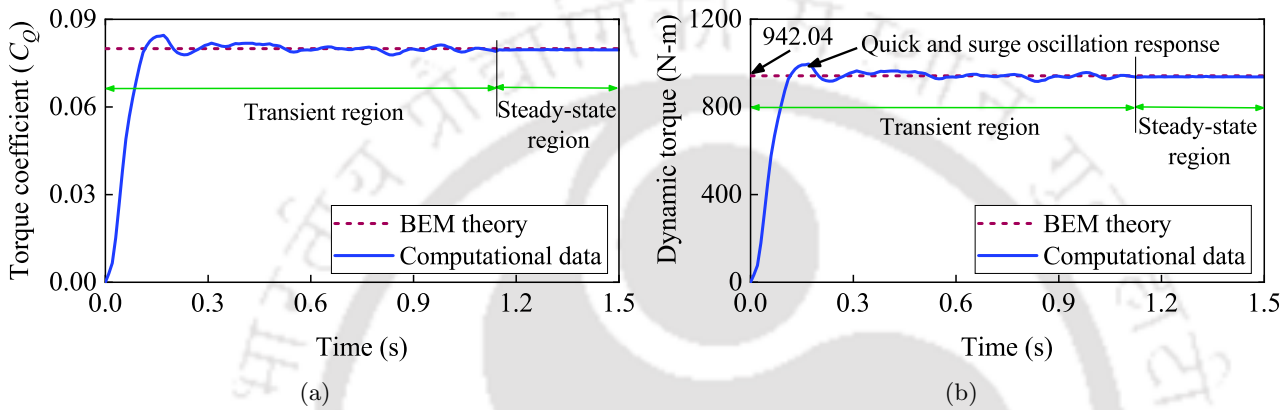


Fig. 3.14: The time-dependent response for R_1 (a) Variation of the C_Q ; (b) Variation of the T_c .

3.7.2.2 Case-2: The Torque Coefficient and Generated Torque Response with R_2 (WT_{R2})

Figs. 3.15(a) and 3.15(b) shows the instantaneous generated torque by the wind turbine with radius R_2 using the computational model. It is observed that the C_Q and T_c response reaches its peak value at near 0.2 s and reaches its steady-state value in 1.5 s. In this case, the time-averaged C_Q and T_c values are 0.07974 and 117.42 N·m, respectively.

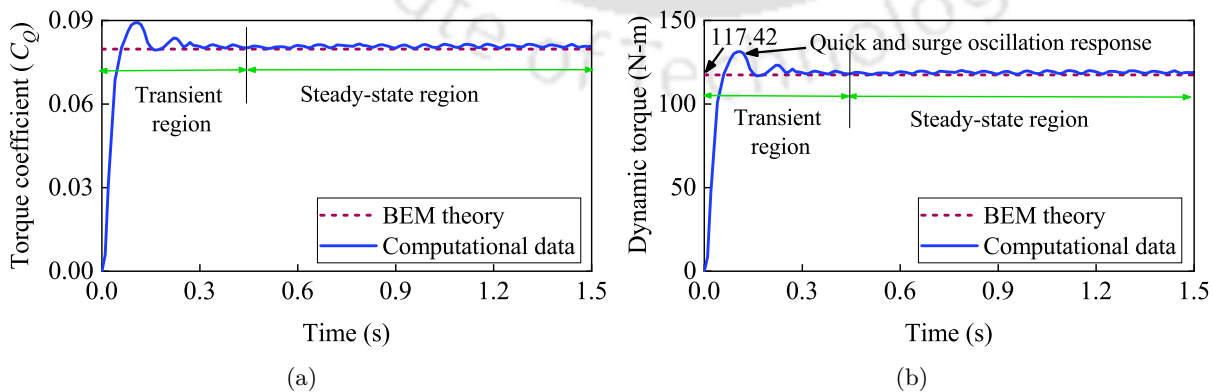


Fig. 3.15: The time-dependent response for R_2 (a) Variation of the C_Q ; (b) Variation of the T_c .

3.7.2.3 Case–3: The Torque Coefficient and Generated Torque Response with R_3 (WT_{R3})

Figs. 3.16(a) and 3.16(b) shows the instantaneous generated torque by the wind turbine with radius R_3 using the computational model. It is observed that the C_Q and T_c response reaches its peak value at near 0.15 s and reaches its steady-state value in 0.32 s. In this case, the time-averaged C_Q and T_c values are 0.07964 and 37.22 N·m, respectively.

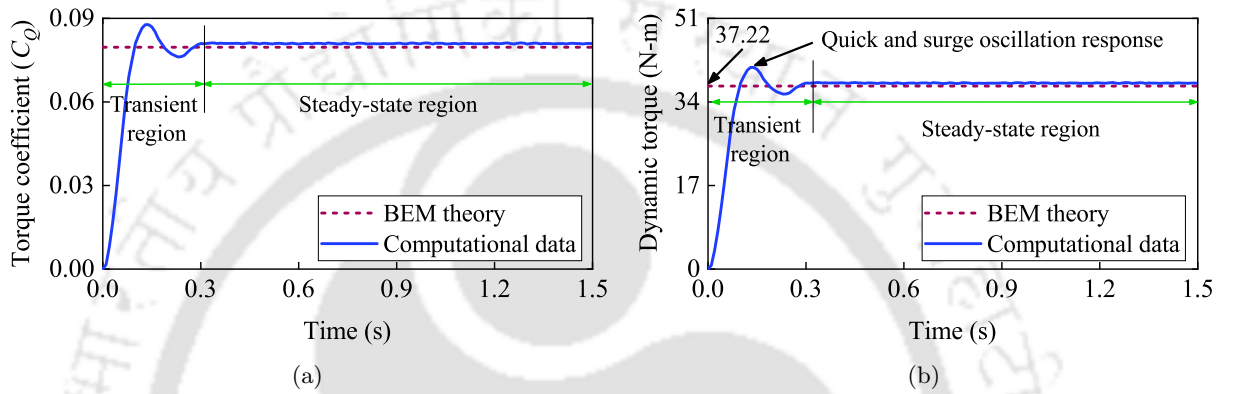


Fig. 3.16: The time-dependent response for R_3 (a) Variation of the C_Q ; (b) Variation of the T_c .

In this section, the aerodynamic performance of the different rotating wind turbines has been analysed. However, the computational technique takes significant time for obtaining the solution *i.e.*, takes approximately 24 h for each 3–D simulation. Therefore, there is a need to utilize these simulation results in developing a simple transfer function model which approximately represents the torque response. These developed models could be used in real-time control applications.

3.7.3 Accuracy of the developed approximate transfer function to represent the torque response

The steady-state aerodynamic response of the wind turbines can be predicted quite accurately using the BEM theory as presented in Algorithm 2. Since, the Algorithm 2 gets implemented very quickly, hence, it is used to provide steady-state torque, whereas the dynamic performance is modeled as a second-order transfer function. The procedure for validating the accuracy of the developed model is shown in Fig. 3.17.

Finally, the step response obtained from these transfer functions is compared with the CFD simulation. The values of MSE in $(\text{N}\cdot\text{m})^2$ as defined in (3.53) is used to quantify the accuracy of the

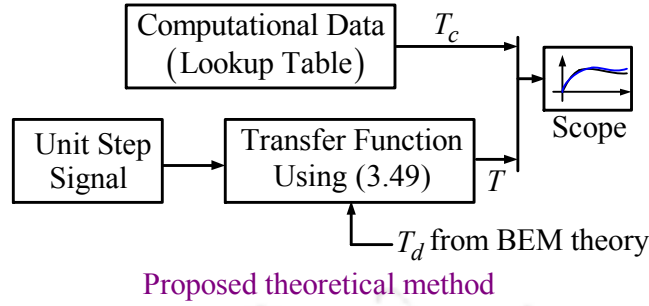


Fig. 3.17: Procedure for validating the accuracy of the developed model.

proposed second-order dynamical model.

$$\text{MSE} = \frac{1}{n} \sum_{i=1}^n [T_c(i) - T_d(i)]^2 \quad (3.53)$$

where, N is the size of the sample, $T_c(i)$ is the data points obtained from the computation simulation results (using ANSYS/Fluent), $T_d(i)$ is the data points received from the proposed theoretical method (which is combined BEM theory algorithm and second-order system).

The modal mass (m_a) parameter is measured using Pro/ENGINEER to estimate the aerodynamic damping ratio for Case-1, 2 & 3. The slope of the lift coefficient with angle of attack (C'_L) equals to 2π . Finally, the calculated damping ratios (ξ) are found to be 0.6653 for WT_{R1} , 0.5542 for WT_{R2} , and 0.5129 for WT_{R3} , respectively. These values are constant for a particular wind turbine as they are independent of the tip speed ratio and wind velocity.

The generated torque response of the proposed theoretical method for Case-1, 2 & 3 is shown in Figs. 3.18, 3.19 and 3.20, respectively. From the results, it is observed that the torque response using the proposed theoretical method is very close to the torque response obtained through CFD simulations.

These transfer functions which provide an approximate torque response are estimated for the turbine of different radius at a particular tip speed ratio and wind velocity. Here, the proposed second-order system parameters such as natural frequency (ω_n) is presented in Tables 3.5 and 3.6.

3.8 Summary

The present work uses the optimal rotor theory to design the blade geometries such as chord length, and twist angle along the radial span. The steady-state aerodynamic performance such as torque and power coefficients (*i.e.*, C_Q and C_P) of the wind turbine is calculated using the blade

Table 3.5: Calculation of natural frequency, developed torque and MSE at different tip speed ratio.

λ	$R_1 = 5 \text{ m}$			$R_2 = 2.5 \text{ m}$			$R_3 = 1.7053 \text{ m}$		
	ω_n (rad/s)	T_d (N·m)	MSE	ω_n (rad/s)	T_d (N·m)	MSE	ω_n (rad/s)	T_d (N·m)	MSE
2	10.08	618.17	7.7696	20.16	75.70	1.3430	29.55	23.97	0.4188
2.5	12.60	712.96	6.9520	25.20	87.29	1.5379	36.94	27.64	0.3734
3	15.12	797.90	7.8301	30.24	97.38	1.8133	44.33	30.82	0.3332
3.5	17.64	865.19	7.7764	35.28	105.46	1.8452	51.72	33.37	0.5197
4	20.16	958.87	6.8913	40.32	117.00	1.5813	59.11	37.03	0.2378
4.5	22.68	996.15	6.4331	45.36	121.76	1.7014	66.50	38.54	0.5202
5	25.20	1011.22	7.8811	50.40	124.08	1.8040	73.89	39.28	0.1177
5.5	27.72	999.77	8.0907	55.44	123.50	2.0697	81.28	39.12	0.4208
6	30.24	942.51	8.3903	60.48	117.48	2.1307	88.66	37.24	0.1491
6.5	32.76	857.49	7.6053	65.52	107.57	1.2490	96.05	34.14	0.6537
7	35.28	767.04	6.7188	70.56	97.01	1.1885	103.44	30.60	0.3424
7.5	37.80	673.40	6.6699	75.60	85.94	1.9366	110.83	27.36	0.6158
8	40.32	555.11	7.5476	80.64	71.93	1.4052	118.22	22.92	0.2009
8.5	42.84	453.64	6.6967	85.68	59.64	1.6958	125.61	19.03	0.1483
9	45.36	328.07	6.0008	90.72	44.37	1.2217	133.00	14.21	0.1166

3. Evaluation of Aerodynamic Performance of Wind Turbine

Table 3.6: Calculation of natural frequency, generated torque and MSE at different wind velocity.

v_o	$R_1 = 5 \text{ m}$			$R_2 = 2.5 \text{ m}$			$R_3 = 1.7053 \text{ m}$		
	ω_n (rad/s)	T_d (N·m)	MSE	ω_n (rad/s)	T_d (N·m)	MSE	ω_n (rad/s)	T_d (N·m)	MSE
3	12.96	9.11	0.1362	25.92	0.26	0.0001	38.00	0.05	0.0000
3.5	15.12	106.42	4.6281	30.24	13.50	0.3463	44.33	4.29	0.1002
4	17.28	226.70	4.0799	34.56	28.00	1.2210	50.67	8.87	0.1883
4.5	19.44	344.23	3.1934	38.88	42.21	1.3192	57.00	13.37	0.1032
5	21.60	467.83	4.6471	43.20	57.47	1.1283	63.33	18.19	0.1398
5.5	23.76	580.78	6.3146	47.52	71.79	1.1329	69.67	22.74	0.2491
6	25.92	692.46	7.7354	51.84	86.31	1.8499	76.00	27.36	0.2492
6.5	28.08	804.92	7.5632	56.16	100.81	1.7514	82.33	31.98	0.1754
7	30.24	918.79	8.3903	60.48	115.41	2.1307	88.66	36.65	0.1491
7.5	32.40	1039.27	8.4404	64.80	131.12	1.9961	95.00	41.67	0.1294
8	34.56	1172.24	8.4430	69.12	148.06	1.4830	101.33	47.06	0.2080
8.5	36.72	1302.01	7.6508	73.44	163.87	1.8997	107.66	52.12	0.3727
9	38.88	1452.57	8.1921	77.76	183.02	2.1226	114.00	58.21	0.2661
9.5	41.04	1611.62	8.2295	82.08	203.06	2.2093	120.33	64.59	0.2952
10	43.20	1772.24	7.3579	86.40	224.12	2.2645	126.66	71.27	0.4540
10.5	45.36	1942.36	8.2141	90.72	245.86	2.9057	133.00	77.93	0.6964

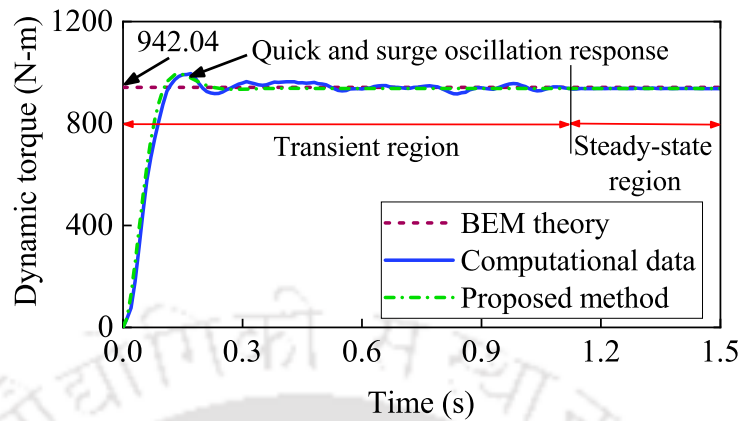


Fig. 3.18: Comparison of the developed, computational and proposed torque response for Case-1.

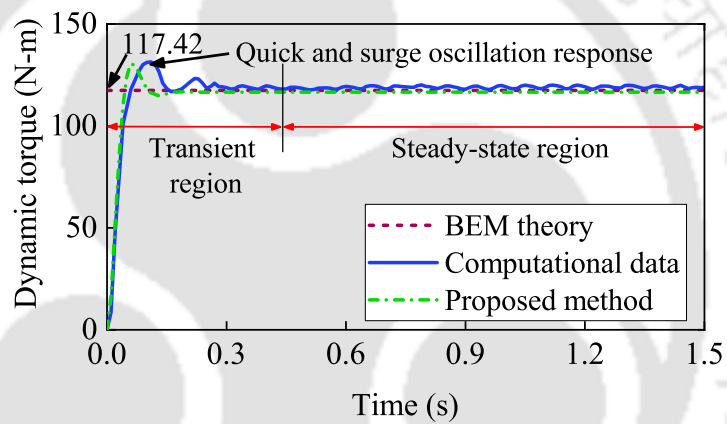


Fig. 3.19: Comparison of the developed, computational and proposed torque response for Case-2.

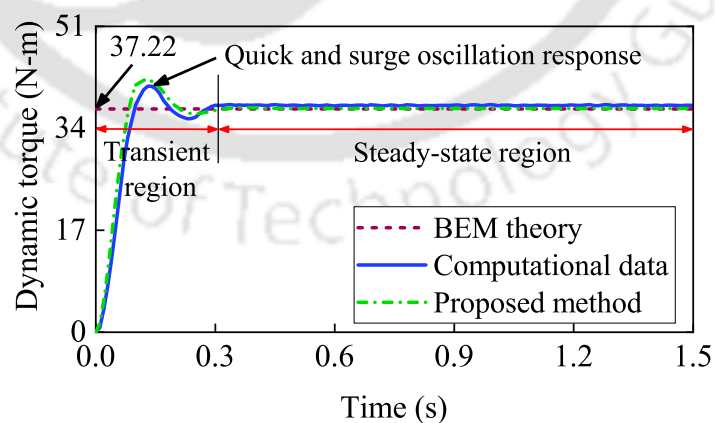


Fig. 3.20: Comparison of the developed, computational and proposed torque response for Case-3.

element momentum (BEM) theory. Further, the computational fluid dynamics (CFD) simulations are carried out using ANSYS/Fluent to get the aerodynamic performance. It is observed that the

3. Evaluation of Aerodynamic Performance of Wind Turbine

steady-state results obtained by the two approaches are very close to each other, thus verifies the results obtained by these approaches.

It is observed that the BEM theory procedure provides steady-state aerodynamic performance which is very close to the steady-state aerodynamic performance as obtained from the CFD simulations. Since, the CFD simulations take significant computational time, hence, the present Chapter proposes a second-order transfer function that uses BEM theory results to get parameters related to the steady-state torque. Further, the other parameters of the model such as natural frequency and damping ratio are calculated based on the available literature in this area. Finally, the comparison of the CFD simulation and the torque response by the transfer function are done. It is observed that the developed transfer function could approximately model the dynamic behavior of the wind turbine at a particular wind speed. This developed transfer function could be quite useful in real-time control of the wind turbine.

4

Development of Fault Ride Through for DFIG System

Contents

4.1	Introduction	96
4.2	Modeling of Turbine and Control Strategy	99
4.3	Proposed ThyBT-NSFCL Power Circuit Configuration and its Operating Principle	102
4.4	Analytical Analysis of the ThyBT-NSFCL	106
4.5	Design Methodologies and Estimation of Parameters for Proposed ThyBT-NSFCL	110
4.6	Results and Discussion	112
4.7	Summary	118

Objective

Wind power generation is observing a significant use of doubly-fed induction generator (DFIG) due to its improved efficiency, but the converter used in the configuration is sensitive to the presence of a fault in the grid. This work presents a fault ride-through (FRT) configuration, which includes a thyristor-based bridge-type non-superconducting fault current limiter (ThyBT-NSFCL) augmented with a buck converter. It is observed that the proposed topology works fine under a temporary symmetrical fault. The analytical analysis is carried out to observe the operating principle of the proposed ThyBT-NSFCL under both normal and fault conditions. A comparative study with other topologies such as switched impedance transformer-type non-superconducting fault current limiter (TT-NSFCL), series dynamic breaking resistor (SDBR), and without any current limiter (WCL) have been done to show the effectiveness of the proposed topology. The simulation results show that the proposed ThyBT-NSFCL is a better fault current limiter as compared with other limiters like TT-NSFCL, SDBR, and WCL. The simulation of the proposed ThyBT-NSFCL connected in series with a DFIG system is carried out using PSCAD/EMTDC software. The performance of the proposed topology is quite good, and it can be used as a reliable limiter for future wind energy applications.

4.1 Introduction

It is noticed that in the field of wind power production, the doubly-fed induction generator (DFIG) is used extensively due to its lower installation cost and controllable active or reactive power outputs [171, 172]. The DFIG-based wind energy system is observed to be sensitive to the presence of faults in the grid. Due to this fact, the grid-connected DFIG system requires some protection mechanism to protect it from any abnormal grid disturbances [18]. When a fault occurs in the electrical grid, the stator current rapidly increases and thus, resulting in abrupt voltage sags at the stator terminals. As a result, the rotor side converter (RSC) may become uncontrollable, and hence, the wind turbine is eventually tripped out from the system [28, 173]. Therefore, there is a need to improve the fault ride-through (FRT) capability of the wind turbine system so that it remains connected with the grid [174, 175].

Presently, several methods is suggested in the literature to improve the FRT capability of the DFIG system such as the one given in the references [26, 28, 57–59, 176–181]. A fuse is a self-triggering, small, economical, and reliable protection device, which can interrupt fault currents without utilizing sensors

and actuators, but it is a single-use device and required manual restoration [60]. In addition, the circuit breaker (CB) is also a piece of a protective device, which can automatically or manually trip, but the CB has high-current interrupting capabilities and the CB is an expensive electromechanical equipment [60,61]. The primary goal of a fault current limiter (FCL) is to reduce the flow of excessive fault current in the machine during abnormal conditions [75,182]. One of the very widely used techniques for limiting the fault current used in the wind energy system (WES) is the crowbar [183]. Crowbar utilizes a non-linear dynamic resistor to control the rotor fault current, and hence, it has a fixed dynamic response to all levels of faults. Thus, to have more flexibility, several authors and researchers have proposed different topologies and control strategies of the auxiliary devices to enhance the transient stability of the DFIG system, such as static synchronous compensation (STACOM) has been used to regulate the reactive power [184,185], and series dynamic breaking resistor (SDBR) [67,68] to provide voltage protection to limit the rotor over-current but, they have limitation like it allows a sudden rise of fault current instantaneously. In [186], a combined superconducting fault current limiter-magnetic energy storage (SFCL-MES) based fault current limiter has been proposed, where the output can be used to compensate the voltage dip and support critical loading under fault. However, the SFCL-MES has relatively significant conduction losses across the multiple series devices in the high current DC reactor circuit.

Unlike the traditional fault current limiters (FCL), the FCLs based on the solid-state devices are classified into three major types, *i.e.*, series switch-type, bridge-type, and resonance-type [182,187]. In [69], authors have focused on the bridge-type fault current limiter (BTFCL), which utilizes a $1-\phi$ diode bridge rectifier connected to an inductor using the superconducting coil. Similarly, in [70], a $3-\phi$ rectifier-type FCL has been reported with a superconducting coil as a DC reactor without a DC-bias voltage source. These superconducting coil based FCL is costly and requires more maintenance. In [74], a capacitor-based non-superconducting fault current limiter (CB-NSFCL) is proposed, which also suffers from the disadvantage of high cost due to the presence of the voltage source and capacitor. In [75,76], the non-superconducting fault current limiter (NSFCL) topology uses the diode bridge as a DC-bias voltage source and non-superconducting coil with controllable switches connected across the breaking resistor. In normal operation, the current flows through the DC reactor and switches, and during the fault, the current flow through the fault reactor, breaking resistor and diode bridge. Since, the fault current flows through the DC reactor and diode bridge, the current rating of them is quite

4. Development of Fault Ride Through for DFIG System

high, thus increasing the cost of its implementation. In [77], the switched impedance transformer-type non-superconducting fault current limiter (TT-NSFCL) topology is used to protect the DC reactor against high fault and uses a battery for loss compensation during normal operation. The use of the constant battery is not very effective in voltage compensation; moreover, it also increases the cost of the system, and hence, not economically feasible.

As per the authors' knowledge from literature, it is found that the study on the loss compensator circuits augmented with the buck converter to compensate the forward voltage drop under the normal operation is missing. In the previously introduced structures [77] ignored the utilization of an AC/DC converter or DC/DC converter coupled to the voltage transformer/rectifier, which results to be expensive for the power system application with the DFIG system. Therefore, a loss compensator circuit is used as the DC voltage source in the place of a battery. The battery needs charging/replacement, and the circuit operation may get interrupted; therefore, it reduces the lifetime of devices.

The main objective of this chapter is to develop a FCL that is more robust, efficient, and less costly. To archive this objective, the authors tried to suggest some modification in existing NSFCL as given in [75,77], and proposed a thyristor-based bridge-type non-superconducting fault current limiter (ThyBT-NSFCL). The proposed ThyBT-NSFCL designed a loss compensator circuit consisting of a DC-bias voltage source (includes voltage transformer and uncontrolled diode bridge rectifier) along with the buck converter to effectively compensate the voltage drops across the forward voltage drops on the semiconductor devices and the DC reactor resistance. This results in the short-circuit of the secondary side of the transformer. Hence, the losses in the primary side are significantly reduced. Moreover, with the use of the thyristor bridge rectifier, the losses during the normal mode are further reduced. The analytical analysis of circuit operation is established in both normal and fault conditions.

To show the effectiveness of the proposed ThyBT-NSFCL, the simulation has been done for a symmetrical fault at the point of interconnection (PoI) of the system. It is observed through the simulation results that the proposed ThyBT-NSFCL structure keeps the voltage level higher than the SDBR and TT-NSFCL under grid fault. Here, the simulation of the system is done using PSCAD/EMTDC software.

The rest of this chapter is structured as follows: Section 4.2 presents the controlled strategy of the DFIG system. Section 4.3 describes the system configuration, operation, and control strategy of the proposed ThyBT-NSFCL. The analytical analysis is presented in Section 4.4. In Section 4.5, the

design methodologies and estimation of parameters are presented. Section 4.6, the simulation studies and discussion are presented. Lastly, in Section 4.7 the conclusion is presented.

4.2 Modeling of Turbine and Control Strategy

The wind turbine model with the DFIG-based grid connected wind energy system along with its control strategy is shown in Fig. 4.1. The proposed ThyBT-NSFCL is connected between the stator terminal of the DFIG system and the grid source. The RSC, which controls the operation of the DFIG system, consists of an IGBT based voltage source converter.

The proposed RSC control scheme of the DFIG-based wind turbine connected with the ThyBT-NSFCL.

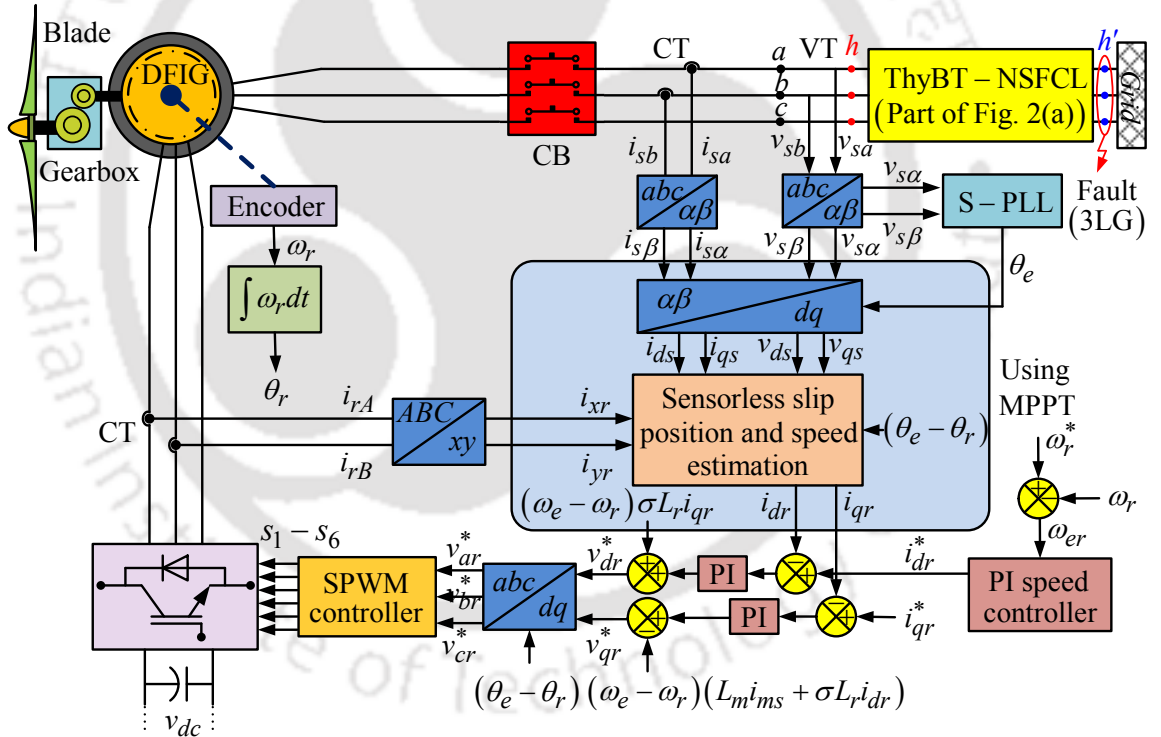


Fig. 4.1: The proposed RSC control scheme of the DFIG wind turbine connected with the ThyBT-NSFCL.

4.2.1 Dynamic Model of Wind Turbine

The mechanical power capture from wind resources is given by the aerodynamic equation (4.1) [89] as

$$P_m = \frac{1}{2} a_t \rho v_o^3 C_P(\lambda, \beta) \quad (4.1)$$

4. Development of Fault Ride Through for DFIG System

where, a_t is the projected rotor area of the actuator disc (or rotor), ρ is air density, v_o is free wind velocity, C_P is the power coefficient, β is blade pitch angle and λ is the tip speed ratio (TSR) (*i.e.*, $\text{TSR} = \omega R/v_o$, where R is rotor radius and ω is the angular speed of the blades).

4.2.2 Control Strategy of the RSC

The block diagram of the control algorithm implementation for the RSC is described and identified in Fig. 4.1.

The sensed actual stator voltages (v_{sa} and v_{sb}) are transferred into 2- ϕ stationary frame using Clarke's transformation is given as

$$v_{s\alpha} = v_{sa} \quad (4.2)$$

$$v_{s\beta} = \frac{1}{\sqrt{3}}v_{sa} + \frac{2}{\sqrt{3}}v_{sb} \quad (4.3)$$

Similarly, the sensed actual stator currents (i_{sa} and i_{sb}) are transferred into 2- ϕ stationary frame ($i_{s\alpha}$ and $i_{s\beta}$) and the sensed actual rotor currents (i_{rA} and i_{rB}) are transferred into 2- ϕ rotor frame (i_{xr} and i_{yr}). Next, the α and β -axis stator voltages ($v_{s\alpha}$ and $v_{s\beta}$) are transferred into d and q -axis voltage as

$$\begin{bmatrix} v_{ds} \\ v_{qs} \end{bmatrix} = \begin{bmatrix} \cos \theta_e & \sin \theta_e \\ -\sin \theta_e & \cos \theta_e \end{bmatrix} \begin{bmatrix} v_{s\alpha} \\ v_{s\beta} \end{bmatrix} \quad (4.4)$$

where, the stator voltage vector angle (θ_e) is calculated using the simple-phase locked loop (S-PLL), which is used to transform the 3- ϕ stator voltage and current into the d - q frame [188].

The purpose of the RSC is to maintain the voltage and frequency of the stator at the variable wind speed and varying loads. Most existing models widely used a conventional vector control based on a stator flux orientation (SFO) [189] reference frame. So, a decoupled control of the instantaneous stator active and reactive powers have been done by controlling d and q -axis rotor currents (i_{dr} and i_{qr}), respectively. The terminal voltage at the stator is controlled by controlling d -axis rotor current (i_{dr}). Generally, the q -axis reference rotor current (i_{qr}^*) is chosen, such that the stator reactive power (Q_s) is fixed to zero. The i_{qr}^* is chosen for injecting the required reactive power in the DFIG system. The d -axis reference rotor current (i_{dr}^*) is obtained by processing the rotor speed error (ω_{er}) between reference and sense rotor speed (ω_r^* and ω_r) through the proportional integral (PI) speed controller [190]. However, PI controllers are highly dependent on the tuning of parameters and

accurate tracking of angular information of stator flux/voltage. The tuning of the PI controller used is selected based on a trial & error method [191]. The reference rotor current is expressed as

$$i_{dr}^* = k_{pd\omega} (\omega_r^* - \omega_r) + k_{id\omega} \int (\omega_r^* - \omega_r) dt \quad (4.5)$$

where, ω_r^* is set as the optimal TSR values for a particular wind speed. Here, the proportional and integral gain constants of the speed are defined as $k_{pd\omega}$ and $k_{id\omega}$, respectively.

Using Park's transformation, 2- ϕ rotor frame currents (i_{xr} and i_{yr}) component are transformed into the d and q -axis rotor currents (i_{dr} and i_{qr}) and it is expressed as

$$\begin{bmatrix} i_{dr} \\ i_{qr} \end{bmatrix} = \begin{bmatrix} \cos \theta_{sl} & \sin \theta_{sl} \\ -\sin \theta_{sl} & \cos \theta_{sl} \end{bmatrix} \begin{bmatrix} i_{xr} \\ i_{yr} \end{bmatrix} \quad (4.6)$$

where, the slip angle is calculated as $\theta_{sl} (= \theta_e - \theta_r)$ and θ_r is known as rotor position which is achieved with an encoder.

The d and q -axis components are decoupled by adding compensating terms as

$$v_{dr}^* = k_{pdv} (i_{dr}^* - i_{dr}) + k_{idv} \int (i_{dr}^* - i_{dr}) dt + (\omega_e - \omega_r) \sigma L_r i_{dr} \quad (4.7)$$

$$v_{qr}^* = k_{pqv} (i_{qr}^* - i_{qr}) + k_{iqv} \int (i_{qr}^* - i_{qr}) dt - (\omega_e - \omega_r) (L_m i_{ms} + \sigma L_r i_{qr}) \quad (4.8)$$

where, the leakage factor ($\sigma = 1 - L_m^2/L_s L_r$), L_r is rotor inductance and $i_{ms} = \psi_{ds}/L_m$ is the stator magnetizing current (the stator flux linkage, $\psi_s = \psi_{ds}$ as constant). The proportional and integral gains of the d and q -axis current controllers are denoted by (k_{pdv} and k_{idv}) and (k_{pqv} and k_{iqv}), respectively.

Moreover, the reference rotor voltages (v_{dr}^* and v_{qr}^*) are transformed into the 3- ϕ rotor reference voltages (v_{ar}^* , v_{br}^* , and v_{cr}^*). Thereafter, these values are compared with the triangular carrier wave of switching frequency (f_s) of 2 kHz is used for generating the sine pulse width modulation (SPWM) signals for the converter switches ($s_1 - s_6$). Here, the wind turbine model with the DFIG system is discussed above and used as a complete system of the wind energy system for the simulation study.

4.3 Proposed ThyBT-NSFCL Power Circuit Configuration and its Operating Principle

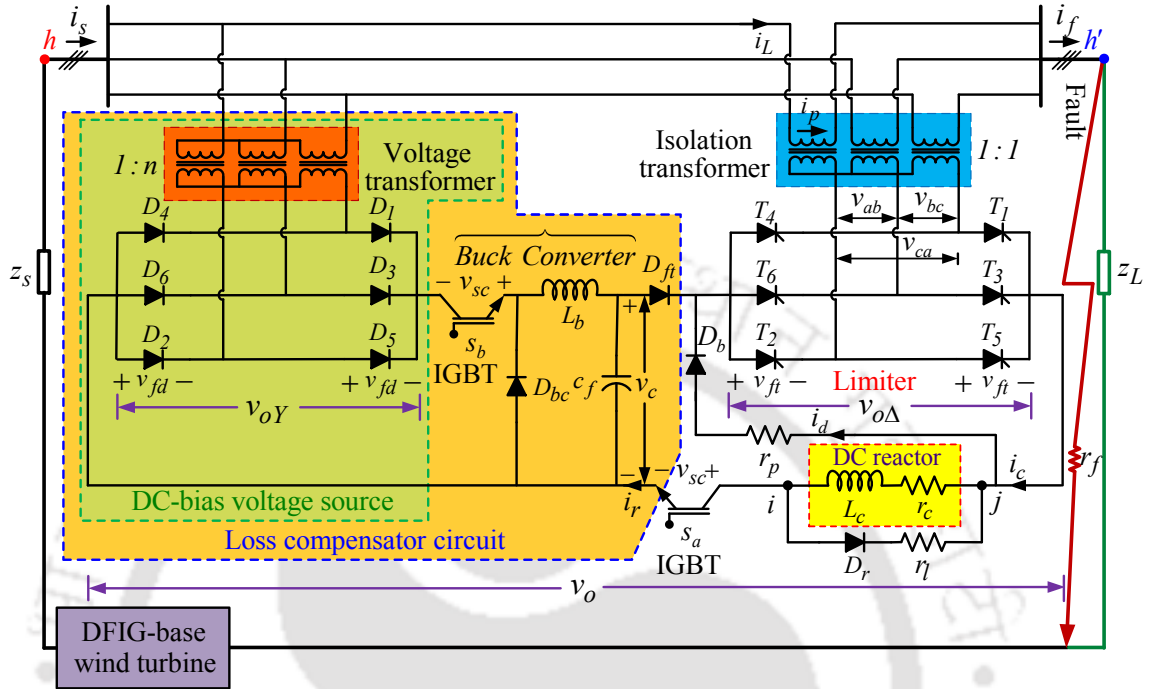
The proposed ThyBT-NSFCL circuit configuration is illustrated in Figure 4.2(a). This arrangement is used to limit the transient fault current at the stator terminal and subsequently reduce the rotor side current of the DFIG, hence improving the FRT capability of the DFIG system.

4.3.1 Proposed ThyBT-NSFCL Circuit Topology

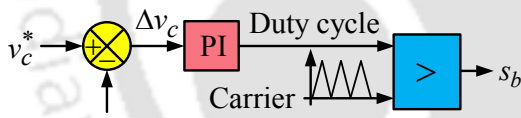
The power circuit configuration of the proposed ThyBT-NSFCL consists of an isolation transformer, thyristor bridge rectifier, voltage transformer feeding a diode bridge rectifier (called a DC-bias voltage source), buck converter, semiconductor switches, fast diodes, DC reactor, and discharging resistor. An isolating transformer is the main part of the ThyBT-NSFCL. The stator line currents flow through the primary side of the transformer winding, and the secondary side is connected to the thyristor bridge rectifier. To control the fault current, a DC reactor is connected to the secondary side of an isolation series transformer (here, three $1-\phi$ transformers are used as a series transformer with a turn ratio is equal to one ($1 : 1$)). The thyristor bridge rectifier (T_1-T_6) consists of six thyristors, which convert the secondary AC side voltage (*i.e.*, proportional to the current flowing in the stator winding) to an equivalent DC reactor current. The voltage drops associated with the semiconductor devices and the resistance of the inductor requires to be compensated by a compensating circuit. The loss compensator circuit consists of a voltage transformer (step down) with a turns ratio ($1 : n$) and feeds the $3-\phi$ diode bridge rectifier (D_1-D_6), and the bridge rectifier via a buck converter for providing the proper DC voltage. The DC-bias voltage source has been used to compensate the voltage drop under the normal operation stage. Further, with the use of the thyristor bridge rectifier, the voltage drop in the DC circuit are compensate by controlling the firing angle. Here, the contribution of a buck converter in the proposed scheme is used to provide regulated DC voltage to compensate the voltage drop in the DC circuit in a controlled manner.

Fig. 4.2(a) provides a schematic diagram of the proposed ThyBT-NSFCL with the DFIG-based wind turbine. During the healthy operation of the DFIG system, in the ThyBT-NSFCL, the IGBT switch (s_a) is in ON mode, and hence, the current flows through the DC reactor, IGBT switch (s_a) and loss compensation circuit (*i.e.*, $i_c = i_L$). The buck converter, consisting of IGBT switch (s_b), fast freewheeling diode (D_{bc} & D_{ft}), filter inductor (L_b) and filter capacitor (c_f) is utilized to keep

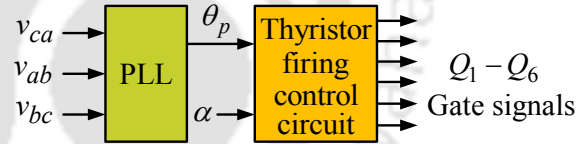
4.3 Proposed ThyBT-NSFCL Power Circuit Configuration and its Operating Principle



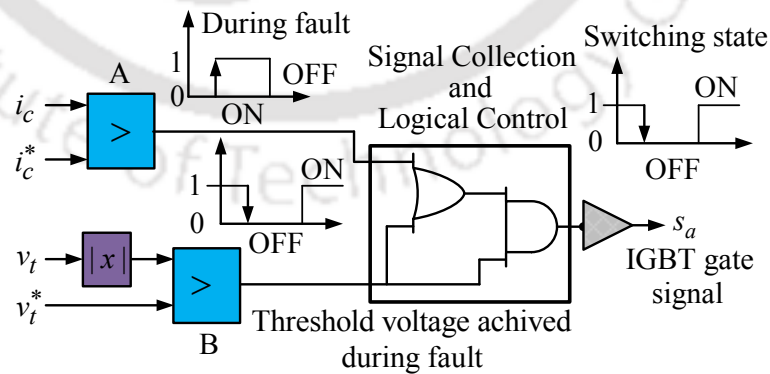
(a)



Part – I: Buck converter controller.



Part – II: Thyristor rectifier firing circuit and its gate signals.



Part – III: Controller of the ThyBT – NSFCL.

(b)

Fig. 4.2: Specific diagram of the proposed ThyBT-NSFCL (a) configuration; (b) control logic blocks.

4. Development of Fault Ride Through for DFIG System

the output DC voltage (v_c) to a constant reference value. However, the error fed to the PI controller for calculating the duty cycle and compared with symmetric triangle carrier wave to generate the switching signal required to control the buck converter IGBT switch (s_b). The gate signal is generated depending on the duty cycle (D) of the PWM pulse. Here, the carrier frequency is chosen as 5 kHz. The continuous charging and discharging process of the inductor (L_b) and the capacitor (c_f) during ON and OFF of the IGBT switch (s_b) forces DC-bias output voltage to track and follow the reference voltage to operate at a constant voltage. The control strategy of the buck converter is given in Fig. 4.2(b)–Part-I. In this mode, the DC reactor inductor (L_c) in the circuit, and as the drop across the semiconductor switches and DC reactor resistance is approximately compensated by the use of loss compensator circuit. Hence, the secondary side voltage of the transformer is short-circuited, and thus the primary side voltage drops approximately to zero *i.e.*, $v_{ab} = v_{bc} = v_{ca} \approx 0$. This reduces the losses in the primary side of the transformer.

During a fault condition, the DC reactor current (i_c) is sensed using the sensing circuit and is compared with a reference current (i_c^*) to generate a signal to switch OFF the IGBT switch (s_a). Because of the delay associated with the sensing circuit, the control circuit and IGBT switch (s_a) turn OFF time. High current can flow through the IGBT switch (s_a) and may damage it. Hence, a suitable value of the inductor is designed to limit this sudden rise in fault current. A freewheeling circuit is also provided across the DC reactor to prevent a sudden change in the DC reactor inductor current and, thus to relieve the IGBT switch (s_a) from any voltage stress. When the IGBT switch (s_a) is turned OFF, the diode (D_b) starts conducting, and the fault energy is dissipated in the breaking resistor (r_p). Once the DC reactor is replaced in the circuit, then the use of the thyristor bridge rectifier further augments or add towards the fine-tuning of current flowing in the DC reactor to minimize losses during normal operation.

4.3.2 Control Strategy

The firing of controlled bridge rectifier is based on the use of phase lock loop (PLL) utilizing the sensed line-to-line voltage (v_{l-l}) (*i.e.*, v_{ca} , v_{ab} , and v_{bc}). This angle (θ_p) and the reference firing angle (α) is provided to the firing circuit to generate 6-pulse signal, *i.e.*, Q_1 – Q_6 for the thyristor. The schematic of the same is provided in Part–II of Fig. 4.2(b). The output voltage across controller bridge rectifier is denoted as $v_{o\Delta}$ (*i.e.*, $v_{o\Delta} = \frac{3\sqrt{2}}{\pi} v_{rms,l-l} \cos\alpha$; where, $v_{rms,l-l}$ is the line-to-line rms voltage).

4.3 Proposed ThyBT-NSFCL Power Circuit Configuration and its Operating Principle

The uncontrolled diode bridge rectifier output voltage is assumed to be v_{oY} . The reference voltage (v_c^*) for the buck converter is selected in such a way as to compensate for the various loss and to maintain a current, which is approximately equal to the magnetizing current for the inductor. The equation utilized [76,192] to ensure the same is expressed in the equation below

$$v_c \geq r_c i_c + L_c \frac{di_c}{dt} + v_{sc} + 2v_{ft} \quad (4.9)$$

where, i_c is the DC reactor current, L_c is the DC reactor inductance and r_c is its internal resistance, v_{ft} is the forward voltage drop on each of thyristors and v_{sc} is the voltage drop across each of an IGBT switch (s_a).

Under the normal state, the IGBT switch (s_a) carries rectified load current, but with the occurrence of the fault, the IGBT switch (s_a) is turned OFF, and the i_c flows through the breaking resistor to dissipate the fault energy. The DC reactor current is continuously monitored to switch the IGBT switch using the current sensor at point 'j' and terminal voltage (v_t) at POI place 'h'. During normal operation, i_c is less than i_c^* , and hence, the comparator 'A' output is a logic LOW and sensed rms voltage v_t is more than v_t^* , and hence, the comparator 'B' output is logic HIGH. Thus, the IGBT switch (s_a) remains to turn ON during the normal state. Similarly, during the fault condition, i_c is more than i_c^* , and hence, the comparator 'A' output is a logic HIGH and sensed rms terminal voltage v_t is less than v_t^* . Hence, the comparator 'B' output is logic LOW, and thus, the turn OFF signal is sent to the IGBT. The block diagram for the control logic is provided in Part-III of Fig. 4.2(b).

In order to make a fair comparison to observe the effectiveness of the proposed ThyBT-NSFCL topology, the comparative analysis has been done with TT-NSFCL and SDBR. Moreover, the TT-NSFCL and SDBR are well established, and proven technology in the literature [67,68,77,178], it has the ability to enhance the transient stability and improve the FRT capability of the DFIG systems. Without any current limiter (WCL) is considered as a base case system. This system is simply a DFIG-based wind turbine system connected with the grid, and there is no fault current limiter has been uses. In SDBR [67,68,178], the parallel IGBT along with the dynamic resistor is directly connected in series with the line, and hence, the control circuit involves the sensing of the fault and turn OFF of IGBT switch (s_a), *i.e.*, during fault the dynamic breaking resistor is connected in series with the fault. Here, the rating of IGBT switch needs to be significantly high, and three pairs of IGBT switch along with breaking resistor are required. In TT-NSFCL [77], a small battery with constant voltage was

used as a DC-bias voltage source to compensate for the forward voltage drop across semiconductor switches and DC reactor, and flows of current depending on the operating states. As the operating point varies, a constant DC voltage may not be suitable to compensate the variable drop during the normal operation.

4.4 Analytical Analysis of the ThyBT-NSFCL

The analytical analysis of the proposed ThyBT-NSFCL configuration has been examined in this subsection. The analysis has been done for pre-fault and during fault conditions [74]. Fig. 4.3(a) shows analytical analysis and simulation results for both line and DC reactor currents under pre-fault, and during the fault condition. Similarly, the conduction modes of the thyristor (T_1-T_6) and the current flowing through each thyristor are presented in Figs. 4.3(b) and 4.3(c), respectively.

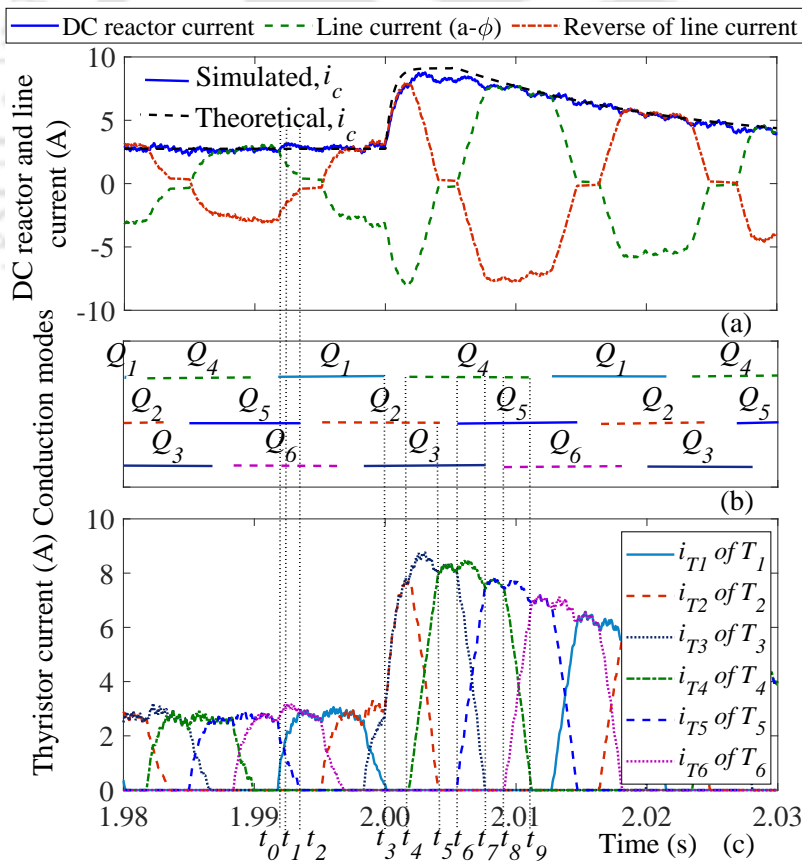


Fig. 4.3: The current conduction modes of thyristors before and during fault (a) DC reactor and line current; (b) gate pulse of each thyristor; (c) current of each thyristor.

Fig. 4.4 shows the equivalent circuits of the thyristor bridge rectifier part for individual modes corresponding to Fig. 4.3 are presented. The thyristors are enumerated in the order of conduction

sequence.

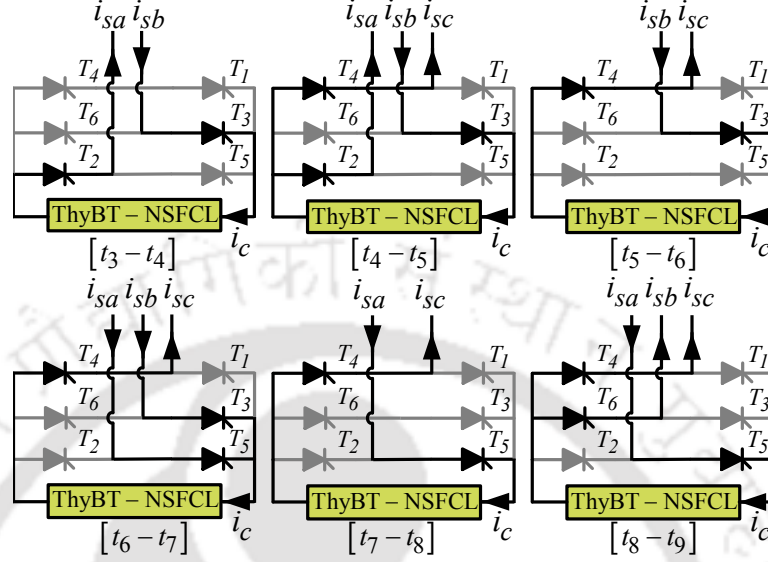


Fig. 4.4: Conduction modes of thyristor under fault (Thyristor of Gray colour \rightarrow OFF state and Black colour \rightarrow ON state).

4.4.1 Under Normal Operating Condition

In this condition, the semiconductor IGBT switch (s_a) remains to turn ON all the time, and the DC reactor, loss compensator circuit, IGBT switch (s_a), and thyristor bridge rectifier are connected in series. During this state, the firing angle of the thyristor is kept at 60° , so that there is a negligible loss in the breaking resistor since, during the charging period of the DC reactor, the diode connected in series with the breaking resistor remains turn ON. The charging or discharging of the DC reactor depends on the polarity of the voltage applied across the DC reactor. When the voltage is positive, the charging of the DC reactor occurs. When the voltage is negative, discharging occurs. The buck converter tries to compensate for the drop of voltages across the thyristor switches. The governing equation during the charging or discharging of the DC reactor during normal operation are

$$kv_m \sin(\omega t + \theta) + v_c = ri_L(t) + L \frac{di_L(t)}{dt} + v_{sc} + 2v_{ft} \quad (4.10)$$

where, $kv_m \sin(\omega t + \theta)$ is the net line voltage induced in the secondary side of the isolation transformer which is in series with the circuit. Here, ω is the power frequency, $z_s = r_s + j\omega L_s$ is source impedance, $z_L = r_L + j\omega L_L$ is load impedance, $r = r_s + r_c + r_L$ is the equivalent resistance; in which r_s , r_c and r_L stands for source, DC reactor and load resistance, and $L = L_s + L_c + L_L$ is the equivalent inductance;

4. Development of Fault Ride Through for DFIG System

in which L_s , L_c and L_L stands for source, DC reactor and load inductance. The value of k , depends on the number of thyristor conducting at that time, *i.e.*, $k = \sqrt{3}$ for two thyristor conducting, whereas $k = 1.5$, when 3 thyristor are conducting. Similarly, the value of θ depends on the voltages in the series to circuit. Now, solving (4.10), the line current is described as follows:

$$i_L(t) = \left\{ i_o - \frac{kv_m}{z} \sin(\omega t_o - \phi + \theta) + \frac{2v_{ft} + v_{sc} - v_c}{r} \right\} \times e^{-\left(\frac{r}{L}\right)(t-t_o)} + \frac{kv_m}{z} \sin(\omega t - \phi + \theta) + \frac{v_c - v_{sc} - 2v_{ft}}{r} \quad (4.11)$$

where, $i_o = i_L(t_o)$, $|z| = \sqrt{r^2 + (\omega L)^2}$ is the equivalent impedance, and $\phi = \tan^{-1}(\omega L)/r$ is the impedance angle. Clearly, $i_L(t) = i_c(t)$, *i.e.*, the line current is the same as the DC reactor current under the charging state.

4.4.2 During Fault Operating Condition

The operation of the ThyBT-NSFCL circuit under fault conditions has been analyzed in two stages.

4.4.2.1 Stage-1

To sense and turn OFF the IGBT switch (s_a) takes some time; hence, *Stage-1* refers to the state during fault when the IGBT switch (s_a) remains ON. Under this condition, the governing equation for fault current is given as

$$kv_m \sin(\omega t + \theta) + v_c = ri_f(t) + L \frac{di_f(t)}{dt} + v_{sc} + 2v_{ft} \quad (4.12)$$

Now, solving (4.12), the DC reactor current can be calculated as follows:

$$i_f(t) = \left\{ i_3 - \frac{kv_m}{z} \sin(\omega t_3 - \phi + \theta) + \frac{2v_{ft} + v_{sc} - v_c}{r} \right\} \times e^{-\left(\frac{r}{L}\right)(t-t_3)} + \frac{kv_m}{z} \sin(\omega t - \phi + \theta) + \frac{v_c - v_{sc} - 2v_{ft}}{r} \quad (4.13)$$

where, $i_3 = i(t_3)$, and the value of $|z|$ and ϕ are given in the previous case. Here, $r = r_s + r_c + r_f$; in which r_f stands for fault resistance, and $L = L_s + L_c$.

4.4.2.2 Stage-2

During this state, the IGBT switch (s_a) is turned OFF, and the firing angle of the thyristor is changed to 0° so that a large amount of power could get dissipated across the breaking resistance. In this mode of operation, the fault current flows through the thyristor bridge, a diode (D_b), and the

breaking resistance (r_p). This stage is related to a time interval between t_4 to t_9 , and the governing equation is given as

$$kv_m \sin(\omega t + \theta) = ri_f(t) + L \frac{di_f(t)}{dt} + v_b + 2v_{ft} \quad (4.14)$$

Now, solving (4.14), the fault current is described as follows:

$$i_f(t) = \left\{ i_4 - \frac{kv_m}{z} \sin(\omega t_4 - \phi + \theta) + \frac{2v_{ft} + v_b}{r} \right\} \times e^{-\left(\frac{r}{L}\right)(t-t_4)} + \frac{kv_m}{z} \sin(\omega t - \phi + \theta) + \frac{-v_b - 2v_{ft}}{r} \quad (4.15)$$

where, $i_4 = i(t_4)$, and the value of $|z|$ and ϕ are given in the previous case. Here, $r = r_s + r_p + r_f$; in which r_p stands for breaking resistance, and $L = L_s$.

4.4.3 Power Loss Calculations of the ThyBT-NSFCL

The proposed ThyBT-NSFCL power losses under normal operation state, which includes losses such as, the DC-bias voltage source, thyristor bridge rectifier, IGBT switches, DC reactor, and the buck converter. While calculating the losses associated with the thyristor bridge rectifier, it assumes that at a time, only two thyristors are conducting. Hence, the total steady-state losses per phase under the normal state is given as follows:

$$\begin{aligned} p_{loss,ThyBT-NSFCL} &= p_{loss,TBR} + p_r + p_{sc} + p_{loss,Buck} \\ &+ p_{loss,DC-bias} \\ &= 2v_{ft}i_{avg} + i_c^2 r_c + 2v_{sc}i_c + v_{In}i_c \\ &+ 2v_{fd}i_c \end{aligned} \quad (4.16)$$

where, $p_{loss,ThyBT-NSFCL}$ is the ThyBT-NSFCL total power losses, $p_{loss,TBR}$ is the thyristor bridge rectifier power losses, p_r is the DC reactor power losses, p_{sc} is the power losses across the IGBT switches (on-state), $p_{loss,Buck}$ is the buck converter losses ($\approx p_{loss,SW} + p_{loss,In}$; where, $p_{loss,SW}$ is the semiconductor switch losses (neglected) and $p_{loss,In}$ is the normal conductor internal resistor power losses), $p_{loss,DC-bias}$ is the DC-bias voltage source power losses ($\approx p_{core,VT} + i_{VT,rms}^2 r_{eq,VT} + 2v_{fd}i_c$; where, $p_{core,VT}$ is the voltage transformer core loss (neglected), $i_{VT,rms}^2$ is the rms value of the line current of voltage transformer (neglected), $r_{eq,VT}$ is the equivalent resistance of the voltage transformer (neglected) and v_{fd} is the forward voltage drop on each of diodes), i_{avg} is the average thyristor current

in each conduction modes, and v_{In} is the input voltage of buck converter.

From (4.16), it can be observed that v_{ft} , r_c , v_{sc} , v_{fd} , and v_{In} are marginally small. Moreover, using the buck converter, the value of i_c has a significant value. Hence, the on-state power losses can not be ignored in practical application.

4.5 Design Methodologies and Estimation of Parameters for Proposed ThyBT-NSFCL

The selection of suitable parameter values/ratings of each part is significant for the successful operation of the DFIG system. If the parameter rating is not proper, then the system may be reliable, but the cost will become very high. The design procedure of the circuit parameters for the satisfactory operation of the FRT capability is presented. The estimated design parameters for the proposed ThyBT-NSFCL are given in the subsection below.

4.5.1 Design for DC Reactor Inductance

During the fault, the high current could flow through the IGBT switch (s_a), since there will be some delay associated with turn OFF the device. These delays are mainly because of sensing delay, control delay, and IGBT turns OFF delay. Thus, by increasing the value of the DC reactor, the fault current passing through the IGBT switch (s_a) could be limited to a safe value until the turn OFF of the device. Thus, the minimum DC inductor required would be given by the expression

$$L_c \geq \frac{\sqrt{3}v_m}{di_{c,max}/dt} \approx \frac{\sqrt{3}v_m \times \tau_d}{i_{c,max}} \quad (4.17)$$

where, $\tau_d = \tau_{Sensor} + \tau_{Control} + \tau_{IGBT,OFF}$, $\sqrt{3}v_m$ is the peak voltage of the net line voltage induced in the secondary of the isolation transformer when only two thyristors are conducting, $i_{c,max}$ is the maximum safe current that can flow through the IGBT switch (s_a).

For detecting the occurrence of fault by the sensing circuit used in the present work, it takes about 200 μ s, which includes the time required for sensing (τ_{Sensor}), control circuit processing ($\tau_{Control}$), and IGBT turn OFF time ($\tau_{IGBT,OFF}$) of 90 ns. For the minimum estimated value of inductance required, $\sqrt{3}v_m$ is taken as 539 V, which corresponds to the peak voltage of the net line voltage induced in the secondary of an isolation transformer. Similarly, the value of $i_{c,max} \approx 6$ A is used to estimate the inductance of the DC reactor. The estimated value of the DC reactor ($L_c \geq 18$ mH) is obtained using (4.17). The resistance of the inductor is taken to be 1 Ω .

The DC reactor inductance value should be sufficient to suppress the rising DC current rate so that i_c does not exceed the maximum acceptable value $i_{c,max}$ before the DC-link of the DFIG system becomes affected.

4.5.2 Design of Breaking Resistor

The necessary condition to be satisfied for the breaking resistor of the proposed ThyBT-NSFCL under 3LG fault to suppress the fault current within the p times of the steady-state current is expressed. Therefore, the necessary breaking resistor of the limiter is

$$r_p \geq \frac{\sqrt{2}v_{rms,l-l}(CT)}{pi_{c,max}} \quad (4.18)$$

where, $v_{rms,l-l}(CT)$ is the net line rms voltage of the current transformer (CT).

Typically, $p = 3$, *i.e.*, the fault current with a value less than 3 times of normal line current is limited by the breaking resistor [193].

The estimated value of discharging resistance r_d is calculated using (4.18) where, $v_{rms,l-l}(CT) = 381$ V, and $pi_{c,max} \approx 18$ A is used to get the estimated value of $r_d \geq 30$ Ω .

4.5.3 Design of Buck Converter for Series Charging Supply

The buck converter supply is designed with an objective to regulate the voltage so that a minimum required DC reactor current at the desired level could be maintained during the normal operation. The design of the buck converter depends on several factors such as the power rating, current, and voltage ripple [194]. The input voltage of the converter is calculated from the diode bridge rectifier output voltage as

$$v_{oY} = \frac{3\sqrt{2}}{n\pi} v_{rms,l-l}(VT) \quad (4.19)$$

where, $v_{rms,l-l}(VT)$ is the net line rms voltage of the voltage transformer (VT).

The buck converter voltage controls the DC-bias voltage source to fed as loss compensation. The reference voltage value is expressed as $v_c = Dv_{oY}$, where, D is the duty cycle of the buck converter decided by the controller.

The output of the filter inductor is calculated as

$$L_b = \frac{(1-D)v_c}{\Delta i_{Lo} f_s} \quad (4.20)$$

4. Development of Fault Ride Through for DFIG System

where, Δi_{Lo} is the peak-to-peak ($p-p$) ripple of an inductor current (here, the internal resistance of the filter inductor, L_b is ignored).

The output of the filter capacitor is calculated as

$$C_f = \frac{\Delta i_{Lo}}{8\Delta v_{Cdf_s}} \quad (4.21)$$

where, Δv_{Cd} is the $p-p$ ripple of the capacitor voltage.

The buck converter has been designed to compensate the voltage drop of $v_c = 8$ V, which includes the forward voltage drop across the semiconductor switches and the DC reactor, isolation transformer, and thyristor bridge rectifier. Here, the input line-to-line rms voltage to voltage transformer ($v_{rms,l-l}(VT) = 415$ V), the voltage transformer turns ratio of $n = 40$ is used in designing the buck converter so that the value of the diode bridge rectifier output voltage, *i.e.*, $v_{oV} = 14.03$ V is calculated using (4.19). The value of the duty cycle of the buck converter, $D = 0.57$ is computed. The other design parameters are $i_c = 2.75$ A, the percentage ripple in current is taken to be 10%, *i.e.*, Δi_{Lo} is 0.275 A. Similarly, the percentage ripple in voltage is taken to be 0.2%, *i.e.*, Δv_{Cd} is taken to be 0.016 V. The switching frequency used in the buck converter design is 5 kHz. Using the above design parameters, the estimated inductance of the filter inductor is $L_b \approx 2.5$ mH, and the output filter capacitor is $C_f \approx 450$ μ F.

4.6 Results and Discussion

A 3 HP rating of 3- ϕ DFIG system has been used in obtaining the simulation results, and the appendix provides the data used in the simulation. In the present work, the DFIG system is connected to the grid, which is considered an infinite bus with a constant voltage of 415 V, 50 Hz. To verify the effectiveness of the proposed ThyBT-NSFCL, it is compared to different protection strategies such as WCL, SDBR, and TT-NSFCL, for a temporary symmetrical 3- ϕ to ground (3LG) is applied at utility grid 'h' as shown in Fig. 4.1. The present analysis assumes that the wind turbine is operating at a constant wind speed of 12 m/s. As discussed in the previous subsection, the calculated parameters of the proposed ThyBT-NSFCL circuit are used in the simulation. The simulation runs for 5 s, the fault is initiated at $t = 2$ s and it is cleared at $t = 2.15$ s (7.5 cycles) from the occurrence of the fault. The simulation runs with a solution time step of 2 μ s on PSCAD/EMTDC [195] software. The whole test system has been simulated and analyzed using PSCAD/EMTDC [195] software.

4.6.0.1 Characteristics of Voltage Dip

At the fault instant, the sudden voltage dips occur at the stator terminal, thus the results in a sharp change in the stator flux. It could abruptly introduce a large transient current into the stator as well as rotor winding, and these incremental currents may damage the RSC converter. According to the Indian grid code IWGC (Indian Wind Grid Code), the wind turbine must resist upto 15 pu of the nominal voltage at its terminals [196,197].

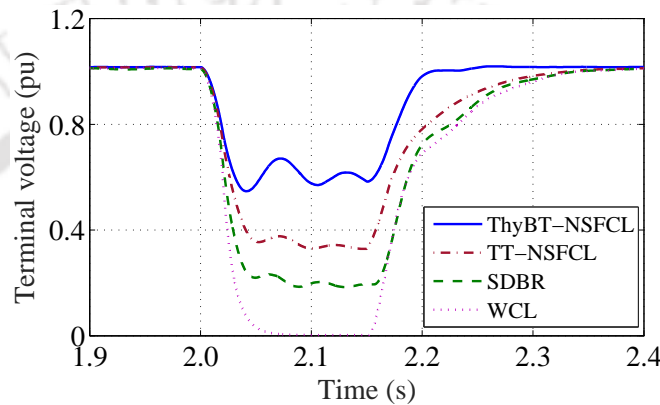


Fig. 4.5: The voltage dip at terminal of the DFIG system.

The simulated RMS value of the voltage dip response at the DFIG-based wind turbine terminal is shown in Fig. 4.5. It observed that

- (i) In the case of WCL, the voltage dip goes to 0 pu, which is below the minimum acceptable voltage of the grid codes. It indicates that the DFIG system will not ride-through during the fault.
- (ii) After adding the series device such as the SDBR, TT-NSFCL, and proposed ThyBT-NSFCL, respectively. The voltage dip is improved and reaches near about 0.19 pu, 0.33 pu, and 0.55 pu, respectively, which is achieved to the acceptable range of the grid code.

As shown in Fig. 4.5, the proposed ThyBT-NSFCL quickly recovers the voltage dip at the machine terminal. The voltage dip improvements with the ThyBT-NSFCL are nearly 100% as compared to WCL, about 65.45% as compared to SDBR, and 40% as compared to TT-NSFCL protection device, respectively. However, the improved terminal voltage of the DFIG system with the ThyBT-NSFCL is acceptable for safety margin and grid codes. Therefore, the overall FRT capability of the DFIG system has been significantly enhanced with the ThyBT-NSFCL.

4.6.0.2 Transient Stator Current Proficiency

The quantitative evaluation of the stator current behavior of the DFIG for without and with ThyBT-NSFCL is presented in Fig. 4.6. The first peak values of the rotor currents (i_{sa} , i_{sb} , i_{sc}) as presented in Fig. 4.6(a) jump to about 14.13 A for $a-\phi$, 13.47 A for $b-\phi$, and 16.16 A for $c-\phi$, respectively. With the presence of the proposed ThyBT-NSFCL, the first peak values of rotor fault current as presented in Fig. 4.6(b) is limited to 7.93 A for $a-\phi$, 8.49 A for $b-\phi$, and 8.50 A for $c-\phi$, respectively. The fault current limiting rate between the stator current without and with the ThyBT-NSFCL are 43.87% for $a-\phi$, 36.97% for $b-\phi$, and 47.40% for $c-\phi$, respectively.

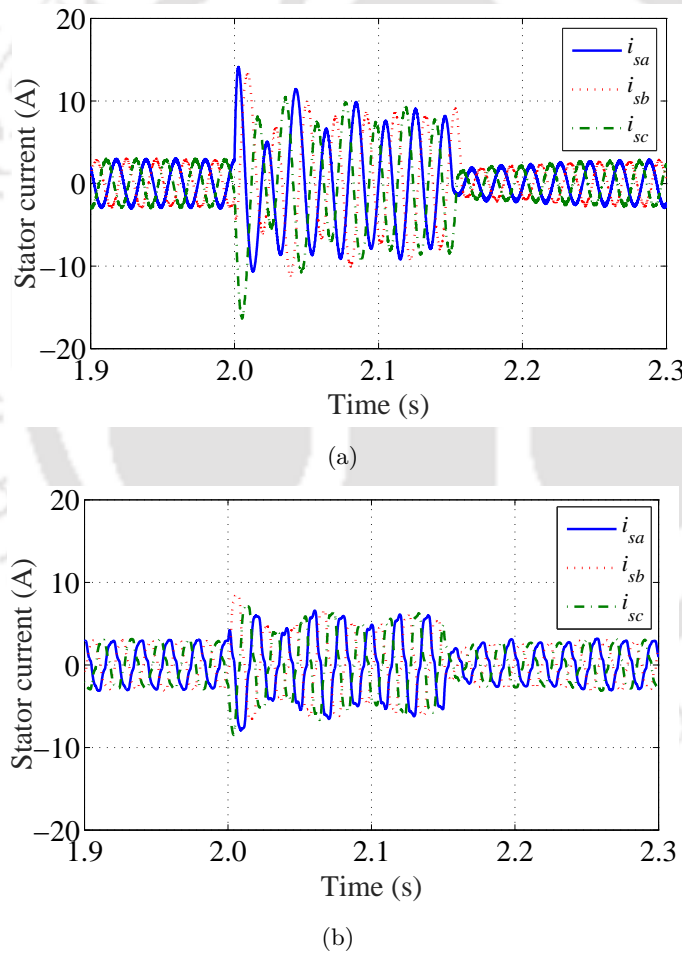
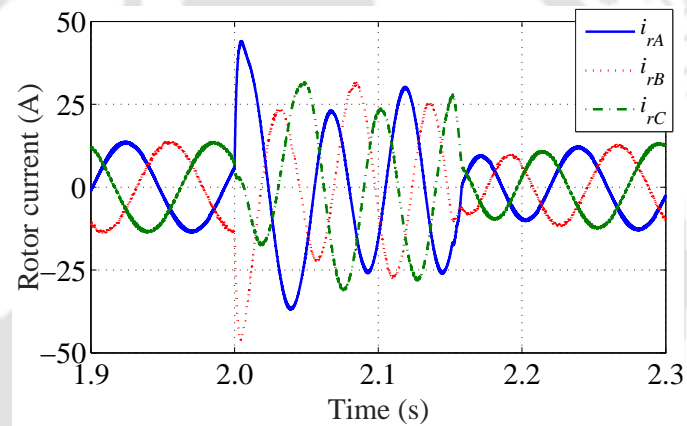


Fig. 4.6: The DFIG system stator current behaviors (a) WCL; (b) with proposed ThyBT-NSFCL.

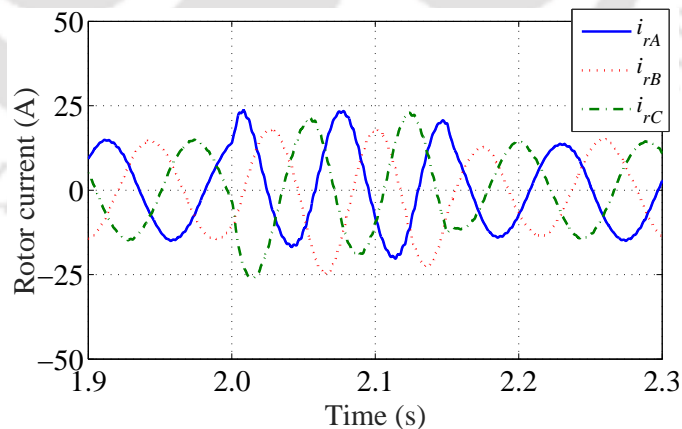
4.6.0.3 Transient Rotor Current Proficiency

The transient rotor current behavior characteristics without and with the ThyBT-NSFCL are presented in Fig. 4.7. The first peak values of the rotor fault currents (i_{rA} , i_{rB} , i_{rC}) as presented

in Fig. 4.7(a) and the current jumps to about 44.13 A for $a - \phi$, 45.72 A for $b - \phi$, and 31.54 A for $c - \phi$, respectively. With the presence of the proposed ThyBT-NSFCL, the first peak value of the rotor current is presented in Fig. 4.7(b), which is limited to 23.62 for $a - \phi$, 18.00 A for $b - \phi$, and 26.03 A for $c - \phi$, respectively. It has been observed that when the ThyBT-NSFCL is placed at the stator terminal of the DFIG system, the rotor fault currents are reduced, thus reducing the RSC ratings. The current limiting rate between the rotor current without and with ThyBT-NSFCL are 46.47% for $a - \phi$, 60.63% for $b - \phi$, and 17.47% for $c - \phi$, respectively. However, when the proposed ThyBT-NSFCL is placed at the stator terminal of the DFIG system, then it is observed that the rotor fault currents are suppressed. Hence, it helps to yield the overcurrent protection for the RSC.



(a)



(b)

Fig. 4.7: The DFIG system rotor current behaviors (a) WCL; (b) with proposed ThyBT-NSFCL.

4.6.0.4 DC-Link Voltage

A DC-link with a voltage of 95 V along with a DC-link capacitor of 2500 μF is utilized in the simulation. The DC-link voltage variations with the different FCLs are shown in Fig. 4.8. From the figure, it is observed that the DC-link voltage oscillations effectively restrained sharply in the presence of ThyBT-NSFCL as compared with the case of WCL, SDBR, and TT-NSFCL. The observations also show that the DC-link voltage drops to a value of 54.13 V with WCL, 65.76 V with SDBR, and 77.41 V with TT-NSFCL, and 83.38 V with proposed ThyBT-NSFCL, respectively. Therefore, the DC-link voltage response noted that the ThyBT-NSFCL provides superior transient stability performance compared to SDBR and TT-NSFCL under fault conditions.

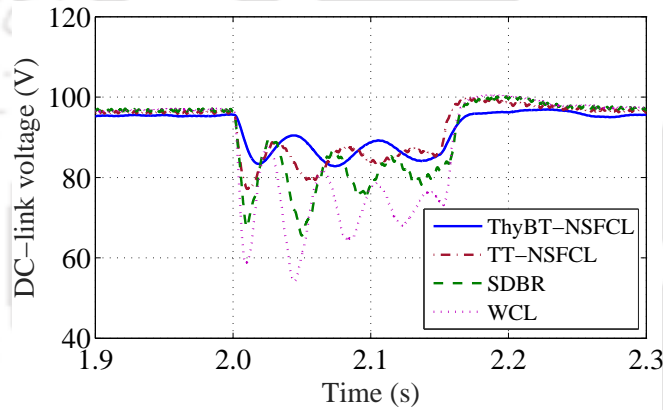


Fig. 4.8: The DC-link voltage behavior.

4.6.0.5 Electrical Torque Command

The electromagnetic torque unbalances cause a continuous and considerable amount of increment in the rotational speed of the DFIG system. Hence, the DC-link voltage falls gradually. So, there is a need for a passive protection device to encounter this problem. The dynamic electrical torque response of the DFIG wind turbine with the different cases of a protection scheme is presented in Fig. 4.9. The first peak of the electrical torque falls to 2.899 pu with WCL, 2.482 pu with SDBR, 1.943 pu with TT-NSFCL, and 1.284 pu with proposed ThyBT-NSFCL, respectively. Other than the proposed scheme, the electromagnetic torque values exceed the mostly used safety margin for the practical DFIG system. Therefore, the proposed ThyBT-NSFCL effectively reduces the variation of the electrical torque during the fault and swings after the fault clearance.

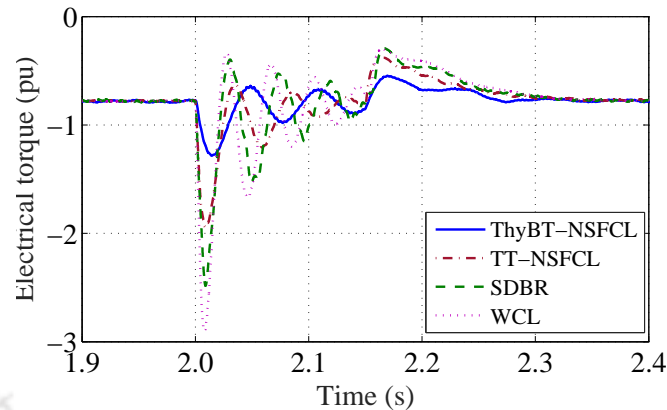


Fig. 4.9: Electrical torque behavior.

4.6.0.6 Active Power Transients

The response of the active power generated by the DFIG system with various FCLs is shown in Fig. 4.10. From the figure, it is observed that the generated active power dropped nearly to zero in the WCL case under fault. So, this effect not only brings oscillation in the electromechanical system but may also cause instability in the power system. To overcome this problem, it is found that the proposed ThyBT-NSFCL is very effective. After connecting the proposed ThyBT-NSFCL, the active power drop is improved to 0.379 kW, whereas with other FCLs are 0.152 kW with SDBR, and 0.369 kW with TT-NSFCL, respectively. Also, it observed that the proposed ThyBT-NSFCL significantly reduces active power fluctuation.

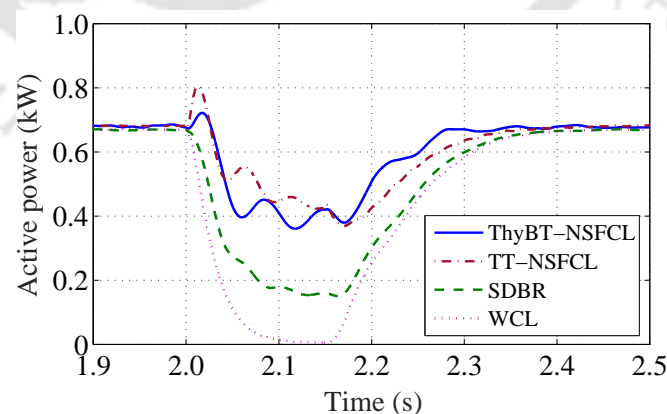


Fig. 4.10: Active power response at the PCC.

4.6.0.7 Voltage Dip at Machine Terminal Voltage

The improved voltage level under fault at the grid achieved 0.702 pu with TT-NSFCL and 0.842 pu with ThyBT-NSFCL at a breaking resistor value of 100 Ω as shown in Fig. 4.11. From the results, it is observed that the amount of voltage level at the machine terminal significantly improved when the breaking resistance values are increased from about 30 to 100 Ω with a step of $\approx 10 \Omega$. When increasing the resistor value then, the total cost of ThyBT-NSFCL is increased. Hence, the selected optimal breaking resistor of the limiter is the minimum to achieve compliance with Indian and international grid codes.

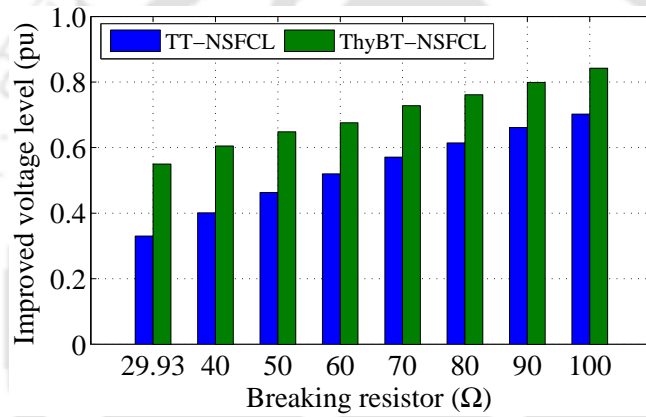


Fig. 4.11: Effects of breaking resistance at the machine terminals.

4.7 Summary

In this work, a thyristor-based bridge-type non-superconducting fault current limiter (ThyBT-NSFCL) is designed with a buck converter to enhance its fault ride-through (FRT) capability and tested with the doubly-fed induction generator (DFIG) system. The critical findings from the simulated results are as follows:

- The analytical analysis of the proposed ThyBT-NSFCL circuit operation is demonstrated for both normal and fault conditions with the symmetrical fault. The presented simulation results show a good and acceptable agreement with the analytical analysis of circuit operation.
- The design procedure of the current limiting parameter values/ratings of the ThyBT-NSFCL for the satisfactory operation is discussed.
- The ThyBT-NSFCL performs better under fault conditions to improve the FRT capability of the wind energy system (WES) in various aspects, and it helps to meet the grid code requirements

of connecting the DFIG system.

- The voltage dip at the terminal of the DFIG system is improved significantly with ThyBT-NSFCL compared to without any current limiter (WCL), series dynamic breaking resistor (SDBR), and switched impedance transformer-type non-superconducting fault current limiter (TT-NSFCL) protection device.
- The ThyBT-NSFCL significantly improves the fluctuation and pulsation of generated active power under fault conditions and circuit breaker opening instant.
- The effects of different breaking resistors at the machine terminal voltage are observed and found satisfactory voltage dip improvement.
- Additionally, the proposed ThyBT-NSFCL has a simple structure that is efficient and economical to utilize in the power system with the DFIG system.

Finally, it manifests from comprehensive simulations and numerical analysis that the proposed ThyBT-NSFCL is a more successful auxiliary protection device to enhance the FRT capability of the DFIG system than the SDBR and TT-NSFCL in every aspect under the symmetrical fault in the power system. This idea can be executed by physical experiments and hardware results to support the claims as a future study.



5

Impact of Integration of Wind Energy into the Micro-Grid

Contents

5.1	Introduction	122
5.2	A Typical Distribution Network with Distributed Generations	123
5.3	Results and Discussion	127
5.4	Summary	138

Objective

Renewable energy-based distributed generation (DG) plays a vital role in developing a sustainable grid. Due to the intermittent nature of renewable energy sources, the power output poses potential technical challenges to the grid and utilities. The technical challenges in the power system are the power quality issues such as voltage flicker, voltage sag, or swell, and rotor angle stability of the microgrid. To study the influence of renewable energy integration into the microgrid, the present work has utilized a modified distribution network of IIT Guwahati (MDN-IITG). To simulate the complete system, Siemens PTI PSS® Sincal software is used in the present steady-state and dynamic analysis. Finally, the fault ride-through capability of the wind generator is observed with the presence of FACTS devices in the system.

5.1 Introduction

The present focus is towards the use of more or more renewable energy sources such as wind, solar, biogas/biomass, hydro, tidal, geothermal, fuel cells, etc., into the grid [198]. Some popular distribution energy generation sources are shown in Fig. 5.1.

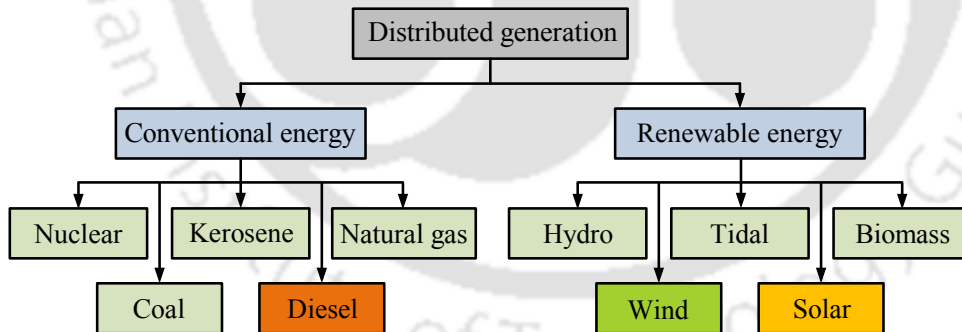


Fig. 5.1: The popular distributed energy generation resources.

Among the various types of wind turbines, the variable speed wind turbines along with the doubly-fed induction generator (DFIG) is widely used in developing a wind energy conversion systems (WECSs). It has many advantages over the fixed speed induction generators or fully-fed synchronous generators such as variable-speed constant frequency (VSCF) operation, reduced flicker, independent control capabilities of active and reactive powers, and relatively reduced-size converter [199]. It is important to study the effect on distribution networks such as voltage regulation, line flows, and stability of the grid with the presence of the renewable energy (RE)-based DGs.

From the literature, it is observed that most of the available research is carried out on the systems primarily located in the USA and Europe. Since, the study conducted by other countries could not be simply adopted without further research on the Indian systems. Therefore, the present study on the modified distribution network of IIT Guwahati (MDN-IITG) tries to address some of these issues related to the Indian system located in the North-East region of the country.

The remaining chapter is planned as follows. Section 5.2 discuss about the distribution network used in the study. It also talks about the profile of the load. Section 5.3 provides the result and its analysis. Finally, conclusion of work is presented in Section 5.4.

5.2 A Typical Distribution Network with Distributed Generations

The distribution system in the study is a modified Distribution System of IIT Guwahati. Here, the network topology and line parameters are taken from the modified distribution system of IIT Guwahati. However, the study purposes, the modified system includes some wind generation.

5.2.1 Detailed Description of Modified Distribution Network of IIT Guwahati (MDN-IITG) System

The interconnected distribution network is designed to deliver power safely and with reliability. The MDN-IITG has an incoming feeder from the grid to the main substation of 33 kV with a rated capacity of 5 MVA. The main substation is connected to other substations through 11 kV feeders. The voltage level at each 11 kV sub-feeder is further stepped down to 0.415 kV through 11/0.415 kV distribution transformers. The major load is of four different types *i.e.*, residential areas: RA (bus 6, 7, 18, 19, & 20), hospital areas: HA (bus 13), central library and playground areas: CLPA (bus 10 & 11).

The network topology of the MDN-IITG system is shown in Fig. 5.2. The MDN-IITG grid-connected microgrid consists of RE-based DGs (wind) as the energy sources. The distributed generation (DG) consist of 1.3 MW DFIG-based wind turbine. A shunt capacitor bank with a 1 MVAR rating is connected at bus 1. To further regulate the reactive power demand, a distribution static synchronous compensator (D-STATCOM) with the rated capacity of 0.25 MVAR is connected at bus 12. The details about the network and its parameters are given in Appendix E. Further, the detail descriptions of major components of the distributed generation is provided in the subsequent subsections.

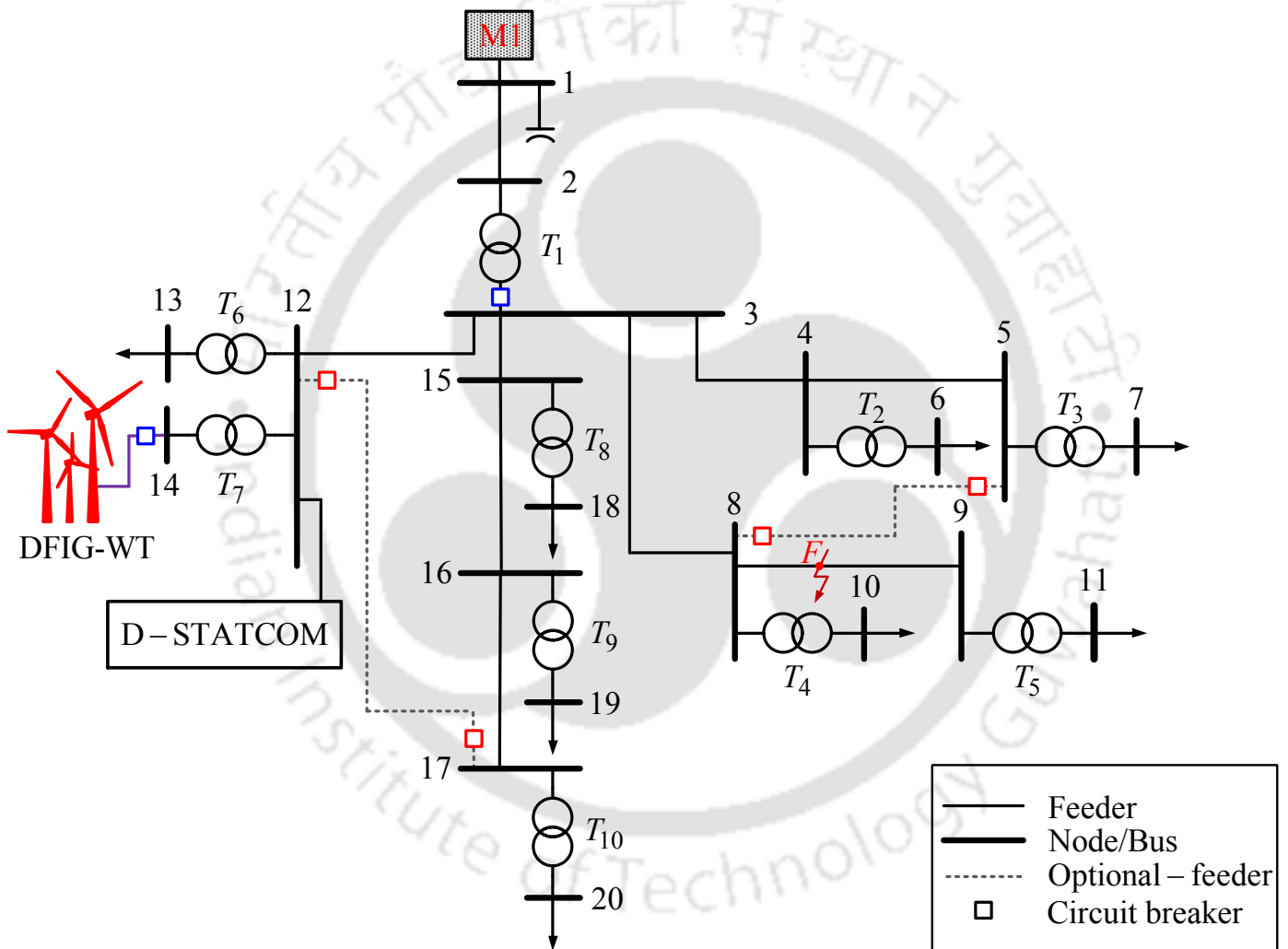


Fig. 5.2: A typical single-line layout of the MDN-IITG test system with renewable energy based DGs and load groups.

5.2.2 DFIG-Based Wind Turbine Power Unit

The DFIG used in the present study can operate in power factor control mode (± 0.95 lagging/leading) or voltage control mode. The slip of the DFIG can vary within 30% to -30% . The DFIG used in the model is an equivalent model representing several small DFIG generators connected to a wind farm. The capacity of the DFIG used in the study has a rated capacity of 1.25 MVA. The machine and its control parameters are given in Appendix E.1.

The wind power is integrated into the microgrid as an aggregated DFIG based WECS. Here in the simulation, the DFIG is interfaced with the grid as a “load flow type DFIG” *i.e.*, DFIG with specified P_W , Q_W , s . The dynamic model of the DFIG utilizes controllers such as voltage regulator, active/reactive power controller, and speed controller present in the library of Siemens PTI PSS®.

5.2.3 Distributed Static Synchronous Compensator (D-STATCOM) Model

Compared to the other flexible AC transmission system (FACTS) devices, the D-STATCOM is a more suitable device to improve the power quality and system dynamics in the distribution network [200]. To simulate a D-STATCOM, an advanced D-STATCOM model is used, which is connected at bus 12. Here, a D-STATCOM is designed with the rated capacity of 250 kVAR capacitor and 50 kVAR inductive reactive power. The zero-sequence resistance and reactance are assigned as 0.567Ω and 0.453Ω , respectively. Here, the D-STATCOM model as a current source (GNE-I) using graphich model builder (GMB) module in Siemens PTI PSS® Sincal software. The parameters associated with the controller are provided in Appendix E.3.

5.2.4 Load Demands Curves

The load demand at buses 6, 7, 18, 19, & 20 is shown in Fig. 5.3. Similarly, Fig. 5.4 shows the load demand at bus 13, and Fig. 5.5 shows the load demand at buses 10 and 11. These load curves are taken from the measured data at load buses of MDN-IITG on a particular day which has been divided into 96 data points with a time interval of 15 minutes. The data was measured at an interval of 15 minutes, the data point 1 ($data_1$) refers to average load demand during 00:00–00:14 h, similarly $data_2$ as 00:15–00:29 h, and so on.

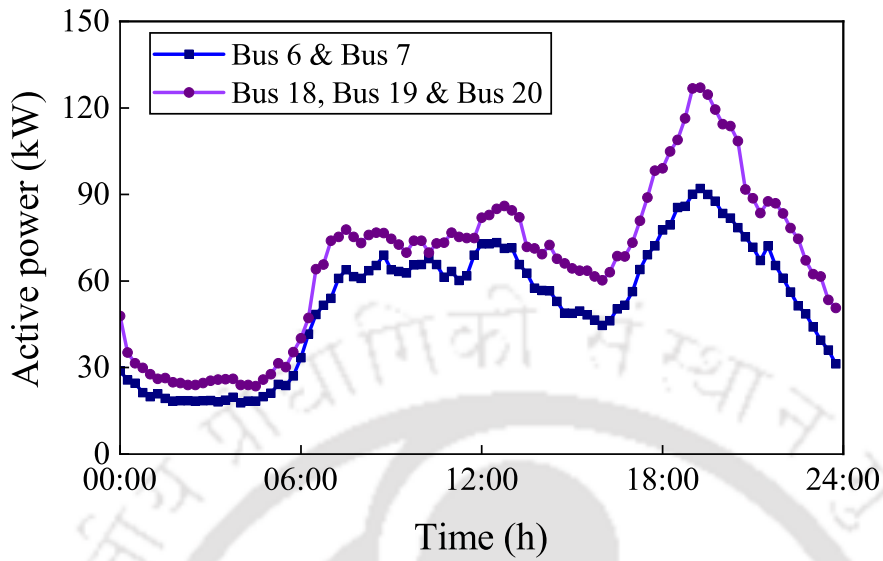


Fig. 5.3: The residential area load profiles.

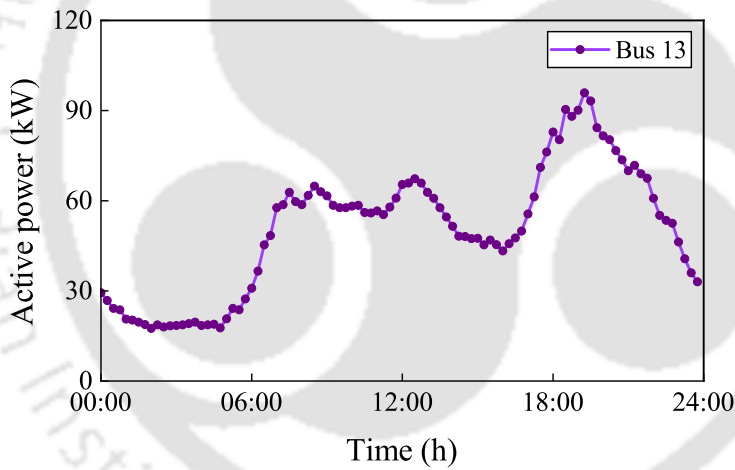


Fig. 5.4: The hospital area load profile.

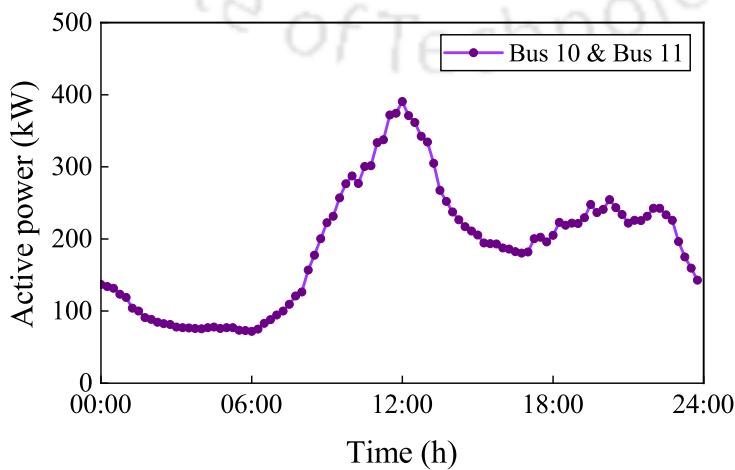


Fig. 5.5: The central library and play ground area load profile.

5.2.5 Wind Generation Profile

The wind generation profile for a day in the per unit (p.u.) is shown in Fig. 5.6. The generation schedule is updated at the interval of 15 minutes.

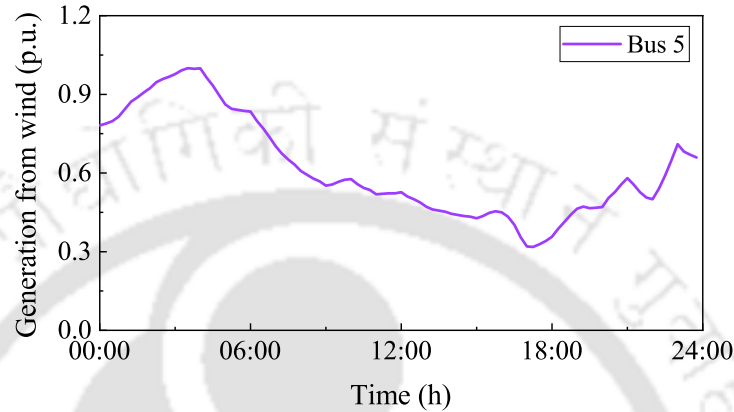


Fig. 5.6: The wind turbine generation profile.

5.3 Results and Discussion

This section presents the steady-state and dynamic analysis of the MDN-IITG test system. While doing the steady-state analysis, the load profile of a particular day is used in the simulation. Further, how a typical wind generation pattern will affect voltage and the line flows is analysed.

The study also includes the power quality analysis of the system with the wind generation through DFIG. Here, two cases are analysed *i.e.*, in the first case the effect of DFIG on the network is considered, while in the second case, the effect of DFIG with D-STATCOM is analyzed.

The test system is developed in Siemens PTI PSS®Sincal platform on Intel® Xeon® E5-2650v4 2.20 GHz Quad-Core CPUs with 8 GB of RAM.

5.3.1 Steady-State Analysis

For a steady-state analysis, two cases are considered in this work. The results of different cases are compared in terms of voltage regulation, power flow, average voltage and voltage deviation at any time of the day and at buses 1, 3, 6, 7, 10, 11, 12, 13 & 20 node. These two cases are defined as follows:

- *Case #1: MDN-IITG without DFIG*– Only loads are connected at different buses without the integration of distributed generators.

5. Impact of Integration of Wind Energy into the Micro-Grid

- *Case #2: MDN-IITG with DFIG*– DFIG-based wind turbine power unit is integrated into the distribution system.

5.3.1.1 Voltage Regulation

The load flow analysis is performed for two cases to investigate the voltage regulation at different buses.

5.3.1.1.1 Case #1: MDN-IITG without DFIG Fig. 5.7 shows that the voltage profile of different buses in the network. Here, bus 1 is considered as the reference bus with the per-unit (p.u.) value of 1.03. It is observed that the node voltages dropped significantly in the middle of the day as load demands were at the maximum values. The bus voltage dropped to the lowest level at 12:00 h, the voltage profile at buses 6, 7, 13, 18, 19, and 20 nodes dropped to approximately 1.025 p.u.; additionally, the voltage profile at buses 10 and 11 nodes dropped to approximately 1.023 p.u. Finally, it is observed that voltage regulation is within the acceptable limit.

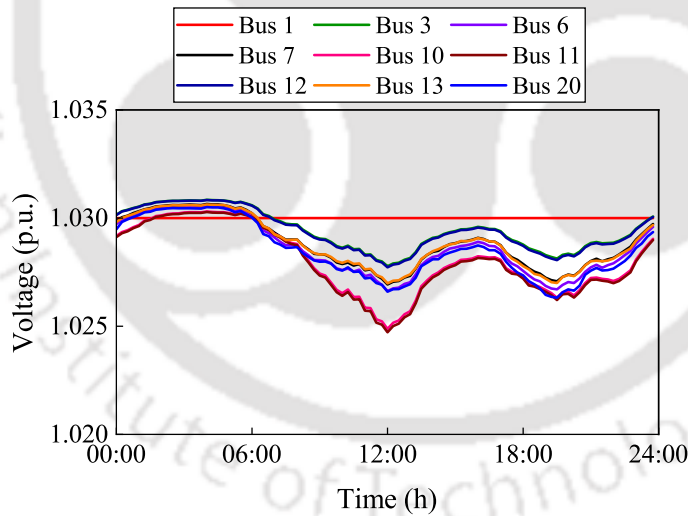


Fig. 5.7: The voltage profile without any distribution generation integration for M_1 in-feeder.

5.3.1.1.2 Case #2: MDN-IITG with DFIG The voltage regulation of buses with the integration of DFIG-based wind energy system is shown in Fig. 5.8. From the figure, it is observed that there is a significant increase in the voltage level at most of the buses, but at the same time, there is also an increase in voltage deviation at the buses. The observed maximum voltage at the DFIG-based wind energy system is 1.038 p.u., which does not exceed the permissible safety limit defined by the Indian Electricity Rules.

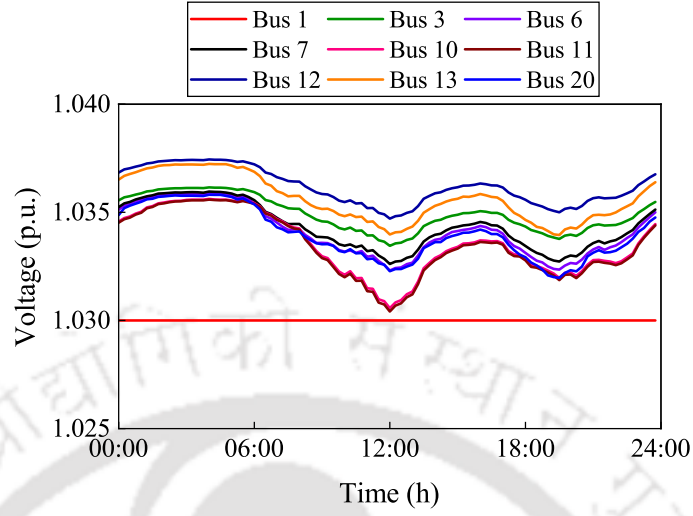


Fig. 5.8: The voltage profile disturbance due to DFIG-based wind turbine integration in M_1 in-feeder.

The average voltage values are obtained for the two cases and their comparison is shown in Table 5.1. The equation used to find the average bus voltage (AV) is given below:

$$AV_{BUS} = \frac{1}{N} \sum_{i=1}^N [V_{BUS}(i)] \quad (5.1)$$

where, N is the number of data points, $V_{BUS}(i)$ is the i^{th} data point corresponding to the voltage magnitude at a particular bus.

Similarly, the voltage deviation (VD) obtained for different cases are compared at different buses. The values of VD in p.u. as defined in (5.2) is used to quantify the deviation in the voltage level.

$$VD = \frac{1}{N} \sum_{i=1}^N |V_{BUS}(i) - AV_{BUS}| \quad (5.2)$$

where, AV_{BUS} represents the average bus voltage at a bus.

From Table 5.1, it is observed that for Case #1 (MDN-IITG without DFIG), the AV_{BUS} values at all buses except the reference voltage is comparatively less as compared with Case #2 (MDN-IITG with DFIG). Similarly, it is also observed that the VD values for these two cases are comparable.

5.3.1.2 Power Flows in Different Lines or Feeders

The average power values are obtained for the two cases and their comparison is shown in Table 5.2. The equation used to find the average line power (AP) in kW is given below:

5. Impact of Integration of Wind Energy into the Micro-Grid

Table 5.1: Calculated average voltage and voltage deviation values at different buses.

Buses	AV _{BUS} Value (p.u.)		VD Value (p.u.)	
	Case #1	Case #2	Case #1	Case #2
1	1.03	1.03	Reference	Reference
3	1.0294	1.0349	0.000792	0.000696
6	1.0286	1.0341	0.001069	0.000972
7	1.0288	1.0343	0.000997	0.000900
10	1.0280	1.0335	0.001313	0.001214
11	1.0279	1.0335	0.001342	0.001243
12	1.0294	1.0362	0.000806	0.000708
13	1.0288	1.0356	0.000991	0.000893
20	1.0285	1.0339	0.001090	0.000992

$$AP_{\text{LINE}} = \frac{1}{N} \sum_{i=1}^N [P_{\text{LINE}}(i)] \quad (5.3)$$

where, N is the number of data points, $P_{\text{LINE}}(i)$ represents i^{th} data point corresponding to active power flow in a particular line. Whereas, AP_{LINE} represents the average power of the same line.

Similarly, the power deviation (PD) obtained for different cases are compared in different lines. The values of PD in kW as defined as (5.4) is used to quantify the deviation in feeder active power flow in the line.

$$PD = \frac{1}{N} \sum_{i=1}^N |P_{\text{LINE}}(i) - AP_{\text{LINE}}| \quad (5.4)$$

This subsection analyses the power flow in different lines over a period of 24 h for the two cases. Fig. 5.9 shows that the power flows in the lines without any distribution generation integration *i.e.*, for Case #1. Similarly, Fig. 5.10 shows that the power flows in the lines with distribution generation *i.e.*, for Case #2.

From Table 5.2, it is observed that for Case #1 (MDN-IITG without DFIG), the AP values in all lines are positive values means that power is flowing from grid or feeder to loads/customers, but in Case #2 (MDN-IITG with DFIG), AP values of line flow 1–2 and 3–12 has the negative values other than the line flow 3–4, 3–8 and 3–15, because the DFIG unit generate power to supply the customer requirement if there is any surplus power, then it is fed-back to the main grid. Similarly, it

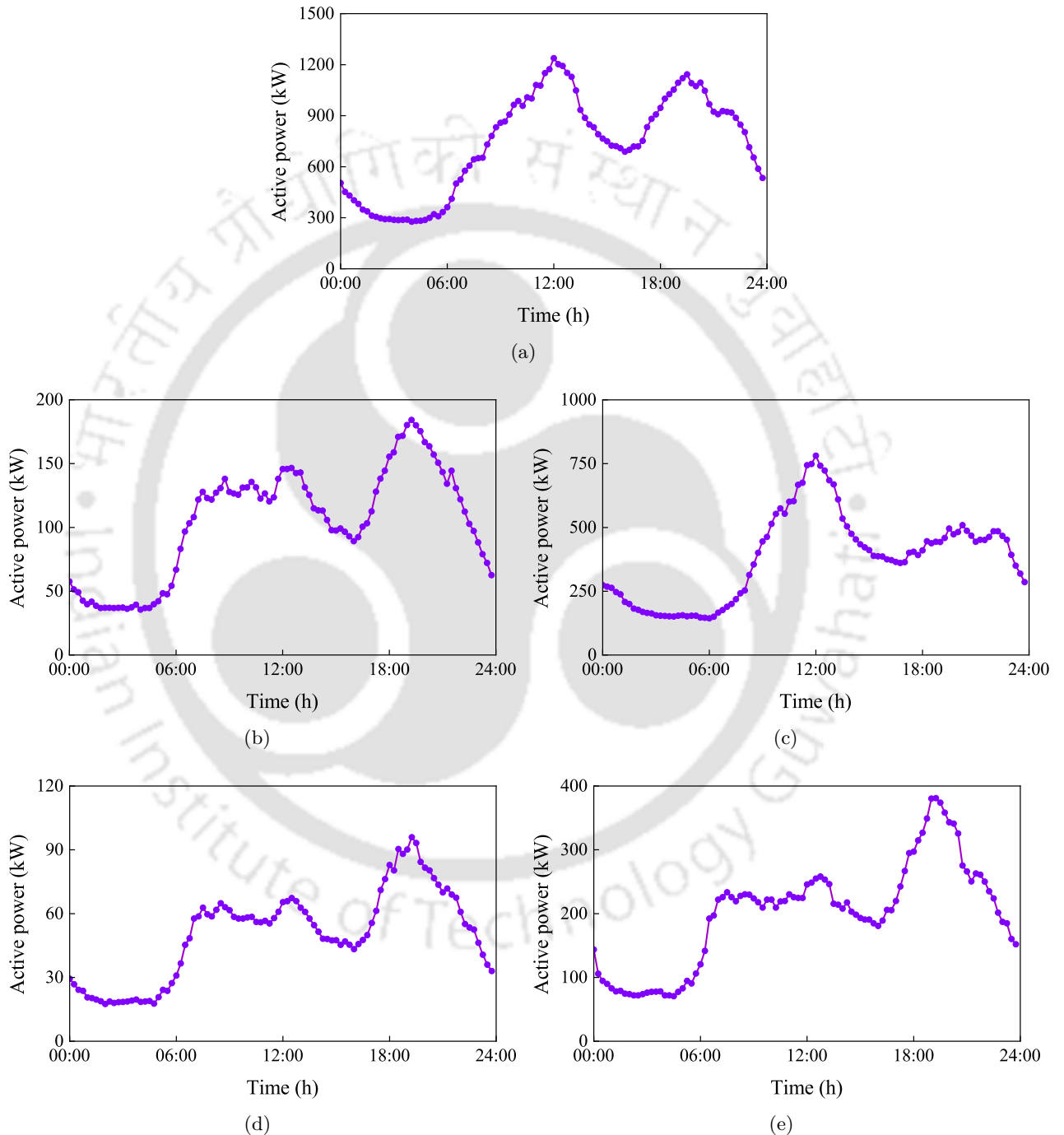


Fig. 5.9: The power distribution in the MDN-IITG test system for Case #1 & #2 (a) line flow 1–2; (b) line flow 3–4; (c) line flow 3–8; (d) line flow 3–12; (e) line flow 3–15.

5. Impact of Integration of Wind Energy into the Micro-Grid

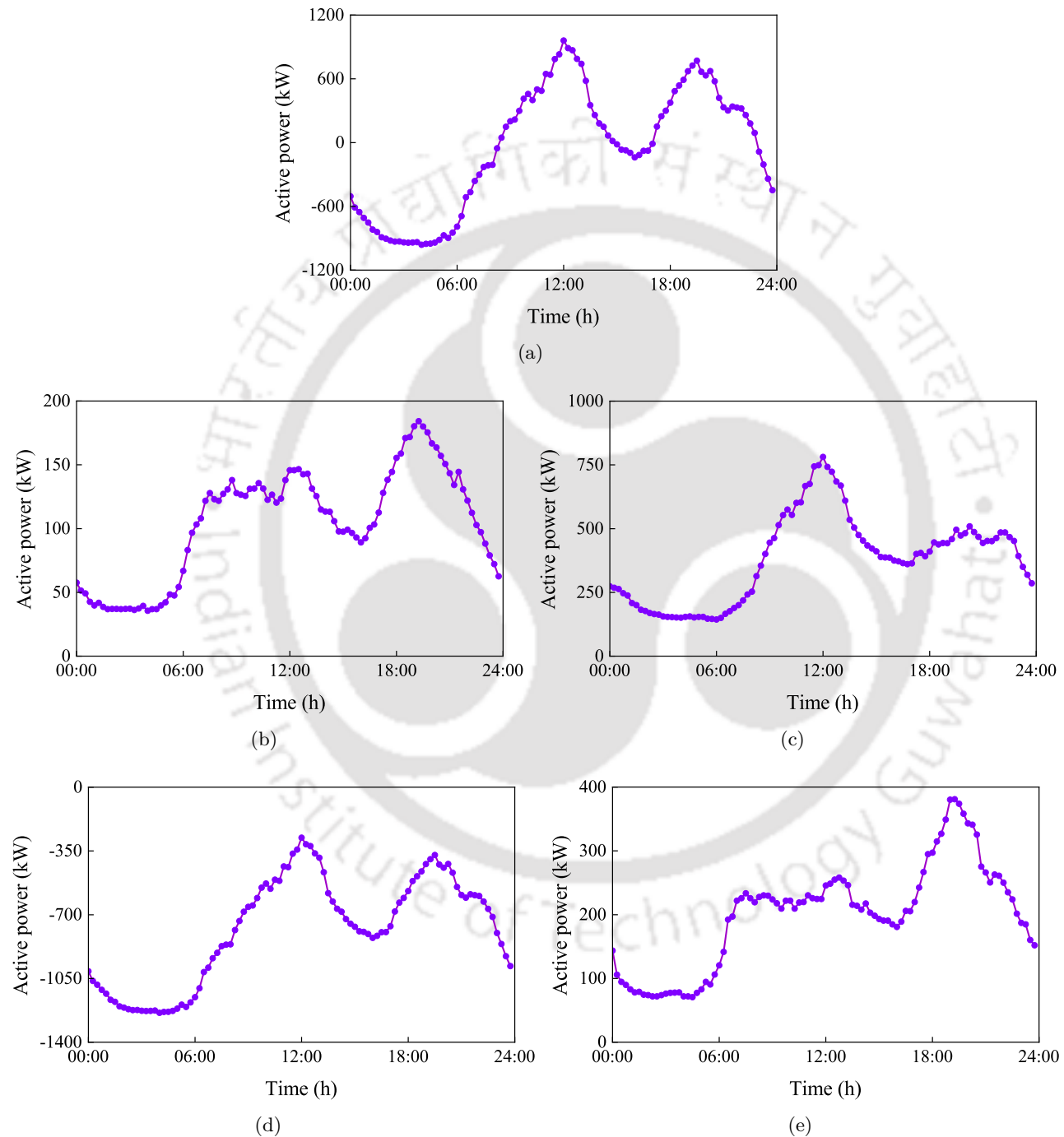


Fig. 5.10: The power distribution in the MDN-IITG test system for Case #2 (a) line flow 1-2; (b) line flow 3-4; (c) line flow 3-8; (d) line flow 3-12; (e) line flow 3-15.

Table 5.2: Calculated average power and power deviation values in different lines.

Lines	AP _{LINE} Value (kW)		PD Value (kW)		Maximum Value (kW)		Minimum Value (kW)	
	Case #1	Case #2	Case #1	Case #2	Case #1	Case #2	Case #1	Case #2
1–2	735.58	-44.35	251.47	502.72	1238.49	-961.25	277.21	960.79
3–4	104.28	104.28	36.78	36.78	184.20	184.20	35.60	35.60
3–8	381.02	381.02	141.69	141.69	781.00	781.00	144.00	144.00
3–12	50.52	-779.75	17.47	251.35	95.90	-1238.17	17.50	-277.19
3–15	199.58	199.58	64.69	64.69	381.05	381.05	70.62	70.62

is also observed that the PD values of Case #1 is less than or equals as compared to Case #2.

5.3.2 Dynamic Model Evaluation

This subsection presents the dynamic analysis on a MDN-IITG test system in the presence of the DFIG system. Here, two cases are considered, which are as shown below:

- *Case #1: DFIG without fault ride through (FRT) device*– Only the DFIG without any FRT device is connected at bus 14.
- *Case #2: DFIG with D-STATCOM as FRT device*– DFIG-based wind turbine power unit with D-STATCOM as FRT device is connected at bus 12.

In order to analyze the dynamic stability for the two cases, a 3- ϕ line-to-ground (3L-G) fault is simulated on line 8–9 at $t = 2$ s, and is cleared after 150 ms (7.5 cycles).

5.3.2.1 Dynamic Stability Analysis Under Symmetrical (3L-G) Fault

Figs. 5.11 shows the dynamic response of DFIG-base wind turbine at the MDN-IITG integrated point. The terminal voltage at buses 12 & 14, electrical torque, rotor, rotor position, rotor speed, slip, active and reactive power generated by the DFIG are presented in the presence of 3L-G fault.

Figs. 5.11(a) and 5.11(b) shows the DFIG terminal voltage response at buses 12 & 14 under small disturbances. Without any current limiter (WCL), the DFIG terminal voltage goes almost zero right after a fault and continues to remain at that voltage level until the circuit breakers open. With the presence of D-STATCOM, which is connected to the system at bus 12, it is observed that the voltage profile improves. However, the improvement in the voltage profile of other buses is based on the proximity of the bus to the bus where the D-STATCOM is connected *i.e.*, the buses which are nearer

5. Impact of Integration of Wind Energy into the Micro-Grid

to the bus to which D-STATCOM have more improvement in the voltage profile as compared to far end buses.

The electromagnetic torque fluctuation causes a continuous and considerable amount of increment in the rotational speed of the DFIG. The dynamic electrical torque response of the DFIG wind turbine is shown in Fig. 5.11(c). The negative peak of the electrical torque falls to 0.02 N·m and the positive peak goes to 1.3 N·m in Case #1, moreover, the negative peak of the electrical torque improves to 0.6 N·m and positive peak comes to 0.9 N·m in Case #2. Using D-STATCOM, the electromagnetic torque values do not exceed the widely used safety margin typically specified for the practical DFIG system.

Fig. 5.11(d) shows the response of the actual rotor position. It is observed that there are some oscillations in the rotor position during 2–4 s. The actual rotor speed curves of the DFIG for both cases are shown in Fig. 5.11(e). It is observed that the machine speed of the DFIG with the D-STATCOM controller has lower oscillation compared to Case #1.

Fig. 5.11(f) shows the deviation of the slip of the DFIG under both cases. In Case #1, the slip fluctuates up 30%, while in Case #2, the deviation of the slip value is limited to 20%, which is just 4% more than its steady-state value of DFIG.

Fig. 5.11(g) shows generated active power by the DFIG in both cases. In Case #1, the DFIG active power goes to zero right after the fault, but with the use of D-STATCOM the generated active power during the fault is maintained close to its pre-fault condition.

In a normal situation, the total reactive power generated by the DFIG is 0.3 p.u. While during the fault, the generated reactive power varies from -0.5 p.u. to 1.2 p.u. However, after connecting the D-STATCOM, the reactive power of the DFIG varies from 0.01 p.u. to 0.5 p.u., as shown in Fig. 5.11(h).

Hence, it can be said that with the presence of FRT (*i.e.*, the D-STATCOM) the oscillations decays much faster, thus, improving the stability of the power system.

Figs. 5.12(a)-5.12(h) shows the bus terminal voltage with and without D-STATCOM of Case #1 & 2 under a 3L-G fault. From Fig. 5.12(a), it is observed that with D-STATCOM there is much better regulation of the voltages of the buses. Moreover, it is also observed that under fault conditions, the D-STATCOM controller is much more effective in controlling the voltage profile of the buses which are near to the D-STATCOM as compared to the remote buses.

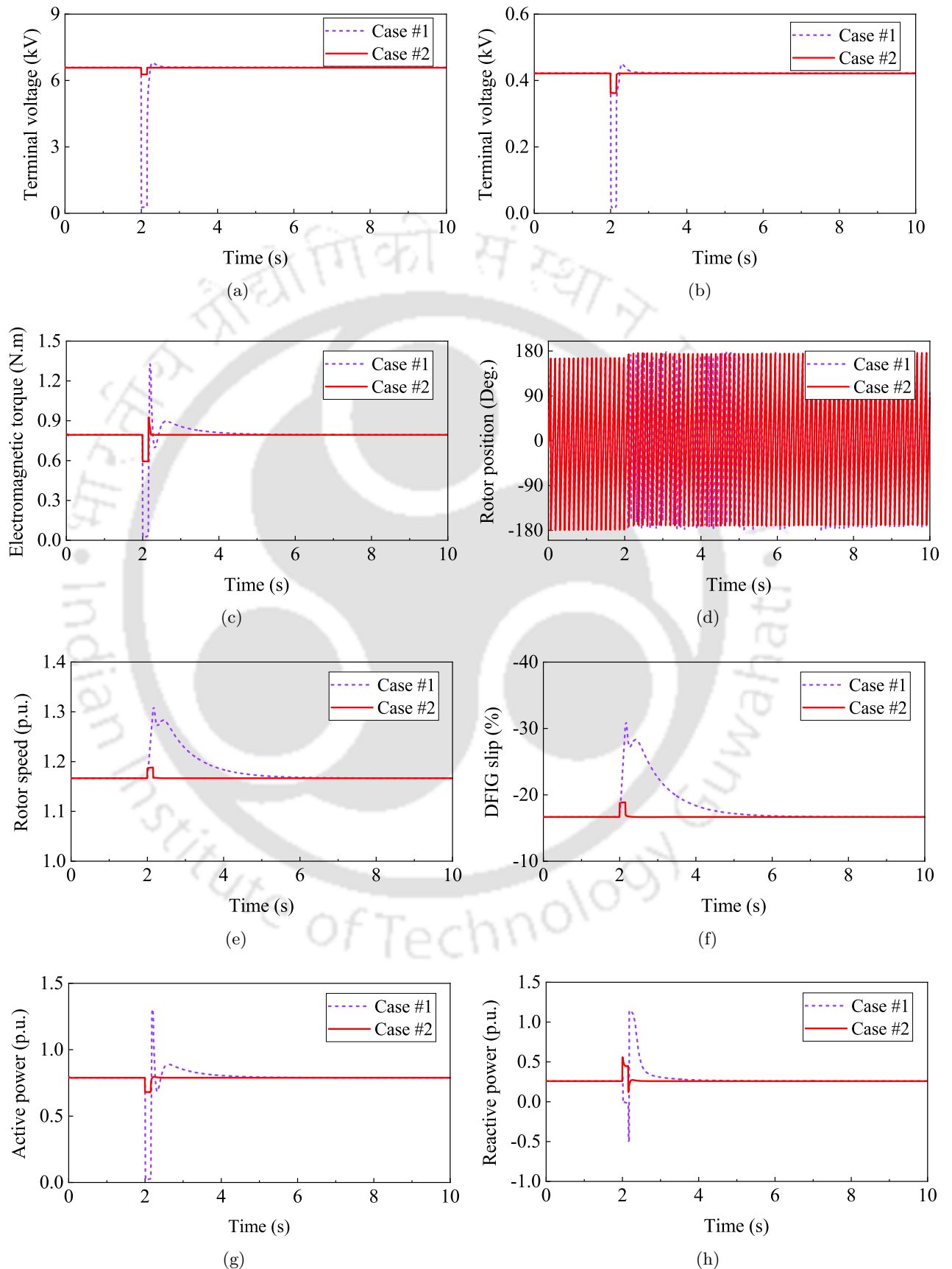


Fig. 5.11: The DFIG system with and without STATCOM device in the MDN-IITG test system (a) terminal voltage at bus 12; (b) terminal voltage at bus 14; (c) electromagnetic torque; (d) rotor position; (e) rotor speed; (f) DFIG slip; (g) active power; (h) reactive power.

TH-3228_11610226

5. Impact of Integration of Wind Energy into the Micro-Grid

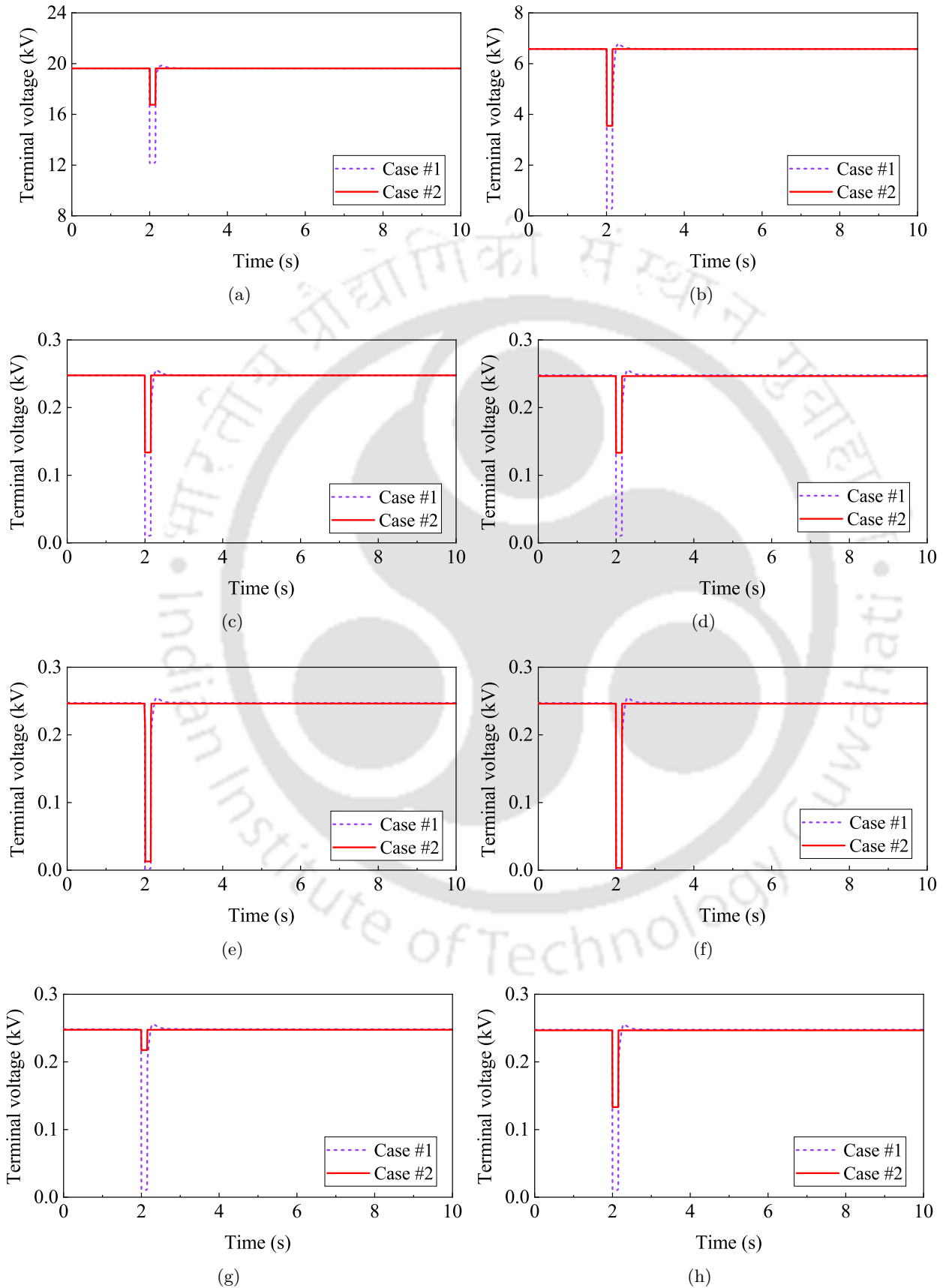


Fig. 5.12: The terminal voltage of the DFIG-WT in the MDN-IITG test system for Case #1 & 2 (a) at bus 1; (b) at bus 3; (c) at bus 6; (d) at bus 7; (e) at bus 10; (f) at bus 11; (g) at bus 13; (h) at bus 20

Figs. 5.13(a)-5.13(e) shows the power flow in the lines under both the cases for a 3L-G fault. From the figure, it is observed that the active power supply from the DFIG during the 3L-G fault is significantly improved with the use of the D-STATCOM.

Therefore, it can be concluded that D-STATCOM plays an active role to suppresses both the fault current and power fluctuation in the MDN-IITG.

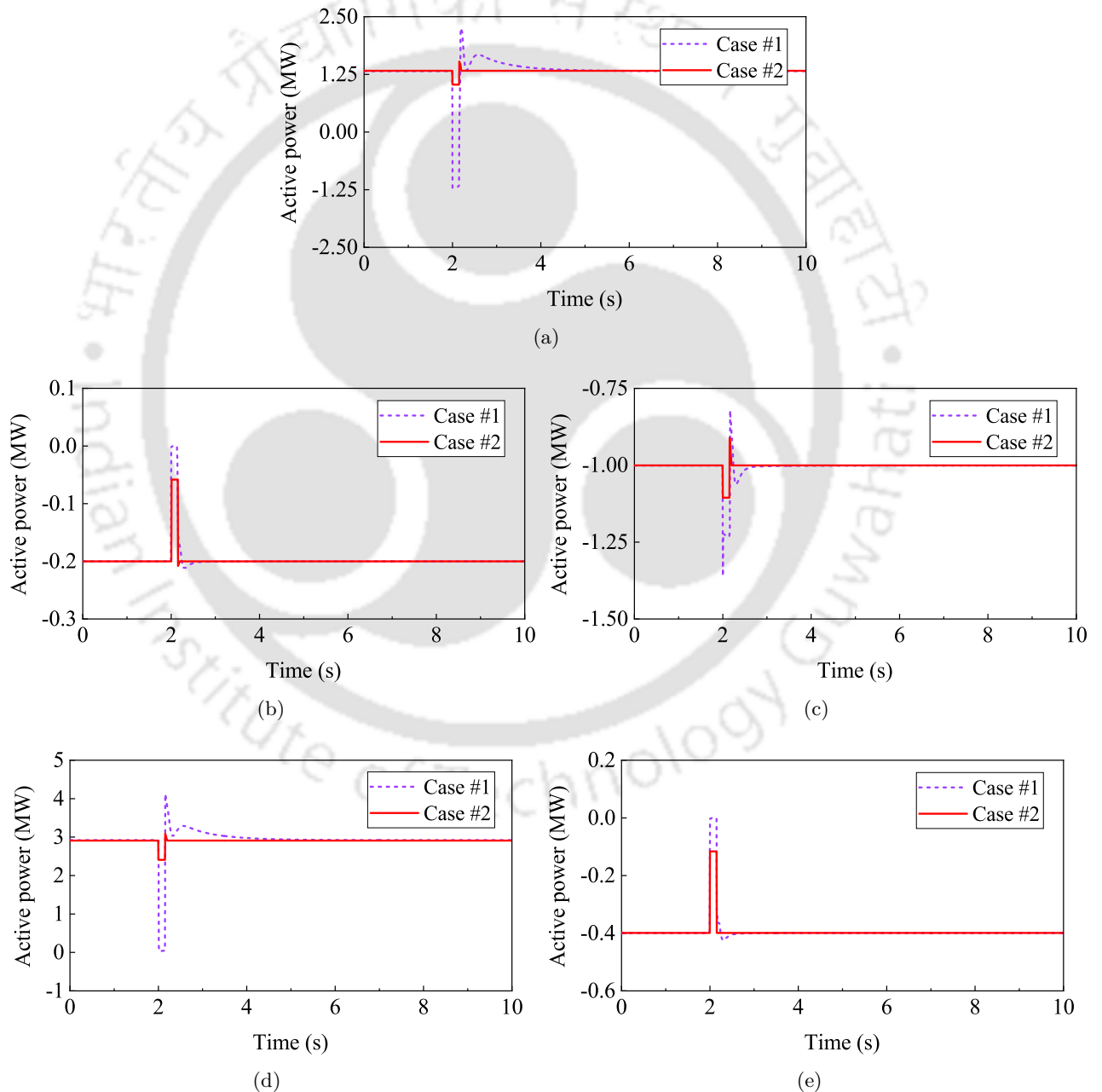


Fig. 5.13: The power flow in the MDN-IITG test system for Case #1 & #2 (a) line flow 1–2; (b) line flow 3–4; (c) line flow 3–8; (d) line flow 3–12; (e) line flow 3–15.

5.4 Summary

A modified distribution network of IIT Guwahati (MDN-IITG) test system is developed to investigate the potential challenges of integrating wind energy as a distributed generation into the network. The networks combine the graphical user interface of Siemens PTI PSS@Sincal software with the computing power of Siemens PTI PSS@NETOMAC program library. They are available as macros, linked to a network defined in Siemens PTI PSS@Sincal. The main potential challenges are voltage variations and poor power flow of the distribution network.

In this chapter, it is observed that integration of D-STATCOM increases the stability of the MDN-IITG *i.e.*, it improves voltage deviation and power regulation of the network. The dynamic simulations are performed to analyze the impacts of DFIG with D-STATCOM integration into the network. Moreover, the D-STATCOM device controller suppresses the fault current, compensates for the voltage dip, smoothing the power fluctuation, and accelerate the whole recovery process for the DFIG-based wind turbine. The outcome of the work is to be utilized as a guideline to the utilities for integrating renewable energy based distributed generation into the distribution network.

6

Impacts of Wind Power Penetration on Dynamic Stability of Power System

Contents

6.1	Introduction	140
6.2	Description of Test Cases	142
6.3	Results and Discussion	144
6.4	Summary	150

Objective

This chapter analyzes the impact of the integration of wind power generators. Here, a conventional synchronous generator is replaced by a doubly-fed induction generator (DFIG) of the same power ratings. Further, a static synchronous compensator (STATCOM) is also connected along with the DFIG to augment the reactive power support. The system utilized for the study is the reduced North Eastern Regional Electricity Board of 29-bus (NEREB-29) Indian power system. The simulations are performed using the Siemens PTI PSS@Sincal software.

6.1 Introduction

Several work has been done recently to observe the impacts of large-scale integration of different wind power generators on dynamic stability study [85,201–203]. The impact of wind generators on the oscillation and damping has been calculated after replacing the SG from IG (either FSWT or VSWT) [88,89]. The effects of electro-mechanical mode has been evaluated [89]. The impact due to penetration of wind power generators on electro-mechanical and voltage state has been analyzed [204,205]. The limits on the voltage stability with different wind generators integration and its replacement have been presented in [89,206]. After fault occurrence, the load attributes are closely related to voltage instability [207,208]. The impact of large-scale DFIG based integration into the wind parks on power systems for dynamic stability has been studied [209]. The dynamic stability can be improved with the use of a DFIG to some extent [85,210], but during a fault, the DFIG behaves as a conventional IG with an increase in rotor resistance [90], hence, losing its effectiveness in improving the stability of the system. The large-scale wind parks connected through the long transmission line often result in the formation of a weak grid which further reduces the stability of the system [211].

The DFIG can control its reactive power to operate at a given power factor or can be set on voltage control mode. However, the voltage control capability of DFIG is comparatively less compared with the synchronous generator. Thus, the stability of the power system is affected when the controller could not control voltage to its reference value in a DFIG-based WECS [85].

The reactive power of the DFIG can be enhanced by increasing the size of the converters. However, this solution increases the overall cost, which is one of the main advantages of DFIG over the full power converter-based interface of the wind turbines [86]. The effect of reactive power supplied by wind generation on the rotor angle stability is examined [87]. The study concludes that the transient

stability could be improved, and the oscillations damped more quickly if the terminal voltage of the wind generation is controlled. Furthermore, the synchronous generator rotor angle is influenced by the control strategy utilized by wind generators.

The transient stability can be improved by some level when a DFIG system replaces a specified synchronous generator [85]. However, the DFIG behaves as a conventional induction generator under fault conditions [90]. The generator types used in wind turbines do not participate in power system oscillations. Instead, the wind power penetration will have a damping effect due to a reduction in the size of synchronous generators that engage in power system oscillations [89]. The increased wind power penetration is accompanied by congestion at weak interconnection lines, leading to reduced damping [91].

As a consequence, some transmission lines are heavily loaded and the system stability becomes a power transfer limiting factor. With the continuous increase in wind power penetration into power systems, power system stability becomes a very important issue which needs to be properly investigated. The FACTS controllers are used for solving various power system control problems such as enhancing power system stability and power flow control [212]. The dynamic stability is concerned with small disturbances lasting for a long time with automatic control devices.

This chapter addresses the detailed of dynamic stability of power system when replacing a conventional SG by a aggregated DFIG wind turbine of the same size. The main objective is to improve rotor angle stability, as it maintain equilibrium between electromagnetic and mechanical power of each generators in the power system. Integration of the wind turbine generator such as DFIG to reduced NEREB Indian power grid. The simulation is perform under 3- ϕ line-to-ground (3L-G) fault on the transmission line using Siemens PTI PSS@Sincal package [213].

The rest of this chapter is organized as follows. In this chapter, the impacts of wind power penetration on power system dynamic stability based on NEREB of India grid in which replacing SG with the DFIG wind turbine has been studied. Section 6.2 gives a full description of the test cases utilized for the simulation. Simulation results and discussion are presented in the Section 6.3, and lastly conclusions are drawn in Section 4.7.

6.1.1 Stability Evaluation Index

The typical dynamic stability studies are based on rotor angles measurement relative to a synchronous rotating reference frame. It has been considered as one of the parameters to test the stability

of the system. The extremity of a contingency of the system after a small disturbance can be assessed by evaluating the dynamic stability index (I). The I is obtained into reduced NEREB Indian power system using Siemens PTI PSS®Sincal software.

$$I = \frac{360^\circ - \delta_m}{360^\circ + \delta_m}, \quad -100^\circ < I < 100^\circ \quad (6.1)$$

thus, $I > 0$, correspond to stable condition

and $I \leq 0$, correspond to unstable condition

where, δ_m is the maximum angle difference between any two generators in the system after fault at same time. The main purpose of dynamic stability analysis to investigate when system is disturbed by the small disturbance to analyze the dynamic stability. If the operating δ_m is initially large and close to the stability limit index but SG at the two ends of the line may lose his synchronism with respect to each other after fault occurs.

6.2 Description of Test Cases

To analyze the stability, the dynamic analysis is done on the reduced NEREB Indian power system. To simulate the above systems, the authors have used the Siemens PTI PSS® Sincal software.

6.2.1 Reduced NEREB Indian Power System

A 54-synchronous machines, 232-bus NEREB of Indian grid is reduced to an equivalent 16-synchronous machines, 29-bus system. The single line schematic diagram of reduced NEREB Indian power system with DFIG based wind turbine is shown in Fig. 6.1. The reduced equivalent system includes 16 unit of synchronous machines, 14 loads and 25 transmission line (*i.e.*, all transmission lines in this study are of similar type) with total generation of 3536.8 MW [214]. In this work, the authors have replaced the SG plant of 165 MW, -36 MVar placed at bus 6715 with a wind power plant of same capacity consisting of an equivalent DFIG model from library of Siemens PTI PSS® Sincal to observe the effectiveness of wind generation into the system.

In this study, all SG are represented using a six-order model, with magnetic saturation neglected, the test case system with governor and excitation controls has been used to initially model of generators. Here, during the faults, the generators input has been assume to be constant. The dynamic model of SGs at buses 6145, 6146, 6504, 6506, 6509, 6636, 6640, 6643, and 6700 is a round rotor

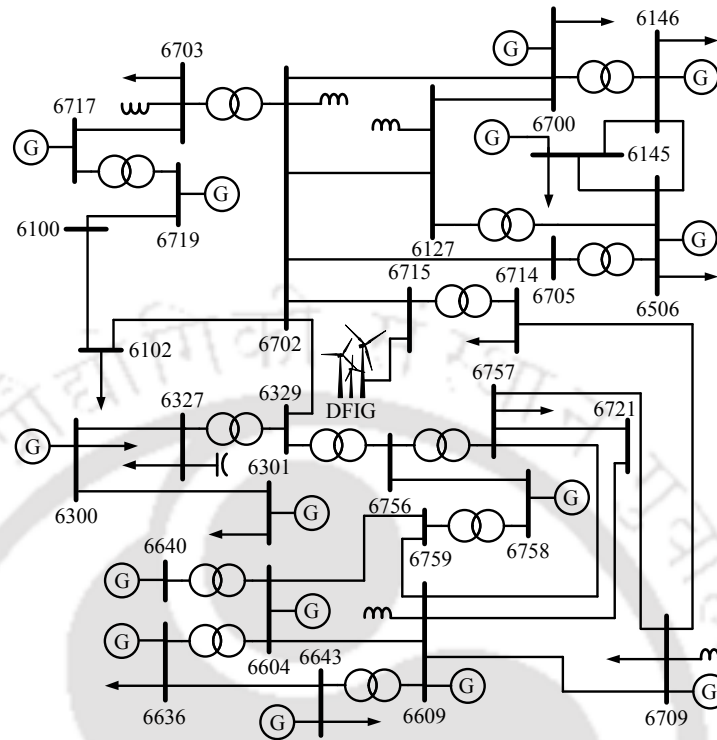


Fig. 6.1: One-line diagram of reduced NEREB Indian power grid with DFIG system.

generator, similarly, for buses 6300, 6301, 6709 and 6715 and at buses 6717 and 6719. The exciter system at buses 6145, 6146, 6300, 6301, 6504, 6506, 6509, 6636, 6640, 6643, 6715, 6717 and 6719 is *IEEET1* type, while at buses 6700 and 6709 is *IEEET2* type model. The turbine governor of all SGs are modeled by a standard gas turbine model. The loads are represented by P and Q scaled type to observe the effect of the loads dynamic characteristics. The dynamic model of a wind plant used for the DFIG system consists of *WT3G1*, electrical control model is *WT3E1*, turbine model is *WT3T1* and pitch control model is *WT3P1* from dynamic model library of PSS/E for dynamic simulations.

Simulation studies have carried out to demonstrate and compared the dynamic performance of reduced NEREB system with and without wind power integration as shown in Fig. 6.1 using Siemens PTI PSS® Sincal software. To evaluate system dynamic stability performance, the 3L-G fault occurs on line corresponding to buses [6757–6709] which is 132 kV on 40% distance from the bus 6757 at $t = 2$ s with fault duration of 150 ms (7.5 cycles) is simulated. The selected fault impedance with resistance of 0.5Ω . A base case study has been carried out on the original reduced NEREB Indian with out DFIG. This is used as an reference for the comparative studies.

6.3 Results and Discussion

The simulation results related to the dynamic stability analysis of a reduced NEREB Indian grid with wind power integration are presented in this section. The simulation uses DFIG with crowbar protection for the integration of wind power into the grid. The parameters of the DFIG are taken from [215] and are presented in Appendix F. Three cases are used to study the dynamic analysis, which are presented as given below:

- i) **Case #1:** It represent a case with conventional synchronous generators (SGs). It acts as a base case to observe the impact of wind energy integration.
- ii) **Case #2:** The system with wind power penetration *i.e.*, replacing a conventional SG by aggregated DFIG based WECS.
- iii) **Case #3:** The system with wind power penetration *i.e.*, replacing a conventional SG by aggregated DFIG based WECS along with a STATCOM.

6.3.1 Dynamic Stability on Reduced NEREB Indian Power System

On bus 6715, a DFIG is placed as a “load flow type” with a rated active power of 165 MW and a rated reactive power of 36 MVAR at a slip of -16% . For dynamic simulation, a 3L-G fault is applied on the 132 kV line [6757–6709] and is cleared after 7.5 cycles.

6.3.1.1 Terminal Voltage of Generators

Fig. 6.2 shows the terminal voltages of 15 numbers of synchronous generators connected in a reduced NEREB Indian power system. It is observed that the generators which are close to bus 6715 (*i.e.*, the bus to which DFIG is placed) such as buses 6506, 6145, 6146, 6700, 6717, and 6719 show significant improvement in terminal voltage profile during fault for Case #3 *i.e.*, the one with STATCOM. Further, the terminal voltage of generator falls to 0.84 p.u. in Case #1 at bus 6145 during the fault and recovered quickly to its normal value after fault is cleared. However, in Case #2, the terminal voltage falls to about 0.8 p.u. during fault. However, the DFIG with STATCOM *i.e.*, Case #3, the terminal voltage rise to about 0.92 p.u. during the fault. Hence, it may be concluded that STATCOM may play a significant role in improving the voltage stability of the system.

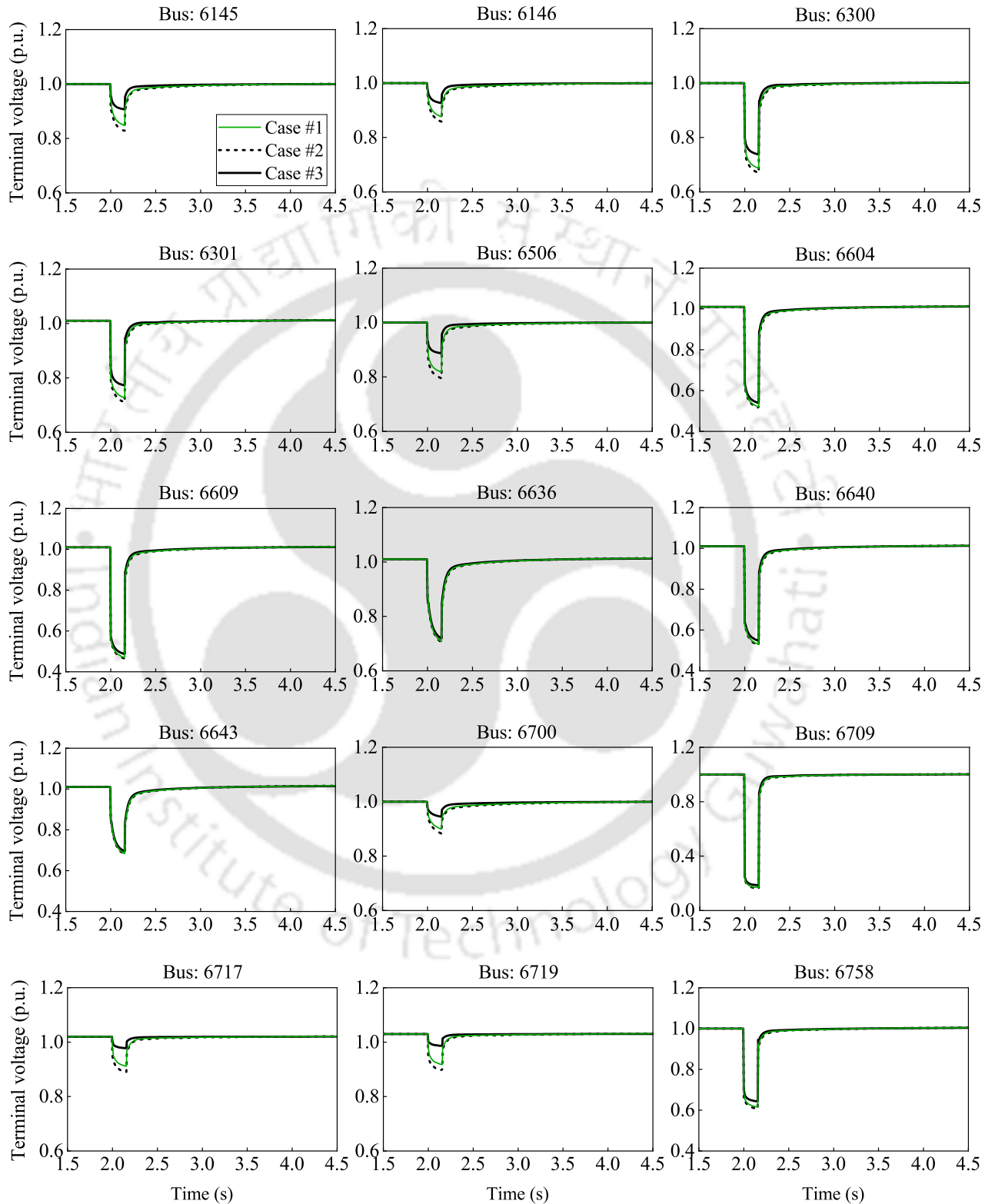


Fig. 6.2: The terminal voltage of generators at different buses into reduced NEREB Indian power system for Case #1, #2 & #3

6.3.1.2 Rotor Angle of Generators

Fig . 6.3 shows the oscillations of the rotor angles of SG connected in the reduced NEREB Indian system. The rotor angle of the generator deviates from 36.9° to 39.2° in Case #1 at bus 6145 during the fault and recovered to its normal value after the fault is cleared. However, in Case #2, the rotor angle deviates from 36.4° to 40.2° during the fault. In Case #3, the rotor angle deviates from about 37.2° to 38.9° during the fault. The magnitude of deviation of the rotor angle in Case #1 & #3 is slightly lower compared to Case #2. It is further observed that the deviation of the rotor angle of the synchronous generator is minimum for Case #3 *i.e.*, the DFIG with STATCOM. Hence, it may be said that the STATCOM significantly improves the stability of the system.

6.3.1.3 Rotor Speed of Generators

Fig. 6.4 shows the rotor speed of the synchronous generators. The rotor speed of the generator deviates from 0.9996 p.u. to 1.0007 p.u in Case #1 at bus 6145 during the fault and recovers to its normal value after the fault is cleared. However, in Case #2, the rotor speed of the generator deviates from 0.999 p.u. to 1.0015 p.u during the fault. In Case #3, the rotor speed of the generator deviates from about 0.9998 p.u. to 1.0004 p.u during the fault. From the figure, it is observed that rotor speed oscillations of the synchronous generator settle down in 3 s in Case #3. This is mainly due to the STATCOM dynamic reactive power support, which suppresses the rotor speed oscillations of the synchronous generators. From the figure, it can be observed that rotor speed oscillations settle down to the pre-fault steady-state value of 1.001 p.u. and stabilized with a settling time of 1 s. Hence, it can be concluded that STATCOM help in reducing the speed deviation by providing proper reactive power support.

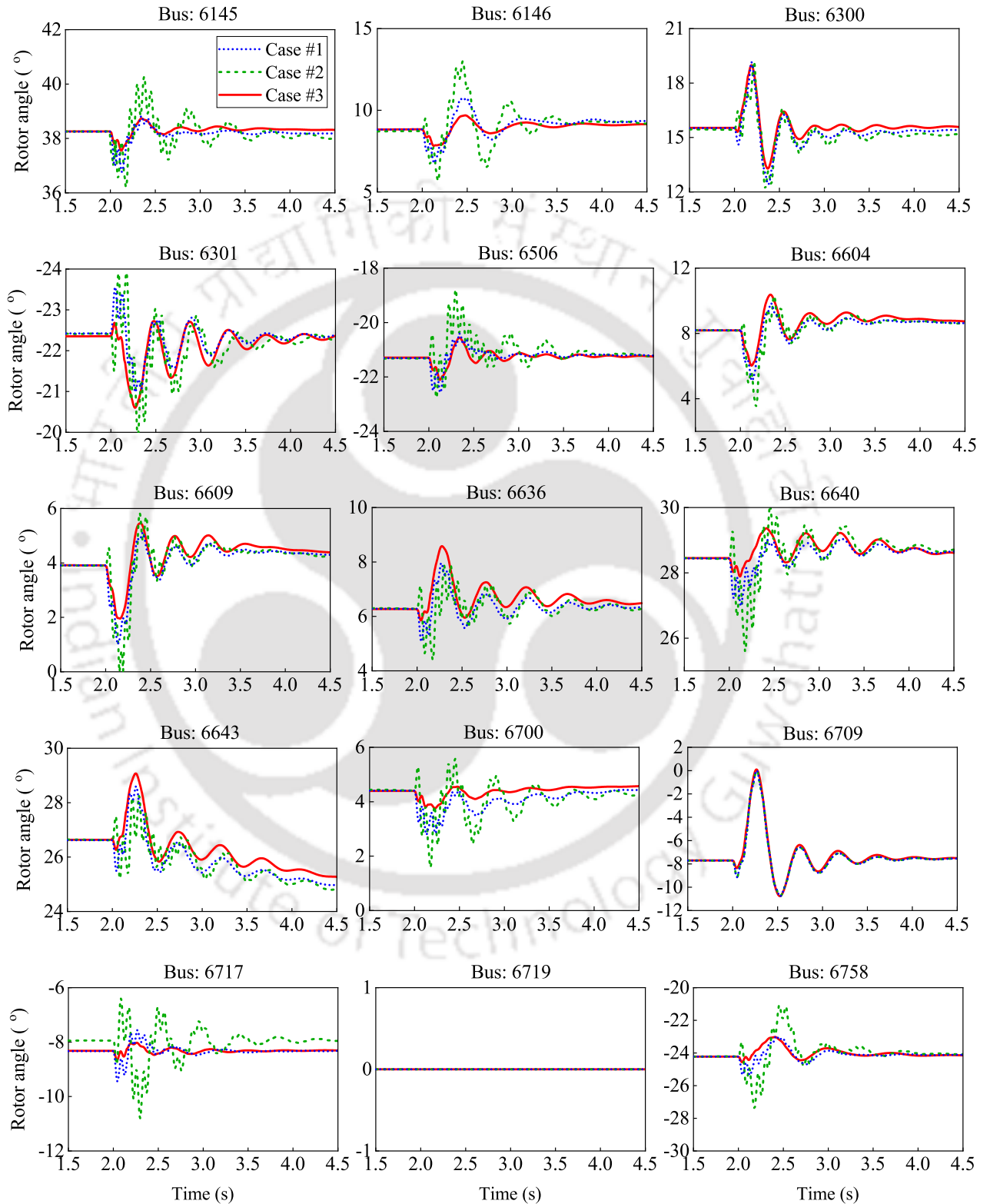


Fig. 6.3: The rotor angle of synchronous machine at different buses of the NEREB test system for Case #1, #2 & #3

6. Impacts of Wind Power Penetration on Dynamic Stability of Power System

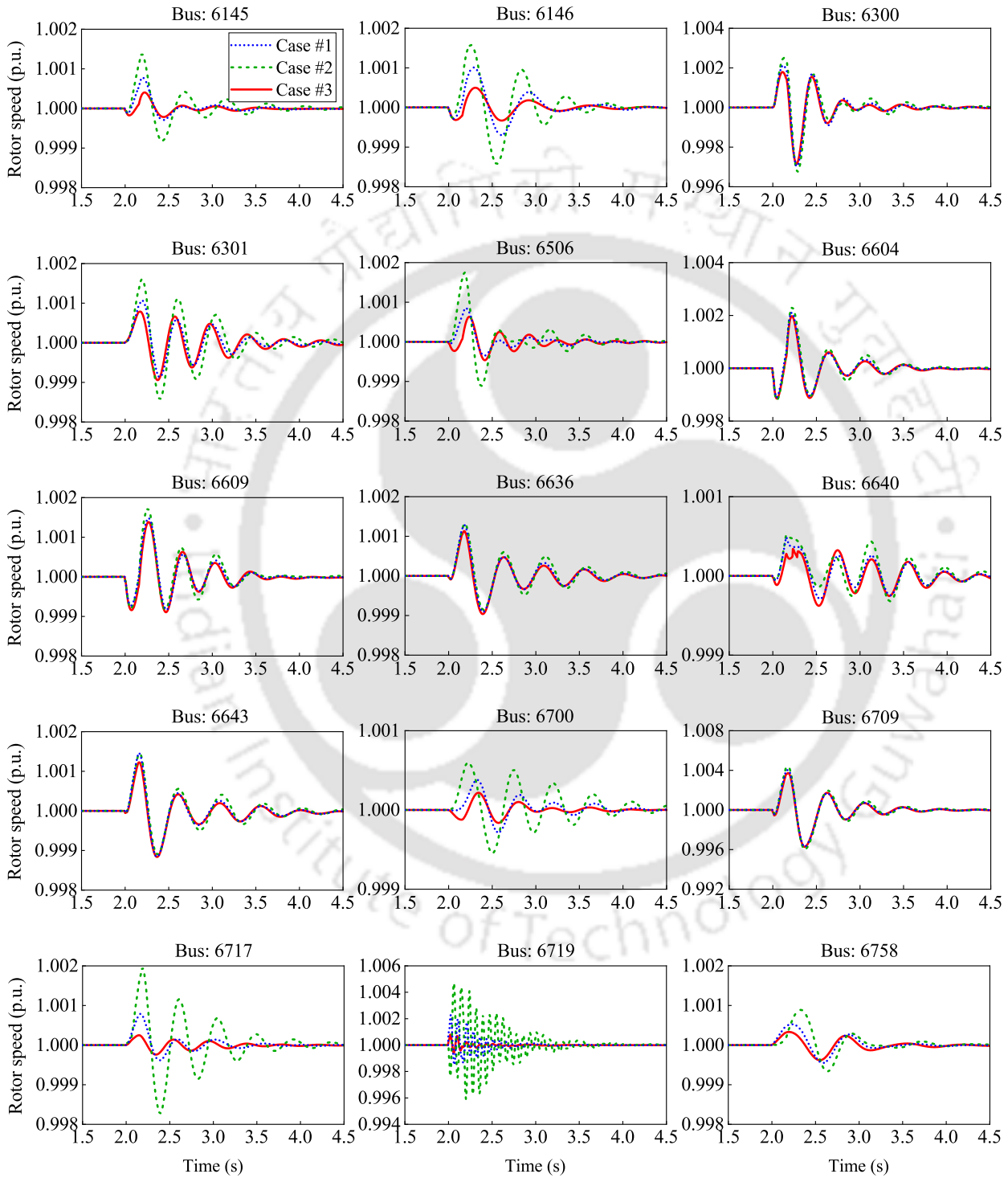


Fig. 6.4: The rotor speed of synchronous machine at different buses of the NEREB test system for Case #1, #2 & #3

Table 6.1: Stability index at different buses.

Bus Number	Case #1			Case #2			Case #3		
	Pre	During	Post	Pre	During	Post	Pre	During	Post
6145	0.7265	0.5579	0.721	0.7255	0.5114	0.7111	0.7301	0.6339	0.7313
6146	0.8317	0.5518	0.8711	0.8314	0.5019	0.8617	0.8329	0.6629	0.8878
6300	0.7081	0.3406	0.7558	0.6834	0.2926	0.7214	0.7484	0.4369	0.7941
6301	0.5527	0.0718	0.5666	0.5516	0.0674	0.5662	0.5589	0.0817	0.5678
6506	0.0098	0.1103	0.1681	0.0087	0.0725	0.1282	0.0186	0.1214	0.1853
6604	0.8011	0.0448	0.8732	0.8010	0.0313	0.8186	0.8197	0.0571	0.8809
6609	0.8377	0.4701	0.8863	0.8371	0.4546	0.8768	0.8381	0.4993	0.8893
6636	0.6692	0.0026	0.6786	0.6624	0.0032	0.6633	0.6755	0.0035	0.6849
6640	0.8515	0.0152	0.8575	0.8486	0.0111	0.8566	0.8546	0.0318	0.8588
6643	0.7399	0.0398	0.7399	0.7382	0.0321	0.7351	0.7460	0.0510	0.7530
6700	0.9262	0.8399	0.9358	0.9252	0.8228	0.9139	0.9291	0.9075	0.9418
6709	0.5499	0.9948	0.9963	0.5338	0.9938	0.9945	0.5548	0.9952	0.9971
6715*	0.7905	0.1073	0.8044	—	—	—	—	—	—
6717	0.6888	0.1502	0.6933	0.6855	0.0584	0.6837	0.7208	0.5421	0.7219
6719	0.5782	0.2626	0.5906	0.5204	0.1634	0.5297	0.6450	0.5277	0.6456
6758	0.8198	0.1854	0.8989	0.7558	0.1588	0.8977	0.8568	0.1901	0.9180

6.4 Summary

This chapter presents, the impact of wind power integration in a reduced NEREB Indian power grid. From the dynamic simulation, it is observed that for Case #2 (*i.e.*, replacing a conventional synchronous generator (SG) by aggregated DFIG based WECS) there is a significant deviation in the terminal voltages of synchronous generators during fault as compared with Case #1 (*i.e.*, without any wind generator). Similarly, more deviation in the rotor angle and speed of the SGs are observed for Case #2 as compared with Case #1. But with the use of STATCOM with DFIG *i.e.*, in Case #3, there is a significant improvement in voltage deviation at the terminal of SGs. Similarly, much less deviation in the rotor angle and speed of the SGs are observed in Case #3. Hence, it may be concluded that DFIG with STATCOM may be a suitable choice for wind power integration.

7

Summary and Conclusions

Contents

7.1	Important Findings	152
7.2	Contributions	154
7.3	Future work	155

Objective

This chapter provides the important findings of the present work. It also summarizes the important contribution of the thesis and finally discuss the future scope of the work.

7.1 Important Findings

In Chapter 2, a computational fluid dynamics (CFD) model (2-D) is developed to study the aerodynamic efficiency of NACA 63-415 and NACA 63-412 airfoils at a different angle of attack. For computational analysis, the Reynolds-averaged Navier-Stokes (RANS) equations with three different turbulence models such as shear stress transport $k-\omega$ (SST), realizable $k-\epsilon$ (RKE), and standard $k-\epsilon$ (SKE) models are used to analyze the fluid flow over the airfoils. The simulation results for NACA 63-412 airfoil obtained from different turbulence models are compared with Xfoil solver, whereas the simulation results obtained for NACA 63-415 airfoil are compared with the experimental data available in the literature. From the present computational analysis, the following significant findings are drawn:

- (i) The computational fluid dynamic analysis shows that the SST model provides results that are closer to the Xfoil solver and experimental data. Therefore, the SST model is used to for finding the optimum angle of attack.
- (ii) With the increase of angle of attack, initially, the lift coefficients increase, but this increase is till the angle of attack of 14° for NACA 63-415, whereas for NACA 63-412 it increases till 13° . After these angles, the lift coefficient decreases. Regarding the drag coefficients, it increases linearly till the angle of attack is approximately equal to 5° . However, after this angle, there is an exponential rise in the drag coefficient.
- (iii) The optimum angle of attack which corresponds to maxima of sliding ratio is observed at an angle of attack of $\alpha \simeq 6^\circ$ for NACA 63-415 airfoil, and at $\alpha \simeq 5^\circ$ for NACA 63-412 airfoil with the wind speed of $v_o = 7$ m/s.
- (iv) From the pressure coefficient (C_p) distribution curves, it is observed that the difference of pressure coefficient increases as the angle of attack increases up to the optimum angle of attack, and it is significantly higher on the leading edge than trailing edge.
- (v) The computational results of the velocity gradient and pressure contours for different turbulence models are compared.

Chapter 3 uses the optimal rotor theory to design the blade geometries such as chord length, and

twist angle along the radial span. The steady-state aerodynamic performance such as torque and power coefficients (*i.e.*, C_Q and C_P) of the wind turbine is calculated using the blade element momentum (BEM) theory. Further, the computational fluid dynamics (CFD) simulations are carried out using ANSYS/Fluent to get the aerodynamic performance. Since, the CFD simulations take significant computational time, hence, the Chapter 3 proposes a second-order transfer function that uses BEM theory results to get parameters related to the steady-state torque. Further, the other parameters of the model such as natural frequency and damping ratio are calculated based on the available literature in this area. Finally, the comparison of the CFD simulation and the torque response by the transfer function are compared. It is observed that the developed transfer function could approximately model the dynamic behavior of the wind turbine at a particular wind speed.

In Chapter 4, a thyristor-based bridge-type non-superconducting fault current limiter (ThyBT-NSFCL) is designed with a buck converter to enhance its fault ride-through (FRT) capability and tested with the doubly-fed induction generator (DFIG) system. The critical findings from the simulated results are as follows:

- The analytical analysis of the proposed ThyBT-NSFCL circuit operation is demonstrated for both normal and fault conditions with the symmetrical fault. The presented simulation results show a good and acceptable agreement with the analytical analysis of circuit operation.
- The design procedure of the current limiting parameter values/ratings of the ThyBT-NSFCL for the satisfactory operation is discussed.
- The ThyBT-NSFCL performs better under fault conditions to improve the FRT capability of the wind energy system (WES) in various aspects, and it helps to meet the grid code requirements of connecting the DFIG system.
- The voltage dip at the terminal of the DFIG system is improved significantly with ThyBT-NSFCL compared to without any current limiter (WCL), series dynamic breaking resistor (SDBR), and switched impedance transformer-type non-superconducting fault current limiter (TT-NSFCL) protection device.
- The ThyBT-NSFCL significantly improves the fluctuation and pulsation of generated active power under fault conditions and circuit breaker opening instant.
- The effects of different breaking resistors at the machine terminal voltage are observed and found satisfactory voltage dip improvement.

7. Summary and Conclusions

- Additionally, the proposed ThyBT-NSFCL has a simple structure that is efficient and economical to utilize in the power system with the DFIG system.

In Chapter 5, a modified distribution network of IIT Guwahati (MDN-IITG) test system is developed to investigate the potential challenges of integrating wind energy as a distributed generation into the network. The networks combine the graphical user interface of Siemens PTI PSS@Sincal software with the computing power of Siemens PTI PSS@NETOMAC program library. They are available as macros, linked to a network defined in Siemens PTI PSS@Sincal. The main potential challenges are voltage variations and poor power flow of the distribution network. It is further observed that integration of D-STATCOM increases the stability of the MDN-IITG *i.e.*, it improves voltage deviation and power regulation of the network. The dynamic simulations are performed to analyze the impacts of DFIG with D-STATCOM integration into the network. Moreover, the D-STATCOM device controller suppresses the fault current, compensates for the voltage dip, smoothing the power fluctuation, and accelerate the whole recovery process for the DFIG-based wind turbine. This work may be utilized that the outcome of the work is to be utilized as a guideline to the utilities for integrating RE-based distributed generation into the distribution network.

In Chapter 6, the impact of wind power integration in a reduced NEREB Indian power grid. From the dynamic simulation, it is observed that for Case #2 (*i.e.*, replacing a conventional synchronous generator (SG) by aggregated DFIG based WECS.) there is a significant deviation in the terminal voltages of synchronous generators during fault as compared with Case #1 (*i.e.*, without any wind generator). Similarly, more deviation in the rotor angle and speed of the SGs are observed for Case #2 as compared with Case #1. But with the use of STATCOM with DFIG *i.e.*, in Case #3, there is a significant improvement in voltage deviation at the terminal of SGs. Similarly, much less deviation in the rotor angle and speed of the SGs are observed in Case #3. Hence, it may be concluded that DFIG with STATCOM may be a suitable choice for wind power integration.

7.2 Contributions

The major contributions of the research work reported in this thesis includes as follows:

- The aerodynamic loads and the flow physics over a particular blade profile are examined in detail to calculate the optimum angle of attack.
- The primary blade design, such as the optimum chord length and twist angle of the HAWT

blade, are calculated using optimal rotor theory.

- The numerical computational results are validated with the BEM theory for different airfoil profile-based wind turbines at various rotating conditions. This numerical technique takes too much computational resources and time, hence, an equivalent second-order transfer function model of HAWT is developed to estimate aerodynamic performance.
- The thesis includes the development of a cost-effective and efficient fault ride-through (FRT) technique. The proposed configuration effectively reduces the DC reactor conduction losses, thus, increasing its effectiveness.
- It includes a study on the impact of wind power generation on the stability of a microgrid. The network utilized for the analysis is the modified distribution network of IIT Guwahati (MDN-IITG). For the interface of wind power, a DFIG is used along with the D-STATCOM device.
- A study has been conducted to analyze the power system stability when the wind power is integrated into a reduced North Eastern Region Electricity Board (NEREB) 29-bus Indian power system. Further, the study includes the impact of integrating a STATCOM along with the DFIG in the system.

7.3 Future work

Based on the outcome of this thesis work, this section suggest some of the possible future research works.

- While finding the optimal angle of attack, the surface roughness of the blade can be also be included in subsequent studies *i.e.*, the study of flow patterns and how it influences the optimum angle of attack for different airfoil profiles.
- The CFD simulation in the present work used the Reynolds-averaged Navier–Stokes (RANS) equations, but the present work can be extended with Direct numerical simulation (DNS) for better resolution.
- In Chapter 3, an equivalent second-order transfer function model of HAWT is developed to estimate aerodynamic performance which even utilizes BEM theory to get the torque response. The work can be extended with the development of the artificial intelligence-based model.
- The work on the proposed fault ride-through (FRT) techniques may be extended with its

7. Summary and Conclusions

experimental validation.

- Chapters 5 and 6, include the stability analysis of the integration of wind energy on a microgrid and a reduced NEREB 29-bus Indian power system, respectively. The analysis may further include harmonic and other power quality issues.





A

Airfoil Data

Contents

A.1 Airfoil Coordinates Data	158
A.2 Boundary Conditions of Airfoil for the Numerical Simulations.	159

A.1 Airfoil Coordinates Data

Coordinates are shown in Tables A.2 and A.1 named airfoils specification of NACA 63-412 and NACA 63-415, respectively.

A.1.1 Profile of NACA 63-415 Airfoil Geometry Data for 2-D Simulation Modeling

The normalized coordinates of the NACA 63-412 and NACA 63-415 airfoils [3] are listed in Tables A.1 and A.1. The chord-wise dimensions (x) and thickness dimensions (y) are normalized by the chord length (c_r).

Table A.1: Coordinates of NACA 63-415 airfoil section.

Coordinate	Upper surface		Coordinate	Lower surface	
	x/c_r	y/c_r		x/c_r	y/c_r
1	0.00000	0.00000	27	0.00000	0.0000
2	0.00300	0.00700	28	0.01287	-0.01087
3	0.00525	0.00975	29	0.01585	-0.01305
4	0.00991	0.01509	30	0.02074	-0.01646
5	0.02198	0.02802	31	0.02964	-0.02220
6	0.04660	0.05340	32	0.04264	-0.03000
7	0.07147	0.07853	33	0.05261	-0.03565
8	0.09647	0.10353	34	0.06077	-0.04009
9	0.14669	0.15331	35	0.07348	-0.04656
10	0.19705	0.20295	36	0.08279	-0.05095
11	0.24750	0.25250	37	0.08941	-0.05361
12	0.29800	0.30200	38	0.09362	-0.05474
13	0.34852	0.35148	39	0.09559	-0.05439
14	0.39905	0.40095	40	0.09527	-0.05243
15	0.44955	0.45045	41	0.09289	-0.04909
16	0.50000	0.50000	42	0.08871	-0.04459
17	0.55039	0.54961	43	0.08298	-0.03918
18	0.60070	0.59930	44	0.07595	-0.03311
19	0.65093	0.64907	45	0.06780	-0.02660
20	0.70106	0.69894	46	0.05877	-0.01989
21	0.75109	0.74891	47	0.04907	-0.01327
22	0.80102	0.79989	48	0.03900	-0.00716
23	0.85085	0.84915	49	0.02885	-0.00193
24	0.90059	0.89941	50	0.01884	0.00184
25	0.95028	0.94972	51	0.00931	0.00333
26	1.00000	1.00000	52	0.00000	0.00000

Figs. A.1 and A.2 shows the section geometric shapes.

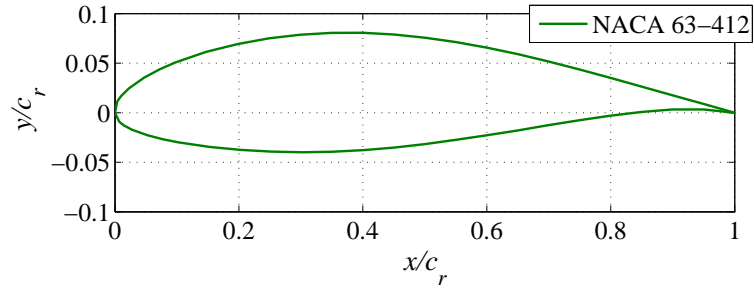


Fig. A.1: Geometric shape of NACA 63-412 airfoil section [3].

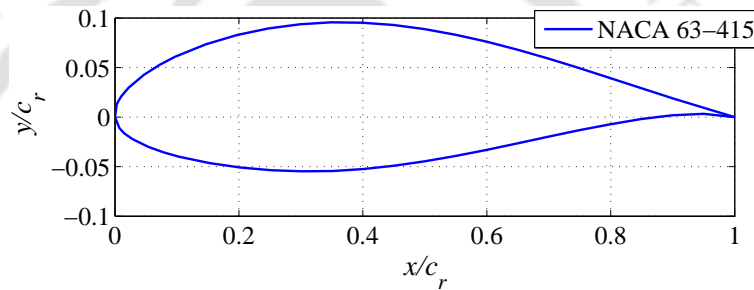


Fig. A.2: Geometric shape of NACA 63-415 airfoil section [3].

A.2 Boundary Conditions of Airfoil for the Numerical Simulations.

The whole computational domain builds with specified BCs as shown in Fig. 2.6. Some initial inputs and computational conditions for the problems are chosen as given in Table A.3.

A. Airfoil Data

Table A.2: Coordinates of NACA 63-412 airfoil sections.

Upper surface			Lower surface		
Coordinate	x/c_r	y/c_r	Coordinate	x/c_r	y/c_r
1	0.00000	0.00000	27	0.00000	0.0000
2	0.00336	0.01071	28	0.00664	-0.00871
3	0.00567	0.01320	29	0.00933	-0.01040
4	0.01041	0.01719	30	0.01459	-0.01291
5	0.02257	0.02460	31	0.02743	-0.01716
6	0.04727	0.03544	32	0.05273	-0.02280
7	0.07218	0.04379	33	0.07782	-0.02685
8	0.09718	0.05063	34	0.10282	-0.02995
9	0.14735	0.06138	35	0.15265	-0.03446
10	0.19765	0.06929	36	0.20235	-0.03745
11	0.24800	0.07499	37	0.25200	-0.03919
12	0.29840	0.07872	38	0.30160	-0.03984
13	0.34882	0.08059	39	0.35112	-0.03939
14	0.39924	0.08062	40	0.40076	-0.03778
15	0.44964	0.07894	41	0.45035	-0.03514
16	0.50000	0.07567	42	0.50000	-0.03164
17	0.55031	0.07125	43	0.54969	-0.02745
18	0.60057	0.06562	44	0.59943	-0.02278
19	0.65076	0.05899	45	0.64924	-0.01799
20	0.70087	0.05153	46	0.69913	-0.01265
21	0.75089	0.04344	47	0.74911	-0.00764
22	0.80084	0.03492	48	0.79916	-0.00308
23	0.85070	0.02618	49	0.84930	0.00074
24	0.90049	0.01739	50	0.89951	0.00329
25	0.95023	0.00881	51	0.94977	0.00330
26	1.00000	0.00000	52	1.00000	0.00000

A.2 Boundary Conditions of Airfoil for the Numerical Simulations.

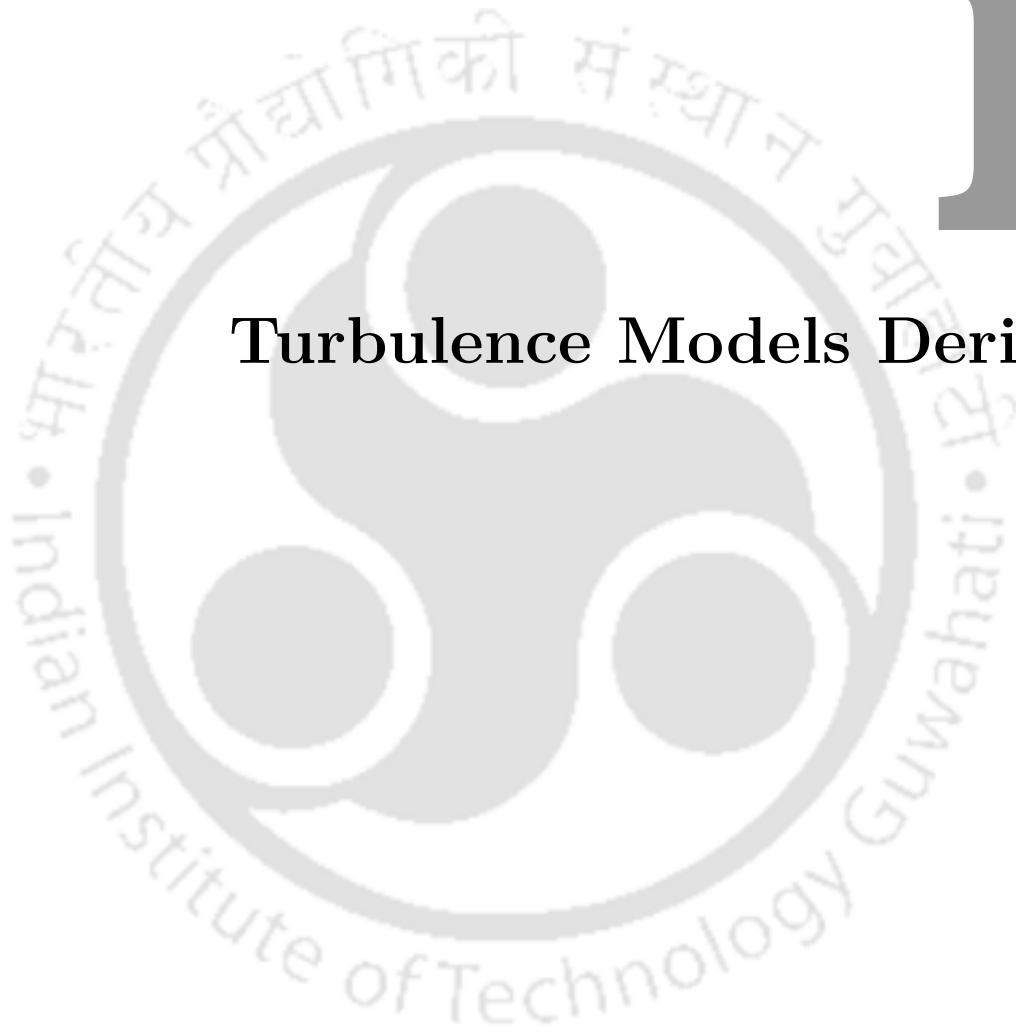
Table A.3: The boundary conditions of the 2–D airfoils for the numerical simulations [ANSYS USER GUIDE].

Parameter	Values
Airfoil	NACA 63-412 and NACA 63-415
Simulation type	Steady simulation
Turbulence model	SST, SKE and RKE
Fluid material	Air
Temperature	25°C
Dynamic viscosity	1.789×10^{-5} kg/m·s
Air density	1.225 kg/m ³
Flow type	Incompressible flow
INLET boundary condition	Flow velocity = 5, 7, 10, 15 & 20 m/s
OUTLET boundary condition	Gauge pressure = 0 Pa
CFD algorithm	Simple (Default option)
Interpolating scheme	Pressure-velocity coupling Least-squares cell based Pressure (Standard) Density (Second-order upwind) Momentum (Second-order upwind) Turbulent kinetic viscosity (Second order upwind) Specific dissipation rate (Second-order upwind)
Solution controls	Pressure: 0.55 Momentum: 0.52 Density: 1.2 kg/m ³ Turbulent kinetic energy: 0.65
Boundary condition	Velocity inlet (7 m/s) Pressure outlet (Gauge pressure: 0) Stationary wall with no-slip shear condition
Number of mesh cells	About 3,25,290 and 3,26,594
Force monitors	Lift and drag coefficients
Residual convergence value	1×10^{-6}



B

Turbulence Models Derivation



Contents

B.1 Turbulence Model Derivations	164
--	-----

B.1 Turbulence Model Derivations

In the present study, a brief theoretical overview of the turbulence flow models are characterized to solve the flow governing equations are as follow:

- Standard $k - \epsilon$ Model
- Realizable $k - \epsilon$ Model
- Shear-stress transport $k - \omega$ Model

B.1.1 Standard $k - \epsilon$ Model

The standard $k - \epsilon$ turbulence model is semi-empirical model based on model transport equation has been defined for the two-parameters that are being solved, the first is the turbulent kinetic energy (k) and second is the turbulent dissipation rate (ϵ) [216]. The model transport equation for k is derived from the exact equation, while the model transport equation for ϵ is obtained using the physical reasoning and bears little resemblance to its mathematically exact counterpart. The standard $k - \epsilon$ has become the workhorse of practical engineering flow calculations [217]. It is simplest of two-equation turbulence model in which the solution of 2-separate transport equation. Robustness, economy, and reasonable accuracy for a wide range of turbulent flows explain its popularity in industrial flow and heat transfer simulations. It is a semi-empirical model, and the derivation of the model equation relies on phenomenology considerations and empiricism.

In the derivation of the $k - \epsilon$ model, the assumption is that the flow is fully turbulent, and the effects of molecular viscosity are negligible. The standard $k - \epsilon$ model is therefore valid only for fully turbulent flows. The standard $k - \epsilon$ transport equations [218] are obtained as follow:

$$\frac{\partial}{\partial t}(\rho k) + \frac{\partial}{\partial x_i}(\rho k u_i) = \frac{\partial}{\partial x_j} \left[\left(\mu + \frac{\mu_t}{\sigma_k} \right) \frac{\partial k}{\partial x_j} \right] + G_k + G_b - \rho \epsilon - Y_M + S_k \quad (\text{B.1})$$

$$\frac{\partial}{\partial t}(\rho \epsilon) + \frac{\partial}{\partial x_i}(\rho \epsilon u_i) = \frac{\partial}{\partial x_j} \left[\left(\mu + \frac{\mu_t}{\sigma_\epsilon} \right) \frac{\partial \epsilon}{\partial x_j} \right] + C_{1\epsilon} \frac{\epsilon}{k} (G_k + C_{3\epsilon} G_b) - C_{2\epsilon} \rho \frac{\epsilon^2}{k} + S_\epsilon \quad (\text{B.2})$$

In (B.1) and (B.2), G_k represents the generation of turbulence kinetic energy due to the means velocity gradients, G_b represents the generation of turbulence kinetic energy due to buoyancy, Y_M represents the contribution of the fluctuating dilatation in compressible turbulence to all over dissipation rate, $C_{1\epsilon}$, $C_{2\epsilon}$, and $C_{3\epsilon}$ are constants. σ_k and σ_ϵ are user-defined source terms.

The turbulence (or eddy) viscosity, μ , is computed by combining for k and ϵ as follows:

$$\mu_t = \rho C_\mu \frac{k^2}{\epsilon} \quad (\text{B.3})$$

where, C_μ is a constant.

The model constants: $C_{1\epsilon} = 1.44$, $C_{2\epsilon} = 1.92$, $C_\mu = 0.09$, $\sigma_k = 1.0$, $\sigma_\epsilon = 1.3$

$$G_k = -\overline{\rho u'_i u'_j} \frac{\partial u_j}{\partial x_i} \quad (\text{B.4})$$

$$C_{3\epsilon} = \tanh \left| \frac{v}{u} \right| \quad (\text{B.5})$$

where, v is the component of the flow velocity parallel to the gravitational vector and u is the component of the flow velocity perpendicular to the gravitational vector.

$$Y_M = 2\rho\epsilon M_t^2 \quad (\text{B.6})$$

where, M_t is the turbulence Mach number, defined as:

$$M_t = \sqrt{\frac{k}{a^2}} = \sqrt{\frac{k}{vRT}} \quad (\text{B.7})$$

B.1.2 Realizable $k - \epsilon$ Model

The realizable $k - \epsilon$ model (1995) differs from the standard $k - \epsilon$ model in the following two ways:

- The realizable $k - \epsilon$ model contains a new formulation for the turbulence viscosity.
- A new transport equation for the dissipation rate, ϵ , has been derived from an exact equation for the transport of the mean-square vorticity fluctuation.

The term “realization” means that the model satisfies certain mathematical constraints on the Reynolds stresses, consistent with the physics of turbulent flows. An immediate benefit of the realizable $k - \epsilon$ model is that it more accurately predicts the spreading rate of both planar and round jets. It is also likely to provide superior performance for flows involving rotation, boundary layers under strong adverse pressure gradients, separation, and recirculation.

The realizable $k - \epsilon$ model proposed by [121] was intended to address these deficiencies of traditional $k - \epsilon$ models. One limitation of this model is that it produces non-physical turbulent viscosities in situations when the computational domain contains both rotating and stationary fluid zeros. This is due to the fact that the $k - \epsilon$ model includes the effect of mean rotation in the definition of the

B. Turbulence Models Derivation

turbulent viscosity.

The modeled transport equations for k and ϵ in the realizable $k-\epsilon$ model are:

$$\frac{\partial}{\partial t}(\rho k) + \frac{\partial}{\partial x_j}(\rho k u_j) = \frac{\partial}{\partial x_j} \left[\left(\mu + \frac{\mu_t}{\sigma_k} \right) \frac{\partial k}{\partial x_j} \right] + G_k + G_b - \rho \epsilon - Y_M + S_k \quad (\text{B.8})$$

$$\frac{\partial}{\partial t}(\rho \epsilon) + \frac{\partial}{\partial x_j}(\rho \epsilon u_j) = \frac{\partial}{\partial x_j} \left[\left(\mu + \frac{\mu_t}{\sigma_\epsilon} \right) \frac{\partial \epsilon}{\partial x_j} \right] + \rho C_1 S \epsilon - \rho C_2 \frac{\epsilon^2}{k + \sqrt{\nu \epsilon}} + C_{1\epsilon} \frac{\epsilon}{k} C_{3\epsilon} G_b + S_\epsilon \quad (\text{B.9})$$

where, $C_1 = \max \left[0.43, \frac{\eta}{\eta+5} \right]$, $\eta = S \frac{k}{\epsilon}$, $S = \sqrt{2 S_{ij} S_{ij}}$

The difference between the realizable $k-\epsilon$ model and standard $k-\epsilon$ model is that C_μ is no longer constant. It is computed from

$$C_\mu = \frac{1}{A_o + A_s \frac{k U^*}{\epsilon}} \quad (\text{B.10})$$

$$U^* = \sqrt{S_{ij} S_{ij} + \widetilde{\Omega}_{ij} \widetilde{\Omega}_{ij}} \quad (\text{B.11})$$

$$\widetilde{\Omega}_{ij} = \Omega_{ij} - 2 \varepsilon_{ijk} \omega_k \quad (\text{B.12})$$

$$\Omega_{ij} = \overline{\Omega}_{ij} - \varepsilon_{ijk} \omega_k \quad (\text{B.13})$$

where, $\overline{\Omega}_{ij}$ is the mean rate of rotation tensor in a rotating frame with the angular velocity ω_k .

The model constants, $A_o = 4.04$, $A_s = \sqrt{6} \cos \phi$, $\phi = \frac{1}{3} \cos^{-1} \left(\sqrt{6} \frac{S_{ij} S_{jk} S_{ki}}{S^3} \right)$, $\tilde{S} = \sqrt{S_{ij} S_{ij}}$, $S_{ij} = \frac{1}{2} \left(\frac{\partial u_j}{\partial x_i} + \frac{\partial u_i}{\partial x_j} \right)$

B.1.3 Shear-stress Transport $k-\omega$ Model

The shear-stress transport $k-\omega$ (SST) model was developed by [128] to effectively blend the robust and accurate formulation of the $k-\omega$ model in the near wall region with free-stream independent of the $k-\epsilon$ model in the far field. To achieve this, the $k-\epsilon$ model is converted into a $k-\omega$ formation. The SST $k-\omega$ model is similar to standard $k-\omega$ model, however includes the following refinements:

- The standard $k-\omega$ model and transferred $k-\epsilon$ model are both multiplied by a blending function and both are added together. The blending function is designed to be one in the near wall region, which activates the standard $k-\omega$ model, and zero away from the surface, which activates the transformation $k-\epsilon$ model.
- The SST $k-\omega$ model incorporates a damped cross diffusion across diffusion derivative terms in the ω equation.
- The definition of the turbulent viscosity is modified to account for the transport of the turbulent

shear stress.

- The modeling constant are different.

These features make the SST $k - \omega$ model more accurate and reliable for wide class of flows (*e.g.* adverse pressure gradient, flow over airfoils, shock waves, rotating flows etc.) than the standard $k - \omega$ model.

The SST $k - \omega$ model has a similar form to the standard $k - \omega$ model turbulent kinetic energy, k , and the specific rate, ω , are obtained from the following transport equations:

$$\frac{\partial}{\partial t}(\rho k) + \frac{\partial}{\partial x_i}(\rho k u_i) = \frac{\partial}{\partial x_i} \left[\Gamma_k \frac{\partial k}{\partial x_j} \right] + \tilde{G}_k - Y_M + S_k \quad (\text{B.14})$$

and

$$\frac{\partial}{\partial t}(\rho \varepsilon) + \frac{\partial}{\partial x_i}(\rho \varepsilon u_i) = \frac{\partial}{\partial x_i} \left[\Gamma_\omega \frac{\partial \omega}{\partial x_j} \right] + G_\omega - Y_\omega + D_\omega + S_\omega \quad (\text{B.15})$$

where, D_ω represents the cross-diffusion term.

The effective diffusivities for the $k - \omega$ model are given by

$$\Gamma_k = \mu + \frac{\mu_t}{\sigma_k} \quad (\text{B.16})$$

$$\Gamma_\omega = \mu + \frac{\mu_t}{\sigma_\omega} \quad (\text{B.17})$$

The equation for Γ_k and Γ_ω are same as used in the standard $k - \omega$ model ((B.16) and (B.17)).

However, the turbulent viscosity, μ_t , the turbulent Prandtl numbers σ_k and σ_ω are computed as follows:

$$\mu_t = \frac{\rho k}{\omega} \frac{1}{\max \left[\frac{1}{\alpha^*}, \frac{SF}{\alpha_{1\omega}} \right]} \quad (\text{B.18})$$

where, S is the strain rate magnitude and

$$\sigma_k = \frac{1}{(F_1/\sigma_{k,1}) + ((1 - F_1)/\sigma_{k,2})} \quad (\text{B.19})$$

$$\sigma_\omega = \frac{1}{(F_1/\sigma_{\omega,1}) + ((1 - F_1)/\sigma_{\omega,2})} \quad (\text{B.20})$$

The blending functions, F_1 and F_2 are given by:

$$F_1 = \tanh(\varphi_1^4) \quad (\text{B.21})$$

$$\varphi_1 = \min \left[\max \left(\frac{\sqrt{k}}{0.09\omega y}, \frac{500\mu}{0.09\omega y} \right), \frac{4\rho k}{\sigma_{\omega,2} D_\omega^+ y^2} \right] \quad (\text{B.22})$$

B. Turbulence Models Derivation

$$D_\omega^+ = \max \left[2\rho \frac{1}{\sigma_{\omega,2}} \frac{1}{\omega} \frac{\partial k}{\partial x_i} \frac{\partial \omega}{\partial x_j}, 10^{-10} \right] \quad (\text{B.23})$$

$$F_2 = \tanh(\varphi_2^2) \quad (\text{B.24})$$

$$\varphi_2 = \max \left[2 \frac{\sqrt{k}}{0.09\omega y}, \frac{500\mu}{\rho y^2 \omega} \right] \quad (\text{B.25})$$

where, y is the distance to the next surface, $\alpha = 0.31$, $\sigma_{k,1} = 1.176$, $\sigma_{k,2} = 1$, $\sigma_{\omega,1} = 2$, $\sigma_{\omega,2} = 1.168$,

$$Y_k = \rho \beta_1 \omega^2 \quad (\text{B.26})$$

Instead of having a constant value of β_i , in this model it is given by:

$$\beta_1 = F_1 \beta_{i,1} + (1 - F_1) \beta_{i,2} \quad (\text{B.27})$$

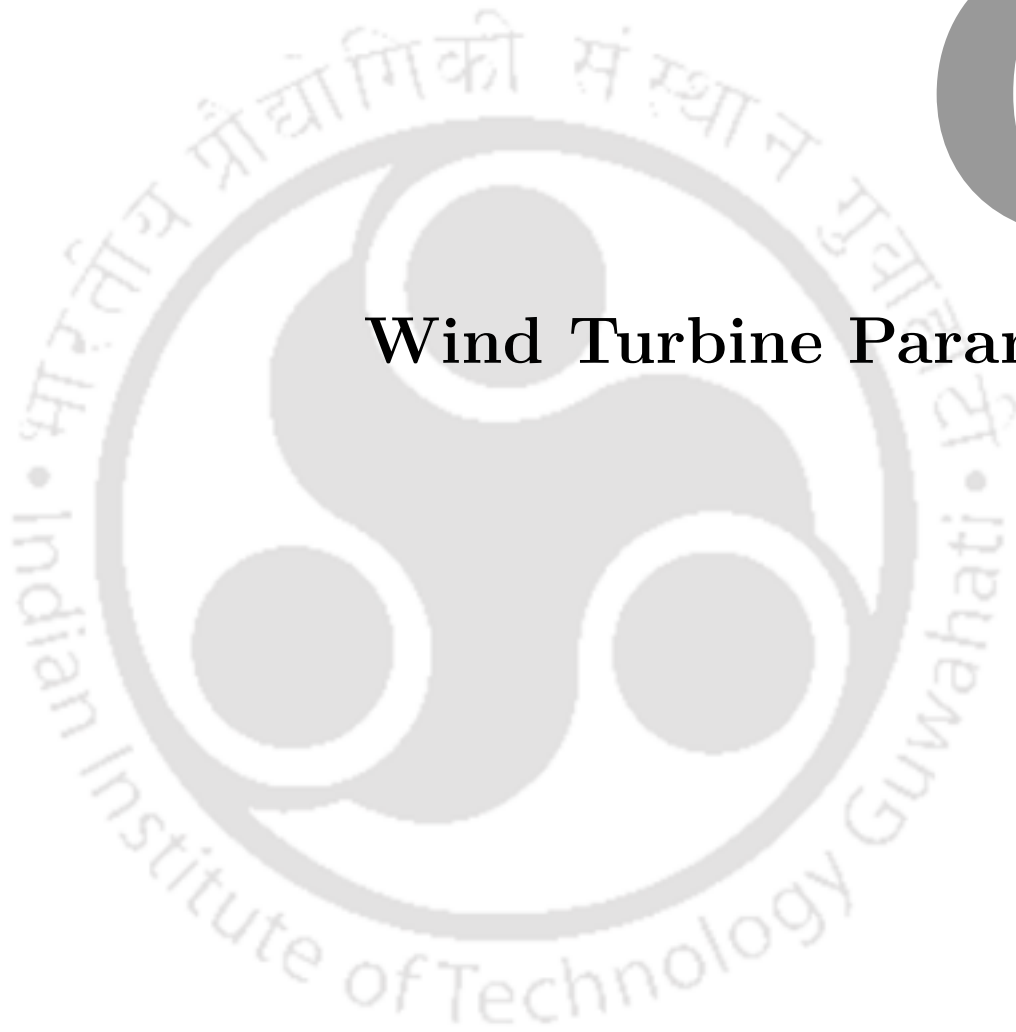
where, $\beta_{i,1} = 0.075$, $\beta_{i,2} = 0.0828$

The cross-diffusion term D_ω is given by:

$$D_\omega = 2(1 - F_1) \rho \sigma_{\omega,2} \frac{1}{\omega} \frac{\partial k}{\partial x_j} \frac{\partial \omega}{\partial x_j} \quad (\text{B.28})$$

C

Wind Turbine Parameters



Contents

C.1	Wind Turbine Blade Design Calculation	170
C.2	Boundary Conditions of Wind Turbine for the Numerical Simulations. . .	172

C.1 Wind Turbine Blade Design Calculation

C.1.1 Sectional Geometry Data of Optimum Blades Design for 3–D Simulation Modeling (For Optimum Chord Distribution)

The wind turbine blade span is divided into 18 number of elements and force coefficient data of NACA 63-415 is applied along the span. To model optimum blades design, the airfoil coordinates from Appendix A.1 is acquired. The blade consists of airfoil with various chord length and twist angle distributions (preliminary blade design) at each radial position. The blade geometry specifications are detailed in Table C.1.

Table C.1: Geometry of the blade made of the wind turbine.

Blade elements number	Sectional radius, r (m)	r/R	Twist angle, γ (°)	Chord length, c_r (m)	c_r/R	Sectional TSR, λ_r (–)
1	0.75	0.15	22.52	0.7641	0.15282	1.125
2	1.0	0.20	17.22	0.6717	0.13434	1.500
3	1.25	0.25	13.47	0.5852	0.11704	1.875
4	1.50	0.30	10.73	0.5129	0.10258	2.250
5	1.75	0.35	8.66	0.4540	0.0908	2.625
6	2.0	0.40	7.05	0.4059	0.08118	3.000
7	2.25	0.45	5.76	0.3662	0.07324	3.375
8	2.50	0.50	4.71	0.3333	0.06666	3.750
9	2.75	0.55	3.84	0.3055	0.06110	4.125
10	3.0	0.60	3.11	0.2818	0.05636	4.500
11	3.25	0.65	2.48	0.2614	0.05228	4.875
12	3.50	0.70	1.94	0.2437	0.04874	5.250
13	3.75	0.75	1.47	0.2282	0.04564	5.625
14	4.0	0.80	1.06	0.2145	0.0429	6.000
15	4.25	0.85	0.69	0.2023	0.04046	6.375
16	4.50	0.90	0.37	0.1914	0.03828	6.750
17	4.75	0.95	0.07	0.1779	0.03558	7.125
18	5.0	1	0	0.1752	0.03504	7.500

C.1.2 Adopted Blade Design (For Linearised Chord Distribution)

Based on the the analytic procedure outlined in Section 3.2.3, the optimal chord length and twist angle distributions of the turbine model is presented in Table C.2

The airfoil selections were set to NACA 63-415 to simplify the model being used. The values of [TH-3228_11610226](#)

Table C.2: Adopted blade design calculation.

Blade elements number	Sectional radius, r (m)	r/R	Twist angle, γ ($^\circ$)	Chord length, c_r (m)	c_r/R	Sectional TSR, λ_r (-)
1	0.75	0.15	22.52	0.7641	0.15282	1.125

Table C.3: The specifications of the wind turbine characteristics.

Rotor characteristics	Specification	Units
Wind turbine type	SS-HAWT	—
Rotor orientation	Upwind	—
Rated power, P	22	kW
Blade length, R	5	m
Hub diameter, r'_h	0.1	m
Number of blades, n_b	3	—
Rated wind speed, v_o	10	m/s
Cut-IN speed, v_{ci}	4	m/s
Cut-OUT speed, v_{co}	25	m/s
Air density, ρ	1.225	kg/m ³
Rotational speed	72	rev/min
Blade profile	NACA 63-415	—
Number of blade, n_b	3	—
Rotor orientation	Upwind	—
Windmill brake state model	Advanced brake state model	—
Tip loss model	Prandtl	—
Type of blade	Varied chord and twisted blade	—
Section pitch angle	0, uniform	$^\circ$

C. Wind Turbine Parameters

AoA, lift coefficients and drag coefficient was selected on the basis of giving the maximum lift/drag (*i.e.*, γ) ratio as shown in Table C.5.

Table C.4: Maximum glide ratio used for optimal calculation.

Design parameters	Value
Design AoA, α	5.25°
Lift coefficient, C_L	0.9461
Drag coefficient, C_D	0.00797
Glide ratio, γ	118.71

Table C.5: Wind turbine material properties.

Design parameters	Value
Young Modulus	3 GPa
Poisson Ratio	0.37
Density	$1.3 \times 10^3 \text{ kg/m}^3$
Damping	$4.54728409 \times 10^{-3} \text{ s}$

Table C.6: Technical properties of the wind turbine.

Property	R_1	R_2	R_3	Units
Rotor radius	5	2.5	1.7053	m
Wind speed	7	7	7	m/s
Hub radius	0.23	0.12	0.08	m

C.2 Boundary Conditions of Wind Turbine for the Numerical Simulations.

The whole computational domain builds with specified BCs as shown in Fig. 2.6. Some initial inputs and computational conditions for the problems are chosen as given in Table C.7.

Table C.7: The boundary conditions of the 2–D airfoils for the numerical simulations [ANSYS USER GUIDE].

Parameter	Values
Airfoil	NACA 63-415
Simulation type	Unsteady simulation
Turbulence model	SST, SKE and RKE
Fluid material	Air
Temperature	10°C
Dynamic viscosity	1.778×10^{-5} kg/m·s
Air density	1.225 kg/m ³
Blade length	$R_1 = 5$ m, $R_2 = 2.5$ m and $R_3 = 1.70345$ m
Flow type	Incompressible flow
INLET boundary condition	Flow velocity = 7 m/s
OUTLET boundary condition	Gauge pressure = 0 Pa
Discretized method	Finite volume method
CFD algorithm	Simple (Default option)
Interpolating scheme	Pressure-velocity coupling Least-squares cell based Pressure (Standard) Density (Second-order upwind) Momentum (Second-order upwind) Turbulent kinetic viscosity (Second order upwind) Specific dissipation rate (Second-order upwind)
Solution controls	Pressure; 0.55 Momentum: 0.52 Density: 1.2 kg/m ³ Turbulent kinetic energy: 0.65
Boundary condition	Velocity inlet (7 m/s) Pressure outlet (Gauge pressure: 0) Stationary wall with no-slip shear condition
Number of mesh cells	About 4,19,911 and 4,16,296
Force monitors	Torque and power coefficients
Residual convergence criteria	1×10^{-6}



D

Parameters of DFIG System

Contents

D.1 Appendices	176
D.2 Parameters of DFIG System	176

D.1 Appendices

Appendix A. Parameters of DFIG System

D.2 Parameters of DFIG System

A 3 HP, 415 V, 50 Hz, 4 pole, 3- ϕ DFIG system has been simulated using PSCAD/EMTDC software.

Stator: 415 V, Y-connected, 4.7 A

Rotor: 200 V, Y-connected, 7.8 A

where, stator resistance (r_s), rotor resistance (r_r), stator inductance (L_s), rotor inductance (L_r) and magnetizing inductance (L_m) are 10.26 Ω , 1.46 Ω , 10.11 mH, 10.11 mH and 365 mH, respectively. The switching frequency (f_s) of the RSC converter is 2 kHz.

E

Data for MDN-IITG System

Contents

E.1	IIT Guwahati Parameter	178
E.2	DFIG-based System Parameter	180
E.3	D-STATCOM Parameter	181

E.1 IIT Guwahati Parameter

One-line diagram of the 20-bus modified distribution network of IIT Guwahati (MDN-IITG) test system is given in Fig. 5.2. There are 1-generator, 9 transmission lines and 8 loads. The following parameters are used for simulation of MDN-IITG test system by Siemens PTI PSS@Sincal software in Chapter 5. Tables E.1, E.2, E.3, E.4 and E.5 show the line, bus, transformer, distributed generation source and fixed shunt data.

Table E.1: Details of transmission line data of the MDN-IITG test system.

Buses		Voltage level (kV)	Length (km)	R (Ω)	X (Ω)	C (nF)
From	To					
1	2	33	0.01	0.00063	0.00101	2.75
3	4	11	0.86	0.08479	0.07826	391.3
3	8	11	0.85	0.08381	0.07735	386.8
3	12	11	0.90	0.08874	0.08190	409.5
3	15	11	0.01	0.00986	0.00091	4.55
4	5	11	0.77	0.07592	0.07007	350.4
8	9	11	0.44	0.04338	0.04004	200.2
15	16	11	0.92	0.09071	0.08372	418.6
16	17	11	1.00	0.09860	0.09100	455.0

Table E.2: Details of load groups data.

Bus number	P (MW)	Q (MVAR)
6	0.100	0.01811
7	0.100	0.01811
10	0.500	0.09053
11	0.500	0.09053
13	0.100	0.01811
18	0.133	0.02408
19	0.133	0.02408
20	0.133	0.02408

Table E.3: Details of fixed shunt data.

Bus number	Voltage level (kV)	P (MW)	Q (MVAR)
1	33	0	2

Table E.4: Details of distributed generation sources and load groups.

Elements type	Operating p.f.	Capacity (MW)	Bus number
Wind turbine	0.90	1.3	14
Load	0.95	1.7	6, 7, 10, 11, 13, 18, 19 & 20

p.f.: Power factor.

Table E.5: Details of transformer data for the distribution network.

Transformer	Capacity (MVA)	Voltage ratio (kV)	Tap ratio	Z (%)
T_1	5	33/11	1	8
T_2	0.50	11/0.415	1	4
T_3	0.75	11/0.415	1	4
T_4	0.63	11/0.415	1	4
T_5	1.25	11/0.415	1	4
T_6	0.63	11/0.415	1	4
T_7	1.25	11/0.690	1	4
T_8	0.50	11/0.415	1	4
T_9	0.75	11/0.415	1	4
T_{10}	0.50	11/0.415	1	4

 Z : Short circuit voltage.

E.2 DFIG-based System Parameter

To simulate the behavior of the doubly fed induction generator (DFIG) type system, Siemens PTI PSS⁶Sincal model offers the possibility of adapting all relevant parameters such as time constants and reactance. The DFIG type model is considered as wind machine in this works wind following dynamic model parameters are used for simulation. The parameters are also based on the findings of work and summarized in Table E.6.

Table E.6: DFIG-based wind turbine parameters.

Parameters	Values	Units
Machine data		
Rated Act. Power (Mech.) (P_n)	1.5	MW
Rated voltage (V_n)	0.69	kV
Rated speed (N_n)	1750	1/min
Pole-pair number (p)	2	—
Rated power factor ($\cos \phi$)	0.95	—
Rated efficiency (η_n)	0.958	pu
Current ratio at start-up (I_a/I_n)	5	pu
Resistance/Reactance (R/X)	0.15	pu
Operating state		
Active power (P)	1.3	MW
Reactive power (Q)	0.427	MVAR
Slip (s)	-16.67	%
Equivalent circuit		
Direct current time constant (T_g)	0.1129	s
Armature resistance (R_A)	0.008349	pu
Armature leakage reactance (X_A)	0.167	pu
Dynamic parameters		
Rotor resistance at normal slip (R_2)	0.008286	pu
Rotor stray reactance at normal slip (X_{2s})	0.1323	pu
Converter reactance power (Q_{conv})	0.001	MVAR
No load current (i_o)	0.0132	pu
Rotor time constant (T_{rotor})	2.13254	s
Reinforcement pilot controller (V_{pc})	0.03	—
Crowbar resistance (R_k)	0.15	pu
Internal resistance voltage converter (r_i)	0.001	pu

The DFIG type model is considered as wind machine in this works wind following dynamic model

parameters are used for simulation. The parameters are also based on the findings of work and summarized in Table E.6.

Table E.7: Voltage controller parameters.

Parameters	Values	Units
Armature resistance (R_A)	0.008349	pu
Armature stray reactance (X_A)	0.167	pu
Rotor resistance (R_2)	0.008286	pu
Rotor stray reactance (X_2)	0.1323	pu
No load current (I_{LEER})	0.13246	pu
Converter reactive power (Q_C)	0	MVAR
Start-up time (T_A)	2.1637	s
Reinforcement of the pilot control (V_{ST})	0.03	pu
Crowbar short circuit resistance (R_K)	0.03	pu
Crowbar replacement time (T_{CROW})	0.015	s
Internal resistance voltage converter (R_I)	0.001	pu
PI integral time constant (P_I)	2.5	s
PI reinforcement factor (P_V)	0.04	pu
Pitch control (0 : OFF, 1 : ON) ($PITCH$)	0	—
Voltage correction (0 : OFF, 1 : ON) (U_{CORR})	1	—

E.3 D-STATCOM Parameter

To illustrate further the great modeling flexibility afforded by the D-STATCOM model. The 3- ϕ STATCOM is located in the same location in the network presented in Fig. 5.2. The consumed active power and the reactive power delivered to the grid stand at 250 kVAR capacitive and 50 kVAR inductive reactive power, respectively.

Table E.8: Speed controller parameters.

Parameters	Values	Units
f_{cut} (f_{cut})	0.002	—
K_S constant value (K_S)	21.6	—
K_{LS} (K_{LS})	0.1	—
K_G (K_G)	3	—
K_P amplification K (K_P)	1	—
T_N, T_i or T_n (T_N)	1	s
K_D amplification K (K_D)	1	—
T_D lag time constant T (T_D)	5	s
T_4 lag time constant T (T_4)	0.16	s
K_2 amplification K (K_2)	5	—
T_5 lag time constant T (T_5)	12	s
K_3 amplification K (K_3)	0.5	—
T_6 lag time constant T (T_6)	0.7	s
T_1 lag time constant T (T_1)	0.05	s
SWITCH (<i>SWITCH</i>)	1	—
P_{max} upper limit (P_{max})	1	—
P_{min} lower limit (P_{min})	0	—

Table E.9: Information on D-STATCOM.

Parameters	Values	Units
Capacitive reactive power (Q_c)	250	kVAR
Inductive reactive power (Q_i)	50	kVAR
Zero sequence resistance (R_o)	0.567	Ω
Zero sequence reactance (X_o)	0.435	Ω
Upper voltage limits (V_{ul})	103	%
Lower voltage limits (V_{ll})	97	%

F

Data for Reduced NEREB Indian Power System

Contents

F.1	Data for 29-bus NEREB Indian Power System	184
F.2	DFIG-Based System Parameter	184
F.3	D-STATCOM Parameter	184

F.1 Data for 29-bus NEREB Indian Power System

One-line diagram of the 29-bus North Eastern Regional Electricity Board (NEREB) Indian power system is given in Fig. 6.1. There are total 16-synchronous machine, 25 transmission lines and 14 dynamic loads. The following parameters are used for simulation of NEREB Indian power system by Siemens PTI PSS@Sincal software in Chapter 6. Tables F.1, F.2 and F.3 shows the bus, line and transformer data in p.u. at 100 MVA base, respectively. Fixed shunt is given in Table F.4. Synchronous machine, exciter and governor data are shown in Tables F.5, F.6, F.7 and F.8 [219, 220].

To simulate the behavior of the synchronous generator, Siemens PTI PSS@Sincal model offers the possibility of adapting all relevant parameters such as time constants and reactance. The parameters are also based on the findings of work and summarized in Table F.5.

where, * denotes the wind machine *i.e.*, the doubly fed induction generator (DFIG) type system. The Siemens PTI PSS@Sincal library model. The DFIG type model is considered as wind machine in this works wind following dynamic model parameters are used for simulations are given in the subsequent subsection.

F.2 DFIG-Based System Parameter

To simulate the behavior of the doubly fed induction generator (DFIG) type system, Siemens PTI PSS@Sincal model offers the possibility of adapting all relevant parameters such as time constants and reactance. The DFIG type model is considered as wind machine in this works wind following dynamic model parameters are used for simulation. The parameters are also based on the findings of work and summarized in Table F.9.

The DFIG type model is considered as wind machine in this works wind following dynamic model parameters are used for simulation. The parameters are also based on the findings of work and summarized in Table F.9.

F.3 D-STATCOM Parameter

To illustrate further the great modeling flexibility afforded by the D-STATCOM model. The 3- ϕ STATCOM is located in the same location in the network presented in Fig. 6.1. The consumed active power and the reactive power delivered to the grid stand at 250 kVAR capacitive and 50 kVAR inductive reactive power, respectively.

Table F.1: Details of bus data.

Bus number	Voltage level (kV)	P_G (MW)	P_L (MW)	Q_G (MVAR)	Q_L (MVAR)	$Q_{G(\max)}$ (MVAR)	$Q_{G(\min)}$ (MVAR)
6100	220	0	0	0	0	0	0
6102	220	0	271.99	0	80.76	0	0
6127	220	0	0	0	20.12	0	0
6145	132	120.0	16.00	60.0	2.32	60.0	-28.0
6146	132	68.0	118.00	-13.1	22.06	47.0	-23.5
6300	132	26.0	9.02	18.0	2.25	18.0	2.4
6301	132	62.6	98.66	51.5	29.88	51.5	-15.0
6327	132	0	54.12	0	15.68	0	0
6329	220	0	0	0	0	0	0
6506	132	12.0	160.82	8.0	35.73	8.0	2.0
6604	132	18.0	26.50	10.0	5.30	10.0	-4.0
6609	132	76.0	67.17	24.0	13.43	32.0	4.0
6636	66	36.0	54.11	20.0	10.82	20.0	-8.0
6640	66	6.6	0	6.0	0	6.0	-2.0
6643	66	34.1	10.43	17.5	2.08	20.0	-8.0
6700	220	91.1	7.16	13.5	2.04	28.8	13.6
6702	220	0	129.68	0	39.74	0	0
6703	400	0	64.59	0	17.79	0	0
6705	220	0	0	0	0	0	0
6709	132	70.0	107.12	20.4	20.40	20.0	-15.0
6714	132	0	4.03	0	1.10	0	0
6715	220	165.0	0	36.0	0	36.0	-24.0
6717	400	188.0	0	160.0	0	160.0	-160.0
6719	220	230.9	0	100.0	0	100.0	-100.0
6721	132	0	0	0	0	0	0
6756	400	0	0	0	0	0	0
6757	132	0	61.94	0	16.90	0	0
6758	400	440	0	0	0	0	0
6759	132	0	0	0	0	0	0

F. Data for Reduced NEREB Indian Power System

Table F.2: Details of transmission line data.

Buses		Voltage level (kV)	Length (km)	R (p.u.)	X (p.u.)	B_{SH} (p.u.)
From	To					
6100	6102	220	62	0.00967	0.05156	0.08875
6100	6719	220	2.7	0.00039	0.00222	0.00381
6102	6702	220	130	0.02011	0.10724	0.18460
6127	6700	220	162	0.00969	0.10353	0.29658
6127	6702	220	220	0.01309	0.13985	0.40063
6145	6146	132	60	0.05586	0.13296	0.03060
6145	6506	132	80	0.07448	0.17728	0.04080
6146	6506	132	74	0.27558	0.65594	0.00947
6300	6301	132	17.54	0.01633	0.03807	0.00894
6300	6327	132	0.7	0.00065	0.00155	0.00036
6329	6702	220	113.41	0.01633	0.09322	0.15991
6604	6609	132	35	0.03259	0.07756	0.01785
6604	6759	132	6	0.00559	0.01330	0.00306
6609	6709	132	132.9	0.01237	0.29541	0.06778
6609	6721	132	118.51	0.11034	0.26262	0.06044
6609	6757	132	29	0.02700	0.06400	0.01479
6609	6759	132	37	0.00615	0.06569	0.02439
6636	6643	66	25	0.09310	0.22160	0.00320
6700	6702	220	383.22	0.01325	0.14156	0.40552
6702	6705	220	123.52	0.01779	0.10153	0.17416
6702	6715	220	72.79	0.01048	0.05983	0.10264
6703	6717	400	289.72	0.00521	0.05571	1.74412
6709	6714	132	100.63	0.09369	0.22300	0.05132
6709	6757	132	15	0.01397	0.03324	0.00765
6756	6758	400	247	0.00445	0.04750	1.48694

Table F.3: Details of transformers data.

Buses		Capacity (MVA)	Voltage ratio	Tap ratio	R (p.u.)	X (p.u.)
From	To					
6127	6506	100	220 kV/132 kV	1	0.00625	0.12500
6146	6700	45	132 kV/220 kV	1	0.01250	0.25000
6327	6329	144	132 kV/220 kV	1	0.00391	0.07813
6329	6756	284	220 kV/400 kV	1	0.00198	0.03968
6506	6705	100	132 kV/220 kV	1	0.00625	0.37420
6604	6636	27	132 kV/66 kV	1	0.02083	0.41667
6604	6640	14	132 kV/66 kV	1	0.06250	0.12500
6609	6643	27	132 kV/66 kV	1	0.02083	0.41667
6702	6703	203	220 kV/400 kV	1	0.00198	0.03968
6714	6715	144	132 kV/220 kV	1	0.00391	0.07813
6717	6719	284	400 kV/220 kV	1	0.00198	0.03968
6756	6357	180	400 kV/132 kV	1	0.00313	0.06250
6758	6759	100	400 kV/132 kV	1	0.00500	0.10000

Table F.4: Details of fixed shunt data.

Bus	Voltage level (kV)	G (MW)	B (MVAR)
6127	220	0	-20
6327	132	0	12.6
6609	132	0	-21
6702	220	0	-37
6703	400	0	-225
6709	132	0	-34

F. Data for Reduced NEREB Indian Power System

Table F.5: Synchronous machines data with inertia and governor models.

Generator number	Bus number	Rating (MVA)	x''_d, x''_q (p.u.)	x'_d, x'_q (p.u.)	x_d, x_q (p.u.)	T''_d, T''_q (s)	T'_d, T'_q (s)	J (kg.m ²)
1	6145	187.5	0.13, 0.13	0.327, 0.49	1.97, 1.89	0.021, 0.013	1.05, 0.26	12.7
2	6146	131.09	0.105, 0.105	0.327, 0.49	1.97, 1.89	0.017, 0.011	1.051, 0.259	9.75
3	6300	49	0.12, 0.12	0.28, 0.42	1.09, 0.82	0.021, 0.073	2.02, 0.5	12.7
4	6301	120.6	0.202, 0.202	0.28, 0.42	1.09, 0.42	0.036, 0.012	2.02, 0.5	9.75
5	6506	21.2	0.202, 0.205	0.327, 0.49	1.97, 1.89	0.033, 0.021	1.051, 0.26	12.7
6	6604	30	0.135, 0.135	0.327, 0.49	1.97, 1.89	0.022, 0.014	1.05, 0.26	9.75
7	6609	115.84	0.165, 0.165	0.21, 0.4	1.94, 1.8	0.03, 0.06	0.73, 0.33	12.7
8	6636	60	0.135, 0.135	0.327, 0.49	1.97, 1.89	0.022, 0.014	1.05, 0.26	9.75
9	6640	11.76	0.26, 0.26	0.327, 0.49	1.97, 1.89	0.043, 0.027	1.05, 0.26	12.7
10	6643	56	0.135, 0.135	0.327, 0.49	1.97, 1.89	0.022, 0.013	1.05, 0.26	9.75
11	6700	380.1	0.21, 0.21	0.28, 0.495	2.17, 2.09	0.043, 0.042	0.76, 0.15	12.7
12	6709	88	0.14, 0.14	0.31, 0.85	1.1, 0.85	0.032, 0.012	2.25, 0.5	9.75
13	6715*	168	0.12, 0.12	0.176, 0.46	0.614, 0.46	0.034, 0.013	2.64, 0.5	9.75
14	6717	400	0.11, 0.10	0.2, 0.2	1.2, 1.2	0.033, 0.015	1.5, 1.5	9.75
15	6719	200	0.236, 0.236	0.327, 0.49	1.1, 1.08	0.035, 0.035	1.1, 1.1	12.7
16	6758	856	0.11, 0.15	0.23, 1.23	3.18, 1.8	0.05, 0.019	0.66, 0.6	9.75

x''_d, x''_q → Subtransient reactance, x'_d, x'_q → Transient reactance, x_d, x_q → Synchronous reactance, T''_d, T''_q → Subtransient SC time constant, T'_d, T'_q → Transient SC time constant and J → Inertia constant.

Table F.6: Parameters of the generator exciters (IEEE T1 voltage controllers).

Generator Number	Bus number	T_R (s)	K_A (p.u.)	T_A (s)	V_{RMAX} (p.u.)	V_{RMIN} (p.u.)	K_E (p.u.)	T_E (s)	K_F (p.u.)	T_F (s)	E_1 (p.u.)	$S_E(E_1)$ (p.u.)	E_2 (p.u.)	$S_E(E_2)$ (p.u.)
1	6145	0.01	510	0.02	2.3	-2.3	0.0	30.0	0.6	1.2	3.5	2.0	4.1	0.428
2	6146	0.06	40	0.81	4.0	-4.0	2.2	0.4	0.15	2.5	3.23	0.9	2.3	0.368
3	6300	0.06	70	0.1	2.15	-2.15	0.0	1.8	0.8	4.5	2.48	1.12	0.13	0.535
4	6301	0.05	100	0.02	3.8	-3.8	1.0	0.1	0.3	1.0	2.9	0.65	3.9	0.86
5	6506	0.05	100	0.02	10.3	-10.3	0.0	5.9	0.9	1.0	2.9	0.5	3.9	0.3
6	6604	0.05	200	0.2	3.1	-3.1	1.0	0.3	0.7	1.2	2.9	0.5	3.9	0.86
7	6609	0.04	200	0.02	4.3	-4.3	1.2	1.0	0.5	2.3	1.9	0.5	0.9	1.86
8	6636	0.05	100	0.2	3.3	-3.3	1.0	0.3	0.3	4.0	2.9	0.5	3.9	0.86
9	6640	0.05	100	0.2	2.9	-2.9	2.0	0.3	0.2	1.6	3.2	0.5	4.6	0.986
10	6643	0.05	40	0.02	3.2	-3.2	0.0	0.8	0.32	1.5	3.9	0.5	4.9	0.86
12	6709	0.05	10	0.2	5.3	-5.3	1.5	0.1	0.03	1.0	2.9	0.5	3.9	0.86
13	6715*	0.06	40	0.1	1.0	-1.0	0	0.9	0.9	1.0	1.65	0.12	2.2	0.535
14	6717	0.004	310	0.02	20.3	-20.3	1.0	0.1	0.3	0.82	2.9	0.5	4.1	0.42
15	6719	0.06	40	0.1	1.0	-1.0	0	0.9	0.9	1.0	1.65	0.12	2.2	0.535
16	6758	0.5	200	0.05	2.3	-2.3	0.0	1.5	0.7	0.5	3.9	1.5	2.9	0.86

T_R → Voltage input time constant, K_A → AVR gain, T_A → AVR time constant, V_{RMAX} → Maximum AVR output, V_{RMIN} → Minimum AVR output, K_E → Exciter field gain, T_E → Exciter time constant, K_F → Rate feedback gain, T_F → Rate feedback time constant, E_1 → Exciter saturation point 1, $S_E(E_1)$ → Saturation at E_1 → Exciter saturation point 2, E_2 → Saturation at E_2 and $S_E(E_2)$ → Saturation at E_2 .

Table F.7: Parameters of the generator exciters (IEEE T2 voltage controllers).

Generator Number	Bus number	T_R (s)	K_A (p.u.)	T_A (s)	V_{RMAX} (p.u.)	V_{RMIN} (p.u.)	K_E (p.u.)	T_E (s)	K_F (p.u.)	T_{F1} (s)	T_{F2} (s)	E_1 (p.u.)	$S_E(E_1)$ (p.u.)	E_2 (p.u.)	$S_E(E_2)$ (p.u.)
11	6700	0.05	42	0.2	4.0	-4.0	0.0	0.08	8.9	0.05	0.02	1.02	0.14	1.2	0.51

T_R → Voltage input time constant, K_A → AVR gain, T_A → AVR time constant, V_{RMAX} → Maximum AVR output, V_{RMIN} → Minimum AVR output, K_E → Exciter field gain, T_E → Exciter time constant, K_F → Rate feedback gain, T_{F1} → Rate feedback time constant 1, T_{F2} → Rate feedback time constant 2, E_1 → Exciter saturation point 1, $S_E(E_1)$ → Saturation at E_1 → Exciter saturation point 2, E_2 → Saturation at E_2 and $S_E(E_2)$ → Saturation at E_2 .

Table F.8: Parameters of the governor model (TGOV1 governor model).

Generator number	Bus number	R (p.u.)	T_1 (s)	T_2 (s)	T_3 (s)	V_{RMAX} (p.u.)	V_{RMIN} (p.u.)	D_t
1	6145	0.005	0.1	0.1	0.2	1.0	0.0	0.0
2	6146	0.005	0.1	0.1	0.2	1.0	0.0	0.0
3	6300	0.005	0.1	0.1	0.2	1.0	0.0	0.0
4	6301	0.005	0.1	0.1	0.2	1.0	0.0	0.0
5	6506	0.005	0.1	0.1	0.2	1.0	0.0	0.0
6	6604	0.005	0.1	0.1	0.2	1.0	0.0	0.0
7	6609	0.005	0.1	0.1	0.2	1.0	0.0	0.0
8	6636	0.005	0.1	0.1	0.2	1.0	0.0	0.0
9	6640	0.005	0.1	0.1	0.2	1.0	0.0	0.0
10	6643	0.005	0.1	0.1	0.2	1.0	0.0	0.0
11	6700	0.005	0.1	0.1	0.2	1.0	0.0	0.0
12	6709	0.005	0.1	0.1	0.2	1.0	0.0	0.0
13	6715*	0.005	0.1	0.1	0.2	1.0	0.0	0.0
14	6717	0.005	0.1	0.1	0.2	1.0	0.0	0.0
15	6719	0.005	0.1	0.1	0.2	1.0	0.0	0.0
16	6758	0.005	0.1	0.1	0.2	1.0	0.0	0.0

R → Permanent droop, T_1 → Time constant 1, T_2 → Time constant 2, T_3 → Time constant 3, V_{RMAX} → Maximum valve position, V_{RMIN} → Minimum valve position, D_t → Turbine damping coefficient.

Table F.9: DFIG-based wind turbine parameters.

Parameters	Values	Units
Machine data		
Rated Act. Power (Mech.) (P_n)	190	MW
Rated voltage (V_n)	220	kV
Rated speed (N_n)	1750	1/min
Pole-pair number (p)	2	—
Rated power factor ($\cos \phi$)	0.95	—
Rated efficiency (η_n)	0.958	p.u.
Current ratio at start-up (I_a/I_n)	5	p.u.
Resistance/Reactance (R/X)	0.15	p.u.
Operating state		
Active power (P)	165	MW
Reactive power (Q)	36	MVAR
Slip (s)	-16.67	%
Equivalent circuit		
Direct current time constant (T_g)	5	s
Armature resistance (R_A)	0.25	p.u.
Armature leakage reactance (X_A)	0.25	p.u.
Dynamic parameters		
Rotor resistance at normal slip (R_2)	0.25	p.u.
Rotor stray reactance at normal slip (X_{2s})	0.1	p.u.
Converter reactance power (Q_{conv})	0.001	MVAR
No load current (i_o)	0.01	p.u.
Rotor time constant (T_{rotor})	2.04	s
Reinforcement pilot controller (V_{pc})	0.03	—
Crowbar resistance (R_k)	0.15	p.u.
Internal resistance voltage converter (r_i)	0.001	p.u.

Table F.10: Voltage controller parameters.

Parameters	Values	Units
Armature resistance (R_A)	0.0047	p.u.
Armature stray reactance (X_A)	0.1	p.u.
Rotor resistance (R_2)	0.008	p.u.
Rotor stray reactance (X_2)	0.08	p.u.
No load current (I_{LEER})	0.32	p.u.
Converter reactive power (Q_C)	0	MVAR
Start-up time (T_A)	10	s
Reinforcement of the pilot control (V_{ST})	0.03	p.u.
Crowbar short circuit resistance (R_K)	0.03	p.u.
Crowbar replacement time (T_{CROW})	0.3	s
Internal resistance voltage converter (R_I)	0.001	p.u.
PI integral time constant (P_I)	8	s
PI reinforcement factor (P_V)	0.05	p.u.
Pitch control (0 : OFF, 1 : ON) ($PITCH$)	0	—
Voltage correction (0 : OFF, 1 : ON) (U_{CORR})	1	—

Table F.11: Speed controller parameters.

Parameters	Values	Units
f_{cut} (f_{cut})	0.002	—
K_S constant value (K_S)	21.6	—
K_{LS} (K_{LS})	0.1	—
K_G (K_G)	3	—
K_P amplification K (K_P)	1	—
T_N, T_i or T_n (T_N)	1	s
K_D amplification K (K_D)	1	—
T_D lag time constant T (T_D)	5	s
T_4 lag time constant T (T_4)	0.16	s
K_2 amplification K (K_2)	5	—
T_5 lag time constant T (T_5)	12	s
K_3 amplification K (K_3)	0.5	—
T_6 lag time constant T (T_6)	0.7	s
T_1 lag time constant T (T_1)	0.05	s
SWITCH ($SWITCH$)	1	—
P_{max} upper limit (P_{max})	1	—
P_{min} lower limit (P_{min})	0	—

Table F.12: Details on STATCOM.

Parameters	Values	Units
Capacitive reactive power (Q_c)	250	kVAR
Inductive reactive power (Q_i)	50	kVAR
Zero sequence resistance (R_o)	0.567	Ω
Zero sequence reactance (X_o)	0.435	Ω
Upper voltage limits (V_{ul})	103	%
Lower voltage limits (V_{ll})	97	%

Bibliography

- [1] M. S. M., “Shape memory alloy based stiffening of horizontal axis wind turbine blade for vibration control and fatigue life enhancement,” Ph.D. dissertation, Indian Institute of Technology Guwahati, India, 2021.
- [2] I. Abbott and A. Von Doenhoff, *Theory of Wing Sections, Including a Summary of Airfoil Data*. New York, USA: Courier Corporation, 1959.
- [3] M. Selig, “UIUC airfoil coordinates database,” University of Illinois at Urbana Champaign, Dept of Aerospace Engineering, Urbana, Illinois, Tech. Rep., 2021. [Online]. Available: https://m-selig.ae.illinois.edu/ads/coord_database.html
- [4] C. Bak, F. Risø, P. Fuglsang, J. Johansen, I. Antoniou, and F. Risø, *Wind Tunnel Tests of the NACA 63-415 and a Modified NACA 63-415 Airfoil*, ser. Risø-R. Risø National Laboratory, 2000.
- [5] M. A. Delucchi and M. Z. Jacobson, “Providing all global energy with wind, water, and solar power, Part II: Reliability, system and transmission costs, and policies,” *Energy Policy*, vol. 39, no. 3, pp. 1170 – 1190, 2011.
- [6] G. BoroumandJazi, B. Rismanchi, and R. Saidur, “Technical characteristic analysis of wind energy conversion systems for sustainable development,” *Energ. Convers. Manage.*, vol. 69, pp. 87 – 94, 2013.
- [7] S. Heier, *Grid Integration of Wind Energy Conversion Systems*. Wiley, 1998.
- [8] Global Wind Energy Council (GWEC), 2022.
- [9] World Wind Energy Association (WWEA), 2022.
- [10] Central Electricity Authority (CEA) Report, 2022.
- [11] Ministry of New and Renewable Energy (MNRE) Report, 2023.
- [12] G. Joselin Herbert, S. Iniyar, E. Sreevalsan, and S. Rajapandian, “A review of wind energy technologies,” *Renew. Sustain. Energy Rev.*, vol. 11, no. 6, pp. 1117–1145, 2007.
- [13] Y. He, P. Chan, and Q. Li, “Wind characteristics over different terrains,” *J. Wind Eng. Ind. Aerodyn.*, vol. 120, pp. 51–69, 2013.
- [14] F. Castellani, D. Astolfi, M. Burlando, and L. Terzi, “Numerical modelling for wind farm operational assessment in complex terrain,” *J. Wind Eng. Ind. Aerodyn.*, vol. 147, pp. 320–329, 2015.
- [15] W. Tong, *Wind power generation and wind turbine design*, W. Tong, Ed. Southampton; Boston: WIT Press, 2010.
- [16] C. Bai, F. Hsiao, M. Li, G. Huang, and Y. Chen, “Design of 10 kW horizontal-axis wind turbine (HAWT) blade and aerodynamic investigation using numerical simulation,” *Proc. Eng.*, vol. 67, pp. 279 – 287, 2013.
- [17] M. Tazil, V. Kumar, R. Bansal, S. Kong, Z. Dong, W. Freitas, and H. D. Mathur, “Three-phase doubly fed induction generators: An overview,” *IET Electric. Power Appl.*, vol. 4, pp. 75–89, 2010.
- [18] J. López, E. Gubía, P. Sanchis, X. Roboam, and L. Marroyo, “Wind turbines based on doubly fed induction generator under asymmetrical voltage dips,” *IEEE Trans. Energy Conv.*, vol. 23, no. 1, pp. 321–330, 2008.
- [19] S. Datta, J. P. Mishra, and A. K. Roy, “Operation and control of a DFIG-based grid-connected WECS using NSC during grid fault and with unbalanced non-linear load,” *Int. J. Ambient Energy*, vol. 39, no. 7, pp. 732–742, 2018.

BIBLIOGRAPHY

- [20] E. Muljadi, C. P. Butterfield, B. Parsons, and A. Ellis, "Effect of variable speed wind turbine generator on stability of a weak grid," *IEEE Trans. Energy Conv.*, vol. 22, no. 1, pp. 29–36, 2007.
- [21] A. K. Gupta, "Efficient wind energy conversion: Evolution to modern design," *J. Energ. Resour. Tech. – ASME*, vol. 137, no. 5, p. 51201, 09 2015, 051201.
- [22] A. Betz, *Introduction to the Theory of Flow Machines*. Elsevier, 1966.
- [23] M. R. Hazari, M. A. Mannan, S. M. Muyeen, A. Umemura, R. Takahashi, and J. Tamura, "Stability augmentation of a grid-connected wind farm by fuzzy-logic-controlled DFIG-based wind turbines," *Appl. Sci.*, vol. 8, no. 1, 2018.
- [24] S. M. Muyeen, J. Tamura, and T. Murata, "Stability augmentation of a grid-connected wind farm," 2008.
- [25] Haliade-x offshore turbine. [Online]. Available: <https://www.ge.com/renewableenergy/wind-energy/offshore-wind/haliade-x-offshore-turbine>
- [26] H. Rezaie, S. M. M. Chashmi, M. Mirsalim, and H. Rastegar, "Enhancing LVRT capability and smoothing power fluctuations of a DFIG-based wind farm in a DC microgrid," *Electr. Power Compon. Syst.*, vol. 45, no. 10, pp. 1080–1090, 2017.
- [27] M. S. Alam, M. A. Y. Abido, and I. El-Amin, "Fault current limiters in power systems: A comprehensive review," *Energies*, vol. 11, no. 5, pp. 1–24, 2018.
- [28] S. S. Sahoo, K. Chatterjee, and P. Tripathi, "A coordinated control strategy using supercapacitor energy storage and series dynamic resistor for enhancement of fault ride-through of doubly fed induction generator," *Int. J. Green Energy*, vol. 16, no. 8, pp. 615–626, 2019.
- [29] P. Kundur, J. Paserba, V. Ajjarapu, G. Andersson, A. Bose, C. Canizares, N. Hatziargyriou, D. Hill, A. Stankovic, C. Taylor, T. Van Cutsem, and V. Vittal, "Definition and classification of power system stability IEEE/CIGRE joint task force on stability terms and definitions," *IEEE Trans. Power Syst.*, vol. 19, no. 3, pp. 1387–1401, 2004.
- [30] F. Balduzzi, A. Bianchini, and L. Ferrari, "Microeolic turbines in the built environment: Influence of the installation site on the potential energy yield," *Renew. Energy*, vol. 45, pp. 163–174, 2012.
- [31] M. N. Kaya, F. Kose, D. Ingham, L. Ma, and M. Pourkashanian, "Aerodynamic performance of a horizontal axis wind turbine with forward and backward swept blades," *J. Wind Eng. Ind. Aerod.*, vol. 176, pp. 166 – 173, 2018.
- [32] M. Hansen, J. Sørensen, S. Voutsinas, N. Sørensen, and H. Madsen, "State of the art in wind turbine aerodynamics and aeroelasticity," *Prog. Aerosp. Sci.*, vol. 42, no. 4, pp. 285 – 330, 2006.
- [33] T. Burton, D. Sharpe, N. Jenkins, and E. Bossanyi, *Wind Energy Handbook*, 2nd ed. John Wiley & Sons, Ltd, 2011, ch. Aerodynamics of horizontal-axis wind turbines, p. 780.
- [34] M. Sayed, H. Kandil, and E. Imam Morgan, "Computational fluid dynamics study of wind turbine blade profiles at low reynolds numbers for various angles of attack," *AIP Conf. Proc.*, vol. 1440, pp. 467–479, 06 2012.
- [35] M. A. Sayed, H. A. Kandil, and A. Shaltot, "Aerodynamic analysis of different wind-turbine-blade profiles using finite-volume method," *Energy Conv. Manag.*, vol. 64, pp. 541 – 550, 2012.
- [36] E. Hoogedoorn, G. B. Jacobs, and A. Beyene, "Aero-elastic behavior of a flexible blade for wind turbine application: A 2D computational study," *Energy*, vol. 35, no. 2, pp. 778 – 785, 2010.
- [37] F. Villalpando, M. Reggio, and A. Ilinca, "Numerical study of flow around iced wind turbine airfoil," *Eng. Appl. Comput. Fluid Mech.*, vol. 6, no. 1, pp. 39–45, 2012.
- [38] R. K. Singh, M. R. Ahmed, M. A. Zullah, and Y.-H. Lee, "Design of a low reynolds number airfoil for small horizontal axis wind turbines," *Renew. Energy*, vol. 42, pp. 66 – 76, 2012, international Symposium on Low Carbon and Renewable Energy Technology 2010 (ISLCT 2010).
- [39] C. Suvanjumrat, "Comparison of turbulence models for flow past NACA0015 airfoil using OpenFOAM," *Eng. J.*, vol. 21, no. 3, pp. 207–221, 2017.

- [40] S. Vendan, S. A. Lovelin, M. Manibharathi, and C. Rajkumar, "Analysis of a wind turbine blade profile for tapping wind power at the regions of low wind speed," *Int. J. Mech. Eng.*, vol. 2, no. 2, pp. 1–10, 2010.
- [41] O. Erkan and M. Özkan, "Investigation of the flow over NACA 63-415 airfoil," *Black Sea J. Eng. Sci.*, vol. 3, no. 2, pp. 50 – 56, 2020.
- [42] O. Erkan, M. Özkan, T. H. Karakoç, S. J. Garrett, and P. J. Thomas, "Investigation of aerodynamic performance characteristics of a wind-turbine-blade profile using the finite-volume method," *Renew. Energy*, 2020.
- [43] J. F. Manwell, J. G. McGowan, and A. L. Rogers, *Wind Energy Explained: Theory, Design and Application*. John Wiley & Sons, Ltd, 2009, ch. Wind Turbine Materials and Components, pp. 257–357.
- [44] "NWTC information portal (AeroDyn)." [Online]. Available: <https://nwtc.nrel.gov/AeroDyn>
- [45] L. Prandtl and A. Betz, *Vier Abhandlungen zur Hydrodynamik und Aerodynamik*. Göttinger Nachr.: Göttingen, 1927.
- [46] H. Glauert, *Aerodynamic theory: A general review of progress under a grant of the guggenheim fund for the promotion of aeronautics*, Berlin, Heidelberg, 1935, ch. Airplane Propellers, pp. 169–360.
- [47] M. L. Buhl, Jr, "New empirical relationship between thrust coefficient and induction factor for the turbulent windmill state," National Renewable Energy Laboratory (NREL), Golden, CO (United States), Tech. Rep., 8 2005.
- [48] S. Andrew Ning, R. Damiani, and P. J. Moriarty, "Objectives and constraints for wind turbine optimization," *J. Solar Energy Eng.*, vol. 136, no. 4, 2014.
- [49] R. Lanzafame, S. Mauro, and M. Messina, "Numerical and experimental analysis of micro HAWTs designed for wind tunnel applications," *Int. J. Energy Env. Eng.*, vol. 7, no. 2, pp. 199–210, Jun 2016.
- [50] E. P. N. Duque, M. D. Burklund, and W. Johnson, "Navier-Stokes and Comprehensive Analysis Performance Predictions of the NREL Phase VI Experiment ," *J. Sol. Energy Eng.*, vol. 125, no. 4, pp. 457–467, 11 2003.
- [51] N. Goudarzi, *Advanced Wind Turbine Technology*. Cham: Springer, 2018, ch. Computational Fluid Dynamics Methods for Wind Turbines Performance Analysis, pp. 47–57.
- [52] B. Chen, T. Lu, Y. Hsu, W. Chen, and Z. Lee, "An analytical approach to maximum power tracking and loss minimization of a doubly fed induction generator considering core loss," *IEEE Trans. Energy Convers.*, vol. 27, no. 2, pp. 449–456, 2012.
- [53] J. Hu, H. Nian, B. Hu, Y. He, and Z. Q. Zhu, "Direct active and reactive power regulation of DFIG using sliding-mode control approach," *IEEE Trans. Energy Convers.*, vol. 25, no. 4, pp. 1028–1039, 2010.
- [54] T. Sun, Z. Chen, and F. Blaabjerg, "Flicker study on variable speed wind turbines with doubly fed induction generators," *IEEE Trans. Energy Conv.*, vol. 20, no. 4, pp. 896–905, 2005.
- [55] J. López, P. Sanchis, X. Roboam, and L. Marroyo, "Dynamic behavior of the doubly fed induction generator during three-phase voltage dips," *IEEE Trans Energy Conv.*, vol. 22, no. 3, pp. 709–717, 2007.
- [56] A. Mullane, G. Lightbody, and R. Yacamini, "Wind-turbine fault ride-through enhancement," *IEEE Trans. Power Syst.*, vol. 20, no. 4, pp. 1929–1937, 2005.
- [57] K. E. Okedu, S. M. Muyeen, R. Takahashi, and J. Tamura, "Wind farms fault ride through using DFIG with new protection scheme," *IEEE Trans. Sustain. Energy*, vol. 3, no. 2, pp. 242–254, April 2012.
- [58] M. Firouzi and G. B. Gharehpetian, "Improving fault ride-through capability of fixed-speed wind turbine by using bridge-type fault current limiter," *IEEE Trans. Energy Conv.*, vol. 28, no. 2, pp. 361–369, June 2013.
- [59] M. E. Elshiekh, D. E. A. Mansour, and A. M. Azmy, "Improving fault ride-through capability of DFIG-based wind turbine using superconducting fault current limiter," *IEEE Trans. Appl. Supercond.*, vol. 23, no. 3, pp. 5 601 204–5 601 204, June 2013.

BIBLIOGRAPHY

- [60] L. A. Kojovic, S. P. Hassler, K. L. Leix, C. W. Williams, and E. E. Baker, "Comparative analysis of expulsion and current-limiting fuse operation in distribution systems for improved power quality and protection," *IEEE Trans. Power Del.*, vol. 13, no. 3, pp. 863–869, July 1998.
- [61] C. S. Chang and P. C. Loh, "Integration of fault current limiters on power systems for voltage quality improvement," *Electr. Power Syst. Res.*, vol. 57, no. 2, pp. 83 – 92, 2001.
- [62] T. Sun, Z. Chen, and F. Blaabjerg, "Transient stability of DFIG wind turbines at an external short-circuit fault," *Wind Energy*, vol. 8, no. 3, pp. 345–360, 2005.
- [63] H. Awad, J. Svensson, and M. Bollen, "Mitigation of unbalanced voltage dips using static series compensator," *IEEE Trans. Power Electron.*, vol. 19, no. 3, pp. 837–846, 2004.
- [64] R. G. de Almeida, J. A. P. Lopes, and J. A. L. Barreiros, "Improving power system dynamic behavior through doubly fed induction machines controlled by static converter using fuzzy control," *IEEE Trans. Power Syst.*, vol. 19, no. 4, pp. 1942–1950, 2004.
- [65] A. O. Ibrahim, T. H. Nguyen, D. Lee, and S. Kim, "Ride-through strategy for DFIG wind turbine systems using dynamic voltage restorers," in *IEEE Energy Conver. Cong. Exp.*, 2009, pp. 1611–1618.
- [66] A. Causebrook, D. J. Atkinson, and A. G. Jack, "Fault ride-through of large wind farms using series dynamic braking resistors," *IEEE Trans. Power Syst.*, vol. 22, no. 3, pp. 966–975, March 2007.
- [67] J. Yang, J. E. Fletcher, and J. O'Reilly, "A series-dynamic-resistor-based converter protection scheme for doubly-fed induction generator during various fault conditions," *IEEE Trans. Energy Conv.*, vol. 25, no. 2, pp. 422–432, June 2010.
- [68] M. E. Hossain, "A non-linear controller based new bridge type fault current limiter for transient stability enhancement of DFIG based wind farm," *Electr. Power Syst. Res.*, vol. 152, pp. 466 – 484, 2017.
- [69] H. J. Boenig and D. A. Paice, "Fault current limiter using a superconducting coil," *IEEE Trans. Magn.*, vol. 19, no. 3, pp. 1051–1053, May 1983.
- [70] T. Nomura, M. Yamaguchi, S. Fukui, K. Yokoyama, T. Satoh, and K. Usui, "Single DC reactor type fault current limiter for 6.6 kV power system," *IEEE Trans. Appl. Supercond.*, vol. 11, no. 1, pp. 2090–2093, Mar 2001.
- [71] W. Park, B. C. Sung, and J. Park, "The effect of SFCL on electric power grid with wind-turbine generation system," *IEEE Trans. Appl. Supercond.*, vol. 20, no. 3, pp. 1177–1181, 2010.
- [72] X. Yan, G. Venkataramanan, Y. Wang, Q. Dong, and B. Zhang, "Grid-fault tolerant operation of a DFIG wind turbine generator using a passive resistance network," *IEEE Trans. Power Electron.*, vol. 26, no. 10, pp. 2896–2905, 2011.
- [73] A. Petersson, S. Lundberg, and T. Thiringer, "A DFIG wind turbine ride-through system. influence on the energy production," *Wind Energy*, vol. 8, pp. 251 – 263, 07 2005.
- [74] H. Nourmohamadi, M. Nazari-Heris, M. Sabahi, and M. Abapour, "A novel structure for bridge-type fault current limiter: Capacitor-based nonsuperconducting FCL," *IEEE Trans. Power Electron.*, vol. 33, no. 4, pp. 3044–3051, April 2018.
- [75] M. T. Hagh and M. Abapour, "Nonsuperconducting fault current limiter with controlling the magnitudes of fault currents," *IEEE Trans. Power Electron.*, vol. 24, no. 3, pp. 613–619, March 2009.
- [76] M. Nazari-Heris, H. Nourmohamadi, M. Abapour, and M. Sabahi, "Multilevel nonsuperconducting fault current limiter: Analysis and practical feasibility," *IEEE Trans. Power Electron.*, vol. 32, no. 8, pp. 6059–6068, Aug 2017.
- [77] S. Chen, P. Li, R. Ball, J. de Palma, and B. Lehman, "Analysis of a switched impedance transformer-type nonsuperconducting fault current limiter," *IEEE Trans. Power Electron.*, vol. 30, no. 4, pp. 1925–1936, April 2015.
- [78] L. Che, X. Zhang, M. Shahidehpour, A. Alabdulwahab, and A. Abusorrah, "Optimal interconnection planning of community microgrids with renewable energy sources," *IEEE Trans. Smart Grid*, vol. 8, no. 3, pp. 1054–1063, 2017.

- [79] R. Roofegari Nejad, W. Sun, and A. Golshani, "Distributed restoration for integrated transmission and distribution systems with DERs," *IEEE Trans. Power Syst.*, vol. 34, no. 6, pp. 4964–4973, 2019.
- [80] H. I. Shaheen, G. I. Rashed, and S. Cheng, "Optimal location and parameter setting of UPFC for enhancing power system security based on differential evolution algorithm," *Int. J. Electr. Power Energy Syst.*, vol. 33, no. 1, pp. 94–105, 2011.
- [81] S. R. Inkollu and V. R. Kota, "Optimal setting of FACTS devices for voltage stability improvement using PSO adaptive GSA hybrid algorithm," *Int. J. Eng. Sci. Technol.*, vol. 19, no. 3, pp. 1166–1176, 2016.
- [82] S. H. Song, J. U. Lim, S. W. Jung, and S. I. Moon, "Preventive and corrective operation of FACTS devices to cope with a single line-faulted contingency," in *IEEE Power Energy Soc. Gen. Meet.*, 2004, pp. 837–842 Vol.1.
- [83] L. Gyugyi, "Unified power-flow control concept for flexible AC transmission systems," *Proc. IEE Part C (Gener. Transm. Dist.)*, vol. 139, no. 8, pp. 323–331, July 1992.
- [84] P. Swe, W. Swe, and K. Lin, "Effects of tap changing transformer and shunt capacitor on voltage stability enhancement of transmission networks," *Int. J. Comp. Sci.*, vol. 51, pp. 55–558, 2011.
- [85] M. J. Hossain, H. R. Pota, M. A. Mahmud, and R. A. Ramos, "Investigation of the impacts of large-scale wind power penetration on the angle and voltage stability of power systems," *IEEE Syst. J.*, vol. 6, no. 1, pp. 76–84, March 2012.
- [86] R. Cardenas, R. Pena, S. Alepuz, and G. Asher, "Overview of control systems for the operation of DFIGs in wind energy applications," *IEEE Trans. Ind. Electron.*, vol. 60, no. 7, pp. 2776–2798, 2013.
- [87] E. Vittal, M. O'Malley, and A. Keane, "Rotor angle stability with high penetrations of wind generation," *IEEE Trans. Power Syst.*, vol. 27, no. 1, pp. 353–362, 2012.
- [88] E. Hagstrom, I. Norheim, and K. Uhlen, "Large-scale wind power integration in norway and impact on damping in the nordic grid," *Wind Energy*, vol. 8, no. 3, pp. 375–384, 2005.
- [89] J. Slootweg and W. Kling, "The impact of large scale wind power generation on power system oscillations," *Electr. Pow. Syst. Res.*, vol. 67, no. 1, pp. 9 – 20, 2003.
- [90] W. Qiao and R. G. Harley, "Effect of grid-connected DFIG wind turbines on power system transient stability," in *IEEE Power Eng. Soc. Gen. Meet.*, July 2008, pp. 1–7.
- [91] A. Mendonca and J. Lopes, "Impact of large scale wind power integration on small signal stability," in *Int. Conf. Fut. Power Syst.*, 2005, p. 5.
- [92] F. Geng, I. Kalkman, A. Suiker, and B. Blocken, "Sensitivity analysis of airfoil aerodynamics during pitching motion at a Reynolds number of 1.35×10^5 ," *J. Wind Eng Ind. Aerod.*, vol. 183, pp. 315 – 332, 2018.
- [93] O. Reynolds, "On the dynamical theory of incompressible viscous fluids and the determination of the criterion," *Philosophical Transactions of the Royal Society of London Series A*, vol. 186, pp. 123–164, Jan. 1895.
- [94] D. Jackson and B. Launder, "Osborne reynolds and the publication of his papers on turbulent flow," *Annu. Rev. Fluid Mech.*, vol. 39, no. 1, pp. 19–35, 2007.
- [95] B. Eckhardt, T. M. Schneider, B. Hof, and J. Westerweel, "Turbulence transition in pipe flow," *Annu. Rev. Fluid Mech.*, vol. 39, no. 1, pp. 447–468, 2007.
- [96] J. Leishman, *Principles of Helicopter Aerodynamics*, 2nd ed. Cambridge University Press, Cambridge, New York, USA, 2006.
- [97] A. Varol, C. İlkılıç, and Y. Varol, "Increasing the efficiency of wind turbines," *J. Wind Eng. Ind. Aerod.*, vol. 89, no. 9, pp. 809 – 815, 2001.
- [98] R. Adib, *Renewables 2018: Global Status Report*, REN21, India, 2018.
- [99] U. Chaudhary and S. K. Nayak, "Micro and small-scale HAWT blades airfoils study through CFD for low wind applications," in *Annu. IEEE India Conf.*, 2015, pp. 1–6.

BIBLIOGRAPHY

- [100] W. Z. Wan Omar, M. A. Rahim, and T. M. Mat Lazim, "A CFD study of NACA 63415 with deployment of leading edge and trailing edge surfaces," in *2nd Int. Conf. Mech. Auto. Aero Eng.*, 07 2013.
- [101] S. Jain, N. Sitaram, and S. Krishnaswamy, "Effect of reynolds number on aerodynamics of airfoil with gurney flap," *Int. J. Rotating Mach.*, vol. 2015, p. 10, 2015.
- [102] J. Yao, W. Yuan, Jianliang Wang, J. Xie, H. Zhou, M. Peng, and Y. Sun, "Numerical simulation of aerodynamic performance for two dimensional wind turbine airfoils," *Proc. Eng.*, vol. 31, pp. 80 – 86, 2012, international Conference on Advances in Computational Modeling and Simulation.
- [103] M. Moshfeghi, S. Shams, and N. Hur, "Aerodynamic performance enhancement analysis of horizontal axis wind turbines using a passive flow control method via split blade," *J. Wind Eng. Ind. Aerod.*, vol. 167, pp. 148 – 159, 2017.
- [104] M. M. M. Talukder, M. Rukan, and M. Islam, "Comparative aerodynamic analysis of wind turbine blade profiles," *Int. J. Eng. Res. Tech.*, vol. 5, pp. 96–102, 01 2015.
- [105] F. Villalpando, M. Reggio, and A. Ilinca, "Assessment of turbulence models for flow simulation around a wind turbine airfoil," *Hindawi Publishing Corporation, Modeling and Simulation in Engineering*, 2011.
- [106] I. Zidane, K. Saqr, G. Swadener, X. Ma, and M. Shehadeh, "Computational fluid dynamics study of dusty air flow over NACA 63415 airfoil for wind turbine applications," *Jurnal Teknologi*, vol. 79, no. 7-3, pp. 1–6, Aug. 2017, copyright © 2012 Penerbit UTM Press, Universiti Teknologi Malaysia Funder: Arab Academy for Science, Technology and Maritime Transport.
- [107] J. Anderson, *Fundamentals of Aerodynamics*. McGraw-Hill Education, 2010.
- [108] D. Somers, "The S816, S817, and S818 airfoils," Airfoils, Inc, Tech. Rep., 1992.
- [109] R. Eppler, *Airfoil Design and Data*. Springer-Verlag (Berlin), 1990.
- [110] W. A. Timmer and R. P. J. O. M. van Rooij, "Summary of the Delft University Wind Turbine Dedicated Airfoils," *J. Solar Energy Engg.*, vol. 125, no. 4, pp. 488–496, 11 2003.
- [111] N. Bertagnolio, F.; Sørensen, J. Johansen, and P. Fuglsang, *Wind turbine airfoil catalogue*, Risø National Laboratory, Denmark.. Forskningscenter Risø. Risø-R-1280(EN), 2001.
- [112] *Wind turbines – Part 2: Design requirements for small wind turbines*, Int. Std. IEC 61400-2, 2006.
- [113] J. F. Manwell, J. G. McGowan, and A. L. Rogers, *Wind Energy Explained: Theory, Design and Application*. John Wiley & Sons, Ltd, 2009, ch. Wind Turbine Materials and Components, pp. 257–357.
- [114] A. Fluent, "Ansys user's guide," 2009, fluent Inc., New Hampshire. [Online]. Available: <<http://www.fluent.com>>
- [115] J. Boussinesq, *Théorie de L'Écoulement Tourbillant*. Mém. prés. Acad. Sci., 1877, vol. XXIII.
- [116] P. A. Durbin, *Turbulence Closure Models for Computational Fluid Dynamics*. American Cancer Society, 2017, pp. 1–22.
- [117] D. Paul A., "Some recent developments in turbulence closure modeling," *Annu. Rev. Fluid Mech.*, vol. 50, no. 1, pp. 77–103, 2018.
- [118] P. G. Tucker, "Turbulence modelling of problem aerospace flows," *Int. J. Numer. Methods Fluids*, vol. 51, no. 3, pp. 261–283, 2006.
- [119] B. Launder and D. Spalding, *Lectures in Mathematical Models of Turbulence*. Academic Press, 1972.
- [120] M. Richmond, A. Antoniadis, L. Wang, A. Kolios, S. Al-Sanad, and J. Parol, "Evaluation of an offshore wind farm computational fluid dynamics model against operational site data," *Ocean Eng.*, vol. 193, p. 106579, 2019.
- [121] T.-H. Shih, W. W. Liou, A. Shabbir, Z. Yang, and J. Zhu, "A new $k-\epsilon$ eddy viscosity model for high reynolds number turbulent flows," *Computers & Fluids*, vol. 24, no. 3, pp. 227 – 238, 1995.
- [122] F. R. Menter, "Zonal two-equation $k-\omega$ turbulence models for aerodynamic flows," *AIAA J.*, p. 2906, 1993.

- [123] B. BALDWIN and H. LOMAX, *Thin-layer approximation and algebraic model for separated turbulent flows*. AIAA, 1978, pp. 78–257.
- [124] D. C. Wilcox, “Reassessment of the scale-determining equation for advanced turbulence models,” *AIAA J.*, vol. 26, no. 11, pp. 1299–1310, 1988.
- [125] N. Ince and B. Launder, “Three-dimensional and heat-loss effects on turbulent flow in a nominally two-dimensional cavity,” *Int. J. Heat Fluid Flow*, vol. 16, no. 3, pp. 171 – 177, 1995.
- [126] D. Apsley, W.-L. Chen, M. Leschziner, and F.-S. Lien, “Non-linear eddy-viscosity modelling of separated flows,” *J. Hydraulic Research*, vol. 35, no. 6, pp. 723–748, 1997.
- [127] J. Tu, G. H. Yeoh, and C. Liu, *Computational fluid dynamics: a practical approach*. Butterworth-Heinemann, 2018.
- [128] F. R. Menter and F. R. Menter, “Two-equation eddy-viscosity turbulence models for engineering applications,” *AIAA J.*, vol. 32, no. 8, pp. 1598–1605, Aug 1994.
- [129] Y. Wang, S. Shen, G. Li, D. Huang, and Z. Zheng, “Investigation on aerodynamic performance of vertical axis wind turbine with different series airfoil shapes,” *Renew. Energy*, vol. 126, pp. 801 – 818, 2018.
- [130] K. Gharali and D. A. Johnson, “Numerical modeling of an S809 airfoil under dynamic stall, erosion and high reduced frequencies,” *Appl. Energy*, vol. 93, pp. 45 – 52, 2012, (1) Green Energy; (2) Special Section from papers presented at the 2nd International Energy 2030 Conf.
- [131] R. Lanzafame and M. Messina, “Power curve control in micro wind turbine design,” *Energy*, vol. 35, no. 2, pp. 556 – 561, 2010.
- [132] R. S. Jackson and R. Amano, “Experimental study and simulation of a small-scale horizontal-axis wind turbine,” *J. Energy Resour. Technol.*, vol. 139, no. 5, pp. 051207–19, Mar 2017.
- [133] B. A. Mulugeta and A. Gerawork, “Aerodynamic design of horizontal axis wind turbine blades,” *FME Trans.*, vol. 45, no. 4, pp. 647–660, 2017.
- [134] A. Betz, “Das maximum der theoretisch möglichen ausnützung des windes durch windmotoren,” *Zeitschrift für das gesamte Turbinenwesen*, vol. 26, pp. 307–309, 1920.
- [135] M. Hansen, *Aerodynamics of Wind Turbines*, 2nd ed. Earthscan, 2013.
- [136] R. E. Wilson and P. B. S. Lissaman, “Applied aerodynamics of wind power machines,” *NASA STI/Recon Technical Report N*, vol. 75, Jul 1974.
- [137] G. Ingram, “Wind turbine blade analysis using the blade element momentum method,” *Durham University, Durham*, 2005.
- [138] D. A. Spera, Ed., *Wind turbine technology: Fundamental concepts in wind turbine engineering*. ASME Press, 2009.
- [139] F.-B. Hsiao, C.-J. Bai, and W.-T. Chong, “The performance test of three different horizontal axis wind turbine (HAWT) blade shapes using experimental and numerical methods,” *Energies*, vol. 6, no. 6, p. 2784, 2013.
- [140] K. Maalawi and M. Badr, “A practical approach for selecting optimum wind rotors,” *Renew. Energy*, vol. 28, no. 5, pp. 803 – 822, 2003.
- [141] S. Rajakumar and D. Ravindran, “Iterative approach for optimising coefficient of power, coefficient of lift and drag of wind turbine rotor,” *Renewable Energy*, vol. 38, no. 1, pp. 83 – 93, 2012.
- [142] Z. N. Ashrafi, M. Ghaderi, and A. Sedaghat, “Parametric study on off-design aerodynamic performance of a horizontal axis wind turbine blade and proposed pitch control,” *Energy Conv. Manag.*, vol. 93, pp. 349 – 356, 2015.
- [143] R. L. U. de Freitas Pinto and B. P. F. Gonçalves, “A revised theoretical analysis of aerodynamic optimization of horizontal-axis wind turbines based on BEM theory,” *Renewable Energy*, vol. 105, pp. 625 – 636, 2017.

BIBLIOGRAPHY

- [144] S. Lee, H. Kim, E. Son, and S. Lee, "Effects of design parameters on aerodynamic performance of a counter-rotating wind turbine," *Renewable Energy*, vol. 42, pp. 140 – 144, 2012, international Symposium on Low Carbon and Renewable Energy Technology 2010 (ISLCT 2010).
- [145] E. Kulunk and N. Yilmaz, "Computer-aided design and performance analysis of hawt blades," in *5th International Advanced Technologies Symposium*. Citeseer, 2009.
- [146] A. Sedaghat and M. Mirhosseini, "Aerodynamic design of a 300 kW horizontal axis wind turbine for province of semnan," *Energy Conversion and Management*, vol. 63, pp. 87 – 94, 2012, 10th International Conference on Sustainable Energy Technologies (SET 2011).
- [147] A. Sharifi and M. Nobari, "Prediction of optimum section pitch angle distribution along wind turbine blades," *Energy Conversion and Management*, vol. 67, pp. 342 – 350, 2013.
- [148] X. Liu, L. Wang, and X. Tang, "Optimized linearization of chord and twist angle profiles for fixed-pitch fixed-speed wind turbine blades," *Renewable Energy*, vol. 57, pp. 111 – 119, 2013.
- [149] A. Sedaghat, M. El Haj Assad, and M. Gaith, "Aerodynamics performance of continuously variable speed horizontal axis wind turbine with optimal blades," *Energy*, vol. 77, no. C, pp. 752–759, 2014.
- [150] M. Ozair, S. Sarfaraz, M. Husain, and M. N. Qureshi, "Aerodynamic design and analysis of horizontal-axis wind-turbine," in *Space & Upper Atmosphere Research Commission, Karachi, Pakistan*, 2011.
- [151] P. C. Rocha, H. B. Rocha, F. M. Carneiro, M. V. da Silva, and A. V. Bueno, " k - ω sst (shear stress transport) turbulence model calibration: A case study on a small scale horizontal axis wind turbine," *Energy*, vol. 65, pp. 412 – 418, 2014.
- [152] H. Yang, W. Shen, H. Xu, Z. Hong, and C. Liu, "Prediction of the wind turbine performance by using BEM with airfoil data extracted from CFD," *Renew. Energy*, vol. 70, pp. 107 – 115, 2014.
- [153] G. Richmond-Navarro, W. R. Calderón-Muñoz, R. LeBoeuf, and P. Castillo, "A magnus wind turbine power model based on direct solutions using the blade element momentum theory and symbolic regression," *IEEE Trans. Sustain. Energy*, vol. 8, no. 1, pp. 425–430, Jan 2017.
- [154] S. J. Schreck and M. C. Robinson, "Horizontal axis wind turbine blade aerodynamics in experiments and modeling," *IEEE Trans. Energy Conv.*, vol. 22, no. 1, pp. 61–70, March 2007.
- [155] O. K. G. Tietjens and L. Prandtl, "Applied hydro- and aeromechanics: Based on lectures of L. Prandtl," vol. 2. Courier Corporation: Cambridge University Press, 1957.
- [156] S. O. Gundtoft, *Wind Turbines*. University College of Aarhus, 2009.
- [157] F. Bianchi, H. de Battista, and R. Mantz, *Wind Turbine Control Systems: Principles, Modelling and Gain Scheduling Design*, ser. Advances in Industrial Control. Springer London, 2006.
- [158] S. Roy and U. K. Saha, "Wind tunnel experiments of a newly developed two-bladed savonius-style wind turbine," *Appl. Energy*, vol. 137, pp. 117 – 125, 2015.
- [159] C. Bottasso, F. Campagnolo, and A. Croce, "Computational procedures for the multi-disciplinary constrained optimization of wind turbines," *Scientific Report DIA-SR*, pp. 10–02, 2010.
- [160] A. Chehouri, R. Younes, A. Ilinca, and J. Perron, "Review of performance optimization techniques applied to wind turbines," *Appl. Energy*, vol. 142, pp. 361 – 388, 2015.
- [161] W. Ramberg and S. Levy, "Calculation of stresses and natural frequencies for a rotating propeller blade vibrating flexurally," *J. Res. Natl. Bur. Stand.*, vol. 21, 1938.
- [162] D. J. C. Salzmann and J. V. D. Tempel, "Aerodynamic damping in the design of support structures for offshore wind turbines," in *European offshore wind conf., Copenhagen, Denmark*, 2005.
- [163] X. Liu, C. Lu, G. Li, A. Godbole, and Y. Chen, "Effects of aerodynamic damping on the tower load of offshore horizontal axis wind turbines," *Appl. Energy*, vol. 204, pp. 1101 – 1114, 2017.
- [164] J. Chapman, I. Masters, M. Togneri, and J. Orme, "The Buhl correction factor applied to high induction conditions for tidal stream turbines," *Renew. Energy*, vol. 60, pp. 472 – 480, 2013.

- [165] I. Masters, J. C. Chapman, M. R. Willis, and J. A. C. Orme, "A robust blade element momentum theory model for tidal stream turbines including tip and hub loss corrections," *J. Mar. Eng. Technol.*, vol. 10, no. 1, pp. 25–35, 2011.
- [166] A. Tabesh and R. Iravani, "Small-signal dynamic model and analysis of a fixed-speed wind farm - a frequency response approach," *IEEE Trans. Power Del.*, vol. 21, no. 2, pp. 778–787, April 2006.
- [167] L. A. Viterna and R. D. Corrigan, "Fixed pitch rotor performance of large horizontal axis wind turbines," 1982.
- [168] S. Takahashi, Y. Ohya, T. Karasudani, and K. Watanabe, "Numerical and experimental studies of airfoils suitable for vertical axis wind turbines and an application of wind-energy collecting structure for higher performance," *Journal of Web Engineering*, pp. 327–330, 2006.
- [169] T. Uchida and Y. Ohya, "Micro-siting technique for wind turbine generators by using large-eddy simulation," *Journal of Industrial Aerodynamics*, vol. 96, no. 10-11, pp. 2121–2138, Oct. 2008.
- [170] H. Cao, "Aerodynamics analysis of small horizontal axis wind turbine blades by using 2D and 3D CFD modelling," Master's thesis, Sch. of Comput., Eng. and Phys. Sci., University of Central Lancashire, Preston, England, 2011.
- [171] H. Li and Z. Chen, "Overview of different wind generator systems and their comparisons," *IET Renew. Power Gen.*, vol. 2, no. 2, pp. 123–138, June 2008.
- [172] V. T. Phan and H. H. Lee, "Performance enhancement of stand-alone DFIG systems with control of rotor and load side converters using resonant controllers," *IEEE Trans. Ind. Appl.*, vol. 48, no. 1, pp. 199–210, Jan 2012.
- [173] G. Pannell, D. J. Atkinson, and B. Zahawi, "Analytical study of grid-fault response of wind turbine doubly fed induction generator," *IEEE Trans. Energy Conv.*, vol. 25, no. 4, pp. 1081–1091, Dec 2010.
- [174] M. S. Alam and M. A. Y. Abido, "Fault ride through capability enhancement of a large-scale PMSG wind system with bridge type fault current limiters," *Adv. Electr. Comput. Eng.*, vol. 18, no. 1, pp. 43–50, 2018.
- [175] M. S. Alam, M. A. Y. Abido, A. E.-D. Hussein, and I. El-Amin, "Fault ride through capability augmentation of a DFIG-based wind integrated VSC-HVDC system with non-superconducting fault current limiter," *Sustainability*, vol. 11, no. 5, pp. 1–23, 2019.
- [176] G. Rashid and M. H. Ali, "A modified bridge-type fault current limiter for fault ride-through capacity enhancement of fixed speed wind generator," *IEEE Trans. Energy Conv.*, vol. 29, no. 2, pp. 527–534, June 2014.
- [177] I. Ngamroo and T. Karaipoom, "Cooperative control of SFCL and SMES for enhancing fault ride through capability and smoothing power fluctuation of DFIG wind farm," *IEEE Trans. Appl. Supercond.*, vol. 24, no. 5, pp. 1–4, Oct 2014.
- [178] G. Rashid and M. H. Ali, "Transient stability enhancement of doubly fed induction machine-based wind generator by bridge-type fault current limiter," *IEEE Trans. Energy Conv.*, vol. 30, no. 3, pp. 939–947, Sept 2015.
- [179] M. Firouzi, G. B. Gharehpetian, and B. Mozafari, "Improvement of power system stability by using new switching technique in bridge-type fault current limiter," *Electr. Power Compon. Syst.*, vol. 43, no. 2, pp. 234–244, 2015.
- [180] A. Jalilian, S. B. Naderi, M. Negnevitsky, M. T. Hagh, and K. M. Muttaqi, "Controllable DC-link fault current limiter augmentation with DC chopper to improve fault ride-through of DFIG," *IET Renew. Power Gen.*, vol. 11, no. 2, pp. 313–324, 2017.
- [181] M. S. Alam, M. A. Y. Abido, and I. El-Amin, "Fault current limiters in power systems: A comprehensive review," *Energies*, vol. 11, no. 5, pp. 1–24, 2018.
- [182] A. Abramovitz and K. M. Smedley, "Survey of solid-state fault current limiters," *IEEE Trans. Power Electron.*, vol. 27, no. 6, pp. 2770–2782, June 2012.

BIBLIOGRAPHY

- [183] M. Wang, W. Xu, J. Hongjie, and X. Yu, "A new control system to strengthen the LVRT capacity of DFIG based on both crowbar and DC chopper circuits," in *IEEE Innov. Smart Grid Tech. - Asia (ISGT Asia)*, May 2012, pp. 1–6.
- [184] L. G. Meegahapola, T. Littler, and D. Flynn, "Decoupled-DFIG fault ride-through strategy for enhanced stability performance during grid faults," *IEEE Trans. Sustain. Energy*, vol. 1, no. 3, pp. 152–162, Oct 2010.
- [185] J. J. Justo, F. Mwasilu, and J.-W. Jung, "Doubly-fed induction generator based wind turbines: A comprehensive review of fault ride-through strategies," *Renew. Sust. Energy Rev.*, vol. 45, pp. 447–467, 2015.
- [186] C. Zhao, Z. Wang, D. Zhang, J. Zhang, X. Du, W. Guo, L. Xiao, and L. Lin, "Development and test of a superconducting fault current limiter-magnetic energy storage (SFCL-MES) system," *IEEE Trans. Appl. Supercond.*, vol. 17, no. 2, pp. 2014–2017, June 2007.
- [187] M. Abdolkarimzadeh, M. Nazari-Heris, M. Abapour, and M. Sabahi, "A bridge-type fault current limiter for energy management of AC/DC microgrids," *IEEE Trans. Power Electron.*, vol. 32, no. 12, pp. 9043–9050, Dec 2017.
- [188] G. Abad, J. López, M. A. Rodríguez, L. Marroyo, and G. Iwanski, *Doubly Fed Induction Machine: Modeling and Control for Wind Energy Generation*, M. E. El-Hawary, Ed. John Wiley & Sons, Inc., 2011.
- [189] L. Xu and W. Cheng, "Torque and reactive power control of a doubly fed induction machine by position sensorless scheme," *IEEE Trans. Ind. Appl.*, vol. 31, no. 3, pp. 636–642, 1995.
- [190] N. N. K., Swami and B. Singh, "Experimental implementation of doubly fed induction generator-based standalone wind energy conversion system," *IEEE Trans. Ind. Appl.*, vol. 52, no. 4, pp. 3332–3339, July 2016.
- [191] N. N. K. Swami and B. Singh, "Doubly fed induction generator for wind energy conversion systems with integrated active filter capabilities," *IEEE Trans. Ind. Inform.*, vol. 11, no. 4, pp. 923–933, Aug 2015.
- [192] M. T. Hagh and M. Abapour, "DC reactor type transformer inrush current limiter," *IET Electr. Power Appl.*, vol. 1, no. 5, pp. 808–814, Sept 2007.
- [193] T. Satoh, M. Yamaguchi, S. Fukui, K. Morikoshi, K. Kaiho, T. Matsumura, H. Shimizu, and N. Murayama, "Three-phase fault current limiter with one DC S/N transition element," *IEEE Trans. Appl. Supercond.*, vol. 11, no. 1, pp. 2398–2401, March 2001.
- [194] N. Mohan, W. P. Robbins, and T. M. Undeland, *Power Electronics: Converters, Applications, and Design*, 3rd ed. Hoboken, N. J. J. Wiley, 2007.
- [195] Manitoba, *Users Guide PSCAD 4.2.1*, 4th ed., Manitoba-HVDC Research Centre, Canada, 2008.
- [196] S. Das and R. Pampana, "Indian Wind Grid Code," Center for Energy Technology, Tech. Rep. PRDC/2009-2010/C-WET/831, 2009.
- [197] M. Lasantha, D. Manoj, N. Inam, and C. James, "Role of fault ride-through strategies for power grids with 100% power electronic-interfaced distributed renewable energy resources," *WIREs Energy Environ.*, vol. 7, no. 4, p. e292, 2018.
- [198] A.-M. Borbely and J. F. Kreider, *Distributed generation: The power paradigm for the new millennium*. Boca Raton, FL: CRC Press LLC, 2001.
- [199] R. S. Peña, J. C. Clare, and G. M. Asher, "Doubly fed induction generator using back-to-back PWM converters and its application to variable-speed wind-energy generation," *IET Electr. Power Appl.*, vol. 143, pp. 380 – 387, 10 1996.
- [200] A. M. Shiddiq Yunus, M. A. S. Masoum, and A. Abu-Siada, "Effect of STATCOM on the low-voltage-ride-through capability of Type-D wind turbine generator," in *IEEE PES Innov. Smart Grid Tech.*, 2011, pp. 1–5.
- [201] K. Elkington, V. Knazkins, and M. Ghandhari, "On the stability of power systems containing doubly fed induction generator-based generation," *Electr. Pow. Syst. Res.*, vol. 78, no. 9, pp. 1477 – 1484, 2008.

- [202] L. Shi, S. Dai, Y. Ni, L. Yao, and M. Bazargan, "Transient stability of power systems with high penetration of dfig based wind farms," in *IEEE Power Eng. Soc. General Meeting*, July 2009, pp. 1–6.
- [203] W. T. Liu, Y. K. Wu, C. Y. Lee, and C. R. Chen, "Effect of low-voltage-ride-through technologies on the first taiwan offshore wind farm planning," *IEEE Trans. Sustain. Energy*, vol. 2, no. 1, pp. 78–86, Jan 2011.
- [204] D. Gautam, V. Vittal, and T. Harbour, "Impact of increased penetration of dfig-based wind turbine generators on transient and small signal stability of power systems," *IEEE Trans. Power Syst.*, vol. 24, no. 3, pp. 1426–1434, Aug 2009.
- [205] C. Konstantinou, "A study on the impact of wind generation on the stability of electromechanical oscillations," *CoRR*, vol. abs/1502.00215, 2015.
- [206] M. P. Palsson, T. Toftveaag, K. Uhlen, and J. O. G. Tande, "Large-scale wind power integration and voltage stability limits in regional networks," in *IEEE Power Eng. Soc. Summer Meeting*, vol. 2, July 2002, pp. 762–769.
- [207] M. Hossain, H. Pota, and V. Ugrinovskii, "Short and long-term dynamic voltage instability," *IFAC Proc. Vol.*, vol. 41, no. 2, pp. 9392 – 9397, 2008, 17th IFAC World Congress.
- [208] M. J. Hossain, H. R. Pota, V. Ugrinovskii, and R. A. Ramos, "Excitation control for large disturbances in power systems with dynamic loads," in *IEEE Power Eng. Soc. General Meeting*, July 2009, pp. 1–8.
- [209] M. Moradzadeh, H. Shayeghi, L. Vandeveld, and M. Saif, "Impact of increased penetration of large-scale wind farms on power system dynamic stability - a review," in *15th IEEE Int. Conf. Environment Elect. Eng.*, June 2015, pp. 1522–1526.
- [210] A. Shaik and P. Tripathy, "Development of phasor estimation algorithm for p-class PMU suitable in protection applications," *IEEE Trans. Smart Grid*, vol. PP, no. 99, pp. 1–1, 2016.
- [211] R. Piwko, N. Miller, J. Sanchez-Gasca, X. Yuan, R. Dai, and J. Lyons, "Integrating large wind farms into weak power grids with long transmission lines," in *5th CES/IEEE Conf. Int. Power Electron. Motion Control*, vol. 2, Aug 2006, pp. 1–7.
- [212] W. Qiao, G. K. Venayagamoorthy, and R. G. Harley, "Real-Time implementation of a STATCOM on a wind farm equipped with doubly fed induction generators," *IEEE Trans. Ind. Appl.*, vol. 45, no. 1, pp. 98–107, 2009.
- [213] Siemens PTI, PSS Sincal, Ver. 12.0, Online Documentation, April 2016.
- [214] S. Affijulla and P. Tripathy, "A robust fault detection and discrimination technique for transmission lines," *IEEE Trans. Smart Grid*, vol. PP, no. 99, pp. 1–1, 2017.
- [215] B. Wu, Y. Lang, N. Zargari, and S. Kouro, *Power Conversion and Control of Wind Energy Systems*. John Wiley & Sons, Inc., 2011, ch. Appendix B: Generator Parameters, pp. 319–326.
- [216] W. Jones and B. Launder, "The prediction of laminarization with a two-equation model of turbulence," *Int. J. Heat Mass Tran.*, vol. 15, no. 2, pp. 301 – 314, 1972.
- [217] B. Launder and D. Spalding, "The numerical computation of turbulent flows," *Comput. Methods Appl. M.*, vol. 3, no. 2, pp. 269 – 289, 1974.
- [218] K. Pope, I. Dincer, and G. Naterer, "Energy and exergy efficiency comparison of horizontal and vertical axis wind turbines," *Renew. Energy*, vol. 35, no. 9, pp. 2102 – 2113, 2010.
- [219] Western Electricity Coordination Council (WECC) Renewable Energy Modeling Task Force, "Wind power plant dynamic modeling guide," WECC Modeling and Validation Work Group, Tech. Rep., 2010.
- [220] North-Eastern-Load-Dispatch-Center, "NERLDC power system guide," PGCIL, India, Tech. Rep., 2014.



List of Publications

Journal Publications

- **Published Papers**

1. **Umesh Chaudhary**, Praveen Tripathy, and Sisir Kumar Nayak, “Application of Thyristor Bridge-Type Non-Superconducting FCL with Buck Series Charging to Improve the FRT Capability of the DFIG System”, in *Electr. Power Compon. Syst.*, vol. 48, no. 18, pp. 1898–1911, 2021. (doi: 10.1080/15325008.2021.1906788)

- **Manuscripts Under Preparations**

1. **Umesh Chaudhary**, Praveen Tripathy and Sisir Kumar Nayak, “Analysis of Aerodynamic Performance of Distinct Airfoil Profiles Using the Finite-Volume Approach”, (Journal under preparation).
2. **Umesh Chaudhary**, Praveen Tripathy and Sisir Kumar Nayak, “Minimizing the Computational Load for Predicting the Aerodynamic Performance of Wind Turbine Using BEM Theory”, (Journal under preparation).

Conference Publications

1. **Umesh Chaudhary**, Praveen Tripathy and Sisir Kumar Nayak, “Application of Bridge-Type FCL for Betterment of FRT Capability for DFIG-Based Wind Turbine”, in 6th *IEEE POWER INDIA International Conference (PIICON 2014)*, New Delhi, pp. 1–6, Dec. 2014. (doi: 10.1109/POWERI.2014.7117687)
2. **Umesh Chaudhary**, Prosenjit Mondal, Praveen Tripathy, Sisir Kumar Nayak and Ujjwal K. Saha, “Modeling and Optimal Design of Small HAWT Blades for Analyzing the Starting Torque Behavior”, in 18th *National Power System Conference (NPSC 2014)*, IIT Guwahati, pp. 1–6, Dec. 2014. (doi: 10.1109/NPSC.2014.7103886)
3. **Umesh Chaudhary**, and Sisir Kumar Nayak, “Micro and Small-Scale HAWT Blades Airfoils Study through CFD Analysis for Low Wind Applications”, in 12th *IEEE India International Conference (INDICON 2015)*, New Delhi, pp. 1–6, Dec. 2015. (doi: 10.1109/INDICON.2015.7443703)



Bio-data of the Author

Mr. Umesh Chaudhary was born in Bihar, India, in 1986. He received the B.Sc. (Engg.) degree in Electrical Engineering from Bhagalpur College of Engineering, Bhagalpur, India, in April-2009 and M.E. degree in Electrical Engineering from Indian Institute of Science, Bangalore, India, in June-2011. He next joined the Ph.D. program in Electronics and Electrical Engineering at IIT Guwahati, and thesis submitted for degree in April-2022.

Permanent Address: S/O Babu Lal Chaudhary
Head Manpur "Big Well"
Buniyadganj (Post)
Gaya-823 003
Bihar, India

Contact Address: D-116, Lohit Hostel
Indian Institute of Technology Guwahati
Amingaon, North Guwahati-781 039
Assam, India

Contact Number: (+91)-995-4181507

His research interests lie in wind turbine blade modeling, applications of power electronics in renewable energy especially wind turbine, fault current limiter, power quality issues, power system dynamics and stability.

